Ultrafast Dynamics of Correlated Electrons

Im Fachbereich Physik
der Freien Universität Berlin
eingereichte Dissertation

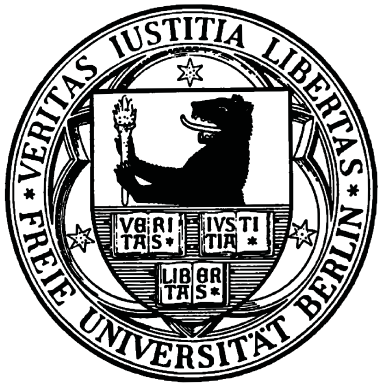

Laurenz Rettig

May 2012

This work was done between October 2008 and May 2012 in the group of Martin Wolf at the Freie Universität Berlin and the group of Uwe Bovensiepen at the Universität Duisburg-Essen

Berlin, in May 2012

Erstgutachter: Prof. Dr. Martin Wolf

Zweitgutachter: Prof. Dr. Martin Weinelt

Drittgutachter: Prof. Dr. Walter Pfeiffer

Datum der Disputation: 09.07.2012

Abstract

This work investigates the ultrafast electron dynamics in correlated, low-dimensional model systems using femtosecond time- and angle-resolved photoemission spectroscopy (trARPES) directly in the time domain. In such materials, the strong electron-electron (e-e) correlations or coupling to other degrees of freedom such as phonons within the complex many-body quantum system lead to new, emergent properties that are characterized by phase transitions into broken-symmetry ground states such as magnetic, superconducting or charge density wave (CDW) phases. The dynamical processes related to order like transient phase changes, collective excitations or the energy relaxation within the system allow deeper insight into the complex physics governing the emergence of the broken-symmetry state. In this work, several model systems for broken-symmetry ground states and for the dynamical charge balance at interfaces have been studied.

In the quantum well state (QWS) model system Pb/Si(111), the charge transfer across the Pb/Si interface leads to an ultrafast energetic stabilization of occupied QWSs, which is the result of an increase of the electronic confinement to the metal film. In addition, a coherently excited surface phonon mode is observed. In antiferromagnetic (AFM) Fe pnictide compounds, a strong momentum-dependent asymmetry of electron and hole relaxation rates allows to separate the recovery dynamics of the AFM phase from electron-phonon (e-ph) relaxation. The strong modulation of the chemical potential by coherent phonon modes demonstrates the importance of e-ph coupling in these materials. However, the average e-ph coupling constant is found to be small. The investigation of the excited quasiparticle (QP) relaxation dynamics in the high-T_c superconductor $Bi_2Sr_2CaCu_2O_{8+\delta}$ reveals a striking momentum and fluence independence of the QP life times. In combination with the momentum-dependent density of excited QPs, this demonstrates the suppression of momentum scattering along the d-wave gap and establishes the Cooper pair recombination in a strong bottleneck regime as dominating relaxation channel. Finally, spectroscopy of the occupied and unoccupied band structure of the prototypical CDW material RTe_3 (R = rare-earth element) using a position-sensitive time-of-flight (pTOF) spectrometer demonstrates the Fermi surface (FS) nesting driven CDW formation and reveals several details that go beyond a simple Tight-Binding description. The pTOF enables the observation of the ultrafast closing of the CDW gap and the reformation of a continuous, metallic FS within < 200 fs after optical excitation. The determination of the transient CDW order parameter reveals a momentum-dependent, asymmetric closing of the CDW gap, that is explained by a transient modification of the nesting condition. The temperature dependence of the CDW amplitude mode shows a characteristic frequency softening, and the collective nature of the amplitude mode is demonstrated by its coherent control.

Deutsche Kurzfassung

Diese Arbeit untersucht die ultraschnelle Elektronendynamik in korrelierten, niedrigdimensionalen Modellsystemen mittels femtosekunden zeit- und winkelaufgelöster Photoelektronenspektroskopie direkt in der Zeitdomäne. In solchen Materialien führt die starke Elektron-Elektron Wechselwirkung und die Ankopplung an andere Freiheitsgrade des komplexen Vielteilchen-Quantensystems, wie Phononen, zu neuen, emergenten Eigenschaften, welche durch Phasenübergänge in Grundzustände mit gebrochener Symmetrie charakterisiert sind, wie etwa magnetische und supraleitende Phasen sowie Ladungsdichtewellen (charge density waves, CDWs). Die mit auftretender Ordnung verbundenen dynamischen Prozesse, wie transiente Phasenänderungen, kollektive Anregungen oder die Energierelaxation innerhalb eines Systems bieten tieferen Einblick in die komplexe Physik, welche das Auftreten der Zustände gebrochener Symmetrie beherrscht. In dieser Arbeit wurden mehrere Modellsysteme für Grundzustände mit gebrochener Symmetrie und für dynamische Ladungsumverteilung an Grenzflächen untersucht.

In dem Modellsystem für Quantentröge (quantum well states, QWSs) Pb/Si(111) führt der Ladungstransfer über die Pb/Si Grenzfläche zu einer ultraschnellen energetischen Stabilisierung der besetzten QWSs, welche aus der Zunahme der elektronischen Einschränkung auf den Metallfilm resultiert. Zusätzlich wird ein kohärent angeregtes Oberflächenphonon beobachtet. In antiferromagnetischen (AFM) Fe-Pniktid-Materialien erlaubt eine starke Asymmetrie in den Elektronen- und Lochrelaxationsraten, die Wiederherstellungsdynamik der AFM Phase von der Elektron-Phonon (e-ph) Relaxation zu trennen. Die starke Modulation des chemischen Potentials durch kohärente Phononenmoden unterstreicht die Bedeutung der e-ph Kopplung in diesen Materialien. Trotzdem wird eine kleine durchschnittliche e-ph Kopplungskonstante beobachtet. Die Untersuchung der Relaxationsdynamik angeregter Quasiteilchen (quasiparticles, QPs) in dem Hochtemperatur-Supraleiter $Bi_2Sr_2CaCu_2O_{8+\delta}$ zeigt eine auffällige Impuls- und Fluenzunabhängigkeit der QP-Lebensdauern. Dies zeigt, in Verbindung mit der impulsabhängigen Dichte von angeregten QPs, die Unterdrückung der Impulsstreuung entlang der *d*-Wellen Energielücke und zeigt die Cooper-Paar-Rekombination unter Einfluss eines starken Nadelöhrs als dominierenden Zerfallskanal auf. Die Spektroskopie der besetzten und unbesetzten Bandstruktur des prototypischen CDW Materials RTe_3 (R = Seltenerdenelement) mittels eines positionsempfindlichen Flugzeitspektrometers (pTOF) veranschaulicht die durch Verschachtelung der Fermioberfäche (Fermi surface, FS) ausgelöste Bildung der CDW und deckt verschiedene Details auf, welche über die Beschreibung durch ein einfaches Tight-Binding Modell hinausgehen. Das pTOF ermöglicht die Beobachtung eines ultraschnellen Verschwindens der CDW Bandlücke und die Wiederherstellung einer durchgehenden, metallischen FS innerhalb von < 200 fs nach der optischen Anregung. Die Bestimmung des transienten CDW Ordnungsparameters zeigt eine impulsabhängige, asymmetrische Schließung der CDW Bandlücke auf, welche durch eine transiente Modifikation der Verschachtelungsbedingung erklärt wird. Die Temperaturabhängigkeit der CDW Amplitudenmode zeigt eine charakteristische Frequenzaufweichung, and die kollektive Natur der Amplitudenmode wird durch ihre kohärente Kontrolle belegt.

Contents

List of Figures

List of Acronyms

1D one-dimensional

2D two-dimensional

2PPE two-photon photoemission

3D three-dimensional

4D four-dimensional

AFM antiferromagnetic

ARPES angle-resolved photoemission spectroscopy

BBO β-bariumborate

BCS Bardeen-Cooper-Schrieffer

BSCCO $Bi_2Sr_2CaCu_2O_{8+\delta}$

BZ Brillouin zone

CBE conduction band edge

CCD charge coupled device

CDW charge density wave

CFD constant-fraction discriminator

CP Cooper pair

CPA chirped pulse amplification

cw continuous wave

DECP displacive excitation of coherent phonons

DFT density functional theory

DOS density of states

e-e electron-electron

e-h electron-hole

e-ph electron-phonon

EDC energy distribution curve

EXAFS extended x-ray absorption fine structure

FFT fast Fourier transformation

FROG frequency-resolved optical grating

FS Fermi surface

FWHM full width at half maximum

HFB high-frequency boson

HHG high-harmonic generation

hoQWS highest occupied quantum well state

HTSC high-T_c superconductor

IPE inverse photoemission

IR infrared

IS interface state

ISRS impulsive stimulated Raman scattering

KBBF $KBe_2BO_3F_2$

LAPE laser-assisted photoemission

LEED low energy electron diffraction

LEM leading edge midpoint

LMTO linear muffin-tin orbital

LSCO $La_{2-x}Sr_xCuO_4$

MBE molecular beam epitaxy

MCP micro channel plate

MDC momentum distribution curve

MIGS metal-induced gap states

ML monolayer

NIM nuclear instrumentation module

OPA optical parametric amplifier

PES photoemission spectroscopy

ph-ph phonon-phonon

PID proportional-integral-differential

pTOF position-sensitive time-of-flight

QMS quadrupole mass spectrometer

QP quasiparticle

QWR quantum well resonance

QWS quantum well state

RTE Rothwarf-Taylor equations

S/N signal-to-noise

SC superconducting

SDW spin density wave

SHG second harmonic generation

SPV surface photo voltage

STM scanning tunneling microscopy

STS scanning tunneling spectroscopy

swFFT sliding window fast Fourier transformation

TB Tight-Binding

Ti:Sa Ti-doped sapphire

TOF time-of-flight

trARPES time- and angle-resolved photoemission spectroscopy

TTM two-temperature model

UHV ultra high vacuum

UV ultraviolet

VBE valence band edge

VIS visible

XC cross correlation

XUV extreme ultraviolet

1 Introduction

Electronic Correlations

Our modern technology is based on ever smaller structures that are used in applications such as microchips, organic nanomaterials or nanostructured devices. As such structures approach the size of individual atoms and molecules, their quantum mechanical behavior becomes more and more important and a classical, Newtonian description is insufficient to capture the properties of such materials. As a consequence, the complex interplay of quantum mechanical phenomena like entanglement, coherence and elementary excitations present in such structures poses a challenge for their understanding, but also the perspective for new applications and devices.

In this respect, emergent phenomena, i.e. any type of self-organization resulting from correlations, are of great importance, as the collective behavior of many constituents often leads to astonishing new and unexpected properties, that are by times completely different from the properties of the individual parts. In fact, emergence can be found nearly everywhere in nature, starting from the formation of sand dunes from individual grains, the self-organization in biological systems like animal colonies or the human brain up to abstract phenomena such as society, which emerges from the interplay of many individuals. In condensed-matter physics, the complex interaction of many degrees of freedom such as electrons, ions and spins lead to the formation of completely new and intriguing material properties such as superconductivity, magnetism, charge density waves (CDWs) or orbitally ordered states, just to name a few. The emergence of such states is controlled by a competition of correlations and fluctuation effects, that result in a phase transition at a critical temperature, where the correlations lead to coordination within a macroscopic region, resulting in the breaking of a symmetry of the system. Below the transition temperature, a new broken-symmetry ground state is formed, which can possess a variety of novel, emergent properties, that are macroscopically observable. The better understanding and control of this competition of correlations and fluctuations offers many possible applications such as sensors with extraordinary detection efficiency using materials close to a phase transition. In addition, the combination of various materials can lead to additional new phenomena such as the giant magnetoresistance (Nobel prize 2007), which is of great importance for data storage already today. As the properties of such heterostructures depend strongly on the interfaces between the various materials, the better understanding and control of the processes happening at these boundaries also might be relevant for new applications.

A prerequisite for the emergence of such novel phenomena in condensed matter are strong interactions of the constituting particles, i.e. a strong correlation of electrons in the many-body quantum system. Historically, the term strongly correlated electrons refers to electrons exhibiting a strong Coulomb repulsion, but correlation effects can also occur from many other effects such as electron-phonon (e-ph) coupling or the interaction with the electron spins. In the absence of strong correlations, the description of the complex many-body problem in the so called single-particle picture has proven to be very successful, where the interactions of the individual particles are replaced by an effective mean interaction. Single-particle descriptions such as e.g. the Hartree-Fock method are very successful in describing systems with weak correlations and the effect of moderate correlations can be introduced by perturbation methods such as e.g. the

self-energy formalism [Fet03].

In the presence of strong correlations, however, the single-particle approach utterly fails to capture the emergent properties that arise from the complex interactions, and the complete many-body problem has to be considered. Here, the Hubbard model, proposed in 1963 by J. Hubbard [Hub63], plays an important role, which considers electrons hopping between lattice sites and introduces correlations in form of an on-site coulomb repulsion U, that electrons exhibit if they occupy the same lattice site. Despite the simplicity of the model, exact solutions are only known for the one-dimensional (1D) case. Here, at half-filling of an electron band, i.e. one electron per site, the correlations lead to a suppression of the hopping and hence to a transition from a metallic to an insulating phase, known as the Mott metal-to-insulator transition.

One example of such Mott-insulators are the parent compounds of the cuprate high-T_c superconductors (HTSCs). These fascinating materials offer, aside from their unusually high superconducting transition temperatures, a variety of complex phases arising from strong correlations in these systems, such as the mentioned antiferromagnetic (AFM) Mott-insulating phase, a strange metal phase, or the still controversial pseudogap phase [Dam03]. If and in what way these correlations are of importance for the superconductivity in these systems, that emerges at higher doping levels, is up to now unclear, and a consensus on the mechanism of their d-wave superconductivity has yet to be reached. Here, the recent discovery of high-T_c superconductivity in Fe pnictides raised a lot of hope to gain more inside into these systems. While the pnictides also present a complex interplay of competing broken-symmetry phases, at least electronic correlation effects appear to be weaker in these compounds [Nor11]. In contrast, magnetic correlations seem to play a crucial role in these materials, leading to a spin density wave (SDW) phase at low doping levels. The very similar ordered state of a CDW is in its description and its relation to e-ph coupling also closely related to superconductivity and is caused by strong correlations between the electrons and the lattice in a low-dimensional system [Grü94]. Thus, by studying well-defined model systems for such interactions, one can learn more about their basic physics without the complications of the richness of phases found in the HTSCs.

Time and Angle-Resolved Photoemission Spectroscopy

Most processes in nature are happening out of equilibrium. The most compelling example might be life itself, which creates order out of a constant flow of energy; other examples are e.g. the movement of tectonic plates and earthquakes, the constant flow of water through the atmosphere or even the dynamical evolution of the whole universe starting from the Big Bang. On the small scale in e.g. device manufacturing, any process that involves a directed change of material properties is characterized by a non-equilibrium starting point and its dynamical evolution towards a ground state. Thus, a deeper understanding of and a proper theoretical description for the non-equilibrium properties and the related dynamical processes are crucial for the development of novel materials and for the prediction of their behavior.

In general, the dynamical processes as well as emergent properties such as new ground states of broken symmetry are governed by the complex interplay of the various elementary interactions of the conduction electrons present in a solid. These different interactions occur on intrinsically different energy- and timescales, which are determined by the strength of the respective force. While in typical metals this involves electron-electron (e-e) and e-ph scattering rates [DF00, Chu06], in more complex materials with ordered

states emerging in competition with thermal fluctuations, e. g. superconducting (SC), CDW, or magnetically ordered materials, excitations specific to the ordered nature become essential [Sch10]. In the energy domain, close to equilibrium, these interactions are often difficult to disentangle and are mostly present all at a time. In contrast, the investigation of systems far from equilibrium and of the dynamics following optical excitation provides a way to separate different interactions owing to their different intrinsic timescales. As most of these interactions are of considerable strength and hence occur on an ultrafast timescale ranging from attoseconds to picoseconds, this requires appropriate methods for their investigation. Time-resolved photoemission spectroscopy (PES) techniques employ femtosecond (fs) laser pulses in a pump-probe scheme and thus provide such a tool for the study of these interactions directly in the time domain. In addition, with their spectral resolution they combine energy- and time-domain approaches into a powerful method to obtain information on the influence of the various excitations on the electronic band structure in a direct way.

Conventional angle-resolved photoemission spectroscopy (ARPES) has become a very important technique for analyzing the occupied band structure, since it offers direct access to the single-particle spectral function in reciprocal k-space [Hüf03, Dam03]. In the last decades, its contributions had a significant impact on our current understanding of the electronic ground state properties of solid state materials. In particular, in the case of the cuprate [Dam03] and more recently the pnictide [Ric11] HTSCs, ARPES has played a crucial role in determining the effects of correlations on the electronic structure throughout the phase diagram. The time- and angle-resolved photoemission spectroscopy (trARPES) combines this powerful technique with the optical excitation of the sample by an intense fs pump laser pulse, followed by a time-delayed probe pulse which monitors the transient k-resolved band structure out of equilibrium by ARPES. This approach represents a powerful technique that is capable of adding information about emergent phenomena in condensed matter, that are hardly accessible by ARPES alone. Using trARPES, one can observe phase transitions in real time in a highly excited system [Rhi03, Lis05b, Per06, Sch08a, Roh11], that are usually only described using infinitesimally small perturbations in theoretical frameworks such as the linear response theory or Ginzburg-Landau theory [Ash76, Grü94]. This opens completely new benchmarks for theories describing dynamical phase transitions far from equilibrium [Fre09, Mor10], in addition to its potential for allowing ultrafast control of the state of matter at a quantum level [Fau11, Kim12]. Moreover, trARPES allows to investigate the energy transfer between the electrons and other degrees of freedom present in the system, and the coupling of the electronic states to collective excitation such as phonons and magnons can be studied [Bov07]. The dynamical modification of the charge balance at interfaces in heterostructures can also lead to a significant influence on the electronic properties, which are observable by trARPES.

While the spectroscopy of unoccupied states is usually the domain of time- and angle-resolved two-photon photoemission (2PPE) [Fau95, Pet97, Wei02b, Zhu04, Güd05, Kir10, Mat10], trARPES also allows for the spectroscopy of unoccupied states. Moreover, only the use of larger probe photon energies as in trARPES enables the k-resolved investigation of states closely above E_F in a significant part of the Brillouin zone (BZ), which are, however, of vital interest for understanding important material properties such as electrical conductivity. Here, trARPES reveals its potential as a powerful tool for the momentum, energy and time-resolved spectroscopy of states well below and above the Fermi level.

Correlated Electron Model Systems

This work covers the electron dynamics after optical excitation in a number of selected model systems for correlated electrons and for the coupling between various excitations in complex matter. Following a brief theoretical survey of the basic concepts used in this thesis in chapter 2 and a description of the experimental setups and procedures in chapter 3, time-resolved ARPES experiments on four different model systems are presented:

Quantum Well States in ultrathin Metal Films on Semiconductor Surfaces: Pb/Si(111) (chapter 4)

Ultrathin epitaxial films of the simple *sp*-band metal Pb on Si(111) surfaces present a fascinating model system for the study of quantum confinement in a quasi-two-dimensional (2D) structure. In these epitaxial films, electrons are confined by the bandgap of the substrate, and for sufficiently thin films, a series of sharp quantum well states (QWSs) in the occupied and unoccupied band structure can be observed [Wei02a, Kir10]. These distinct QWSs react very sensitively on the precise structure, charge balance and energy alignment at the interface in the heterostructure between the semiconducting substrate and the metallic overlayer. Whereas Pb is strictly speaking not a strongly correlated metal, and the description in a single-particle picture is still valid [Hor84], it exhibits one of the strongest e-ph coupling constants of all metals [Sav96]. This gives rise to superconductivity at comparatively high temperatures, and Pb exhibits a Kohn anomaly in the phonon dispersion [Sav96]. In addition, the confinement to a quasi-2D system strongly influences many of the material properties, such as the superconducting phase [Guo04, Bru09] or the carrier mobility [Vil02], which then by themselves depend on the properties of the interfacial structure.

Here, the focus is set on the dynamics at the interface between the Si substrate and the Pb overlayer and its influence on the electronic structure within the ultrathin metallic film, which is presented in chapter 4. A transient, coverage-dependent energy gain of the QWSs is observed, which is induced by an ultrafast charge redistribution at the interface and a transient increase of the QWS confinement to the metal film. In addition, coherent oscillations of a surface phonon mode demonstrate the remarkable sensitivity of QWSs to modifications of the confinement conditions.

Antiferromagnetism and Electron-Phonon interaction in Fe Pnictide Compounds: $EuFe_2As_2$, $BaFe_2As_2$ and $BaFe_{1.85}Co_{0.15}As_2$ (chapter 5)

The recently discovered new class of Fe based high-T_c superconductors presents a very interesting correlated model system, which has a similarly rich phase diagram as the cuprate HTSCs. However, in the Fe pnictides, the ground state of the parent compounds is an antiferromagnetic metal, which exhibits a spin density wave ordering, instead of the insulating Mott-Hubbard phase in the cuprates. Thus, the smaller electronic correlations and the metallicity of the ground state enables an investigation of the dynamics related to spin correlations in the Fe pnictides, which are one potential candidate for the pairing interaction in both the pnictide and the cuprate HTSCs. Furthermore, the interaction of lattice vibrations with electronic states is of strong interest in these compounds, presenting another possible superconducting glue.

The ultrafast electron dynamics of the hole pocket at the BZ center, representing an important part of the Fermi surface (FS), is investigated in the Fe pnictide parent

compounds $EuFe_2As_2$ and $BaFe_2As_2$ in the SDW phase in chapter 5, allowing to study the collapse and reformation of the AFM order for various temperatures. In addition, various methods to obtain quantitative information on the strength of e-ph coupling in $EuFe_2As_2$, $BaFe_2As_2$ and superconducting $BaFe_{1.85}Co_{0.15}As_2$ are compared. Here, especially the coupling of specific phonon modes to states close to the Fermi level is of importance, which are detected in the coherent response of the system directly in the time domain.

Excited Quasiparticle Dynamics in Cuprate High-T_c Superconductors: $Bi_2Sr_2CaCu_2O_{8+\delta}$ (chapter 6)

The cuprate HTSCs with their exceptionally high critical temperatures offer the opportunity to study the dynamics of the SC phase transition in real time and to observe the collapse and reformation of the SC condensate. The study of these relaxation processes might provide deeper insight into the fundamental interactions relevant in the process of Cooper pair (CP) formation and thus responsible for high-T_c superconductivity. However, their d-wave superconducting gap, which changes in magnitude along the FS, complicates the analysis of the dynamics using k-integrating observation methods such as time-resolved optical or THz spectroscopy. In addition, the identification of competing relaxation channels such as momentum scattering of excited quasiparticles (QPs) demands for a k-resolved analysis of the respective dynamics.

The investigation of $Bi_2Sr_2CaCu_2O_{8+\delta}$ (BSCCO) well in the SC phase using trARPES discussed in chapter 6 allows for such a momentum-resolved analysis of QP relaxation dynamics and to identify the relevant relaxation mechanisms. In addition, it enables the observation of the transient superconducting condensate in a direct and unambiguous manner. The observation of a strong bottleneck in the relaxation of pairing bosons might be helpful to track down the pairing mechanism through the possible relaxation channels available for the various types of interactions. In addition, the momentum dependence of the QP dynamics in the metallic phase for $T > T_c$ can provide important information on the controversial pseudogap phase.

Prototypical Charge Density Wave Materials: RTe_3 (chapter 7)

The layered material RTe_3 with R being a member of the rare-earth family presents a prototypical model system for the formation of a charge density wave and allows to study the effects of strong correlations between electronic and lattice degrees of freedom. In this family of layered binary compounds, the quasi-1D electronic band structure near the Fermi level is almost completely determined by the in-plane orbital overlap in the high-symmetry directions. This results in a quasi-1D, diamond shaped FS, which can be well described in a simple Tight-Binding picture. The strong nesting of the quasi-1D FS leads to the formation of a CDW distortion and a Peierls metal-to-insulator transition, which results in large band gaps opening in the electronic structure close to E_F. The substitution of rare-earth atoms allows to sensitively tune the CDW transition temperature and the size of the band gap, and for the heavier members of the series, also a second CDW transition at lower temperatures is observed.

In chapter 7, high-resolution ARPES data of $HoTe_3$ are presented and the effect of the two CDW transitions present in this system are discussed in comparison to the Tight-Binding model for the *occupied* states. The efficient mapping of *unoccupied* states using trARPES presented for $TbTe_3$ marks the potential of this method for the angle-resolved detection of states closely above E_F. At high excitation densities, an ultrafast collapse of

the CDW gap is observed, which can be tracked in energy and momentum space in both occupied and unoccupied states and in the transient reformation of a continuous, metallic FS. At softer excitation, a coherent collective oscillation of the CDW gap amplitude is observed, which corresponds to the CDW amplitude mode. Its exact influence on the electronic band structure, temperature dependence and coherent control is discussed for $TbTe_3$, $DyTe_3$ and $HoTe_3$, and allows new insight into the nature of the coupling of specific phonon modes to the electronic structure.

In addition to the topics covered here, trARPES experiments on a heavy-Fermion compound exhibiting Kondo physics, $YbRh_2Si_2$, were performed in collaboration with the group of Prof. S. L. Molodtsov from the European XFEL in Hamburg, which are out of the scope of this thesis. Here, important information on the unoccupied band structure was gained and an anomaly in the lifetimes of excited electrons was encountered, which is possibly connected to the strong interaction of delocalized d and localized f electrons present in this system.

2 Theoretical Background

In this chapter, the fundamental theoretical concepts are briefly introduced, that are of importance for the present work on the ultrafast dynamics in complex electronic systems. In the discussion of the various topics, special focus is set on the description of the dynamical processes that are of relevance in this thesis.

First, in chapter 2.1 we discuss the electron-phonon (e-ph) interaction in solids, which is of importance for many aspects like the charge density wave formation investigated in this thesis. Here, the basic treatment of the coupled electron and lattice system in terms of the Fröhlich Hamiltonian and the Eliashberg coupling function is introduced. In addition, the e-ph coupling is discussed in the electron self-energy formalism of quantum many-body physics. From the dynamical point of view, the e-ph interaction is responsible for the energy transfer to the lattice from the electronic system, which couples initially to the laser light field. These processes are usually described in the context of the two-temperature model (TTM), which is introduced in chapter 2.1.2. In addition, the excitation with ultrashort laser pulses can lead to the generation of coherent lattice vibrations, as discussed in chapter 2.1.3.

The phenomenon of superconductivity, which presents a very interesting and useful property emerging from elementary interactions such as the e-ph coupling in many solids at very low temperatures, is introduced in chapter 2.2. We briefly discuss the basic properties and introduce the theoretical description of conventional superconductivity by the Bardeen-Cooper-Schrieffer (BCS) theory, before we give a short introduction into the field of unconventional superconductors. Finally, some models for the description of superconductors out of equilibrium are discussed in chapter 2.2.3.

Another broken-symmetry ground state discussed in this thesis is the formation of coupled instabilities of the electron, lattice and spin systems, called charge density wave (CDW) and spin density wave (SDW) phases. The formation and the properties of these broken-symmetry ground states, which are encountered in particular in low-dimensional structures, are outlined in chapter 2.3. The transition to these ordered phases, which is governed by the divergence of the Lindhard response function due to Fermi surface (FS) nesting, is discussed in the context of the mean-field theory. In addition, collective excitations of the CDW and SDW phases are introduced, which present macroscopic dynamical modulations of the coupled charge and spin density.

Finally, a theoretical description of the photoemission spectroscopy (PES) is given in chapter 2.4, which is the principal experimental tool employed in this thesis. The capabilities of angle-resolved photoemission spectroscopy (ARPES) to investigate the single-particle spectral function are discussed. Special emphasis is put on the femtosecond time- and angle-resolved photoemission spectroscopy (trARPES), which allows to study the transient evolution of the electronic system after optical excitation and is discussed in chapter 2.4.3.

2.1 Electron-Phonon Interaction

The conduction electrons in a solid are moving within the periodic potential of the lattice of ion cores. To a first approximation, this forces the wave functions of the electrons moving in the nearly-free electron gas to obey the periodicity of the lattice. This results in the description of the electronic wave functions by Bloch waves [Ash76, Kit04] and leads to the opening of energy gaps at the Brillouin zone (BZ) boundaries in the electron dispersion. In addition, the presence of the lattice can lead to interactions of the electrons and the ion cores: When an electron moves in the attractive potential of the positively charged ion cores, the ions are attracted by the negatively charged electrons and the lattice becomes transiently polarized.

This mechanism is the basis of the electron-phonon (e-ph) interaction in solids, where a charged quasiparticle (QP) (being an electron surrounded by a screening cloud of interactions with other particles) can generate quantized lattice vibrations, i.e. phonons, through the Coulomb interaction. This process plays an important role in a variety of fundamental properties of solids, such as the electrical conductivity or the relaxation of hot electrons. In addition, the e-ph interaction also influences directly the electronic dispersion due to a renormalization of the electronic band structure and is the basis of emergent phenomena in complex quantum system such as superconductivity or charge density waves (CDWs).

Formally, the e-ph coupled quantum system of conduction electrons and ion cores can be described in second quantization by the Fröhlich Hamiltonian [Frö54, Grü94]

$$\hat{H} = \sum_{\mathbf{k}} \epsilon_{\mathbf{k}} \hat{a}^{\dagger}_{\mathbf{k}} \hat{a}_{\mathbf{k}} + \sum_{\mathbf{q}} \hbar\omega_{\mathbf{q}} \hat{b}^{\dagger}_{\mathbf{q}} \hat{b}_{\mathbf{q}} + \sum_{\mathbf{k},\mathbf{q}} g_{\mathbf{q}} \hat{a}^{\dagger}_{\mathbf{k}+\mathbf{q}} \hat{a}_{\mathbf{k}} (\hat{b}^{\dagger}_{-\mathbf{q}} + \hat{b}_{\mathbf{q}}) \quad . \tag{2.1}$$

Here, $\hat{a}^{\dagger}_{\mathbf{k}}(\hat{a}_{\mathbf{k}})$ and $\hat{b}^{\dagger}_{\mathbf{q}}$ $(\hat{b}_{\mathbf{q}})$ are the creation (annihilation) operators of electrons and phonons, respectively, and $\epsilon_{\mathbf{k}}$ and $\hbar\omega_{\mathbf{q}}$ are the momentum-dependent single particle energy dispersions of electrons and phonons. In the Hamiltonian (2.1), the first term describes the individual Bloch electrons, and the second term describes the phonon oscillations of the solid. The third term is responsible for the interaction of electrons and phonons in the solid. It corresponds to the scattering of an electron in a state $|\mathbf{k}\rangle$ into a state $|\mathbf{k}+\mathbf{q}\rangle$ with the simultaneous emission of a phonon with momentum $-\mathbf{q}$ or the absorption of a phonon with momentum $\mathbf{q}$, as apparent from the arrangement of creation and annihilation operators in this term. Here, also energy conservation applies, which is not explicitly noted. The interaction strength is determined by the coupling constant [Grü94]

$$g_{\mathbf{q}} = i \left(\frac{\hbar}{2M\omega_{\mathbf{q}}} \right)^{1/2} |\mathbf{q}| V_{\mathbf{q}} \quad , \tag{2.2}$$

where M is the ion mass and $V_{\mathbf{q}}$ is the ionic potential of the ion cores in the momentum space.

A physically important quantity derived from the e-ph coupling constant $g_{\mathbf{q}}$ is the scattering probability of an initial electronic state with energy ϵ into all possible final states with energy $\epsilon \pm \hbar\omega$ due to the absorption or emission of a phonon with frequency ω. This transition probability is given by the momentum averaged Eliashberg coupling function $\alpha^2F(\omega)$ [Gri81], which can be written for excitations close to the Fermi level and a spherical Fermi surface (FS) as:

$$\alpha^2 F(\omega) = n(E_{\mathrm{F}}) \int \frac{\mathrm{d}\Omega_{\mathbf{k}}}{4\pi} \int \frac{\mathrm{d}\Omega_{\mathbf{k}'}}{4\pi} |g_{\mathbf{k}'-\mathbf{k}}|^2 \delta(\hbar\omega - \hbar\omega_{\mathbf{k}'-\mathbf{k}}) \quad . \tag{2.3}$$

Here, $n(E_\mathrm{F})$ is the electronic density of states (DOS) at the Fermi level and the integrations are performed on the FS. Two moments of the Eliashberg coupling function $\alpha^2F(\omega)$ are of importance: The dimensionless e-ph coupling constant λ, which appears in the Bardeen-Cooper-Schrieffer (BCS) theory of superconductivity (see chapter 2.2.1), sometimes called e-ph mass enhancement factor, is given by

$$\lambda = -2\int_0^{\omega_\mathrm{max}} \frac{\alpha^2F(\omega)}{\omega}\mathrm{d}\omega \quad , \tag{2.4}$$

where ω_max is the highest phonon frequency in the system. For the energy transfer between electron and lattice system, the quantity

$$2\int_0^{\omega_\mathrm{max}} \omega\alpha^2F(\omega)\mathrm{d}\omega = \lambda\left\langle\omega^2\right\rangle \tag{2.5}$$

is of importance, where $\left\langle\omega^2\right\rangle$ is the second moment of the phonon frequencies. Interestingly, these two quantities are independent of the exact shape of the phonon distribution in the solid [Gri81].

2.1.1 The Electron-Phonon Self-Energy

In the electronic band theory, interactions such as the e-ph coupling of the QPs are described by the electronic self-energy Σ. The effect of the self-energy on the electronic bands is that the free-electron-like QP dispersion $\epsilon_\mathbf{k}$ is modified by the real part of Σ, whereas an imaginary part of Σ introduces a finite lifetime of QPs and leads to the transfer of spectral weight from the sharp coherent QP peak near the free-electron band to a broad incoherent part of the QP dispersion at higher binding energies. The effect of Σ can be viewed as a "dressing" of the "naked" QPs with an interaction cloud, that surrounds it. For the e-ph interaction, the self energy is connected to the electron-phonon coupling constant λ through

$$\lambda = \mathrm{Re}\left(-\frac{\partial\Sigma}{\partial\omega}\right)_{\omega=E_\mathrm{F}} \quad . \tag{2.6}$$

The electronic self energy Σ directly enters the one-particle spectral function $A(\mathbf{k},\omega)$, that is measured in angle-resolved photoemission spectroscopy (ARPES) experiments (see chapter 2.4) through the Green's function $G(\mathbf{k},\omega)$ [Dam03, Hüf03, Fin07]:

$$G(\mathbf{k},\omega) = \frac{1}{\omega-\epsilon_\mathbf{k}-\Sigma(\mathbf{k},\omega)} \quad , \tag{2.7}$$

$$A(\mathbf{k},\omega) = \frac{1}{\pi}\mathrm{Im}G(\mathbf{k},\omega) = \frac{1}{\pi}\frac{\mathrm{Im}\Sigma}{(\omega-\epsilon_\mathbf{k}-\mathrm{Re}\Sigma)^2+(\mathrm{Im}\Sigma)^2} \quad . \tag{2.8}$$

For the coupling of a bosonic mode to the electrons close to E_F, the real part of the electron self energy $\mathrm{Re}\Sigma$ leads to a renormalization of the bare band dispersion, which exhibits an increase of the effective mass by the factor $1+\lambda$ (hence the name mass-enhancement factor) and a modified slope of the electron dispersion close to E_F. The imaginary part $\mathrm{Im}\Sigma$ leads to a broadening of the single particle spectra due to the finite lifetime obtained by the QPs. Thus, the real and imaginary parts of the electronic self energy can be determined from ARPES spectra from the positions and widths of the QP peaks, respectively, as has been demonstrated in various experiments [Val99, LaS00, Dam03, Kir05, Fin07, Sch08b]. In special cases, even the complete energy-resolved e-ph coupling function $\alpha^2F(\omega)$ can be determined from ARPES data [Shi04], which however requires a sophisticated theoretical description of the respective electronic system.

2.1.2 The Two-Temperature Model

The e-ph coupling also dominates the energy relaxation in a metallic system after optical excitation. The excitation photons only couple to the electrons and deposit their energy in the electronic system, but leave the lattice degrees of freedom mostly unaffected, as the ions are too massive to follow the fast oscillations of the light field. The following relaxation of the excited system is thus strongly determined by the energy transfer from the electronic system to the lattice, which usually happens on the timescale of a few hundred femtoseconds to several picoseconds [Fan92, DF00, Ret02, Lis05a]. A simplified model describing these processes in metals, which has been successfully used in the past, is the so-called two-temperature model (TTM) [Ani74, All87, DF00, Ret02, Lis04b, Lis05a]. This model is based on the assumption of two individual heat baths of the electronic and phononic subsystems, which are described by transient temperatures T_{el} and T_{ph}, respectively. It is assumed, that electron-electron (e-e) scattering and phonon-phonon (ph-ph) scattering is much stronger than the e-ph coupling and effectively leads to thermal distributions in both the electronic and phononic subsystems at all times. Then, the temporal evolution of electronic and phononic temperatures is given by two coupled differential equations [Ani74, Lis05a]:

$$\frac{\mathrm{d}T_{\mathrm{el}}}{\mathrm{d}t} = \frac{1}{C_{\mathrm{el}}}\frac{\partial}{\partial z}\left(\kappa_{\mathrm{el}}\frac{\partial}{\partial z}T_{\mathrm{el}}\right) - H(T_{\mathrm{el}},T_{\mathrm{ph}}) + \frac{S}{C_{\mathrm{el}}} \quad , \tag{2.9}$$

$$\frac{\mathrm{d}T_{\mathrm{ph}}}{\mathrm{d}t} = +\frac{C_{\mathrm{el}}}{C_{\mathrm{ph}}}H(T_{\mathrm{el}},T_{\mathrm{ph}}) \quad . \tag{2.10}$$

The electron temperature T_{el} is determined by the absorption of the light pulse S, the energy loss due to e-ph coupling $H(T_{\mathrm{el}},T_{\mathrm{ph}})$ and the diffusive heat transfer mediated by the electronic diffusion coefficient κ_{el}. The energy transfer from the electronic to the phononic system leads to a simultaneous increase of the lattice temperature T_{ph}, where the increase in temperature is given by the ratio of the heat capacity of electrons and phonons, C_{el} and C_{ph}, respectively. Due to the usually much smaller specific heat of the electronic system, the electronic temperatures immediately after excitation can obtain very high values up to several 1000 K. For the rate of energy transfer due to e-ph coupling $H(T_{\mathrm{el}},T_{\mathrm{ph}})$, a particularly simple expression in terms of the second moment of the Eliashberg coupling function $\lambda\langle\omega^2\rangle$ has been obtained [Kag57, All87]

$$H(T_{\mathrm{el}},T_{\mathrm{ph}}) = \gamma_T(T_{\mathrm{el}}-T_{\mathrm{ph}}) = \frac{3\hbar\lambda\langle\omega^2\rangle}{\pi k_B}\frac{T_{\mathrm{el}}-T_{\mathrm{ph}}}{T_{\mathrm{el}}} \quad , \tag{2.11}$$

where the rate of energy transfer is proportional to the temperature difference between electronic and phononic system.

The TTM has been successfully applied in various experiments [Ani74, EA87, All87, DF00, Ret02, Lis04b, Lis05a, Per07, Man10]. In addition, several approaches to describe the situation where the assumption of a thermalized electron and lattice system is violated have been made, such as the inclusion of an auxiliary temperature into an extended version of the TTM to describe the non-thermal part of the electron distribution [Lis04b, Lis05a] or a complete theoretical description with a non-thermal electron model [Gro92, Gro95]. The situation, where the e-ph relaxation is fast compared to the e-e scattering has been also investigated recently [Kab08].

2.1.3 Generation of Coherent Phonons

Another important manifestation of e-ph coupling is the excitation of coherent lattice vibrations by ultrashort light pulses. If the pulse duration of an exciting laser pulse

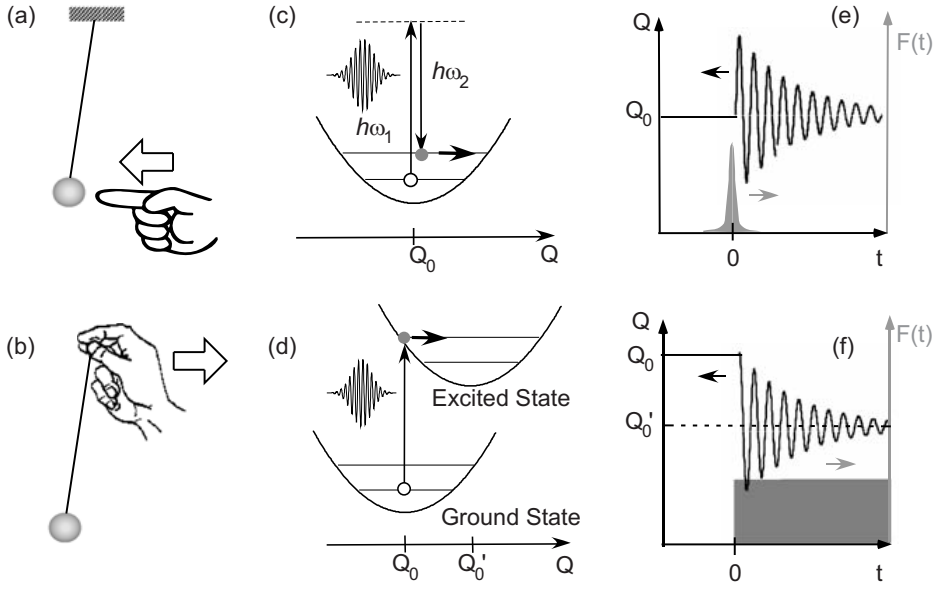

Figure 2.1: Sketch of the excitation of coherent phonons. (a), (c), (e) impulsive stimulated Raman scattering (ISRS). (b), (d), (f) displacive excitation of coherent phonons (DECP). Graphs (e) and (f) display the time evolution of the driving force (gray areas) and that of the displacement (solid curves) for ISRS and DECP, respectively. After [Ish10].

is short compared to the oscillation period of a lattice vibration in a solid, this can lead to a coherent excitation, where all lattice atoms are vibrating in phase with each other over a macroscopic spatial region. This results through e-ph coupling in a coherent modulation of the electronic and optical properties of the solid, which is detectable e.g. by the transient modification of the reflectivity or transmission of the excited system. The observation of such coherent phonons has been demonstrated in a variety of systems such as semi-metals like Bi, Sb or Te [Che90, Che91, Hun95, DeC01, Has02, Kim03, Ish06, Ish08], in semiconductors such as Si [Has03] or GaAs [Cho90, Dek93], or even in the cuprate high-T_c superconductor (HTSC) YBCO [Chw90], just to name a few. Later, coherently excited phonons have been also detected by a number of different experimental techniques such as time-resolved second harmonic generation (SHG) spectroscopy [Mel03, Bov04], transient x-ray scattering [Fri07, Joh09] or time-resolved photoemission [Lis05b, Per06, Sch08a]. Likewise, the coherent optical control of coherently excited phonons using two time-correlated excitation pulses has been demonstrated in a number of materials [Dek93, Has96, Mis07a]. The field of coherently excited phonons has been reviewed under various aspects [Dek00, Mat06, Has10, Ish10].

For the excitation of coherent phonons, traditionally two models have been established [Has05, Ish10], the impulsive stimulated Raman scattering (ISRS) [Yan85] and the displacive excitation of coherent phonons (DECP) [Zei92]. The excitation schemes for these two models are depicted in figure 2.1 (a) and (b), respectively and differ by the shape of the driving force that leads to the excitation of the coherent oscillation. In ISRS, the excitation of a coherent vibration occurs via Raman scattering, which is only active during the ultrashort laser pulse and leads to an impulsive excitation of a coherent oscillation of ion cores around the equilibrium position. The resulting oscillation amplitude is described by a sine-like phase relation with respect to t_0 (figure 2.1 (e)). ISRS is the dominant excitation mechanism in transparent media like insulators and

some semiconductors.

In contrast, the DECP, which dominates in opaque media like metals and semimetals, occurs via an excited electronic state, that exhibits a different position of the potential minimum for the ion cores than the ground state, as depicted in figure 2.1 (d). Here, the excitation force is of displacive nature and the oscillation amplitude is described by a cosine-like phase relation with respect to the excitation. Later, it was shown that DECP can also be understood as a special case of *resonant* stimulated Raman scattering [Gar96].

One important prerequisite for the excitation of coherent phonons is the existence of optical phonons at the BZ center with $q = 0$, as the vanishing momentum of the exciting photons allows only vertical transitions. While the two models discussed above allow only for the excitation of Raman active modes [Has05, Man09], the broken symmetry e.g. at surfaces or in the ordered state of complex materials lifts this restriction to some extend [Mat06]. Here, in principle, the excitation of any bosonic mode that couples to the electronic system is possible by a displacive excitation process [Mat06], such as e.g. the excitation of coupled phonon-magnon modes observed in rare-earth metals [Mel03, Bov07]. Whether or not a coherent oscillation is detected in e.g. time- and angle-resolved photoemission spectroscopy (trARPES) depends on the way the coherent mode couples to the electronic states under investigation, e.g. by modifying the spectral width, position or intensity of peaks in the photoemission spectra.

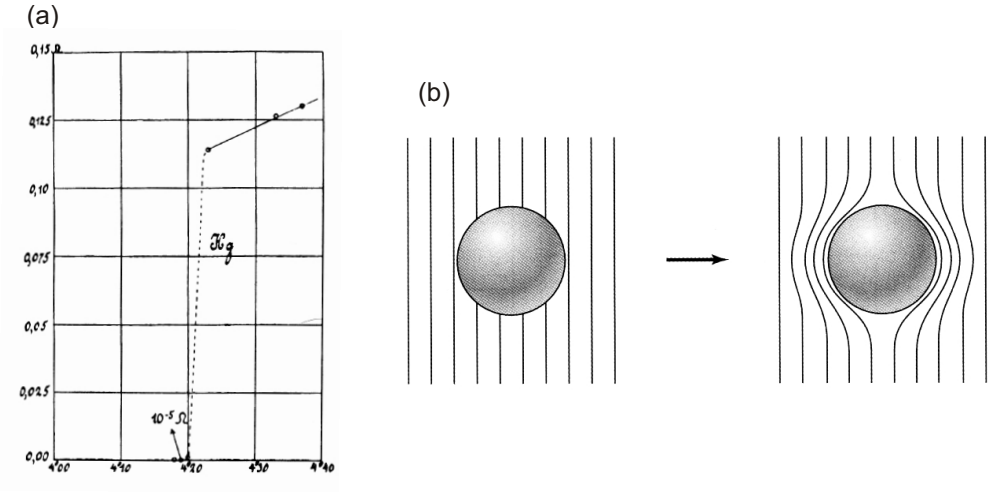

Figure 2.2: Properties of superconductors. (a) Original experiment of Kamerlingh Onnes showing the sudden disappearance of the resistivity of Hg below $T_c = 4.2\,\mathrm{K}$ [Kam11]. (b) The Meissner effect of a superconductor in a magnetic field H completely repels all magnetic flux making the superconductor a perfect diamagnet. After [Kit04].

2.2 Superconductivity

Superconductivity is an intriguing and very useful broken-symmetry ground state found in many metals and alloys at very low temperatures. It is of great importance e.g. for the generation of strong magnetic fields used in nuclear science, plasma research, transportation or medicine, for the electric power transmission or quantum computation, just to name a few, and potential future applications are manifold. Since the discovery of superconductivity more than 100 years ago in 1911 it has become an important topic of Solid State Physics and has inspired lots of theoretical and experimental progress. The main and probably most remarkable fingerprint of superconductivity is the sudden drop of the electrical resistivity below any measurable value in a superconductor below the critical temperature T_c, as illustrated by the historical experiments by Kamerlingh Onnes [Kam11] shown in figure 2.2 (a). One consequence of this behavior is the formation of strong circular currents in the presence of a magnetic field, which makes a superconductor a perfect diamagnet. This effect, which leads to the complete suppression of magnetic fields within a superconductor as sketched in figure 2.2 (b) is known as the Meissner effect of superconductivity [Mei33].

Many efforts were made to understand the phenomenon of superconductivity, however it took more than 40 years until a complete microscopic understanding of superconductivity was established with the famous BCS theory named after their inventors Bardeen, Cooper and Schrieffer in 1956 [Bar57a, Bar57b].

2.2.1 The Bardeen-Cooper-Schrieffer Theory of Superconductivity

The BCS theory of conventional superconductivity is based on an attractive interaction between two electrons in a solid, that can arise under certain conditions. Usually, the screened e-e interaction between two electrons is the dominating contribution, which is always repulsive. However, the electron-phonon (e-ph) coupling can produce an attractive interaction between two electrons in second order perturbation theory due to the exchange of a virtual phonon, as illustrated in figure 2.3. In an oversimplified picture,

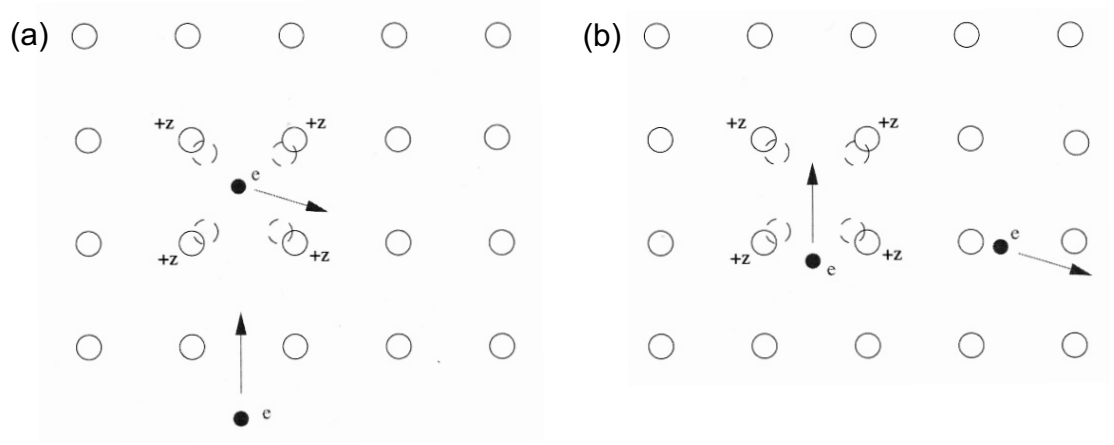

Figure 2.3: Illustration of the attractive e-e interaction mediated by e-ph coupling. An electron moving through a solid leaves behind a polarization cloud of displaced lattice atoms (a). A second electron feels an attractive force due to the polarization cloud. Taken from [Ben08].

this attractive interaction arises from the lattice polarization, which an electron produces in the lattice (figure 2.3 (a)). After this electron has moved away, a second electron is still influenced by the lattice polarization and exhibits an effective attraction towards the first electron (figure 2.3 (b)). If this attractive interaction is strong enough, it can lead to the formation of bound pairs of electrons with opposite momenta $\mathbf{p}$ and $-\mathbf{p}$, so-called Cooper pairs (CPs). Such CPs possess a total spin component of $S = 0$ (singlet pairing) or $S = 1$ (triplet pairing) and thus behave as bosonic particles. Accordingly, all CPs can occupy the same ground state, in analogy to the phenomenon of formation of a Bose-Einstein-Condensate.

The Hamiltonian that describes the BCS ground state of a superconductor is given by

$$\hat{H} = \sum_{\mathbf{k},\sigma} \epsilon_{\mathbf{k}} \hat{c}^{\dagger}_{\mathbf{k}\sigma} \hat{c}_{\mathbf{k}\sigma} + \sum_{\mathbf{k}\mathbf{k}'} V_{\mathbf{k},\mathbf{k}'} \hat{c}^{\dagger}_{\mathbf{k}\uparrow} \hat{c}^{\dagger}_{-\mathbf{k}\downarrow} \hat{c}_{-\mathbf{k}'\downarrow} \hat{c}_{\mathbf{k}'\uparrow} \quad , \tag{2.12}$$

where $\hat{c}^{\dagger}_{\mathbf{k}\sigma}$ and $\hat{c}_{\mathbf{k}\sigma}$ are the creation and annihilation operators of QPs with momentum $\hbar\mathbf{k}$ and spin σ, respectively and $\epsilon_{\mathbf{k}}$ is the QP dispersion of the non-superconducting system [Ben08]. The second term in (2.12) corresponds for an attractive interaction $V(\mathbf{k}, \mathbf{k}')$ to the creation of bound pairs of electrons with $\mathbf{k} \uparrow$ and $-\mathbf{k} \downarrow$ of opposite momentum and spin coordinates, the CPs. This creation of bound pairs of electrons modifies the elementary excitation spectrum in the SC state to

$$E_{\mathbf{k}} = \sqrt{\Delta^2_{\mathbf{k}} + (\epsilon_{\mathbf{k}} - \mu)^2} \quad , \tag{2.13}$$

where μ is the chemical potential. The momentum dependence of the order parameter $\Delta_{\mathbf{k}}$ depends on the symmetry of the pairing interaction, and results for isotropic e-ph mediated pairing $V(\mathbf{k}, \mathbf{k}') \equiv V$ in an isotropic, momentum-independent s-wave pairing Δ. The appearance of the order parameter Δ in the energy dispersion of the SC state corresponds to the creation of an energy gap of 2Δ in the excitation spectrum. Accordingly, the smallest excitation energy possible in the SC ground state corresponds to 2Δ, which results in the breaking of a Cooper pair and the creation of two QPs. The size of the energy gap is determined by the strength of the pairing interaction and corresponds

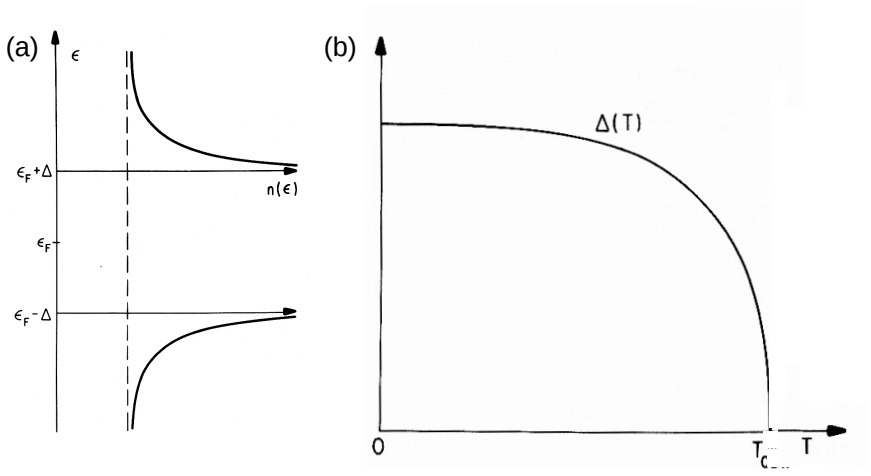

Figure 2.4: (a) Sketch of the DOS close to ϵ_F in the normal (dashed) and SC phase (solid), respectively. The size of the SC gap 2Δ scales with the critical temperature T_c in the BCS theory. (b) Temperature dependence of the SC gap $\Delta(T)$ in the BCS theory. After [Grü94].

to the binding energy of the CPs. The energy gap in the excitation spectrum can be observed experimentally e.g. by tunneling spectroscopy or photoemission spectroscopy and leads to an increase of the DOS below and above the gap edges, as depicted in figure 2.4 (a). Assuming a constant density of states $n(E_\mathrm{F})$ close to the Fermi energy in the normal state, the size of the order parameter is determined by the famous BCS gap equation [Ben08]

$$\frac{1}{\lambda} = \int_0^{\omega_D} \tanh\left(\frac{\epsilon_k}{2k_BT}\right) \frac{\mathrm{d}\epsilon_k}{(\epsilon_k^2 + |\Delta(T)|^2)^{1/2}} \quad , \tag{2.14}$$

with $\lambda \equiv n(E_\mathrm{F})V$ and the Debye frequency ω_D. The temperature-dependent order parameter $\Delta(T)$ is shown in figure 2.4 (b) and reduces for temperatures close to the transition temperature to

$$\frac{|\Delta(T)|}{|\Delta(0)|} = 1.74\left(1 - \frac{T}{T_c}\right)^{1/2} \quad . \tag{2.15}$$

At $T = 0$ in the weak-coupling limit, equation (2.14) yields [Ben08]

$$\Delta(T=0) = 2\omega_D \exp(-1/\lambda) \tag{2.16}$$

for the SC gap size, and for the critical temperature T_c, one obtains

$$k_BT_c = 1.14\,\omega_D \exp(-1/\lambda) \quad . \tag{2.17}$$

Combining equations (2.16) and (2.17) yields the important ratio of SC gap and transition temperature in the weak coupling limit of the BCS theory [Grü94, Ben08]

$$\frac{2\Delta}{k_BT_c} = 3.52 \quad . \tag{2.18}$$

Notably, even many conventional superconductors (e.g. Pb and Hg) exhibit a deviation from equation (2.18) towards higher values, which can be accounted for by improved models such as the Eliashberg theory [Ben08].

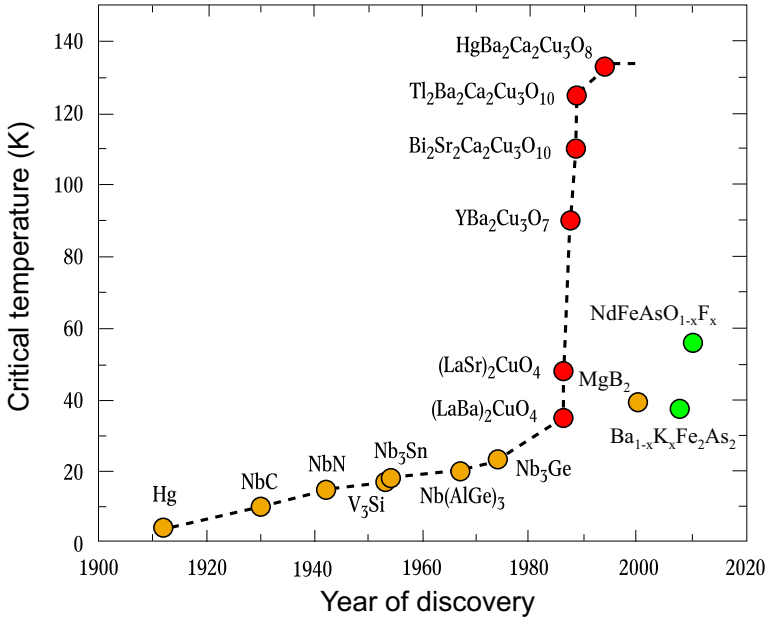

Figure 2.5: Progress in the increase of superconducting transition temperatures. While conventional superconductors reach $T_c \approx 40\,\mathrm{K}$ in MgB_2 (brown), the unconventional cuprate HTSCs reach transition temperatures up to 138 K (red). The recently discovered Fe pnictide HTSC reach $T_c \approx 56\,\mathrm{K}$ (green). After [Esc02].

2.2.2 Unconventional Superconductors

While the critical temperature of conventional superconductors had been slowly increased by empirical means in metallic alloys including mostly Niobium (Nb) over the decades to $T_c \approx 25\,\mathrm{K}$, the discovery of critical temperatures $> 30\,\mathrm{K}$ in the ceramic copper oxides in 1986 by Bednorz and Müller [Bed86] was a great surprise. In very short time, the critical temperatures was raised up to $> 133\,\mathrm{K}$ in similar compounds and even up to $\sim 160\,\mathrm{K}$ under high pressure, see figure 2.5. However, it became clear very quickly, that the BCS theory which was so successful in describing the conventional superconductors could not explain the high critical temperatures on the basis of e-ph coupling [Nor11, Bas11]. Thus, alternative forms of pairing interactions such as the coupling to spin excitations were proposed and a tremendous amount of research was done to unveil the microscopic properties leading to unconventional superconductivity. In the following years, a complexity of phases was found in these materials such as the strong correlation of electrons in the cuprate HTSCs, the occurrence of antiferromagnetism in their parent compounds or the still poorly understood pseudogap phase. In addition, the quasi-two-dimensional (2D) structure is considered to be important for formation of the superconducting condensate, which is strictly located on the copper oxide layers found in all cuprate HTSCs. Many hopes were put onto the Fe based superconductors that were discovered in early 2008, as they possess many similarities to the cuprate HTSCs, such as their layered structure and the doping dependence of the critical temperatures. However, despite an overwhelming number of experiments conducted on these compounds since their discovery, a unifying picture is not yet found and even after almost 30 years of research on the HTSCs, a complete understanding of unconventional superconductivity is still missing.

An important observation for the development of a theory of unconventional su-

perconductivity was the discovery of singlet Cooper pairing in the cuprates and an anisotropic order parameter of $d_{x^2-y^2}$ symmetry, which is characterized by nodes of the momentum-dependent order parameter, where the SC gap vanishes and which indicates a momentum-dependent pairing interaction. Likewise in the Fe pnictides, the order parameter seems not to be of simple s-wave symmetry, but $s_{\pm}$- or a combination of s- and d-wave pairing is discussed [Nor11]. Furthermore, several other complex materials show unconventional types of superconductivity, such as the Ruthenates, heavy-Fermion metals or organic superconductors with SC states close to magnetically ordered phases and anisotropic types of ordering, including triplet pairing. A good overview of the current status of research on unconventional superconductors can be found in [Ben08, Nor11, Bas11].

2.2.3 Nonequilibrium Superconductivity

Additional insight into the elementary interactions governing the ground states of complex quantum matter such as superconductors can be gained from their dynamical behavior following optical excitation on the femtosecond timescale. As different interactions occur on characteristic timescales inherently linked to the respective coupling strength, such an approach is promising to provide information on the relevant processes governing the relaxation towards the ground state.

In the case of the HTSCs, many experiments using time-resolved optical and THz spectroscopy lead to some understanding of the time scales involved in the relaxation of QPs by reformation of CPs [Han90, Dem99, Kai05, Ged05]. In many of these experiments, the QP relaxation dynamics was discussed in terms of a phenomenological model for the recombination of QPs into CPs introduced by A. Rothwarf and B. N. Taylor already in 1967 for the description of non-equilibrium tunneling junctions [Rot67], the so-called Rothwarf-Taylor equations (RTE). In addition to the density of non-equilibrium QPs n, this model also considers the density N of high-frequency bosons (HFBs) with $\hbar\omega > 2\Delta$, that are emitted in the recombination process of two QPs into a CP, and the CP breaking mediated by these bosons. The RTE describe the dynamics of the QP density and the density of HFBs with two coupled differential equations [Rot67]:

$$\frac{\mathrm{d}n}{\mathrm{d}t} = n_0 + \beta N - Rn^2 \quad , \tag{2.19}$$

$$\frac{\mathrm{d}N}{\mathrm{d}t} = N_0 - \beta\frac{N}{2} + R\frac{n^2}{2} - \gamma(N - N_T) \quad . \tag{2.20}$$

Here, n_0 and N_0 are the QP and HFB densities initially created by the excitation, β is the probability of CP breaking by a HFB, and R is the bare QP recombination rate into CPs with the emission of a HFB. N_T is the thermal density of HFBs at temperature T and γ is their decay rate due to relaxation into bosons with $\hbar\omega < 2\Delta$ with insufficient energy to break a CP or their escape into the bulk [Kab05].

In the RTE, two limiting cases can be discussed: For $\gamma/\beta \gg 1$, i.e. a very fast relaxation of HFBs compared to the QP recombination, the QP dynamics is at low T governed by the probability to find a recombination partner and scales with n^2. This case is referred to as the "weak bottleneck regime" and the second-order relaxation has been termed "bi-molecular" recombination dynamics [Kai05]. In contrast, for $\gamma/\beta \ll 1$, the decay of HFBs represents a bottleneck for the relaxation of QPs and a transient equilibrium between QP recombination into CPs and the CP breaking due to HFBs is established. In this so-called "strong bottleneck regime", the QP relaxation dynamics is mainly determined by the decay of HFBs γ.

However, one has to take care as these considerations do not take the symmetry of the order parameter into account, and especially in the case of the cuprate HTSCs, the anisotropic d-wave gap demands for a more sophisticated description of the non-equilibrium state. While some efforts have been made to take the order parameter symmetry into account [Kab99, Nic03], they only consider special cases of QP relaxation.

For the description of the transient state of a superconductor out of thermal equilibrium as encountered in the RTE, two models have been proposed, the μ^* and T^* model [Owe72, Par75, Nic03]. The μ^* model, initially introduced by C. S. Owen and D. J. Scalapino in 1972, is based on the assumption that the non-equilibrium QPs quickly thermalize with the lattice at the equilibrium temperature T. However, as their density is increased with respect to the equilibrium case, these excess QPs are not in chemical equilibrium with the pair state and are described by a transient chemical potential μ^*. This model predicts a first-order transition to the normal state at a certain excitation level, which, however, has not been found experimentally [Owe72, Par75]. To account for this discrepancy, H. W. Parker proposed the T^* model in 1975, which describes the non-equilibrium superconductor based on the thermalization of excess QPs with high-energy phonons with $\hbar\omega > 2\Delta$. These phonons are assumed to be characterized by an effective temperature T^*, while the rest of the phonons stay in thermal equilibrium at T. In the T^* model, only a second-order phase transition to the SC state occurs, if the effective temperature exceeds the critical temperature, $T^* > T_c$ [Par75].

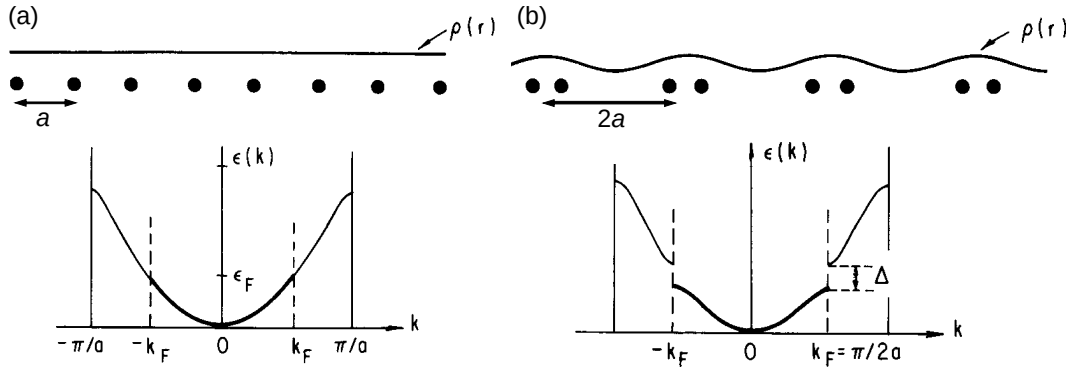

Figure 2.6: Peierls transition in a linear atomic chain. (a) A linear chain of atoms with lattice constant a and constant charge density $\rho(r)$ results in a nearly-free electron parabolic band $\epsilon(k)$, which is half-filled up to the Fermi wave vector $k_\mathrm{F} = \pi/2a$. (b) The periodic distortion of the charge density $\rho(r)$ by the CDW with period $2a$ introduces a new Brillouin zone boundary at $k = \pi/2a$, which leads to the opening of an energy gap Δ at the Fermi energy E_F. After [Grü94].

2.3 Charge- and Spin Density Waves

Another example of an emergent ground state is the spatial modulation of the coupled electron and lattice or spin subsystems, which is called a charge density wave (CDW) and spin density wave (SDW). Such density waves are often found in condensed matter of reduced dimensionality and at low temperature and are characterized by a coupled instability of the electron-lattice or electron-spin subsystem, and often compete with other broken symmetry ground states such as superconductivity. One key ingredient for the formation of CDW and SDW ground states are strong and anisotropic e-ph or e-e coupling constants and a high DOS at the Fermi level $n(E_\mathrm{F})$. The formation of density waves is driven by the energy gain due to the condensation energy $\propto n(E_\mathrm{F})\Delta^2$, where Δ is the order parameter of the density wave describing the creation of energy gaps in the single-particle excitation spectrum that open at the Fermi energy E_F.

Well-known examples for the formation of CDWs are transition metal chalcogenides like $NbSe_3$, $TaSe_3$ and TaS_2, transition metal bronzes such as $K_{0.03}MoO_3$, and quasi-one-dimensional (1D) inorganic and organic conductors like Krogmann's salt KCP and Bechgaard's salt TTF. SDWs have been studied in e.g. Chromium and also in TTF. In the following, we will concentrate on the description of the charge density wave ground state and its implications for the band structure; however, similar concepts hold for the SDW formation [Grü94].

2.3.1 Peierls Transition

The transition to the CDW phase is often referred to as a Peierls metal-to-insulator transition [Frö54, Pei55] because at least part of the FS disappears due to the opening of energy gaps at E_F and cannot be regarded as metallic anymore. As the CDW instability is most pronounced in a 1D system, we will start with the discussion of the basic CDW mechanism in the idealized example of a linear atomic chain in 1D [Grü94].

The band model of a nearly-free electron gas leads in a 1D linear chain of atoms with the lattice constant a and a constant charge density $\rho(r)$ to parabolic bands, as sketched

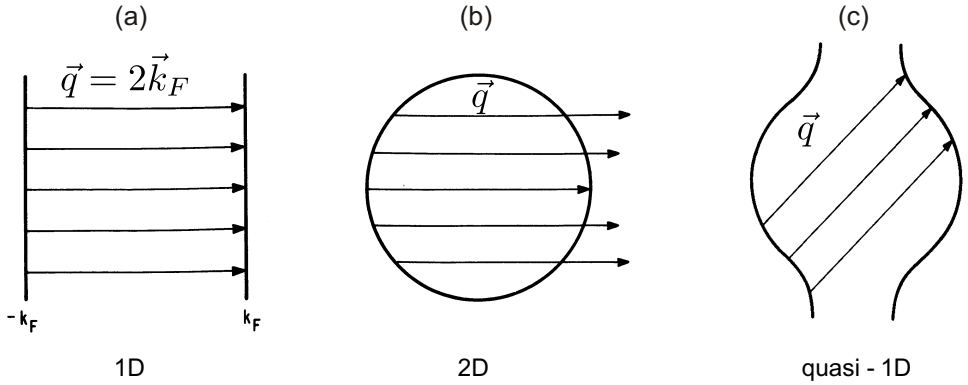

Figure 2.7: Fermi surface in various dimensions. (a) In a 1D system, the FS is perfectly nested by a single nesting vector $\vec{q}$. (b) For a 2D system, the nesting is reduced to two points on the FS. (c) A quasi-1D system can exhibit perfect nesting for a larger part of the FS despite some 2D dispersion. After [Grü94].

in figure 2.6 (a). Assuming one valence electron per atom of the chain, these bands are half-filled up to the Fermi wave vector $k_\mathrm{F} = \pi/2a$. The introduction of a periodic distortion of the atomic position with period $2a$ leads to an additional modulation of the charge density $\rho(r)$. This new periodicity of $2a$ corresponds to a new BZ boundary and the opening of an energy gap Δ in the nearly-free electron bands at $k = \pi/2a$, the value of k_F in the half-filled band, as sketched in figure 2.6 (b). The result is an energy gain of the electronic states near E_F, which is the driving force for the CDW formation. Due to the opening of the energy gap Δ at the Fermi energy, the FS, which consists in the metallic state of the two points $-k_\mathrm{F}$ and k_F, is destroyed and the CDW ground state becomes insulating.

The response of an electronic system to an external periodic perturbation is in the linear response theory determined by the Lindhard response function $\chi(\vec{q})$, which is also known as the general susceptibility. Its pronounced dependence on dimensionality and temperature governs the CDW mechanism [Lin54, Grü94], as discussed in the following. $\chi(\vec{q})$ describes the response of a nearly-free electron gas to a periodic perturbation potential

$$\phi(\vec{q}) = \int d\vec{r}\, \phi(\vec{r})\, e^{-i\vec{q}\cdot\vec{r}} \quad , \tag{2.21}$$

where $\vec{q}$ is the momentum vector corresponding to the periodic perturbation in the reciprocal space. The induced charge density

$$\rho_\mathrm{ind}(\vec{q}) = \chi(\vec{q})\, \phi(\vec{q}) \tag{2.22}$$

is proportional to the potential and the Lindhard response function which is given in d dimensions by

$$\chi(\vec{q}, T) = \int \frac{\mathrm{d}\vec{k}}{(2\pi)^d} \frac{f(T,\vec{k}) - f(T,\vec{k}+\vec{q})}{\epsilon(\vec{k}) - \epsilon(\vec{k}+\vec{q})} \quad . \tag{2.23}$$

Here, $f(T,\vec{k})$ is the electron distribution function and determines the temperature dependence of the response function.

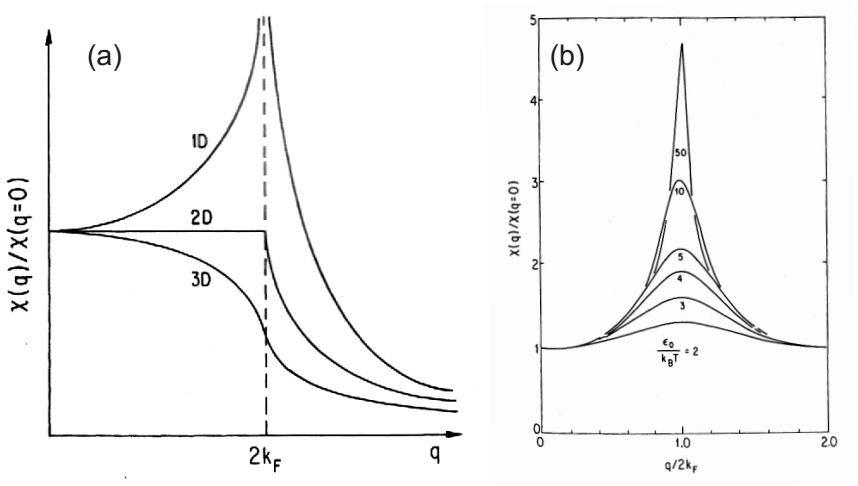

Figure 2.8: Dependence on dimensionality and temperature of the Lindhard response function. (a) $\chi(\vec{q})$ at $T = 0$ for one, two and three dimensions. In the 1D case, the response function diverges at $q = 2k_\mathrm{F}$. (b) Temperature dependence of the 1D Lindhard response function. For $T > 0$, the divergence is replaced by a finite value. After [Grü94].

The charge density induced by such an external perturbation will itself cause an induced variation in the potential at the same wave vector due to a redistribution of the electrons:

$$\phi_\mathrm{ind}(\vec{q}) = -g\ \rho_\mathrm{ind}(\vec{q}) \quad . \tag{2.24}$$

Here, g is some coupling constant, e.g. the e-ph coupling constant for CDWs, which is assumed to be momentum independent and small compared to ϵ_F in the weak-coupling limit.

Considering equation (2.22) with the external perturbation potential ϕ_ext and the induced potential ϕ_int

$$\rho^\mathrm{ind}(\vec{q}) = \chi(\vec{q})[\phi_\mathrm{ext}(\vec{q}) + \phi_\mathrm{ind}(\vec{q})] \quad , \tag{2.25}$$

we get together with equation (2.24) the mean field induced charge density

$$\rho^\mathrm{ind}(\vec{q}) = \frac{\chi(\vec{q})\,\phi_\mathrm{ext}(\vec{q})}{1 + g\chi(\vec{q})} \quad . \tag{2.26}$$

This quantity is suggestive of an instability of the charge density for $1 + g\,\chi(\vec{q}, T) = 0$. For small negative e-ph coupling constants g, an actual formation of a CDW requires a large value of χ. From the denominator in equation (2.23), $\epsilon(\vec{k}) - \epsilon(\vec{k} + \vec{q})$, we recognize a possible divergence of $\chi(\vec{q}, T)$, if $\epsilon(\vec{k}) = \epsilon(\vec{k} + \vec{q})$. This condition, the so-called FS nesting condition, is fulfilled for $q = 2k_\mathrm{F}$, i.e. for vectors that connect two points on the FS and strongly depends on the dimensionality d. This becomes apparent from the FS of a 1D nearly-free electron gas depicted in figure 2.7 (a), which consists of two lines in k-space that are perfectly nested by $\vec{q} = 2\vec{k_\mathrm{F}}$. In the case of a 2D FS, which is a circle in the k space, nesting can only occur for two points on the FS by a single vector $\vec{q}$, as shown in figure 2.7 (b). According to (2.23), the divergence of the Lindhard response function depends critically on the FS nesting condition and thus on the dimensionality d, as shown in figure 2.8 (a). For a three-dimensional (3D) system, χ is a smooth function

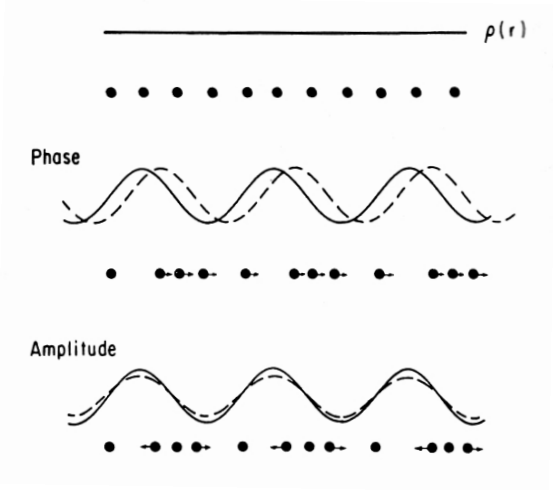

Figure 2.9: Collective excitations of the CDW state. Top: Shift of the phase of the modulated electron density $\rho(r)$ (dashed) with respect to the modulation in the CDW ground state (solid). Bottom: Modulation of the CDW amplitude. After [Grü94].

of q and exhibits a discontinuity of the first derivative at $q = 2k_\mathrm{F}$ in two dimensions. In contrast, for a 1D system, χ shows a divergence at $q = 2k_\mathrm{F}$, which describes a critical susceptibility to a disturbance with $\vec{q} = 2\vec{k}_\mathrm{F}$ and can induce an instability of the electron density in such systems, leading to the formation of the density wave ground state. For layered materials, the case of a quasi-one-dimensional FS is of importance, as shown in figure 2.7 (c). In such systems with only weakly 2D dispersions, perfect nesting can still be obtained for large parts of the FS.

For higher temperatures $T > 0$, the divergence in χ is replaced by a large finite value, which depends on T,

$$\chi(2k_\mathrm{F}, T) = e_0^2 n(\epsilon_\mathrm{F}) \ln \frac{1.14\epsilon_0}{k_B T} \quad , \tag{2.27}$$

as depicted in figure 2.8 (b). Here, ϵ_0 is an arbitrary cutoff which is usually chosen as $\epsilon_0 = \epsilon_\mathrm{F}$ [Grü94]. This behavior indicates that the CDW state only occurs below a transition temperature T_CDW, as known from other broken-symmetry ground states such as superconductivity. Indeed, due to the similarity in the description of the CDW formation and superconductivity, the formalism of the BCS theory of conventional superconductivity can be applied to the density waves [Grü94], see also chapter 2.2.1. Thus, the CDW order parameter Δ is related to the CDW transition temperature by the same mean-field relation found for the SC state,

$$2\Delta = 3.52\, k_B T_\mathrm{CDW}^\mathrm{MF} \quad , \tag{2.28}$$

and the CDW phase transition temperature depends exponentially on the electronic DOS $n(E_\mathrm{F})$ and the strength of the e-ph coupling g:

$$k_B\, T_\mathrm{CDW}^\mathrm{MF} = 1.14\, \epsilon_0\, \exp\left(\frac{-1}{g\, n(E_\mathrm{F})}\right) \quad . \tag{2.29}$$

The order parameter Δ determines the CDW gap around E_F, which opens in the DOS around E_F in the gapped CDW state, similar to the SC gap (compare figure. 2.4 (a)). In addition, the temperature dependence of the order parameter is determined by the BCS gap equation (2.14), as depicted in figure 2.4 (b).

2.3.2 Collective Excitations of the Order Parameter

Due to the coupled nature of underlying lattice distortion and the modulated charge density, CDW systems can undergo collective motions around the new equilibrium position

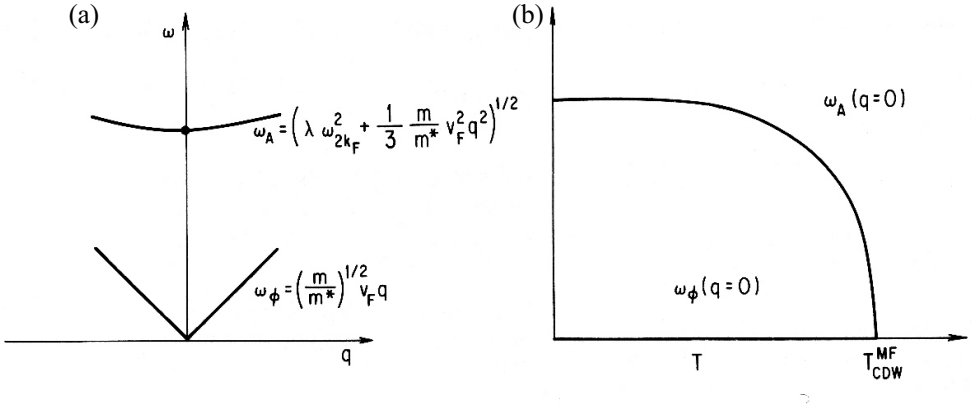

Figure 2.10: (a) Dispersions of the amplitude mode $\omega_A(q)$ and phase mode $\omega_\phi(q)$ [Lee74]. The phase mode vanishes at $q = 0$. (b) Temperature dependence of ω_A and ω_ϕ at $q = 0$. After [Grü94].

determined by the broken-symmetry ground state, which are usually described using the time-dependent Ginzburg-Landau theory [Grü94] and will be discussed here briefly. The spatially and temporally dependent complex order parameter can be written as

$$\Delta(x,t) = \{|\Delta| + \delta(x,t)\}\, e^{i\phi(x,t)} \quad , \tag{2.30}$$

where $|\Delta|$ is the spatially and temporally averaged magnitude of the order parameter, and $\delta(x,t)$ and $\phi(x,t)$ describe fluctuations of the amplitude and phase of Δ [Grü94]. These fluctuations lead to the appearance of collective excitations of the amplitude and phase of the complex order parameter, known as the amplitude and the phase modes of the density wave. In the $q = 0$ limit, the phase mode corresponds to a translational excitation of the undistorted density modulation, as depicted in figure 2.9 (a). As such motions usually do not change the condensate energy, its frequency in the long-wavelength limit vanishes,

$$\omega_\phi(q=0) = 0 \quad . \tag{2.31}$$

In contrast, the collective excitations of the amplitude mode, as sketched in figure 2.9 (b) correspond to a fluctuation of the size of the single particle gap $\delta\Delta$ with a frequency ω_A, which leads to fluctuations of the ionic displacements $\delta(\Delta u)$ in the case of a CDW [Grü94]. This corresponds to a modulation of the condensate density and the frequency of the amplitude mode at $q = 0$ can be written as

$$\omega_A(q=0) = \lambda^{1/2}\omega_{2k_F} \quad , \tag{2.32}$$

where λ is the dimensionless e-ph coupling constant (see chapter 2.1) and ω_{2k_F} is the frequency of the phonon mode responsible for the FS nesting [Grü94].

For finite wave vectors $q > 0$, amplitude and phase mode exhibit characteristic dispersions as depicted in figure 2.10 (a). As collective modes of the CDW condensate, the amplitude mode frequency is closely linked to the temperature-dependent size of the order parameter. It undergoes a characteristic softening with increasing temperature which closely follows the temperature dependence of the CDW gap,

$$\omega_A(T) = \lambda^{1/2}\omega_{2k_F}\,[f_d(T)]^{1/2} = \omega_A(0)\left[\frac{\pi}{4}\frac{|\Delta(T)|}{T_{CDW}}\right]^{1/2} \quad , \tag{2.33}$$

with the condensate density in the dynamic limit $f_d(T)$, the temperature-dependent order parameter $|\Delta(T)|$ and the mean-field CDW transition temperature T_{CDW} [Grü94]. This temperature dependence of the amplitude mode frequency for $q = 0$ is depicted in figure 2.10 (b). For temperatures close to T_{CDW}, this reduces to a power-law dependence,

$$\omega_A \sim \frac{1.55}{4}\lambda^{1/2}\omega_{2k_{\mathrm{F}}}\left(1 - \frac{T}{T_{\mathrm{CDW}}}\right)^{1/4} \quad . \tag{2.34}$$

2.4 Photoemission Spectroscopy

In this thesis, the electronic band structure is investigated using photoemission spectroscopy (PES). The PES measures the energy and momentum of photoelectrons emitted from a non-insulating solid due to the photoelectric effect [Ein05]. This method provides direct access to the electronic structure of metals, semiconductors and adsorbate molecules and has been established as a standard tool in solid state research[1]. Angle-resolved photoemission spectroscopy (ARPES) yields direct access to the electronic band structure via the single-particle spectral function $A(E, \vec{k})$ [Hüf03, Dam03] directly in the k-space. Especially for the study of the electronic structure and of the electronic correlation effects in the High-T_c cuprates [She95, Dam03] and more recently of the Fe pnictides [Ric11], ARPES has played an important role.

The PES is based on the photoelectronic effect, where electrons are emitted from a solid by photons with a photon energy $h\nu$ exceeding the sample work function Φ. Their kinetic energy is given by

$$E_{\mathrm{kin}} = h\nu - \Phi - E_{\mathrm{B}} \quad , \tag{2.35}$$

where E_{B} is the binding energy of the electrons with respect to the Fermi level. Thus, the binding energies of electronic states can be determined by measuring the energy spectrum $I(E_{\mathrm{kin}})$ of the outgoing photoelectrons. In addition, the emission angle of photoelectrons allows to determine the in-plane momentum component $k_{\parallel}$, which is conserved in the PES process, as will be discussed in section 2.4.2. In more detail, the PES intensity is a direct measure of the single-particle spectral function $A(E, \vec{k}_{\parallel})$ and is given by [Hüf03]

$$I(\vec{k}_{\parallel}, E) = M\, f(E,T)\, A(\vec{k}_{\parallel}, E) \quad , \tag{2.36}$$

where M is a (generally angle- and photon-energy-dependent) photoemission matrix element and $f(E,T)$ is the Fermi-Dirac distribution function. Via the spectral function $A(E, \vec{k}_{\parallel})$, ARPES is sensitive to many-body effects like electron correlation or e-ph interactions, that are described by the electron self-energy Σ, see chapter 2.1.1.

In general, the PES is a very surface sensitive probe as a result of the finite escape depth of the photoelectrons in solids [Sea79, Zan88]. The mean free path of electrons in solids, as depicted in figure 2.11, is nearly independent of the material and shows a strong variation with the kinetic energy of the photoelectrons given by the so-called "universal curve". The escape depth exhibits a minimum of only a few Å at $E_{\mathrm{kin}} \sim 30\,\mathrm{eV}$, where the PES is most surface sensitive. For the low kinetic energies at a probe photon energy of 6 eV as used in this thesis, the escape depth amounts to a ~ 30 Å.

As the final state of the PES process is described by the photoemitted electron, PES does not directly measure the electron energies of the unperturbed N particle system but the energy of the $N-1$ particle system, where one electron has been removed. In this context, an important approximation used for the description of the PES is the sudden approximation, which assumes that the photoemission process occurs much faster than it takes the electronic system to relax the excited electronic state. In reality, electronic interactions lead to the relaxation of the excited $N-1$ particle state and result in so-called final state effects on the measured energies, such as an incoherent background or satellite peaks in the PES spectra. However, in practice, the influence of these effects on the binding energies are rather small and the sudden approximation is widely used.

[1] The Nobel prize 1981 was awarded to Kai M. Siegbahn "for his contributions to the development of high-resolution electron spectroscopy".

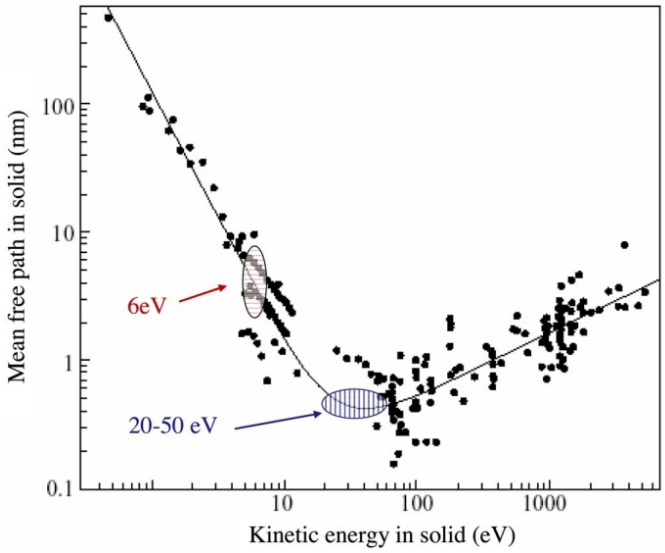

Figure 2.11: The mean free path of photoelectrons in solids is mostly material independent and determined by the kinetic energy of the photoelectrons via the "universal curve" of the mean free path of electrons, which exhibits a pronounced minimum around $E_{\mathrm{kin}} \sim 30\,\mathrm{eV}$. After [Sea79, Kor07].

The validity of the sudden approximation has been questioned at small kinetic energies. However, recent investigations comparing spectra using different photon energies seem to confirm its validity even for very low kinetic energies such as used in this thesis [Kor06a].

2.4.1 The 3- and 1-step Model of Photoemission

For a complete theoretical description of the photoemission process, all initial and final states have to be known and considered, which requires a solution to a complicated many-body problem. Here, some phenomenological models, such as the 3- and 1-step model of the photoemission process have been established. The simpler 3-step model [Ber64a, Ber64b] (see figure 2.12 (a)) breaks the photoemission process up into three distinct processes:

1. Localized excitation of an electron from an occupied initial state into unoccupied bands above the vacuum level. The transition is vertical in the reduced zone scheme of the band structure due to the small photon momentum (direct excitation).

2. Transport of the photoelectron to the surface. Here, scattering processes such as e-e scattering or scattering at defects can modify the electron momentum and energy, which contributes to the background of the photoemission signal in form of secondary electrons. In this step, the energy-dependent mean free path of the photoelectrons determines the surface sensitivity of the photoemission process [Sea79], see figure 2.11.

3. Emission of the electron into the vacuum, which requires the conservation of the momentum component parallel to the surface $k_{\parallel}$. The perpendicular component $k_{\perp}$ is altered by the work function.

A more sophisticated description of the PES process, which is, however, of less practical importance, is given by the 1-step model [Pen76]. In this model, the photoemission

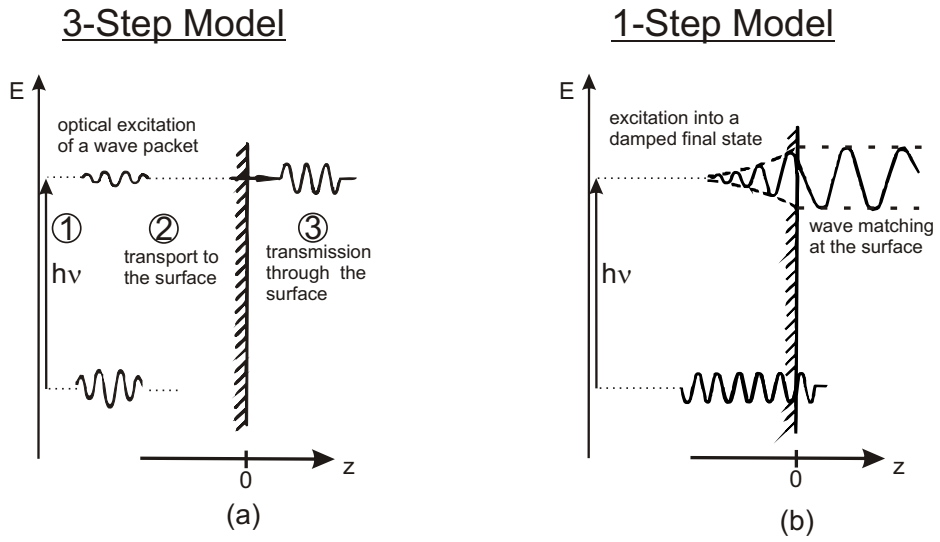

Figure 2.12: (a) 3-step model of photoemission: Optical excitation of a wave packet into a state above the vacuum level (1), propagation to the surface (2) and emission into the vacuum (3). (b) 1-step model: The optical field couples an initial Bloch-state residing within the bulk to a final quasi-free inverse LEED state, which is located in the vacuum and decays exponentially into the bulk. After [Hüf03].

process is described by the optical coupling of a Bloch wave inside the crystal to plane wave states in the vacuum, which decay exponentially into the bulk crystal, as depicted in figure 2.12 (b). These states can be depicted as the time-reversal of electrons impinging on a surface and penetrating within the escape depth such as encountered in low energy electron diffraction (LEED). For this reason, these states are termed time-reversed or inverse LEED states [Mah70a, Mah70b, Feu78]. In the 1-step model, a complete description of all initial and final states, all scattering channels and of the remaining photohole is necessary.

2.4.2 Angle-resolved Photoemission Spectroscopy

In the photoemission process, the momentum component[2] parallel to the surface, $\vec{k}_{\parallel}$ is conserved, as long as no scattering in the final state occurs and the momentum of the photons is small compared to the electron momentum. The momentum conservation during the transmission of a photoelectron into the vacuum is depicted in figure 2.13. From the emission angle Θ_e of a photoelectron, its momentum component parallel to the surface can be determined:

$$k_{\parallel}(\Theta_e, E_{\mathrm{kin}}) = \sin\Theta_e \sqrt{\frac{2m_e}{\hbar^2} E_{\mathrm{kin}}} = 0.5123\ \text{Å}^{-1}\mathrm{eV}^{-1/2}\ \sin\Theta_e \sqrt{E_{\mathrm{kin}}} \quad . \tag{2.37}$$

Here, m_e is the free electron mass. Thus, by measuring the photoemission intensity as a function of the kinetic energy and emission angle, one can map out the complete

[2]Strictly speaking, the physical momentum $\vec{p}$ is proportional to the wave vector $\vec{k}$, $\vec{p} = \hbar\vec{k}$. However, for simplicity, in this work the distinction of momentum and wave vector is omitted and $\vec{k}$ is treated as momentum.

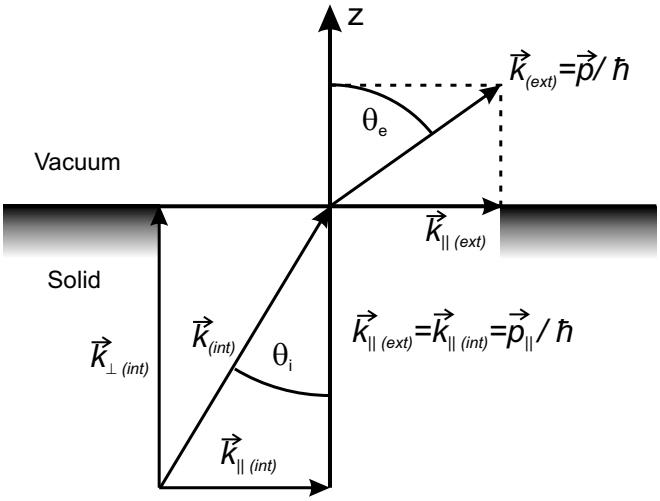

Figure 2.13: In the photoemission process of an electron with emission angle Θ_e, the momentum component parallel to the surface $k_\parallel$ is conserved, which is accessible by angle-resolved detection. The perpendicular component $k_\perp$ is altered by the work function and is determined by the photon energy.

electronic band structure parallel to the surface as s function of the in-plane momentum, which results in detailed information on the electronic dispersions especially in low-dimensional systems. State-of-the-art photoelectron detectors allow for a very efficient simultaneous detection of kinetic energy and angular distributions, and thus for a comprehensive view on the electronic band structure.

The momentum component perpendicular to the surface $k_\perp$ is generally not conserved and altered in the transmission into the vacuum. However, as the photoemission process is characterized by vertical transitions in the electronic band structure and the final state momentum is known, the perpendicular momentum component $k_\perp$ is in principle accessible. By assuming a transmission into parabolic free-electron states above the vacuum level, the perpendicular momentum component $k_\perp$ is determined by [Plu82, Hüf03]

$$E_{\mathrm{kin}} = \frac{\hbar^2}{2m_e}(k_\perp + k_\parallel)^2 - V_0 \quad , \tag{2.38}$$
$$k_\perp = \sqrt{\frac{(E_{\mathrm{kin}} + V_0)2m_e}{\hbar^2}} - k_\parallel \quad .$$

Here, V_0 is an inner potential, which determines the offset of the free-electron final state dispersion with respect to the vacuum level. In practice, V_0 is determined either from band structure calculations or experimentally from the periodicity of electron dispersions as a function of incident photon energy. Typical values of V_0 are in the order of $10 - 15\,\mathrm{eV}$ [Hüf03, Vil09]. Combining equations (2.37) and (2.38) allows to effectively map out the entire 3D band structure by measuring the ARPES intensity as a function of kinetic energy, emission angle and photon energy. However, for small photon energies as used in this thesis, the final states close to the vacuum level might considerably deviate from free-electron dispersions, and thus the applicability of equation (2.38) might be questionable [Shi10].

2.4.3 Time- and Angle-Resolved Photoemission Spectroscopy

One important drawback of ARPES is its limitation to the spectroscopy of occupied states with $E < E_\mathrm{F}$, as initial states have to be occupied for photoemission. Albeit certain procedures such as division by the resolution-broadened, temperature-dependent Fermi-Dirac distribution function allow to access a small fraction of the unoccupied band structure, these methods are fairly limited and restricted to a small energy window above

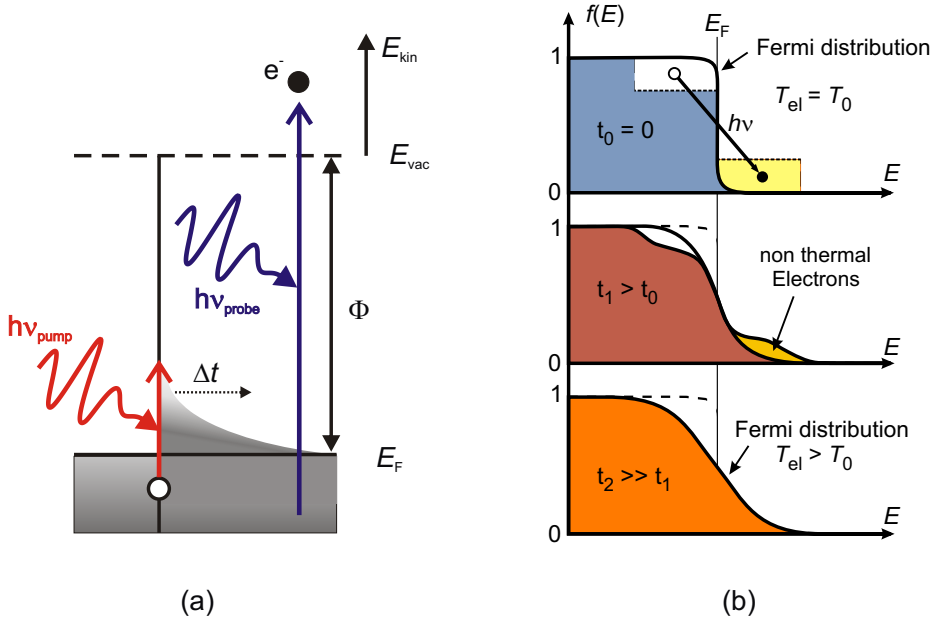

Figure 2.14: (a) Sketch of the time- and angle-resolved photoemission spectroscopy (trARPES) process. An intense pump pulse with a photon energy $h\nu_{\mathrm{pump}} = 1.5\,\mathrm{eV}$ creates a significant population of excited electrons above E_{F}. A time-delayed UV probe pulse with $h\nu_{\mathrm{probe}} = 6\,\mathrm{eV}$ probes both the transient change of the occupied band structure as well as the transient population of states above E_{F} by photoemission. (b) Sketch of the time-dependent electron distribution and of the thermalization process after [Lis05a]. The excitation around time zero projects part of the equilibrium electron distribution, which initially is described by a Fermi-Dirac distribution of temperature T_0, into states above E_{F}, resulting in a strongly non-thermal distribution. With increasing pump-probe delay, inelastic e-e scattering of these excited carriers reestablishes a Fermi-Dirac distribution at an elevated electronic temperature $T_{\mathrm{el}} > T_0$.

E_{F}. Thus, a more complete access to the unoccupied states above E_{F} is of considerable interest, as these states determine important material properties such as e.g. the optical absorption. For the spectroscopy of unoccupied states, the two-photon photoemission (2PPE) has been established, which uses ultrashort laser pulses to transiently excite electrons into states with $E > E_{\mathrm{F}}$, which are subsequently photoemitted by a second laser pulse. In addition, this allows to monitor the temporal evolution of the transient population of unoccupied states by varying the delay between the two pulses with fs resolution. The 2PPE has been established as a powerful tool to study the dynamics of hot electron distributions and of surface- and image potential states [Pet97, Wei02b, Ech04] at energies high above the Fermi level. In the usual scheme of 2PPE, both photon energies are below the metal work function in order to suppress the strong signal of the direct photoemission, and the excitation densities are usually weak in order to study a small perturbation of the system.

In contrast, time- and angle-resolved direct photoemission (trARPES) uses a probe photon energy that is larger than the work function, which allows for the spectroscopy of both occupied and unoccupied electronic states. As an experimental technique, trARPES was developed in the 1980's [Fuj84, Fan92, Hai95] and has come to broader attention only recently. By giving access to the temporal evolution of the transient spec-

tral function $A(\omega, k, t)$, it provides unique access to the non-equilibrium dynamics of the occupied band structure. In comparison to other time-domain techniques such as optical or THz spectroscopy, trARPES offers the advantage of direct access to the electronic states in the energy domain, which is free of any model assumptions. In addition, the momentum resolution provided by trARPES allows for a detection of dynamical processes in electronically anisotropic systems, which are often hard to disentangle using momentum-integrating techniques.

In trARPES, a usually fairly strong excitation pulse with pump fluences ranging from $F \sim 50\,\mu\mathrm{J/cm^2}$ to $F \sim 2\,\mathrm{mJ/cm^2}$ is used to excite the sample, that strongly perturbs the system and creates a significant amount of excited carriers[3]. A subsequent, time-delayed UV probe pulse with a photon energy $h\nu_{\mathrm{probe}} > \Phi$ larger than the work function probes the transient evolution of the occupied band structure below E_F as well as the unoccupied states above E_F, as depicted schematically in figure 2.14 (a). In systems that are very sensitive to optical excitations such as SC states, also weak perturbations with $F < 10\,\mu\mathrm{J/cm^2}$ can lead to significant transient effects, see chapter 6.

The excitation and subsequent equilibration of the transient electronic population around E_F typically encountered in metals is discussed schematically in figure 2.14 (b). The pump pulse excites part of the electrons below E_F, which are characterized before excitation by a Fermi-Dirac distribution with an electronic temperature equal to the equilibrium sample temperature $T_\mathrm{el} = T_0$, to states above E_F. This results in a strongly non-thermal distribution of electrons, that is not characterized by a Fermi-Dirac distribution. Experimentally, this manifests in a deviation from the exponential decrease of the Fermi-Dirac distribution found for $E \gtrsim k_B T$ in the trARPES spectra. Mediated mainly by e-e scattering, this non-thermal electron distribution transforms withing several tens to hundreds of femtoseconds into a Fermi-Dirac distribution, which is characterized by a higher transient electronic temperature $T_\mathrm{el} > T_0$ [Fan92, Ret02, Lis05a]. This whole process, which leads to the creation of a large number of secondary electron-hole (e-h) pairs, is termed thermalization of electrons. Remarkably, the reduced e-e scattering rate e.g. in low-dimensional materials can lead to very long thermalization times in the order of several hundreds of femtoseconds or even picoseconds (see chapter 7).

The excitation of a large number of charge carriers and the resulting high electronic temperatures can have drastic influence on the occupied and unoccupied electronic structure. On the one hand, the sudden change of the electron density at E_F due to the excitation and the redistribution of carriers can change the electronic screening in the system and modify the Coulomb interaction, termed photo-doping. This can lead to collective excitation in the time domain, such as coherently excited phonon oscillations [Bov04, Lis05b, Per06, Per08, Sch08a]. On the other hand, trARPES monitors the single-particle spectral function in the energy domain, just like conventional ARPES does. As a combination of these two complimentary regimes, trARPES enables the observation of the imprint of coherent excitations on the occupied and unoccupied electronic structure by analysis of the time-, momentum- and energy-dependent single-particle spectral function $A(E, k_\parallel, t)$. Thus, trARPES allows the observation of transient phase transitions far from thermal equilibrium [Per06, Per07, Per08, Sch08a, Sch11a, Roh11, Ret12a] and the identification of the underlying timescales and interactions. In addition, by employing weaker excitation densities that do not perturb the electronic system significantly, and close to the temporal overlap, trARPES allows access to the unoccupied electronic structure close to E_F in a wide range of parallel electron momenta, that is not accessible

[3] Typically, a few % of the electrons close to E_F are excited. For example, Lisowski *et al.* discuss an excitation density of 18% of the electrons close to E_F [Lis04b].

by other methods such as 2PPE (see chapter 7).

For the evaluation of transient trARPES spectra, one can integrate the spectral intensity within certain energy windows, which yields cross correlation (XC) traces that characterize the transient population of occupied or unoccupied states. Alternatively, the time-dependent trARPES spectra are fitted in the energy domain by e.g. Lorentzian peaks and a Fermi-Dirac distribution, which allows for a more sophisticated analysis of the transient spectral function. The resulting fitting parameters then describe the transient peak amplitude, width and position as well as the chemical potential and the electronic temperature and thus yield direct information on the transient electronic structure.

3 Experimental Details

In this thesis, experiments were performed at three different experimental setups, which are described in the following chapter. Most experiments were carried out in the time- and angle-resolved photoemission spectroscopy (trARPES) laboratory in the group of Prof. Martin Wolf at the Freie Universität Berlin, which was available during the whole thesis[1]. This experimental setup is discussed in most detail in chapter 3.1, whereas the other two setups are only briefly introduced, and important modifications made to the experiment during the thesis are introduced. Additional experiments on FeAs compounds were conducted in collaboration with the group of Prof. M. Bauer at the University of Kiel, and the corresponding setup is discussed in chapter 3.2. High-resolution laser angle-resolved photoemission spectroscopy (ARPES) experiments on $HoTe_3$ were performed during a visit to the research group of Prof. Z.-X. Shen at the Stanford University in California, USA. The respective experimental setup is briefly introduced in chapter 3.3. Finally, in chapter 3.4, the preparation of the samples used for this thesis is discussed.

[1] Measurement times had to be shared with another PhD student. At the beginning of 2011, this setup was moved to the Universität Duisburg-Essen.

3.1 trARPES Setup in Berlin

The trARPES combines the experimental approaches of time-resolved spectroscopies using femtosecond laser pulses and the direct access to the electronic structure of solids unique to the ARPES technique. This poses several challenges to the experimental setup and procedures which are combined within one experiment. The setup consists of two main parts: a femtosecond laser system which provides ultrashort pulses in the infrared (IR), visible (VIS) and ultraviolet (UV) range, as well as a sophisticated ultra high vacuum (UHV) apparatus for trARPES measurements and sample preparation. These two parts of the setup will be described in detail in the following.

3.1.1 Laser System

The first main part of the experimental setup is the tunable femtosecond laser system built around a commercial regenerative amplifier system, sketched in figure 3.1. The laser system was fully set up and in working condition at the beginning of this thesis and no major modifications were made during this thesis. The various elements of the laser system and their working principle will be introduced very briefly in the following, as the system was described in much detail in previous thesis work [Kno97, Den99, Hot99, Gah04, Lis05a, Stä07, Ret08, Kir08a, Mey11]. Further details are found in the technical documentation [Coh93, Coh94, Coh97, Coh07] and for a general introduction to femtosecond laser systems we refer to established literature [Boy92, Rul98, Tre02, Dem03].

For the generation of ultrashort laser pulses in the time domain, a large bandwidth of the laser spectrum in the energy domain is necessary due to the Heisenberg uncertainty principle. Thus, a laser medium with a broad emission spectrum is necessary. To this end, the use of Ti-doped sapphire (Ti:Sa) has been established due to its broad emission band at $670 - 1070\,\mathrm{nm}$, which enables the generation of pulses of only a few femtoseconds duration at a central wavelength of $\lambda \approx 800\,\mathrm{nm}$. Furthermore, the absorption band of Ti:Sa is in the range of $500 - 600\,\mathrm{nm}$, which allows efficient pumping of the gain medium with frequency doubled solid state lasers (Nd:YAG, Nd:YVO_2, 532 nm). Another prerequisite for the generation of ultrashort pulses is the realization of phase-coherence of the various cavity modes, called *mode-locking*. Mode-locking is achieved in Ti:Sa based oscillators with passive mode-locking due to the linear optical Kerr effect [Rul98].

The system is pumped by the output of an 18 W continuous wave (cw) solid state laser (Coherent *Verdi* V-18) [Coh07], which is split into two parts to pump a femtosecond seed oscillator and the regenerative amplifier. A smaller fraction ($\sim 5\,\mathrm{W}$) is used to pump the commercial Ti:Sa seed oscillator (Coherent *Mira* 900-B [Coh93]), which delivers femtosecond laser pulses of $\lambda = 800\,\mathrm{nm}$ and a pulse duration of $\sim 40\,\mathrm{fs}$ at a pulse energy of $\sim 3\,\mathrm{nJ}$. However, to drive the nonlinear processes in the optical parametric amplifiers (OPAs) used for the generation of tunable fs laser pulses and to be able to study samples under strong optical excitation conditions, that allow e.g. to induce optical phase transitions, pulse energies of a few μJ are necessary. This is achieved in the regenerative amplifier (Coherent *RegA* 9050 [Coh97]), which is pumped by the remaining output of the Verdi V-18 pump laser. In order to avoid peak powers exceeding the damage threshold of the Ti:Sa crystal in the RegA, the pulses of the seed oscillator are stretched in time before amplification, a process called chirped pulse amplification (CPA). For amplification of the seed pulses in the RegA cavity, a large population inversion is built up in the Ti:Sa crystal due to the suppression of lasing by an acousto-optic modulator (Q-switch). This population inversion is used to amplify a seed pulse during

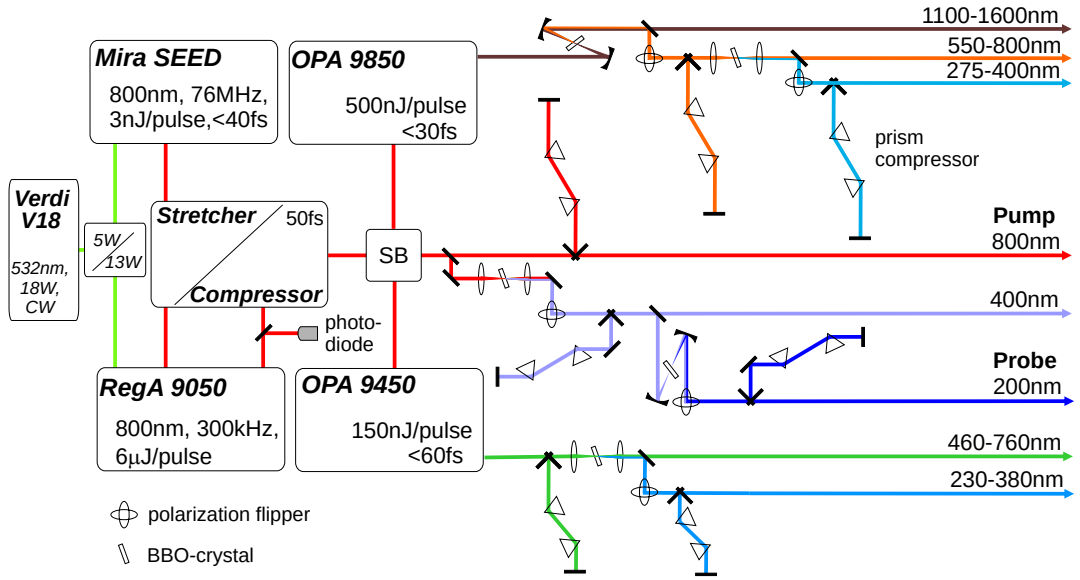

Figure 3.1: Optical setup of the amplified femtosecond laser system. The output of the pump laser (V18) is split to pump the Mira seed oscillator and the regenerative amplifier (RegA 9050). The recompressed output pulses of the RegA are divided in a switch box (SB) and used to pump two OPAs and the 4$^{\text{th}}$ harmonic generation stage for the trARPES experiments. Thus, the laser system provides quasi-continuously tunable laser pulses with wavelengths between $200 - 1600\,\text{nm}$.

several round trips (typically 20-30) in the RegA cavity, which is coupled in and out by another acousto-optic modulator (Cavity dumper) [Coh97]. The RegA amplifies the Mira pulses to $\approx 6\,\mu\text{J}$ pulse energy at a repetition rate of 300 kHz, and the recompressed RegA pulses have a pulse duration of 50 fs. The RegA pulses are linearly polarized with the polarization vector parallel to the laser table (p-polarization).

The amplified RegA pulses can be used to pump two OPAs working in the visible (Coherent *OPA* 9450, $460 - 760\,\text{nm}$, $< 60\,\text{fs}$, 150 nJ) and infrared (Coherent *OPA* 9850 [Coh94], $1100 - 1600\,\text{nm}$, $< 30\,\text{fs}$, 500 nJ) spectral range. By frequency doubling and quadrupling of the OPA pulses in β-bariumborate (BBO) crystals using nonlinear second harmonic generation (SHG), the spectral range is extended to the ultraviolet, see figure 3.1. The free and independent tunability of the photon energies of both pump and probe pulses is advantageous especially for the two-photon photoemission (2PPE) spectroscopy. In this thesis, only the IR-OPA output at $h\nu = 0.95\,\text{eV}$ was used as pump beam for trARPES measurements of Pb/Si(111) quantum well states (QWSs) for excitations below the silicon band gap presented in chapter 4.

For the major part of the experiments, part of the RegA output at 820 nm[2] is used to generate its 4$^{\text{th}}$ harmonic at 205 nm wavelength by two subsequent SHG processes in two BBO crystals. As the SHG process yields s-polarized second harmonic radiation, after each SHG stage, the polarization is flipped back to p-polarization by periscopes and the pulses are recompressed using prism pair compressors [For94], as sketched in figure 3.1. These pulses with a photon energy of $h\nu = 6.0\,\text{eV}$ have a slightly longer pulse duration of 80 fs due to nonlinear effects in the quadrupling process and are used as probe pulses for the trARPES measurements. As pump pulses for trARPES measurements, a

[2]In order to achieve phase matching in the second SHG process, the Mira is tuned to 820 nm.

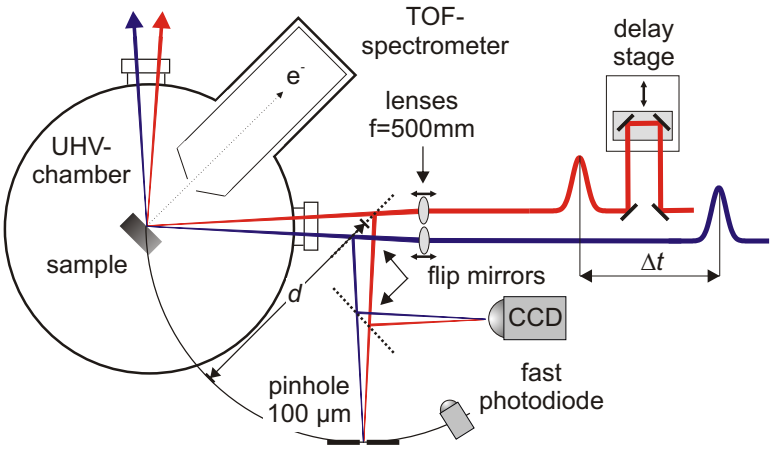

Figure 3.2: Beam incoupling into the UHV chamber. Pump (red) and probe (blue) beams are focused independently onto the sample in front of the TOF spectrometer by two lenses. The time delay between the two pulses is varied by a computer controlled delay stage. The spatial overlap of pump and probe beams on the sample is verified by a pinhole outside the UHV chamber and the beam profile is monitored by a CCD (see figure 3.3). To establish the coarse temporal overlap of pump and probe beam, a fast photodiode is used.

fraction of the fundamental RegA output at $h\nu = 1.5\,\text{eV}$ photon energy is used, with pulse energies up to $1\,\mu\text{J}$ at the sample position. Such excitation conditions allow to trigger and investigate e.g. collective excitations like optically induced ultrafast phase transitions and excitation of coherent oscillations in correlated electron materials [Per06, Per08, Sch08a, Kir08a, Roh11, Sch11a] or high-T_c superconductors (HTSCs) [Per07, Gra11, Cor11, Ret12a]. The quadrupling process yields a photon flux in the order of 10^{13} photons/s in the 205 nm beam, which is comparable with 3$^{\text{rd}}$ generation synchrotron sources [Kor06a] and enables an efficient characterization of the occupied and unoccupied band structure using time- and angle-resolved photoemission spectroscopy.

3.1.2 Beam Incoupling and Characterization

To control the temporal delay between the pump and the probe pulses, the pump beam traverses a computer controlled delay stage with 0.5 fs step size (Physik Instrumente), shown in figure 3.2. In addition, for the three-pulse experiments presented in chapter 7, the pump beam is split into two parts and their respective time delay is controlled by a second delay stage in a Michelson-Morley interferometer. The polarization of pump and probe beams can be controlled independently by $\lambda/2$ wave plates. The incoupling of the time-correlated beams is shown schematically in figure 3.2. The two beams are focused separately by two lenses ($f = 500\,\text{mm}$) onto the sample surface inside the UHV chamber in front of the TOF spectrometer aperture, allowing for the independent control of the focal diameters on the sample. To verify the spatial overlap of the two beams outside the UHV chamber, a flip mirror can be used to mirror the sample position onto a $100\,\mu\text{m}$ pinhole, which is mounted at the same distance d to the mirror as the sample position (see figure 3.2). The quasi-collinear geometry allows to maintain the spatial overlap even for slight sample movements that are unavoidable in angle-dependent measurements. In addition, a CCD can be used to monitor the beam profiles of the two beams (figure 3.3) and the temporal overlap of the two pulses is established within

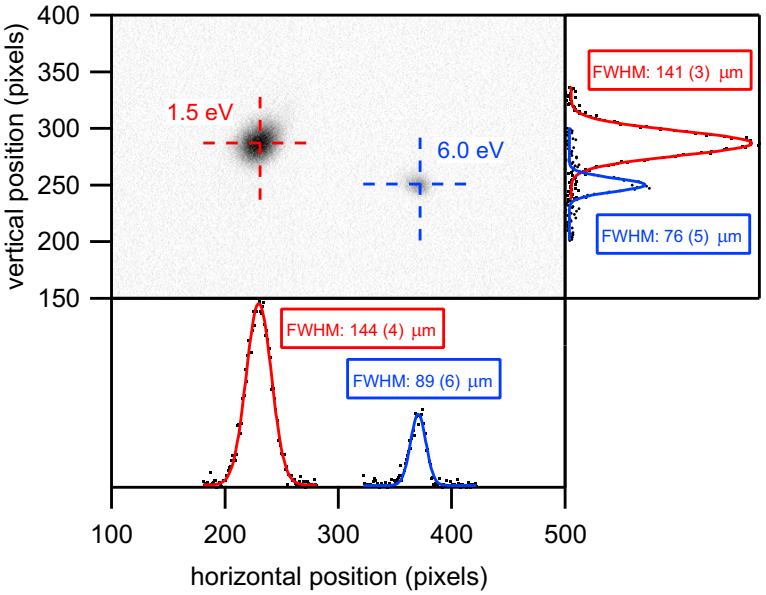

Figure 3.3: Experimental beam profiles of the pump ($h\nu = 1.5\,\mathrm{eV}$) and the probe ($h\nu = 6.0\,\mathrm{eV}$) beams as recorded with the CCD in the focal plane of the sample. Horizontal and vertical beam diameters are determined by the FWHM of Gaussian line fits. The larger diameter of the pump beam ensures a homogeneous pumping of the probed area.

$\sim 100\,\mathrm{ps}$ using a fast photodiode. The femtosecond temporal overlap is found from the transient photoemission signal.

For characterization of the spectral profile of the pump and probe pulses, a UV sensitive fiber-optic grating spectrometer is available, allowing to measure the laser spectra directly in the beam path. The spectral width (full width at half maximum (FWHM)) of the probe pulses is determined to $37(1)\,\mathrm{meV}$, whereas the pump pulses are characterized by a spectral width of $\sim 50\,\mathrm{meV}$. The temporal profile of the pump laser pulses at $1.5\,\mathrm{eV}$ is determined by the frequency-resolved optical grating (FROG) technique using a Grenouille [Tre02, Tre07], which yields typically a pulse duration of $50\,\mathrm{fs}$. The probe pulse duration is determined directly from the trARPES spectra, where the cross correlation (XC) of highly excited electrons without significant life times can be used to determine the probe pulse duration of $\sim 80\,\mathrm{fs}$, yielding a total time resolution of $< 100\,\mathrm{fs}$.

The actual pumping fluence on the sample is determined by the beam profile of the pump beam at the sample position, which can be measured by the CCD mounted in a similar manner as the pinhole at the sample distance to the focusing lenses. Typical beam profiles of pump and probe beams are shown in figure 3.3, which are fitted with Gaussian line profiles to determine the beam diameters. Here, the probe beam diameter is usually chosen considerably smaller than that of the pump beam to ensure a homogeneous pumping within the probed region of the sample. For the determination of the incident pumping fluence F_{in}, the horizontal and vertical FWHM of the pump beam is taken as the beam diameters a and b and the incident pumping fluence is determined by

$$F_{\mathrm{in}} = \frac{T\,P}{r}\frac{\cos\alpha}{\pi\,a\,b} \quad , \tag{3.1}$$

where $T = 0.95$ is the transmission of the UV transmitting CaF_2 incoupling window, P the cw laser power as measured with a power meter in front of the UHV chamber,

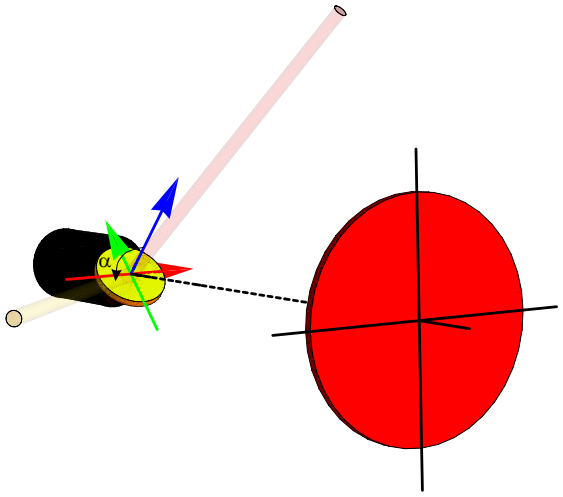

Figure 3.4: Projection of the laser beam onto the sample surface (yellow disk) in front of the spectrometer (red disk). The sample coordinate system is shown by red (x), green (y) and blue (z) arrows and incident and reflected light beams are shown as yellow and red tubes, respectively. The angle of incidence α within the plane of incidence, spanned by surface normal and incident and reflected beams, is indicated.

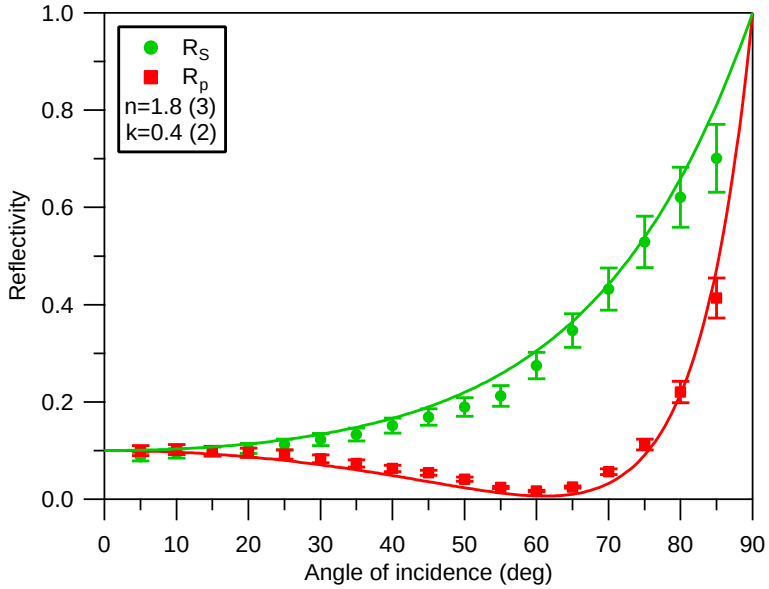

Figure 3.5: Measured optical reflectivity of BSCCO R_s (green) and R_p (red) for s- and p-polarized light, respectively, at $h\nu = 1.5\,\mathrm{eV}$ as a function of angle of incidence. The fit with the Fresnel formula yields the Fresnel coefficients $n = 1.8(3)$ and $k = 0.4(2)$.

r the repetition rate and α the angle of incidence on the sample. Typical pumping fluences in trARPES measurements range from $3\,\mu\mathrm{J/cm^2}$ for weak perturbation of the superconducting state of $Bi_2Sr_2CaCu_2O_{8+\delta}$ (BSCCO) (chapter 6) up to $> 1.5\,\mathrm{mJ/cm^2}$ which allows to observe a transient collapse of the charge density wave (CDW) gap in RTe_3 (chapter 7). In all cases, the pumping fluence was below the damage threshold of the samples, as no irreversible changes to the photoemission spectra were encountered.

The determination of the angle of incidence is straight forward, if the sample surface is mounted perpendicularly to the plane defined by the spectrometer axis and the incident laser beam, as indicated in figure 3.2. For different sample geometries as used with the slanted sample holders necessary to reach the outer Brillouin zone (BZ) (see chapter 3.1.4), the plane of incidence does not coincide with the plane of the laser table, as shown in figure 3.4 for a sample slated 45° upwards. Here, the angle of incidence α is given by the angle between the incident light vector (yellow beam) and the sample surface normal (blue), which together span the plane of incidence.

To determine the absorbed fluence

$$F_{\text{abs}} = F_{\text{in}} - F_{\text{refl}} = (1 - R)F_{\text{in}} \tag{3.2}$$

one has to know the reflected fluence F_{refl}, i.e. the reflectance R of the sample. For normal emission, the reflected beam can be directly measured behind the UHV chamber (see figure 3.2). For other geometries, however, this is not possible. The dependence of the reflectance is highly dependent on the angle of incidence and the incident photon polarization and is determined by the Fresnel formulas [Jac99] and depends on the complex index of diffraction $N = n + ik$. In order to determine these coefficients n and k, the reflectance of the sample is measured outside the chamber as a function of α for s- and p-polarized light, as shown in figure 3.5 exemplarily for BSCCO. The reflectivity is then fitted with the Fresnel formulas to yield the material-dependent diffraction and absorption coefficients, n and k, respectively. Now, the reflectance can be calculated from the projection of the incident light polarization on the plane of incidence and the angle of incidence α, see figure 3.4.

3.1.3 Ultrahigh Vacuum Chamber

As ARPES is a surface sensitive tool (see chapter 2.4), a very good surface quality of the studied samples has to be maintained during experiments. Therefore, the use of ultra high vacuum (UHV) conditions with $p < 10^{-10}$ mbar is required, in order to minimize the adsorption of residual gas atoms and maintain clean sample surfaces during measurements. At such conditions, the time to build up a monolayer (ML) of residual gas atoms is in the range of $\sim$ 10 hours, whereas it takes only one second at $p \sim 10^{-6}$ mbar [Zan88]. In addition, the mean free path of electrons has to be larger than the distance of the sample to the detector, which is only fulfilled for sufficiently good vacuum conditions.

The UHV chamber, where the *in-situ* sample preparation and the trARPES experiments are carried out is the second main part of the experimental setup, as depicted in figure 3.6. The chamber is divided into two levels by a gate valve, the upper preparation level (a) which is used for sample preparation and characterization prior to trARPES measurements and the lower spectrometer level, where the trARPES measurements take place. The UHV chamber is equipped with several surface preparation and characterization tools as discussed in the following. Attached to the chamber is a sample transfer system which is used to transfer new samples into the main chamber without breaking the vacuum (not shown). This is especially relevant for the experiments using small single crystals which are cleaved in the vacuum chamber, as each time a new sample has to be prepared, producing a large sample throughput.

The upper preparation chamber is evacuated by a turbo-molecular pump to $p < 7 \cdot 10^{-11}$ mbar, which is connected to a pre-vacuum of $p \sim 10^{-6}$ mbar obtained by a drag-turbo pump and a four-stage membrane pump. For the preparation of ultrathin Pb films on Si, Pb is evaporated from a water-cooled Knudsen cell. The evaporation rate can be monitored by a quartz micro balance and a retractable shutter is used for the growth of wedge-shaped samples, see chapter 3.4.1. In addition, the chamber is equipped with an IR-pyrometer used to monitor the sample temperature during preparation, and a sputter gun and a quadrupole mass spectrometer (QMS) are available for the preparation of noble metal surfaces. For the cleaving of small single crystals used in most part of this thesis, a screw driver attached to a movable bellow is used to break off a small cleaving pin which is glued on top of the sample surface, as described in chapter 3.4.2. The surface quality of samples can be checked by low energy electron diffraction (LEED).

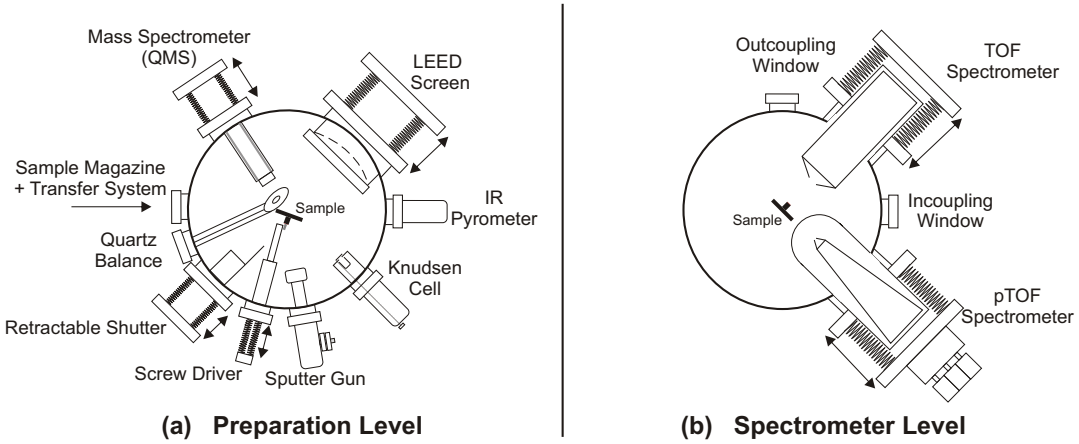

Figure 3.6: Sketch of the UHV chamber. (a) The upper preparation level is connected to a sample transfer system and is equipped with various tools for sample preparation and characterization. A screw driver is used to cleave small crystals of layered materials. (b) The lower spectrometer level is separated from the preparation level by a gate valve. The sample can be placed either in front of the conventional TOF spectrometer or the position-sensitive pTOF, which can be moved into the measurement position by translation stages.

The spectrometer level is evacuated by an ion getter pump and a titan sublimation pump to a base pressure of $p < 3 \cdot 10^{-11}$ mbar, which allows to maintain clean sample surfaces over very long measurement times of several hours up to days, necessary for trARPES measurements. It houses the two time-of-flight (TOF) spectrometers used for electron detection, the conventional TOF spectrometer and the newly built position-sensitive time-of-flight (pTOF) spectrometer. The pTOF was brought to working condition in this thesis and its capabilities are demonstrated in the experiments on RTe_3 presented in chapter 7.

The sample holder, which is depicted in figure 3.7 is connected to a 400 mm liquid helium flow cryostat which is equipped with a heating coil and a silicon diode for temperature control. The setup of the temperature control by a proportional-integral-differential (PID) controller (Lakeshore 330) necessary for temperature-dependent measurements has been part of the improvements achieved during this thesis. Thereby, the sample temperature can be controlled and stabilized within a broad temperature range from ~ 30 K to ~ 340 K to within 1 K. The cryostat is mounted on a sample manipulator allowing for 400 mm vertical and ± 12.5 mm lateral movements. In addition, a differentially pumped rotation feedthrough enables free 360° rotation around the vertical axis of the manipulator. All linear movements are equipped with computer controlled stepper motors which allow for sample positioning with $\sim 10\,\mu$m precision.

A sketch of the sample holder is depicted in figure 3.7. The lower part of the sample holder, the sample boat, can be exchanged by the transfer system and holds the actual sample. On the left side, a cleavable single crystal is shown, glued to a sample post, which is connected to the sample boat. An additional silicon diode mounted on the fixed part of the sample holder measures the temperature close to the sample. The cleaving pin is glued onto the sample itself and a collection wire connects the cleaving pin to the sample boat. On the right side, a silicon sample mounted to the sample boat is shown, which is equipped with a thermocouple (type C) for temperature measurements. Both

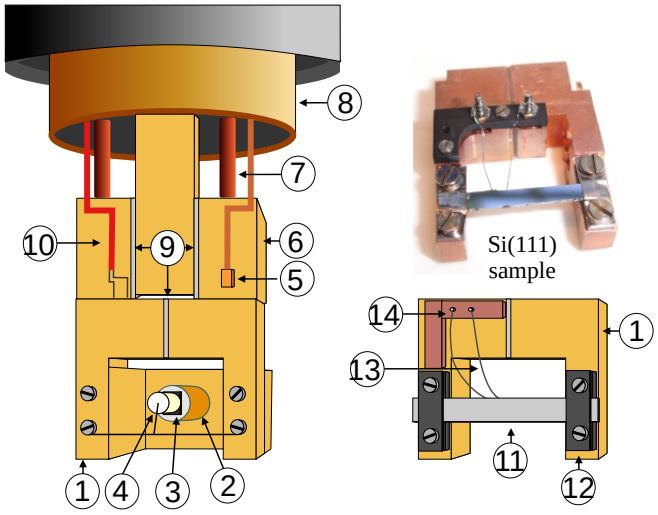

Figure 3.7: Sketch of the liquid helium cryostat and the transferable sample holder. Labeled parts are: (1) Transferable sample boat. (2) Sample post. (3) Cleavable sample. (4) Cleaving pin with collection wire. (5) Silicon diode. (6) Fixed sample holder. (7) Contact wires. (8) Thermal shielding. (9) Sapphire plates. (10) Thermocouple wires. The silicon sample holder consists of: (11) Silicon sample. (12) Tantalum blocks. (13) Thermocouple wire. (14) Thermocouple connector.

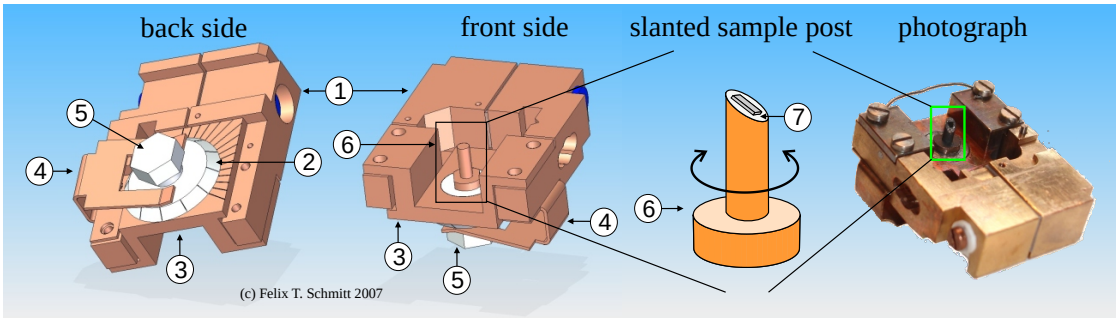

Figure 3.8: Rotatable sample mount used for slanted sample posts in the experiments on BSCCO and RTe_3. (1) Transferable sample boat. (2) Aluminum goniometer for azimuthal sample rotation. (3) Adapter with angular scale to connect sample boat and goniometer. (4) CuBe springs. (5) Allen head to access azimuthal rotation. (6) Sample post. (7) Cleavable sample glued to the slanted sample post. For definition of the sample holder geometry, see chapter 3.1.4.

sides of the sample holder are separated by sapphire sheets which allow a good thermal contact especially at low temperatures and provide electrical insulation. Both sides of the sample holder are connected individually by heating wires, which enable resistive heating of the samples mounted in the sample boat and are used to apply a bias voltage for trARPES measurements. All parts of the sample holder are made from non-magnetic materials such as copper, aluminum, titan or tantalum to ensure the absence of magnetic fields, which can disturb the electron trajectories.

For measurements on BSCCO and RTe_3 the use of very large emission angles $> 45°$ is necessary at the small probe photon energy of 6 eV to reach the Fermi surface (FS) at parallel momenta $k_{\parallel} > 0.5\,\text{Å}^{-1}$. To reach such emission angles, the use of slanted sample holders is mandatory. To gain control of the relative orientation of the sample slant with respect to the manipulator rotation, a special inlay for the sample boat was designed by Felix Schmitt from the Stanford University (see figure 3.8), which allows for the azimuthal rotation of the sample post with the screw driver used for sample transfer. This allows in combination with differently slanted sample posts and orientations of the sample on the sample post to reach large areas of the BZ, as described in the following

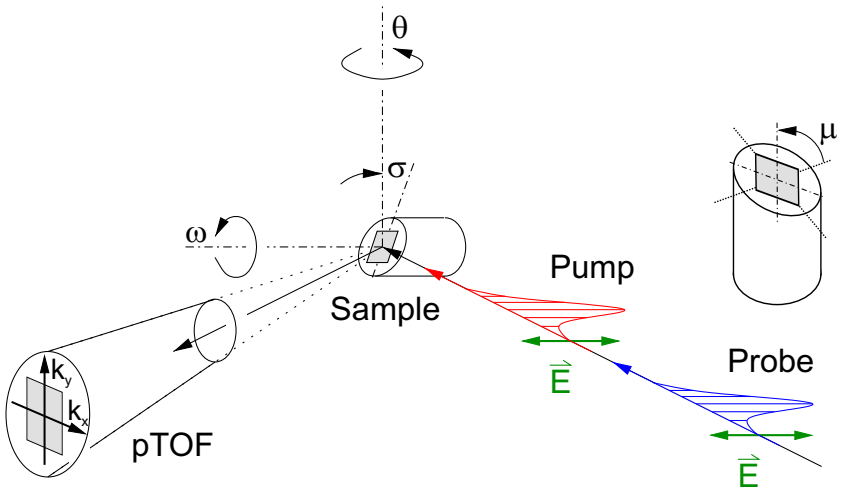

Figure 3.9: Experimental geometry of the slanted sample holder. The following angles are defined in the order of their dependence: θ, the rotation of the long axis. ω, the rotation of the azimuthal angle. σ, the slanting angle of the sample post. μ, the orientation of the sample on the slanted sample post. The light pulses and the pTOF spectrometer are also indicated.

section.

3.1.4 Experimental Geometry

The geometric conventions used for the slanted sample holder geometry are depicted in figure 3.9. The rotations, which are interdependent (non-commuting) are defined in the following. The spectrometer coordinate system is defined such that the z axis points in the direction away from the sample, x lies within the laser table plane and y points upwards, along the long manipulator axis[3]. The notion of the rotational axis in the following is referenced to this coordinate system, which is identical to the sample coordinate system for $\theta = \omega = \sigma = \mu = 0$. The first rotation about y is the rotation about the long axis of the manipulator θ, which turns the whole sample holder. Next, the rotation ω around z of the azimuthal inlay defines the orientation of the sample slant in the x/y plane. The sample slant angle σ corresponds to a rotation around y. The final rotation of μ, which is a rotation around z of the sample orientation on the slanted sample post is only of importance for electronically anisotropic samples such as RTe_3 and BSCCO. Of these four angles, only θ is accessible within the TOF spectrometer and the azimuth ω can be changed in the preparation chamber by the screw driver. The other two angles, σ and μ, are fixed for a given sample and are determined by the sample preparation (see chapter 3.4.2).

The k'_x, k'_y positions in the BZ corresponding to a given sample orientation are determined by a coordinate transformation of the photoelectron emission vector (k_x, k_y, k_z)

[3]This is the usual convention for ARPES and is not to be confused with the manipulator coordinate system, where the z axis is the vertical axis.

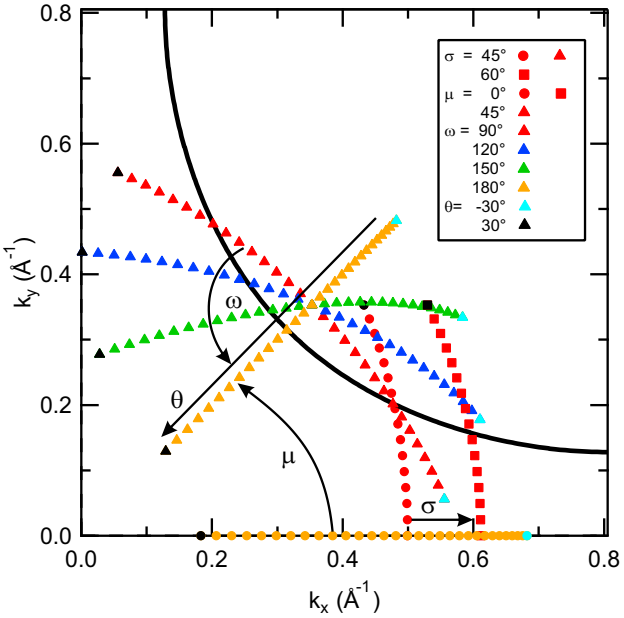

Figure 3.10: One quadrant of the first BZ of BSCCO with selected k-space cuts and corresponding sample geometries. Each arc in k-space corresponds to a θ-scan from $-30°$ to $30°$. The influence of the various rotation angles is indicated.

from the coordinate system of the spectrometer into the sample coordinate system:

$$R_\theta = \begin{pmatrix} \cos\theta & 0 & -\sin\theta \\ 0 & 1 & 0 \\ \sin\theta & 0 & \cos\theta \end{pmatrix} \tag{3.3}$$

$$R_\omega = \begin{pmatrix} \cos\omega & \sin\omega & 0 \\ -\sin\omega & \cos\omega & 0 \\ 0 & 0 & 1 \end{pmatrix} \tag{3.4}$$

$$R_\sigma = \begin{pmatrix} \cos\sigma & 0 & -\sin\sigma \\ 0 & 1 & 0 \\ \sin\sigma & 0 & \cos\sigma \end{pmatrix} \tag{3.5}$$

$$R_\mu = \begin{pmatrix} \cos\mu & \sin\mu & 0 \\ -\sin\mu & \cos\mu & 0 \\ 0 & 0 & 1 \end{pmatrix} \tag{3.6}$$

$$\vec{k}' = \begin{pmatrix} k'_x \\ k'_y \\ k'_z \end{pmatrix} = R_\mu \cdot R_\sigma \cdot R_\omega \cdot R_\theta \cdot \begin{pmatrix} k_x \\ k_y \\ k_z \end{pmatrix} \quad . \tag{3.7}$$

Here, the k_x and k_y coordinates of the initial photoelectron vector (k_x, k_y, k_z) are the momentum components as measured by the pTOF spectrometer and k_z is determined by the kinetic energy of the photoelectron. In case of the conventional TOF spectrometer, $k_x = k_y = 0$.

Exemplary cuts through the BZ of BSCCO are shown in figure 3.10, where the kinetic energy has been chosen according to the work function of BSCCO $\Phi \approx 4.1\,\mathrm{eV}$. Two choices of the slant angle are shown, $\sigma = 45°$ (triangles and circles) and $\sigma = 60°$ (squares), which determines the offset of the rotation origin for ω. The azimuth ω changes the direction of θ cuts from the nodal direction to the direction perpendicular to it, as seen by the colored triangles, which show four different choices of ω from $\omega = 90°$ (red) to $\omega = 180°$ (yellow). Finally, the orientation of the sample on the sample post μ changes the orientation of the cuts around the origin. Here, $\mu = 0$ corresponds to cuts along the k_x-axis, while $\mu = 45°$ corresponds to cuts along the BZ diagonal. Using these

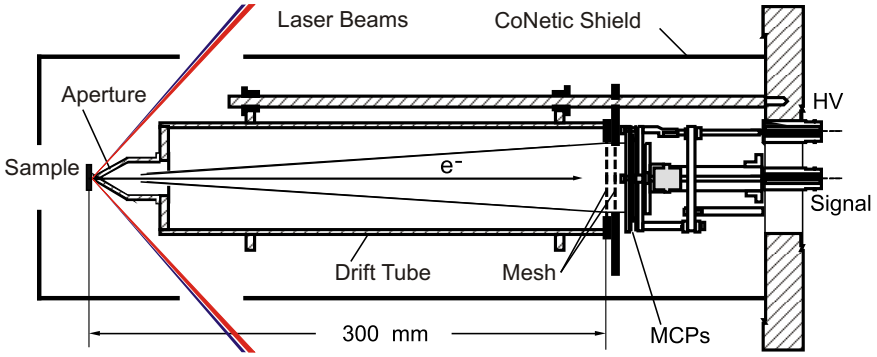

Figure 3.11: The conventional time-of-flight (TOF) spectrometer with 300 mm drift length and an angular resolution of ±3.8° after [Kno97].

various sample geometries, in combination with the angle-resolved pTOF spectrometer allows for a quite complete FS mapping as demonstrated in chapter 7 even with this rather simple manipulator design.

3.1.5 The Photoelectron Spectrometer

The heart pieces of the trARPES experiments are the two TOF spectrometers that are attached to the lower spectrometer chamber. The conventional TOF spectrometer, depicted in figure 3.11 was used for most experiments in this thesis and is the "working horse" of the experimental setup. The kinetic energy of the photoelectrons that enter the spectrometer through the entrance tip is detected by their flight time t in the field-free drift tube of length $L = 300\,\text{mm}$. For non-relativistic electrons, the kinetic energy is given by

$$E_{\text{kin}} = \frac{1}{2} m_e v^2 = \frac{m_e L^2}{2 t^2} \quad , \tag{3.8}$$

where m_e is the electron mass. Here, the kinetic energy is determined with respect to the vacuum potential of the spectrometer, and the electrons have to overcome a potential barrier $e_0 U$, which is determined by the offset of the work functions of sample and spectrometer Φ_{sample} and $\Phi_{\text{spec.}}$, respectively, as well as an applied bias voltage U_{Bias}

$$e_0 U = \Phi_{\text{sample}} - \Phi_{\text{spec.}} + e_0 U_{\text{Bias}} \quad . \tag{3.9}$$

A schematic energy diagram of the energy potentials between sample and spectrometer is shown in figure 3.12. For angle-resolved measurements, the bias voltage is adjusted to compensate the work function difference of sample and spectrometer to ensure a field free region between sample and spectrometer tip.

Photoelectrons are detected by a pair of micro channel plates (MCPs) in a chevron configuration with 40 mm diameter, which defines the acceptance angle of ±3.8°. All parts of the spectrometer are coated by graphite to ensure a homogeneous work function of the spectrometer of $\Phi_{\text{spec}} \approx 4.3\,\text{eV}$. In addition, the whole spectrometer is housed in a μ-metal shielding to avoid external magnetic fields, which distort the trajectories of the slow photoelectrons of a few eV kinetic energy. The energy and momentum resolution of the TOF spectrometer depend on the kinetic energy of the photoelectrons and amounts to $\Delta E_{\text{kin}} \approx 20\,\text{meV}$ and $\Delta k_{\parallel} \approx 0.1\,\text{Å}^{-1}$ at $E_{\text{kin}} = 2\,\text{eV}$, respectively [Hot99]. The effective energy resolution of the experiment is determined not only by the spectrometer

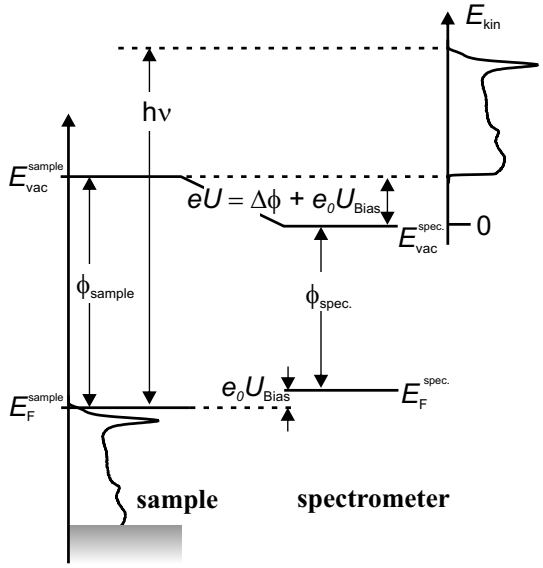

Figure 3.12: Potential gradients between sample and spectrometer. If sample and spectrometer are directly connected ($U_{\mathrm{Bias}} = 0$), both Fermi levels align. A finite value of U_{Bias} allows to compensate a difference in sample and spectrometer work function and to eliminate electric fields between sample and spectrometer entrance, important for the angle-resolved detection of electrons. The kinetic energy is referenced to the vacuum level of the spectrometer, and the vacuum level of the sample defines the secondary cutoff position.

resolution but also by the spectral width of the probe pulses and amounts to typically 50 meV with the 6.0 eV probe beam used for trARPES.

The pTOF Spectrometer

To overcome the limitations of the conventional TOF spectrometer, which exhibits a limited momentum resolution and does not allow for an angle dispersive detection of photoelectrons without rotating the sample, a new position-sensitive time-of-flight (pTOF) spectrometer was designed and built, which allows for the efficient angle-resolved detection of photoelectrons in two dimensions and which has been described in detail in [Kir08c, Kir08a, Ret08]. Here, a short introduction to the working principle is given and important modifications to the pTOF made during this thesis are discussed.

The pTOF is built around a commercial delay line anode (RoentDek *Hex80* hexanode) [Roe06], mounted behind an MCP stack with 80 mm diameter, which allows for the position sensitive detection of photoelectrons, as sketched in figure 3.13. The shorter drift tube of $L = 230$ mm compared to the conventional TOF allows, together with the larger MCP diameter, an opening angle of 22°. Photoelectrons traverse the field-free drift tube maintaining their initial momentum and hit the MCPs, producing an electron cascade of $10^6 - 10^7$ electrons at the back of the MCP stack. This charge cloud is collected by three wound wire layers oriented at 60° with respect to each other, and the resulting current pulses travel along the three wire layers and are detected as voltage pulses at the six wire ends. From the relative arrival times of the six layer signals and the MCP signal, the position and arrival time of the photoelectrons can be reconstructed. Here, the third layer introduces a redundant signal which allows to detect photoelectrons in a multihit regime, a necessity for high count rates [Kir08c].

From the impact position (x, y) of an electron on the delay line anode and its flight time t, the kinetic energy E_{kin} and the momentum components k_x and k_y are determined:

$$E_{\mathrm{kin}} = \frac{m_e d^2}{2t^2} = \frac{m_e \left(x^2 + y^2 + L^2\right)}{2t^2} \quad , \tag{3.10}$$

$$\begin{pmatrix} k_x \\ k_y \end{pmatrix} = \frac{m_e}{\hbar\, t} \begin{pmatrix} x \\ y \end{pmatrix} \quad . \tag{3.11}$$

This energy and momentum resolution of the pTOF depend, like in the conventional TOF, on the kinetic energy and the temporal resolution of the timing circuits and amount

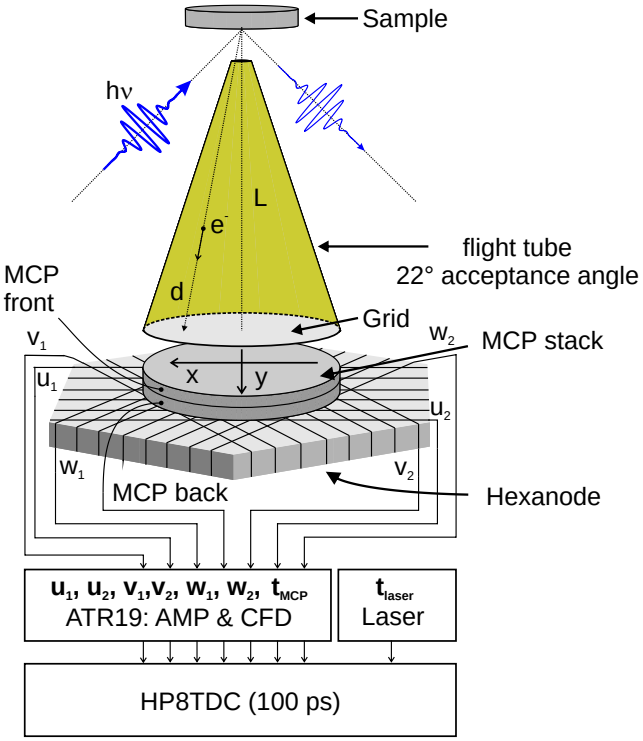

Figure 3.13: Sketch of the position-sensitive time-of-flight (pTOF) spectrometer. The drift tube of 230 mm length allows in combination with the 80 mm Hexanode for an opening angle of $\sim 22°$. The six signals from the three layers of the Hexanode (one signal from each end) encode the arrival time and the impact position of each photoelectron on the MCP stack. Together with the MCP signal and a start pulse from the laser, in total eight signals are discriminated and recorded by the time-to-digital converter HP8TDC with 100 ps time resolution [Kir08c].

for the given setup to $\Delta E_{\mathrm{kin}} < 5\,\mathrm{meV}$ and $\Delta k < 0.01\,\mathrm{Å}^{-1}$ at $E_{\mathrm{kin}} = 2\,\mathrm{eV}$ [Kir08c]. Similar to the conventional TOF, the pTOF is housed in a μ-metal shield to avoid magnetic fields inside the drift tube and is coated with graphite to ensure a homogeneous work function. For the proper functionality of the pTOF, a good magnetic shielding and a homogeneous surface potential is even more crucial than in the conventional TOF, as discussed in the following.

New Tip Design

At the beginning of this thesis, the pTOF spectrometer was principally working [Kir08c, Ret08], however, the spatial distribution of electrons on the anode exhibited serious circular distortions, as depicted in figure 3.14 (c) for a homogeneous Cu sample. These distortions are most pronounced for low kinetic energies and presented a serious problem for the functionality of the spectrometer, as they prevent a direct mapping of the position to the electron momentum. Consequently, the evaluation of the first experiments on In/Si(111) nanowires, which suffered from these distortions, did not produce satisfying results [Kir08a].

In order to investigate the origin of these distortions, trajectory simulations were performed using the SimIon 7.0 software package. A potential origin of the distortions was found in the design of the old entrance tip of the pTOF, which is schematically shown in figure 3.14 (a). Here, the small entrance aperture of 3 mm diameter is used to define the acceptance angle of 22° of the pTOF. This, however, resulted in many electrons passing close to the edge of this very small aperture, indicated by a red circle in figure 3.14 (a). Here, already very small inhomogeneities of the surface potential will have a strong influence on the electron trajectories. To this end, in the simulations, three spots with a 20 meV higher work function were placed in the aperture, corresponding to a higher surface potential. Consequently, electrons are deflected from these spots, and introduce circular distortions in the spatial distribution on the detector, as shown in figure 3.14 (e), which look very similar to the distortions found in the experimental

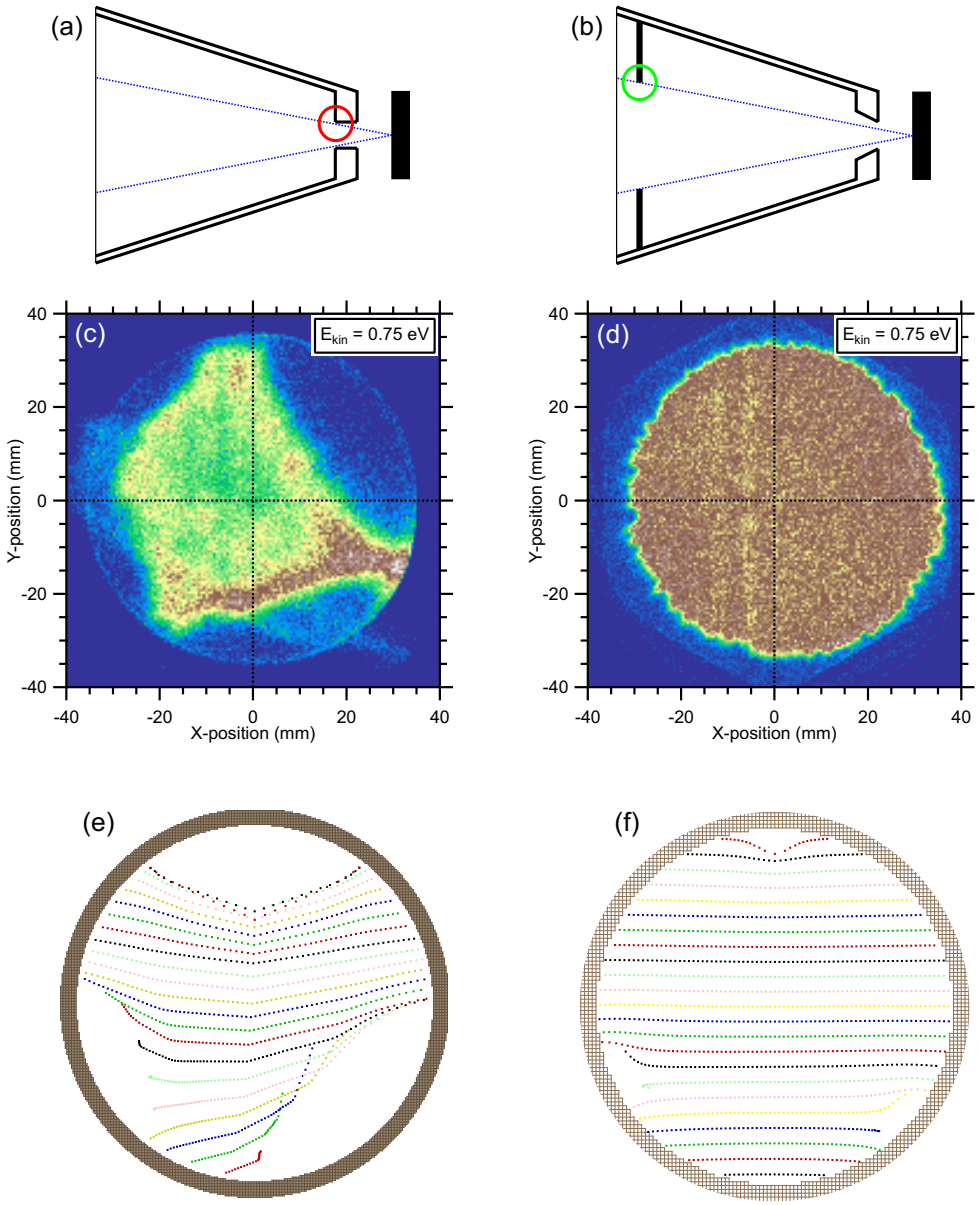

Figure 3.14: Design of the new pTOF tip. (a) Sketch of the old pTOF tip. The passage of the small entrance aperture leads to image distortions (red circle). (b) Modified tip design. The enlarged entrance aperture avoids image distortions. For angular selection, an additional aperture ring is added at the end of the tip region, which introduces much smaller distortions (green circle). (c) Spatial distribution of photoelectrons from Cu on the MCP with the old tip design at $E_{\mathrm{kin}} = 0.75\,\mathrm{eV}$. Circular distortions of the electron distribution are visible. (d) With the modified tip design, only small distortions at the edges remain. (e) Electron distribution on the detector obtained from trajectory simulations ($E_{\mathrm{kin}} = 0.1\,\mathrm{eV}$) using SimIon 7.0 with the old tip design and three spots of 20 mV higher work function placed at the aperture. (f) Results of trajectory simulations with the new tip design and three similar spots placed at the ring aperture. See text.

distribution.

To overcome this problem, a new tip was designed with a widened entrance aperture, as depicted in figure 3.14 (b). To prevent electrons with larger emission angles than the ±11° acceptance angle of the MCPs to enter the flight tube[4], a new ring aperture was added at the end of the tip region. At the position of the aperture, the angular distribution is already much wider than at the tip entrance and thus work function inhomogeneities at the ring aperture have less influence on the electron trajectories (green circle). This is corroborated by the trajectory simulation with the modified tip design shown in figure 3.14 (f), which shows only small distortions at the outermost electron trajectories. In addition, as the ring aperture is coated with graphite separately from the tip, a more homogeneous coating can be achieved than at the aperture of the old tip design. The spatial distribution of electrons from a Cu sample using the new tip is shown in figure 3.14 (d) and exhibits only minor distortions at the outermost edges and a much more homogeneous intensity distribution throughout the MCPs.

In addition a problem with degassing of residual gas atoms from the channel walls of the MCPs at high detection rates was encountered, which leads to a quick sample aging. To solve this problem, a new pair of MCPs was installed and a burn-in procedure for the MCPs known as "scrubbing" was performed [Nor88], which effectively eliminated this problem for count rates < 150 kHz.

3.1.6 Data Acquisition

The data acquisition is controlled by two computer systems, where the first one is specialized for handling the very large data rates of > 10 MBytes/s accumulating during pTOF measurements and the other one is used to control the experimental setup and for measurements using the conventional TOF. All data acquisition is controlled by custom-designed LabView programs. Here, the procedures relevant for measurements using the pTOF are discussed; measurements using the conventional TOF are carried out in a similar manner.

In the TOF measurements, the time-of-flight is determined from the time difference of a start signal obtained from a fast photo diode in the optical path and the stop pulse from the MCPs[5]. In addition to the photodiode signal and the MCP pulses, the timing signals from the six layer ends of the pTOF hexanode are amplified and converted to digitally processable nuclear instrumentation module (NIM) pulses by constant-fraction discriminators (CFDs). These in total eight pulses are fed into a fast 8-channel time-to-digital converter (RoentDek HP8TDC) with 100 ps nominal timing resolution. The HP8TDC allows for the detection of multiple electrons per pulse on the hexanode, avoiding possible distortions in a multihit regime at higher event rates [Kir08c]. During measurements, the raw timing signals are stored separately for each laser pulse to large data files for later evaluation. In addition, a LabView front-end allows for the data visualization during measurements.

For time-dependent trARPES measurements, the time delay between pump and probe pulses is varied by a computer controlled delay stage (Physik Instrumente). Typically 100-400 individual delay points are approached during a time-dependent scan, and ARPES data are collected for $500 - 2000$ ms at each delay point. After each scan, a computer controlled laser shutter allows for the acquisition of the background signal due

[4] Such electrons can scatter off the walls of the flight tube and produce a background in the pTOF spectra.

[5] To obtain the actual time-of-flight, a time offset corresponding to the time difference between the photo diode signal and the arrival of the laser pulse on the sample has to be considered in equation (3.8).

to a multiphoton signal from the pump beam. Delay scans are repeated and accumulated up to 200 times in order to achieve a good signal-to-noise (S/N) ratio of $> 10^4 : 1$, which is necessary for a detailed k-dependent analysis of trARPES data. The achievable S/N level is determined mainly by the counting statistics $\delta N = 1/\sqrt{N}$ of each bin in the (k_x, k_y, E) volume acquired by the pTOF (see below) and thus a high total number of counts is desirable in order to study tiny details of the spectra. The total counting yield achievable in a single experiment depends on the mechanical and temperature stability of the manipulator as well as on the stability of the laser system and is ultimately limited by the life time of the clean sample surface in the UHV environment. The total achievable count rate is in the order of $100 - 200$ kHz for measurements with the conventional TOF and limited by vacuum space charge effects, that start to broaden and shift the spectra at too high count rates [Gra10a]. In the pTOF experiments, the total count rate is limited by the outgassing behavior of the MCPs to about 150 kHz, which is significantly below the space charge limit due to the larger acceptance angle of the pTOF. A time-resolved data set using the pTOF as shown and discussed in chapter 7.4 comprises a total of $> 3 \cdot 10^9$ single electrons and a total data volume of > 450 GBytes divided over 91 delays and 170 scans with 2000 ms integration time. The total measurement time amounted to > 11 h, which is at the limit of the stability of the current setup.

3.1.7 Data Analysis

The kinetic energy E_{kin} and the momentum position (k_x, k_y) of each individual electron is calculated according to equations (3.10) and (3.11) and the transformation matrix (3.7) and stored into a three-dimensional (3D) data volume $I(k_x, k_y, E_{\mathrm{kin}})$. In order to combine the data of associated scans along the θ direction, the individual data volumes for various values of θ are merged in the (k_x, k_y) direction of the scan into a single data volume. For data visualization, the ARPES intensity is integrated along certain cuts through the 3D data volume. In case of cuts perpendicular to the k_x or k_y axis[6], this yields the energy-dispersion $I(k_y, E)$ and $I(k_x, E)$ at the given k_x and k_y position. Alternatively, cuts perpendicular to the energy axis yield the momentum distribution $I(k_x, k_y)$, e.g. the FS for the Fermi energy E_{F}. Examples for such cuts are shown e.g. in figure A.1. For time-dependent measurements, such a 3D volume $I(k_x, k_y, E)$ is recorded at each delay, composing a four-dimensional (4D) data volume $I(k_x, k_y, E, t)$. Here, respective cuts as discussed before create 3D volumes $I(k_y, E, t)$, $I(k_x, E, t)$, and $I(k_x, k_y, t)$, respectively, which can be visualized as movies of the respective cuts in the time domain. Corresponding movie frames at certain delays can be found e.g. in figure 7.8. Further reducing the dimensionality with additional cuts yield e.g. the energy distribution at a given (k_x, k_y) as a function of pump-probe delay as shown in figure 7.9, which corresponds to the two-dimensional (2D) plots obtained by the conventional TOF, except for the energy-dependent conversion from emission angle to $k_{\parallel}$. These transient spectra can then e.g. be fitted by model functions.

[6] Even arbitrary paths through the k-space are possible.

3.2 HHG trARPES Setup in Kiel

Despite the extension of the accessible regions of the BZ by means of slanted sample holders as discussed in chapter 3.1.4, the probe photon energy of $h\nu = 6.0\,\mathrm{eV}$ available in the trARPES setup at the FU Berlin limits the accessible parallel momenta to $k_{\parallel} \lesssim 0.6\,\mathrm{\AA}^{-1}$. This was sufficient for most samples studied in this thesis, where the important parts of the FS where located in this region. However, the electron pockets in the Fe pnictides, located at the BZ corner (X-point) at $k_{\parallel} \approx 1.1\,\mathrm{\AA}^{-1}$ represent an important part of the multiband structure of the FeAs compounds, and thus an investigation of the hole pockets at the Γ point is insufficient to gain a complete picture of the electron dynamics in the Fe pnictides.

To investigate the electron dynamics at the X-point of the BZ, additional experiments were performed at a high-harmonic generation (HHG)-based trARPES setup in collaboration with the research groups of Prof. M. Bauer and Prof. L. Kipp at the University of Kiel (see chapter 5.4). The setup (see figure 3.15), which provides ultrashort laser pulses at a photon energy of $h\nu = 43\,\mathrm{eV}$ and thus enables access to the whole BZ, is described briefly in the following. A detailed description can be found in [Mat07, Roh11].

The extreme ultraviolet (XUV) light source used for this trARPES setup is pumped by a 3 kHz Ti:Sa amplifier system (KMLabs Dragon, itself pumped by an Empower 30, Spectra Physics), delivering infrared pulses at 790 nm, 1.2 mJ pulse energy and 32 fs pulse duration. 80% of the pulse energy is used to generate femtosecond XUV pulses in an argon-filled hollow-fibre waveguide (XUUS, KMLabs, $p_{\mathrm{Ar}} \sim 100\,\mathrm{mbar}$) by an HHG process. The HHG is a highly nonlinear process occurring at very high electric fields in the gas phase. It is based on the field-assisted tunneling of electrons in the laser field, which results in ionization, acceleration, and subsequent recollision of the outer electrons in the gas atoms during the changing phases of the light field [McP87, Fer88]. The energy gained in this process is emitted during the recollision process and results in a photon spectrum consisting of multiple odd harmonics of the fundamental photon energy. A pair of multilayer mirrors (total reflectivity 13%) is used to select the 27^{th} harmonic at a photon energy of $h\nu = 43\,\mathrm{eV}$ out of the high harmonic spectrum and to focus it onto the sample mounted in the UHV system, yielding a photon flux of $\sim 10^9$ photons/s at the sample position. To block the residual pumping radiation, a pair of Al filters, which transmit the XUV radiation, is installed within the beam path.

The experimental chamber is equipped with a 6-axis manipulator allowing for precise sample alignment in the trARPES experiments. A liquid N_2 cryostat is used to cool the sample to $T < 110\,\mathrm{K}$ during the measurements. For photoelectron detection, the chamber is equipped with a hemispherical electron analyzer (SPECS Phoibos 150), which allows for the simultaneous detection of photoelectrons within an angular range of ±11°. For characterization of the samples prior to trARPES measurements, also a He-discharge lamp was installed at the chamber. As no incoupling window can be used at these photon energies, a differential pumping stage in combination with the aluminum filters is used to maintain a pressure of $< 5 \cdot 10^{-10}$ mbar during measurements. The residual 20% of the amplifier output is available as a pump beam. The temporal overlap and the temporal resolution of the setup was characterized by laser-assisted photoemission (LAPE) [MA06, Saa08] directly on the $BaFe_2As_2$ samples and yielded an XC width of 35 fs. The overall energy resolution of the setup was about 700 meV in the experiments, as determined from a fit of the Fermi edge. This comparativly low energy resolution is determined by the spectral width of the XUV beam and the slid width of the spectrometer optimized for high electron transmission. trARPES delay scans were recorded with an integration

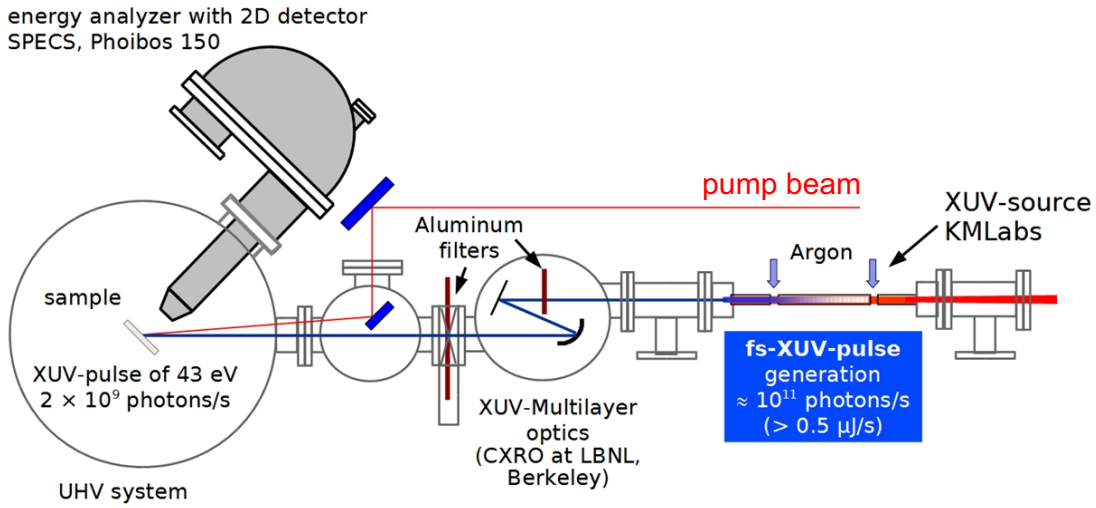

Figure 3.15: Experimental setup of the HHG-trARPES experiment in Kiel. fs pulses in the extreme ultraviolet (XUV) spectral range are created by HHG in a capillary filled with argon gas. The 27^{th} harmonic at a photon energy of $h\nu = 43\,\text{eV}$ is selected by a pair of XUV multilayer mirrors and focused into the experimental chamber. UHV conditions are maintained during measurements by differential pumping stages and the aluminum filters, that are used to block the fundamental radiation. The chamber is equipped with a hemispherical electron analyzer for photoelectron detection.

time of 10 s and typically 10 scans, yielding a total integration time per delay of $\sim 100\,\text{s}$.

3.3 ARPES Setup in Stanford

The high-resolution laser ARPES measurements of $HoTe_3$ presented in chapter 7 were performed using a 7 eV laser ARPES system at the Stanford University in collaboration with Felix Schmitt from the group of Prof. Z.-X. Shen. The advantages of high-resolution laser-based ARPES compared to synchrotron radiation sources lie in the very high energy and momentum resolution achievable with laser light sources and the high photon flux enabling efficient mapping of the electronic states close to E_F [Kor06a]. In addition, with the availability of 7 eV quasi-cw lasers [Che96, Tog03, Kis05], the limitations of the low photon energies obtainable with Ti:Sa systems can be overcome to some extend. The ARPES setup is described in detail in [Sch11b]; here, we briefly describe the generation of the 7 eV light and the main components of the UHV chamber used for photoemission experiments.

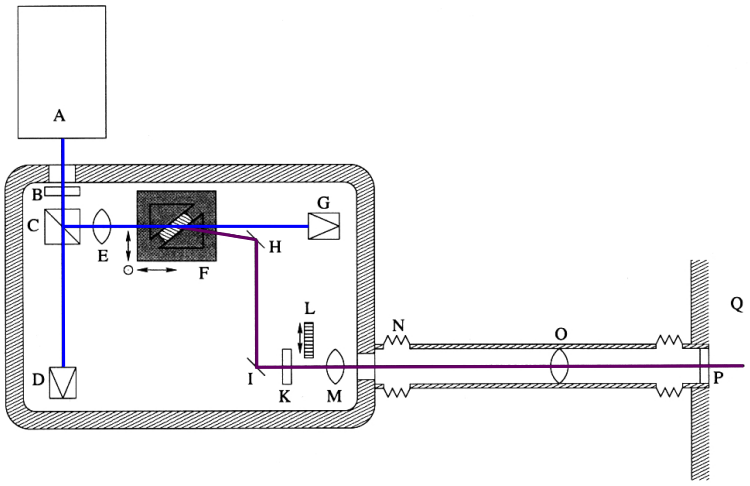

Figure 3.16: Schematics of the 7 eV laser system at the Stanford University. A: pump laser, B: beam polarizer, C: polarizing beam splitter, D, G: beam dumps, E: focusing lens, F: KBBF crystal in prism mount, H, I: steering mirrors, K: $\lambda/4$ plate, L: photodiode, M: correction lens, N: port aligner, O: focusing lens, P: incoupling window, Q: UHV chamber. Beams of 3.5 eV and 7 eV are drawn in blue and purple, respectively [Sch11b].

The 7 eV light used for photoemission is generated by frequency doubling the light of a Palladium mode-locked UV laser. The laser produces 4 W of 355 nm radiation ($h\nu = 3.5$ eV) at a repetition rate of 80 MHz by a third-harmonics-generation process in a KD*F nonlinear crystal. For the SHG process, a special nonlinear crystal, KBBF, is used, which allows for phase matching in an SHG process at $h\nu = 7.0$ eV, in contrast to BBO, which allows only phase matching up to 6.0 eV and exhibits an absorption edge around 6.3 eV. The KBBF crystal is mounted between two prisms, which are used to couple the 355 nm light into the crystal at the corresponding phase matching angle, as sketched in figure 3.16. The SHG process yields 177 nm ($h\nu = 7$ eV) radiation with a spectral width of 1 meV allowing for a very high resolution in ARPES experiments. The average power in the 7 eV beam of ~ 0.1 mW and the long pulse duration of several picoseconds ensures the absence of space charge in the photoemission spectra [Sch11b]. As the 177 nm radiation is efficiently absorbed by oxygen and water in air, the whole SHG process is housed in an air-tight chamber that is purged with nitrogen gas. All important optical components are equipped with motorized controls to allow adjustement of the beam path.

The UHV chamber used for ARPES experiments is equipped with a 5-axis manipulator and a liquid He flow cryostat allowing to reach sample temperatures down to $< 15\,\mathrm{K}$. For photoelectron detection a hemispherical analyzer (SIENTA SES2002) is used, which has been especially calibrated for the use of very low kinetic energies. Thus, an overall energy resolution of $< 3\,\mathrm{meV}$ can be achieved. In addition, the angular resolution of $< 0.3°$ allows, together with the large angular spread of photoelectrons at the small kinetic energies of laser ARPES, for an extremely high momentum resolution of $< 0.005\,\mathrm{\AA}^{-1}$, which enables the detection of very small details such as the bilayer splitting in the occupied band structure of $HoTe_3$, discussed in chapter 7.

3.4 Sample Preparation

The preparation of the samples used for this thesis was twofold: For the experiments on Pb/Si(111) quantum well states presented in chapter 4, samples were prepared *in situ* in the preparation chamber using a Pb evaporation source. For the other experiments, samples were grown and provided for measurements by various collaborating groups. For measurements, a fresh sample surface was exposed by cleaving the samples in the UHV chamber. Here, we give a brief overview of the sample preparation procedures.

3.4.1 Preparation of Ultrathin Pb Films on Si(111)

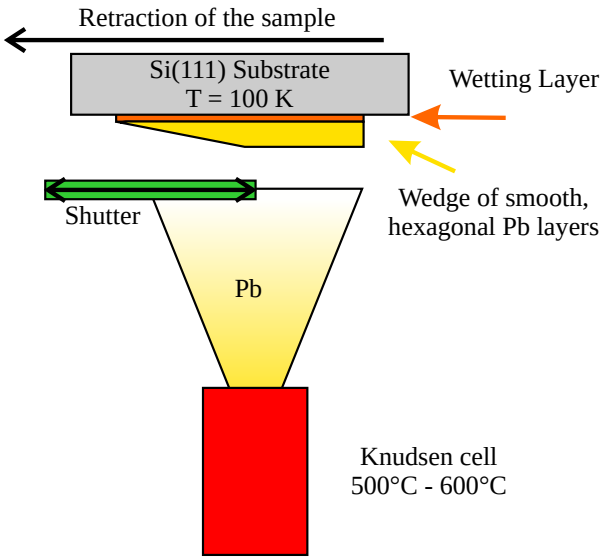

Figure 3.17: Preparation of epitaxial Pb films on Si(111). Pb is evaporated from a Knudsen cell onto the silicon substrate, which has been prepared with a Si(111)-$\sqrt{3} \times \sqrt{3}$-R30°-Pb wetting layer. For the growth of wedge shaped samples, a retractable shutter blocks part of the Pb beam and the sample is slowly moved behind the shutter.

The growth of epitaxial Pb films on Si(111) surfaces has been described in much detail in previous thesis work [Ret08, Kir08a]; here, only a brief introduction into the necessary steps is given. First, the surface of the silicon wafers was cleaned by repeated flashing to 1470 K using current heating, followed by a slow cooling ramp of ~ -1 K/min down to 970 K. This procedure cleans the surface by evaporating contaminations and allows to form the Si(111)-7×7 surface reconstruction, which saturates most dangling bonds of the Si(111) surface. Next, a few monolayers (MLs) of Pb are deposited on the surface and the sample is flashed once to 500 K. This procedure allows for the desorption of excess Pb and to form the Si(111)-$\sqrt{3} \times \sqrt{3}$-R30°-Pb surface reconstruction, which is used as a wetting layer for the growth of epitaxial Pb films [Kir07, Kir08a]. For the evaporation of Pb, a home-build, water-cooled Knudsen cell [Dil06, Kir07] was available and the evaporation rate of $\sim$ 0.5 ML/min was monitored by a quartz micro balance before and after deposition. The epitaxial Pb films were grown in a wedge shape by slowly moving the sample behind a retractable shutter, that blocked part of the Pb beam, as depicted in figure 3.17. The use of wedge-shaped samples facilitates measurements of various film thicknesses on a single sample preparation and the precise determination of the film thickness from the contrast in photoemission intensity, see [Ret08, Kir08a]. Here, the use of shallow thickness gradients of < 0.5 ML/mm in combination with the small laser spot size of $< 100\,\mu$m ensured the homogeneity of the electronic structure within the measured area [Kir10]. To suppress surface diffusion of Pb atoms and island formation [Upt04], the samples were kept at $T = 100$ K during the experiments. After each preparation step, the cleanliness and ordered structure of the surface was verified using low energy electron diffraction (LEED).

3.4.2 Preparation of Cleaving Samples

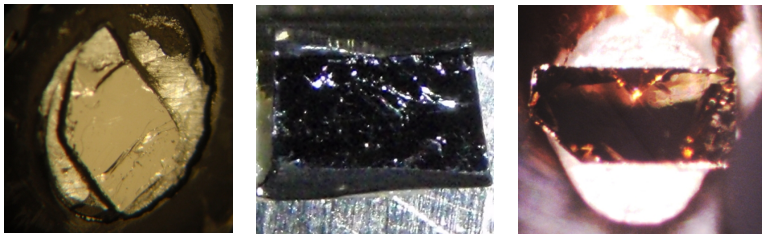

Figure 3.18: Exemplary photographs of the single crystalline samples used for this thesis. (a) $BaFe_2As_2$ crystal mounted to a flat sample post. The flat, shiny surface with the color of silver is suitable for trARPES measurements. (b) Large BSCCO crystal. The black and shiny sample is cleaved very easily. (c) $TbTe_3$ crystal glued to a 45° slanted sample post. The flat, dark-colored surface is nearly free of defects and indicates an excellent cleave.

For samples of complex, layered materials such as the CDW and superconducting (SC) materials studied in this thesis, an in-situ growth of the samples is very challenging and often unfeasible. Instead, single crystals of the material under investigation are usually grown *ex-situ* by various methods and then broken apart within the UHV chamber to reveal a fresh surface of the sample, suitable for ARPES measurements. For layered materials, which break preferentially along the high-symmetry axes, this procedure is called cleaving and the location where the cleave occurs is called the cleaving plane. As the cleaving process inherently possesses a certain amount of randomness, often several cleaves are necessary in order to obtain a flat and uniform surface without many defects, as necessary for trARPES measurements. For crystal surfaces with large defect densities, field enhancements at step edges lead to a large photoelectron emission due to multi-photon absorption of the IR pump beam [Bor10], prohibiting efficient excitation of the electronic system.

The single crystals of Fe pnictides were grown and provided for our measurements by a number of collaborating groups. Crystals of $BaFe_2As_2$ and $BaFe_{1.85}Co_{0.15}As_2$, grown from self-flux or Tn-flux in alumina crucibles were provided by T. Wolf from the Karlsruhe Institute of Technology [Har09]. A typical cleaved crystal of $BaFe_2As_2$ sized approximately $\approx 2 \times 2 \times 0.2\,\mathrm{mm}^3$ is shown in figure 3.18 (a). The crystals are of shiny metallic color and pretty hard to cleave. Usually, the cleave exposes an at least partially flat surface suited for trARPES measurements (figure 3.18 (a)). Samples of $EuFe_2As_2$ grown by a Bridgman method [Jee08] were provided by H. Jeevan from the group of Prof. P. Gegenwart at the University of Göttingen and exhibit similar properties as the Ba-based compounds.

The nearly optimally doped $Bi_2Sr_2CaCu_2O_{8+\delta}$ (BSCCO) samples were prepared by the traveling-solvent floating-zone technique [Eis04] in the group of Prof. H. Eisaki from the Nanoelectronic Research Institute (AIST) in Tsukuba, Japan. In order to obtain the exact oxygen concentration δ for optimally doped samples, the as-grown samples are annealed in O_2 atmosphere for several hours. Successive ac magnetic susceptibility measurements were performed to determine the $T_c = 88\,\mathrm{K}$ of the samples. A large single crystal ($\approx 3 \times 4 \times 0.5\,\mathrm{mm}^3$) of BSCCO is shown in figure 3.18 (b). The samples are of black color and cleave very easily along the a/b plane, revealing a shiny and flat surface.

Finally, single crystalline samples of RTe_3 were grown by slow cooling of a binary

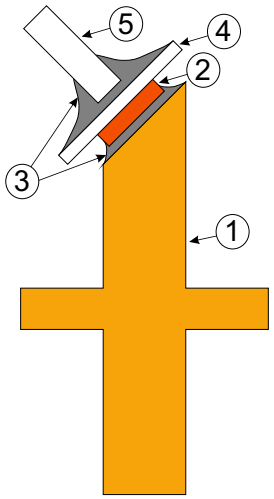

Figure 3.19:
Preparation of cleaving samples. (1) Slanted sample post. (2) Cleavable single crystal sample. (3) Silver epoxy glue. (4) Sapphire plate. (5) Small ceramic pin for cleaving.

melt [Ru08] by J.-H. Chu from the group of Prof. I. Fisher at the Stanford University. The samples possess a color slightly darker than gold and are very soft, comparable to lead. Due to the layered structure of the crystals, similar to graphite, often flakes of the material stick together upon cleaving and lead to patchy surfaces. In addition, the softness of the material often leads to a warping of the cleaved surface. Thus, the cleave of these crystals is particularly delicate and especially larger crystals helped to obtain surfaces suitable for trARPES measurements. In addition, crystals of RTe_3 oxidize very quickly in air, and thus the samples were stored in an UHV chamber and prepared in a glove box under constant flow of an N_2 protective atmosphere. An excellently cleaved sample of $TbTe_3$ is depicted in figure 3.18 (c) ($\approx 3 \times 1 \times 0.3\,\mathrm{mm}^3$), where the dark surface area presents excellent conditions for trARPES measurements.

The preparation of the single crystals on the slanted sample posts, which is done *ex-situ*, requires several steps, that are discussed briefly in the following. First, the single crystals are glued with an UHV compatible and conducting silver epoxy glue (Epo-Tek H20E) onto the flat surface of the slanted sample post. Here, the slant angle of the sample post determines the angle σ of the photoemission geometry (see figure 3.9). In addition, at this step the relative orientation of the sample's a and b-axis[7] with respect to the sample post slant μ has to be aligned, which is achieved by x-ray Laue diffraction before curing the silver-epoxy glue[8]. In the second step, a thin sapphire plate is glued on top of the sample, which allows to evenly distribute the cleaving force across the sample surface, helping to reduce the warping of the surface during the cleave[9]. In a last step, a small ceramic rod used as cleaving pin is glued on top of the sapphire plate. A schematic cross-section of a sample ready for cleaving is shown in figure 3.19. This sample preparation puts the predetermined cleaving plane in the center of the sample and allows for a good cleaving behavior. Finally, the sample is mounted onto the sample boat (figure 3.8) and the top of the cleaving pin is connected to the sample boat by a thin tantalum wire to prevent the cleaving pin from falling into the UHV chamber and to recycle the part of the sample that remains on the cleaving pin. After each preparation step, the Ag epoxy glue is cured at $T = 150\,\mathrm{K}$ for approximately 30 min.

[7] For RTe_3, the b axis is the longer axis perpendicular to the planes and the orientation refers to the a and c axis.

[8] The Laue diffraction is not capable to separate the a and c axis of RTe_3. As a consequence, there exists an ambiguity whether the selected ARPES geometry allows access to the gapped region of the BZ or the metallic pocket, which is determined from the ARPES spectra.

[9] The sapphire plate was only used for the soft RTe_3 samples; for the much harder FeAs and BSCCO samples, the cleaving pin is glued directly onto the sample.

4 Dynamics of occupied Quantum Well States in Pb/Si(111)

The structure and energetics of interfaces between semiconductors and metals are of importance both from a fundamental and from a technological point of view. In semiconducting devices like integrated circuits, solar cells or light-emitting diodes, interfaces to metal electrodes play a crucial role for device functionality. Thus, semiconductor surfaces and semiconductor-metal junctions have been intensely studied in a variety of systems [Moe93]. Especially on Silicon surfaces, the most commonly used semiconductor for device fabrication, a variety of interface structures and reconstructions with various metal adsorbates have been investigated [Hes90, Car92, Moe93, Zha98, Hup03, Ric04]. Already for sub-monolayer (ML) coverages of metal atoms, the occupation of metal-derived surface states within the semiconductor band gap leads to a charge transfer between substrate and adsorbate atoms. This results in a space charge region near the semiconductor interface and the buildup of a Schottky energy barrier [Moe93], which determines the energy band alignment at the interface. In the non-equilibrium regime under optical excitation, a transient modification of the space charge region and a charge redistribution known as surface photo voltage (SPV) occurs [Moe93], which relaxes on a a slow picosecond to nanosecond timescale [Sif02, Wid03, Pie07, Mur08]. However, the detailed response of the energy alignment and the charge distribution at the interface to an optical excitation on an ultrafast time scale received only little attention so far.

Time-resolved photoemission techniques have been quite successful to investigate the dynamics of excited electrons directly in the time domain. While time-resolved two-photon photoemission (2PPE) is sensitive to unoccupied electronic states and has been intensely used to study the dynamics of hot electron distributions and of surface- and image potential states [Sch94, Pet97, Kno98, Cao98, Wei02b, Ech04, Mer04, Mat10], linear time- and angle-resolved photoemission spectroscopy (trARPES) analyzes the occupied electronic bands under optical excitation. However, to investigate the electronic dynamics *within* the bulk of normal metals, one has to overcome several challenges. First, electronic bands with a strong dispersion perpendicular to the surface, like in many bulk metals, usually show only broad energetic features that limit a comprehensive analysis, due to the finite $k_\perp$ resolution in photoemission spectroscopy caused by the finite photoelectron escape depth (see chapter 2.4). Second, electronic transport effects can drastically influence the observed dynamics and can be hard to disentangle from other effects [Kno98, Aes00, Lis04a]. The use of ultrathin metal films is one approach to overcome these difficulties. The ultrathin metal film breaks the periodicity along the surface normal and the resulting electron confinement gives rise to sharp quantum well states (QWSs) at discrete energies in the occupied and unoccupied parts of the quantized band structure [Pag99, Chi00, Mil02, Kir10]. Due to their quasi-two-dimensional (2D) character, QWSs show no $k_\perp$ dispersion [Mil02] and their confinement to the ultrathin film effectively inhibits electron transport [Kir10] for electron states with energies within the substrate band gap.

The QWS system of ultrathin epitaxial films of Pb on Si(111) presents a nearly ideal realization of such a quasi-2D model system, which has been intensely studied in the past [Yeh00, Wei02a, Upt04, Zha05, Dil06, Hon09, Bru09, Zha10, Slo11], including previous work done by our group [Kir07, Kir08b, Kir10]; for a comprehensive introduction to

the topic of QWSs and Pb/Si(111), we refer to the author's Diploma thesis thesis [Ret08] and the PhD thesis of P. Kirchmann [Kir08a]. Due to the efficient confinement of the electronic wave functions to the metal film by the band gap of the semiconducting substrate, the system exhibits a series of well-defined and sharp QWSs in the occupied and unoccupied band structure [Upt04, Dil06, Kir07, Kir10]. First investigations of the electron dynamics focused on the electron lifetime in unoccupied QWSs [Kir08b, Kir10]. An ultrafast shift of the binding energy of occupied QWSs observed after strong optical excitation was initially discussed in the context of transient screening effects [Ret08, Kir08a], which, however, presented a very qualitative discussion.

In this chapter, we focus on this ultrafast dynamics of occupied QWSs and of states located at the Pb/Si interface after photoexcitation and present a systematic study as a function of film thickness and on p- and n-doped Si substrates. First, in chapter 4.1, we discuss the influence of the SPV on the photoemission spectra of films on substrates with different doping levels. To establish the origin of the transient peak shift found for all occupied states in Pb/Si(111) after photoexcitation, we make use of the selection of Pb coverage and the respective QWS binding energies, as the latter are very sensitive to the energy alignment and the interface structure [Yeh00, Ric04, Slo11]. Thus, these states can serve as a probe for the ultrafast processes at the metal-semiconductor interface. In addition, the laser-based photoemission with low kinetic energies is characterized by an enhanced bulk sensitivity [Kor06a, Kis08], which allows the detection of interface states at the buried Pb/Si interface. By comparing the size of the peak shift with the binding energy of QWSs and interface states (ISs), we establish a transient shift of the relative position of the Si band gap with respect to the metal's Fermi level as origin of the peak shift in chapter 4.2. This conclusion is corroborated by model calculations using the phase accumulation model, presented in chapter 4.3. Finally, we analyze coherent oscillations of the QWS peak position found at higher excitation levels in chapter 4.4. These oscillations, which were already discussed previously as coherent phonon modes of the Pb film [Kir08a] are assigned here more specifically to coherent surface oscillations on the basis of a recent slab calculation [Ynd08], and a possible scenario for their excitation and coupling to the QWS band structure is discussed.

The preparation of epitaxial Pb/Si(111) films on top of the reconstructed Si(111)-$\sqrt{3} \times \sqrt{3}$-R30°-Pb surface is described in chapter 3.4.1, yielding high-quality wedge-shaped Pb films covering several monolayers of film thickness. During the experiments, the samples were kept at $T = 100\,\mathrm{K}$. trARPES measurements were performed using the fundamental pump photon energy $h\nu_{\mathrm{Pump}} = 1.5\,\mathrm{eV}$ and the probe photon energy $h\nu_{\mathrm{Probe}} = 6.0\,\mathrm{eV}$ in normal emission at the $\overline{\Gamma}$-point. Alternatively, the output of the IR-OPA at $h\nu_{\mathrm{Pump}} = 0.95\,\mathrm{eV} < E_{\mathrm{G}}$ below the indirect Si band gap was used for pumping to suppress substrate contributions.

The main part of this chapter has been published during this thesis in the New Journal of Physics [Ret12b].

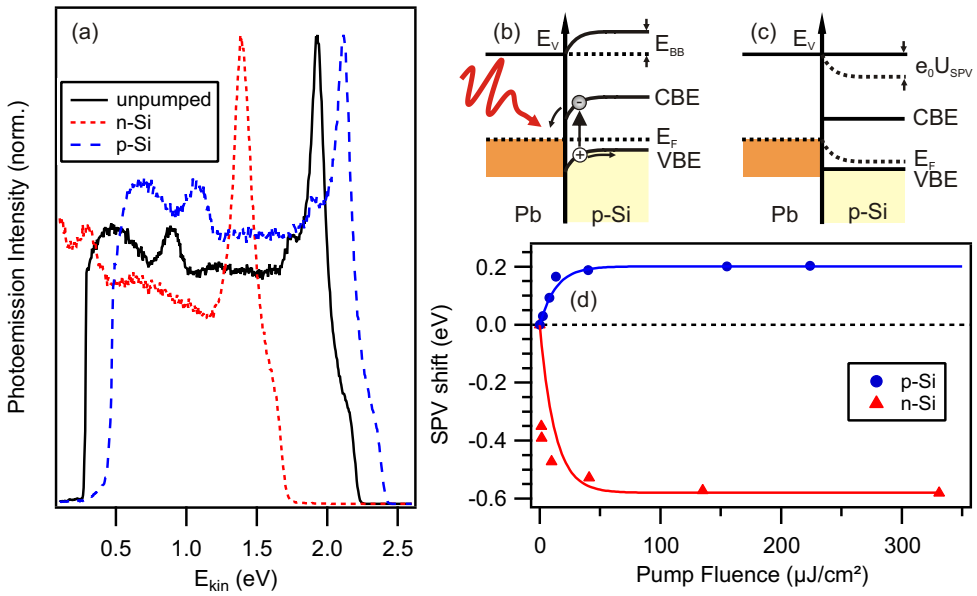

Figure 4.1: (a) Effect of surface photo voltage (SPV) on the photoemission spectra of 5 ML Pb/Si(111). The solid black line shows a reference spectrum without the pump beam. Red (small dashed) and blue (large dashed) spectra are taken with a pump fluence of $F = 40\,\mu\mathrm{J/cm^2}$ on n-Si and p-Si substrates, respectively. Due to the SPV, the whole spectra are shifted in kinetic energy. (b) Sketch of the Schottky junction in equilibrium. The Fermi level pinning at the interface leads to a space charge region and to band bending E_{BB}. Conduction band edge (CBE), valence band edge (VBE) and vacuum level (E_{V}) are indicated. An incident photon with an energy above the band gap excites electron-hole pairs across the band gap, which are separated in the space charge region. (c) Schottky junction after optical excitation. The SPV reduces the band bending, leading to flat bands for sufficient excitation densities. The Fermi level at the interface is shifted by the SPV. (d) Measured SPV shift as a function of pump fluence for p-Si (blue circles) and n-Si (red triangles) substrates, respectively. Lines are guides to the eye.

4.1 Fermi Level Pinning and Surface Photo Voltage

The metal-semiconductor interface between the Si substrate and the Pb film leads to a charge transfer between substrate and metal film, as the Fermi level E_{F} is pinned by localized charges at the interface, the so-called metal-induced gap states (MIGS) [Moe93]. This results in a space charge region of typically several 100 nm thickness within the Si substrate and leads to band bending near the surface depending on the doping level as sketched in figure 4.1 (b) for a p-doped substrate. Photo-generated electron-hole (e-h) pairs are separated in the space charge region and lead to the reduction of the band bending, see figure 4.1 (c). This results in a potential difference between interface and bulk, known as surface photo voltage (SPV) [Moe93].

The SPV manifests in a photoemission experiment as a rigid shift of the spectra, as the energy reference of the spectrometer is determined by the bulk Fermi level [Dem86, Alo90]. Figure 4.1 (a) shows photoemission spectra of 5 ML Pb/Si(111) with and without excitation by the pump pulse arriving shortly after the probe pulse, i.e. at negative pump-probe delays. The details of the spectra will be discussed below. On a p-Si substrate, the spectrum is – in comparison to a reference spectrum taken without optical

excitation (solid black line) – rigidly shifted to higher kinetic energy (large dashed blue line), including the secondary cutoff at low kinetic energies, which is determined by the sample work function. In contrast, on an n-Si substrate, the spectrum is shifted towards lower kinetic energy. This is well understood from the opposite orientation of the space charge field for n- and p-doped semiconductors, leading to a reversed charge separation. Additionally, the shift on an n-Si substrate is considerably larger. The amount of the SPV has been determined for various fluences F for both n- and p-Si, as shown in figure 4.1 (d). We note that (i) the SPV saturates for fluences $F > 50\,\mu\mathrm{J/cm^2}$ and (ii) is considerably weaker on p-Si. Thus, the usage of p-Si substrates and excitation fluences $F > 50\,\mu\mathrm{J/cm^2}$, as used for all time-resolved measurements, if not otherwise stated, minimizes the effect of the SPV and ensures flat-band conditions as shown in figure 4.1 (c). Since the dynamics of the SPV happens on a nanosecond timescale [Wid03], it can be considered as constant within the time interval of a few picoseconds after excitation investigated here[1]. An SPV induced by the probe beam is negligible as was checked by a variation of the probe fluence.

[1] Although the SPV is built up by the pump pulse, the shift of trARPES spectra is also found for negative delays close to time zero as explained in [Wid03].

4.2 Coverage-dependent Peak Shift of occupied Quantum Well States

Let us now turn to the spectral features and their modification with optical excitation. Figure 4.2 (a) shows spectra of a 5 ML Pb film on Si(111) with a moderate excitation fluence of $F = 60\,\mu\mathrm{J/cm^2}$ before (filled black symbols) and at $t = 100$ fs after excitation (open red symbols). Besides the high-energy cutoff at the Fermi energy and the sharp low energy cutoff (secondary edge) at $E - E_\mathrm{F} = -1.9$ eV, determined by the sample work function of $\Phi = 4.1$ eV, we find three main features in the spectrum. The most prominent peak at $E - E_\mathrm{F} = -0.26$ eV is the highest occupied quantum well state (hoQWS), which resides well above the silicon valence band edge (VBE) at $E - E_\mathrm{F} \sim -0.4$ eV. Its sharpness and high intensity evidence the strong confinement to the Pb surface layer, in agreement with earlier photoemission work [Upt04, Kir07, Kir10]. In contrast, the broad quantum well resonance (QWR)[2] at $E - E_\mathrm{F} = -0.94$ eV lies within the Si valence band and is degenerate with bulk Si valence band states. The third feature at $E - E_\mathrm{F} = -1.39$ eV is assigned to an IS at the Pb/Si(111) interface, as it appears at all coverages at roughly the same energy and does not show the characteristic energy dispersion of the QWSs in Pb/Si(111) [Wei02a, Kir08b, Ret08, Kir08a, Kir10]. Moreover, this state is also present on the bare Si(111)-$\sqrt{3} \times \sqrt{3}$-R30°-Pb surface and is less pronounced for higher Pb coverages, as photoemitted electrons from the interface have to traverse a thicker Pb film before emission into the vacuum.

Upon photoexcitation, all states exhibit an energy shift ΔE to higher binding energies, as recognized from the solid and dashed lines in figure 4.2 (a), which mark the peak position before and after the laser excitation, respectively. This shift is rather small for the hoQWS, whereas it is considerably larger for the QWR and the IS. Quantum well states near the Si VBE, like the hoQWS of a 3 ML film shown in figure 4.2 (c), are characterized by a pronounced asymmetry of the line shape, indicating the transition from QWSs to QWRs, as the confinement weakens in the vicinity of the VBE. Upon excitation, however, in addition to the peak shift, this asymmetry is considerably reduced. As will be discussed in the following, this change in the line shape indicates a transient enhancement of the electronic confinement conditions of the QWSs.

At this point, we note that the shift in binding energy is qualitatively different from the energy shift induced by the SPV effect. The SPV leads to a shift of the whole spectrum, including the Fermi and secondary edge (see figure 4.1) and does not change the peak position relative to the Fermi level. This is in contrast to the shift in binding energy after photoexcitation, which effects only the peak positions relative to the secondary edge and E_F. This is apparent from the secondary edge and the Fermi cutoff in figure 4.2 (a), which do not shift. Furthermore, the effect of the SPV is constant in the time window discussed here, and its direction depends on the doping level of the substrate. In contrast, the peak shift of the hoQWS occurs in the same direction also on n-doped Si samples, as shown in figure 4.3 (a).

The dynamics of the peak shift is analyzed in a false color representation of the trARPES intensity as a function of the pump-probe delay, shown in figure 4.2 (b). The peak position of the hoQWS, indicated by the blue markers, shows that the peak shift occurs on a very short timescale of ~ 100 fs after excitation, followed by a slower relaxation towards the initial peak position. For a more quantitative analysis, the relative peak shift ΔE is determined by fitting the trARPES spectra with a series of Lorentzian lines

[2] Actually, this peak corresponds to the QWR of the neighboring coverage of 4 ML, which originates from a crosstalk of that coverage, see figure 4.6 (c).

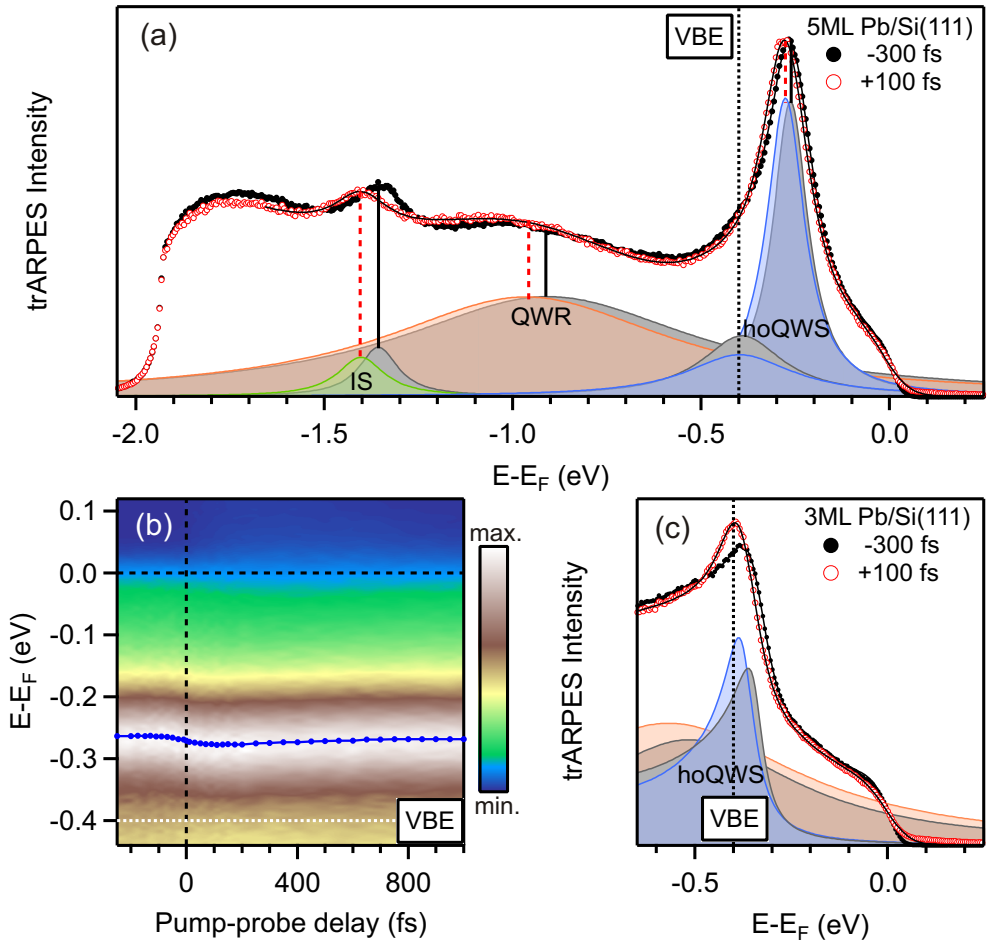

Figure 4.2: (a) Time-resolved photoemission spectra of a 5 ML Pb film before (black filled circles) and at $t = 100$ fs after optical excitation (red open circles). Solid lines are fits to the data (see text). The pronounced peak at $E - E_F = -0.26$ eV is the highest occupied quantum well state (hoQWS). In addition, a broad quantum well resonance (QWR) and an interface state (IS) at the Pb/Si(111) interface are observed. The peaks used in the fitting model are shown as shaded areas and the peak positions as determined by the fits are indicated, exhibiting a peak shift ΔE to higher binding energy. The small shoulder at $E - E_F \sim -0.4$ eV is the hoQWS of small areas with 3 ML coverage within the probed spot. (b) trARPES intensity for 5 ML coverage in a false color plot as a function of pump-probe delay. The blue line and symbols mark the peak position of the hoQWS obtained by fitting the spectra (see text). (c) trARPES spectra as in (a), but for 3 ML Pb/Si(111). Note the pronounced asymmetry of the hoQWS line shape near the silicon valence band edge (VBE), which is reduced upon excitation.

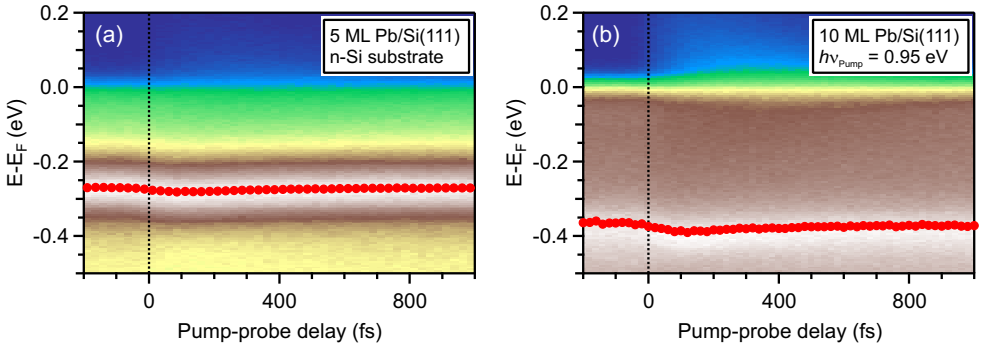

Figure 4.3: Substrate doping and pump photon energy dependence of the peak shift. (a) Transient trARPES data of the hoQWS of 5 ML Pb/Si(111) on an n-doped Si substrate. Peak positions are marked with red dots. (b) Transient trARPES data of the hoQWS of a 10 ML film on a p-Si substrate, using a pump photon energy of $h\nu_{\mathrm{Pump}} = 0.95$ eV. In both cases, a similar peak shift is observed.

and an exponential background function, multiplied with a Fermi-Dirac distribution and convoluted with an instrument function. The fits and the contributing peak functions are shown as thin black lines and shaded areas, respectively, in figure 4.2 (a) and (c). For the hoQWS of 3 ML Pb/Si(111) (figure 4.2 (c)) a Doniach-Šunjić line shape [Don70] has been used in order to account for the pronounced peak asymmetry. The fit yields a Doniach-Šunjić asymmetry parameter of $\alpha = 0.51(1)$, which reduces significantly to $\alpha = 0.35(1)$ after photoexcitation, see figure 4.2 (c).

The resulting peak shifts are shown in figure 4.4 (a) for the three states in figure 4.2 (a) as a function of pump-probe delay. For comparison, figure 4.4 (b) shows the pump-probe pulse cross correlation (XC), determining the temporal resolution of the experiment and the temporal overlap of pump and probe pulse (time zero, t_0). To determine the maximal peak shift ΔE_{max} and the timescale of its recovery τ, exponential decay functions,

$$\Delta E(t) = -\Delta E_{\mathrm{max}} \cdot \exp(-t/\tau) + B \quad ,$$

convoluted with the pump-probe envelope, are fitted to the data. Here, B accounts for a transient equilibrium after relaxation of the initial dynamics. For the hoQWS, we find a small maximal peak shift of $\Delta E_{\mathrm{max}}^{\mathrm{hoQWS}} = 17(2)$ meV. In contrast, the QWR and the IS show a much stronger peak shift of $\Delta E_{\mathrm{max}}^{\mathrm{QWR}} = 66(6)$ meV and $\Delta E_{\mathrm{max}}^{\mathrm{IS}} = 52(4)$ meV, respectively. The relaxation times of all three states are found to be around 500 fs ($\tau_{\mathrm{hoQWS}} = 460(90)$ fs, $\tau_{\mathrm{QWR}} = 610(150)$ fs and $\tau_{\mathrm{IS}} = 600(90)$ fs).

The comparison of the peak shift transients with the pulse XC reveals that the initial buildup of the peak shift occurs within the time-resolution of our experiment. We consider this ultrafast timescale as evidence for the electronic origin of the responsible processes, as e-h pairs are initially excited by the laser pulse. The energy transfer to the lattice occurs at later times and thus effects related with lattice dynamics are in metals typically limited to slower timescales. Electron thermalization and electron-lattice equilibration has been intensely studied in metallic systems [Fan92, Lis04b] and can be described phenomenologically in the context of the TTM [Ani74, All87, DF00, Ret02, Lis04b], see chapter 2.1.2. Although this model bears several limitations and simplifications, e.g. the assumption of a constant density of states or a thermalized electron system, model calculations of the TTM can be used to estimate the electron-lattice equilibration time in Pb/Si(111), as shown in the inset of figure 4.4 (a). In the

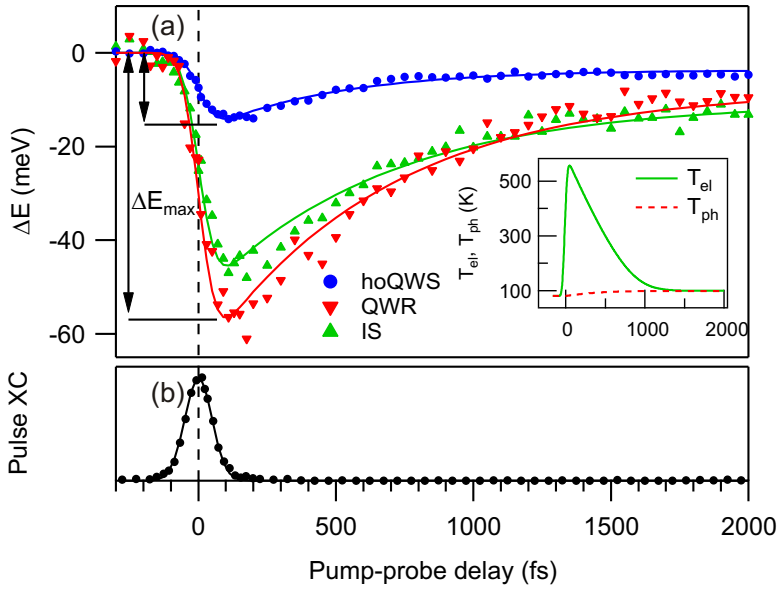

Figure 4.4: (a) Peak shift ΔE of the three states shown in figure 4.2 (a) as a function of pump-probe delay. Solid lines are exponential fits to the data (see text). The buildup of the peak shift occurs for all three peaks within the pulse-duration of ~ 100 fs. The maximal peak shift ΔE_{max} is reached for all peaks at ~ 100 fs, followed by a relaxation towards a transient equilibrium. The inset shows the transient electron and lattice temperatures, T_{el} and T_{ph}, respectively, obtained from a TTM simulation (see text). (b) Cross correlation (XC) trace of the two laser pulses obtained from excited electrons at $E - E_{\mathrm{F}} > 1.4$ eV.

calculation, electronic diffusion and transport processes have been neglected to account for the confinement to the ultrathin metal film and the experimental excitation conditions have been used. The calculated electronic temperature T_{el} shows a steep rise at t_0 and a relaxation within ~ 1 ps, comparable to the relaxation of the peak shift. In contrast, the lattice temperature T_{ph} increases only slightly after several 100 fs, further supporting the electronic origin of the peak shift.

To compare the peak shifts found on different coverages of Pb/Si(111), the maximal peak shift ΔE_{max} of interface and quantum well states is plotted in figure 4.5 for various film thicknesses as a function of the respective equilibrium peak position. We find a pronounced dependence of ΔE_{max} from the peak position relative to the Si VBE: below the VBE, for QWRs and the interface state, we find a comparatively strong shift of ~ 60 meV, which does not depend within our accuracy on the energetic position. Above the VBE, however, for QWSs which are well confined to the Pb film, the peak shift reduces to only ~ 10 meV at energies above -0.2 eV. This clear correlation of the size of the peak shift with the peak position relative to the Si valence band, which we establish here, indicates its relation to the silicon band gap. Furthermore, as already mentioned before in the context of figure 4.2 (c), states close to the VBE exhibit in addition to the peak shift a sharper and more symmetric line shape upon excitation, which we explain as a transient increase in confinement of the QWSs to the Pb film. This corresponds to a transient shift of the Si band gap relative to the Fermi level within the metal film, i.e. a modification of the Fermi level pinning position at the interface.

In order to determine the amount of band gap shift, we recall that the interface states at higher binding energies are located at the Pb/Si interface and are derived from Si

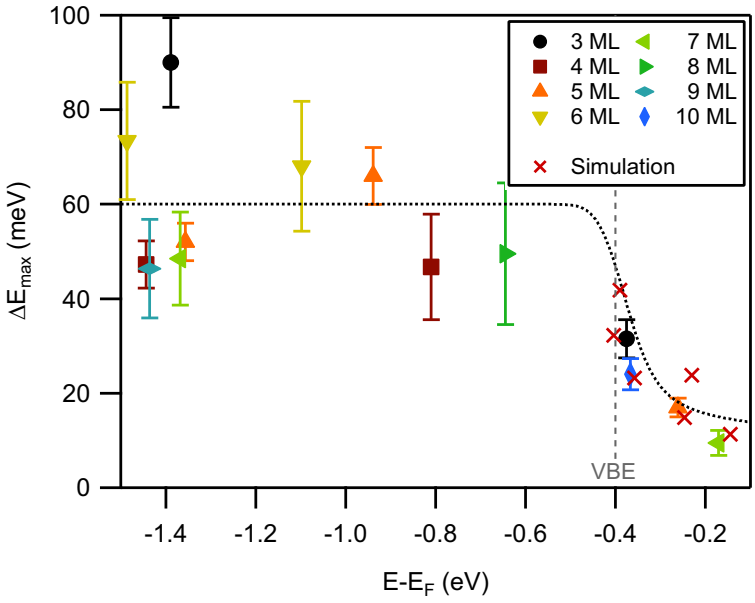

Figure 4.5: Maximal peak shift $\Delta E_{\max}$ of interface and quantum well states as a function of peak position for various film thicknesses. Red crosses mark the results of a model calculation of the phase accumulation model (see text). The dashed line is a guide to the eye. Note the strong reduction of $\Delta E_{\max}$ for QWSs confined above the silicon VBE.

states. Thus, these states are fixed to the energy reference of the Si substrate, i.e. the position of the Si band edges. Hence, we can use the peak shift of the interface states as a marker for the transient band gap shift, which, in turn, leads to a change of the confinement and a shift of the QWS binding energy.

4.3 Phase-Accumulation Model Calculations

To test this hypothesis, we have performed a simulation in the framework of the phase accumulation model [Mil02, Luh02, Upt04]. The energy position of a QWS is determined by the confined wave function along the metal film's normal direction. In this model, electrons propagating between the Pb/Si interface and the Pb surface are reflected at each interface, exhibiting a phase shift Φ_i and Φ_s, respectively, as sketched in figure 4.6 (a). According to the Bohr-Sommerfeld quantization rule, the total phase accumulated during a round trip, Φ, has to equal a multiple of 2π for a stationary state:

$$\Phi = 2k\Theta d + \Phi_i + \Phi_s = n \cdot 2\pi \quad . \tag{4.1}$$

Here, k is the electron wave number, Θd is the film thickness with Θ the number of monolayers and d the thickness of one ML, and n an integer quantum number. This condition determines the allowed electron wave vectors and hence the energetic positions of the QWSs. The phase factors Φ_i and Φ_s are energy dependent and two approximations are commonly used for these expressions. The surface potential is usually described by the image potential, leading to a phase shift of [Mil02]

$$\Phi_s = \pi \left(\left[\frac{3.4}{E_\mathrm{V} - E} \right]^{1/2} - 1 \right) \quad , \tag{4.2}$$

where E_V is the vacuum energy level. For modeling of the phase shift Φ_i at the Pb/Si interface, an empirical formula for the phase shift of π across a band gap in a two band model is used [Smi85, Luh02, Upt04]:

$$\Phi_i = \mathrm{Re}\left[-\arccos\left(2\frac{E - E_\mathrm{VBM}}{E_\mathrm{G}} - 1 \right) \right] + \Phi_0 \quad , \tag{4.3}$$

with the valence band maximum E_VBM and the size of the band gap E_G. Φ_0 denotes a phase offset used as a fit parameter to adjust the model to the data.

To numerically determine the energy positions of the QWSs, equation (4.1) is rewritten in terms of a coverage-dependent phase shift Φ_Θ and a quantum number-dependent phase shift Φ_n,

$$\Phi_\Theta \equiv 2k\Theta d = n \cdot 2\pi - (\Phi_i + \Phi_s) \equiv \Phi_n \quad . \tag{4.4}$$

The phase shifts Φ_Θ (blue) and Φ_n (red) for $\Theta = 1 - 10\,\mathrm{ML}$ and $n = 1 - 6$ are shown in figure 4.6 (b) as a function of energy. The phase shift of π across the Si band gap is clearly visible in the quantum number-dependent phase shift Φ_n. Now, the QWS binding energy corresponding to quantum number n and coverage Θ can be determined graphically from the intersection of the corresponding phase shift, as indicated by black circles. The resulting binding energies determined by the phase accumulation model for $\Phi_0 = -0.44\,\pi$ are shown in figure 4.6 (c) as a function of Pb coverage and binding energy on top of the experimental photoemission data of occupied QWSs. Despite the simplicity of the model, we achieve reasonable agreement with the energy positions of the QWSs within the band gap [Kir10] and reproduce the characteristic 2 ML periodicity of the dispersion of QWS binding energies with thickness [Wei02a]. The deviations found for states below the Si band gap can be attributed to the empirical formula used for the phase shift at the interface Φ_i, which does not take the interfacial structure into account and does not describe the phase shift correctly for QWRs inside the Si valence and conduction band.

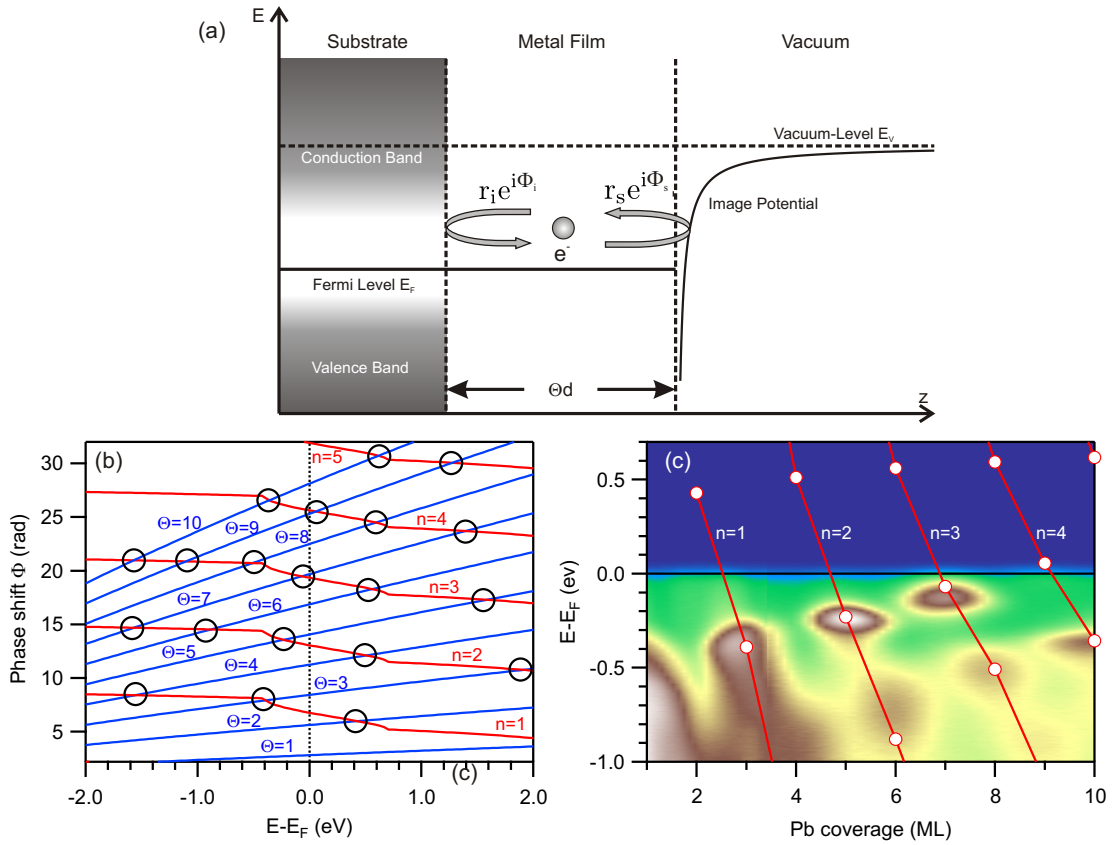

Figure 4.6: Results of the phase accumulation model. (a) Sketch of the phase accumulation model. The electron wavefunction is reflected at the surface and at the interface, exhibiting a phase shift Φ_s and Φ_i, respectively. (b) Coverage-dependent (blue) and quantization number-dependent (red) phase shift Φ_Θ and Φ_n for various Θ and n as a function of energy $E - E_\mathrm{F}$, respectively. QWS binding energies are determined by the crossing points of Φ_Θ and Φ_n. (c) Photoemission intensity of occupied QWSs as a function of Pb coverage and energy $E - E_\mathrm{F}$. Symbols mark QWS positions of the phase accumulation model and lines connect QWSs with the same quantum number n.

The effect of a band gap shift on the QWS energies was determined by shifting the band edge in the model by $\Delta E_\mathrm{VBM} = -60\,\mathrm{meV}$, the value that we determined from the interface state in the experiment. The resulting shift in QWS binding energy is plotted as red crosses in figure 4.5. We find a close agreement with the experimentally determined peak shifts, which increase strongly towards the Si valence band edge, as indicated by the dashed line. Within the model, this is understood by the increasing slope of the arccos function near the band edge in equation (4.3), which results in a stronger response to the shift in the band gap at these energies, see also figure 4.6 (b).

Now we discuss possible origins of the transient band gap shift at the interface. Since this shift occurs in the same direction on n- and p-doped silicon samples, we can exclude a direct influence of the space charge layer, as this is inversed in n-doped silicon and would lead to a reversed effect. Furthermore, the effect is also present for excitation wavelengths below the Si bulk band gap (figure 4.3 (b)), where no excitation within the silicon substrate is possible by a one-photon absorption process. Thus, the shift of the band gap must be due to changes happening at the interface or within the Pb overlayer. Since the pinning position of the Fermi level at the interface is directly determined by

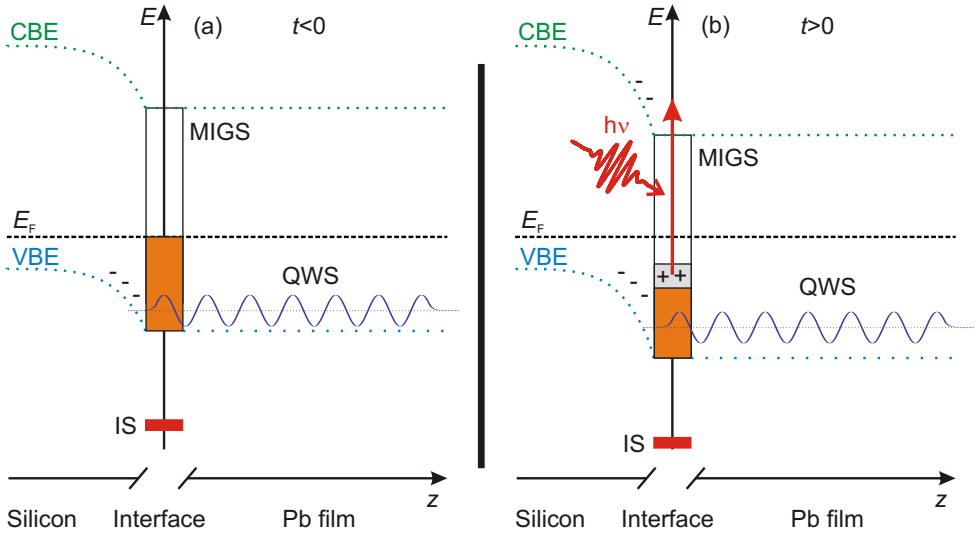

Figure 4.7: Schematic energy diagram near the Pb/Si interface. (a) Before excitation, the metal-induced gap states (MIGS) at the interface are populated to a certain level, pinning the Fermi level E_F. This leads to band bending and a space charge region within the substrate, as sketched for p-type doping. Valence band edge (VBE) and conduction band edge (CBE) are indicated by dashed green and blue lines, respectively. (b) Photoexcitation leads to a depopulation of MIGS and a charge transfer towards the bulk. This increases the band bending and shifts the band gap to lower energies. The interface state (IS) is shifted by the same amount. Due to the modified confinement conditions by the shifted band gap, the QWS binding energies are likewise shifted away from E_F.

the charge transfer at the interface and the population of MIGS, a modification of this charge balance upon excitation is the most likely origin of the observed effect.

Still, the direction of the peak shift towards *higher* binding energy is intriguing. A usual expectation would be, that additional energy delivered by the optical excitation leads to a destabilization of the system, i.e. a softening of the electronic bonds and a decrease of binding energies. Here, however, we find an energetic *stabilization* upon photoexcitation, contrary to this expectation. From the experimentally observed increase in binding energy, we conclude that the strong perturbation by the optical excitation leads to a transient depopulation of metal-induced gap states and an electron transfer from the film to the bulk, as sketched in figure 4.7. This results in a stronger band bending on p-Si, as more bulk acceptors become negatively charged, and a downshift of the band gap relative to the Fermi level on an ultrafast timescale. In n-Si, the charge transfer leads to a reduction of the band bending, as additional bulk donors are neutralized. The IS located at the Pb/Si interface is shifted along with the band gap. In turn, the shifted band gap results in a change in the confinement condition for the QWSs in the metal film, which leads to a shift of their binding energies. Simultaneously, states near the band edge, that are only weakly confined before excitation and show asymmetric peak shapes, become more symmetric after excitation due to the enhanced confinement by the shifted band edge.

4.4 Coherent Surface Phonon Excitation in Pb/Si(111)

In addition to the incoherent peak shift induced by the transient modification of the confinement condition, we find a coherent response of the system to the optical excitation, if we increase the excitation by a factor of ~ 20. Figure 4.8 (a) depicts the transient trARPES intensity of 5 ML Pb/Si(111) with an absorbed fluence of $F = 1.1\,\mathrm{mJ/cm^2}$ in a false color map. The larger shift of the hoQWS ($\Delta E_{\max} = 41(4)\,\mathrm{meV}$) and the depletion of the intensity at $E - E_\mathrm{F} < -0.4\,\mathrm{eV}$ evidence the stronger excitation of the system. The gray contour lines highlight the population of unoccupied states induced by the strong optical excitation. From the spectral weight in the excited state spectrum we estimate an excitation level of $> 9\%$ of the valence electrons in a window of 1 eV around E_F. The distinct unoccupied state at $E - E_\mathrm{F} = 1.1\,\mathrm{eV}$ visible through the closed contour line around zero pump-probe delay is identified as the lowest unoccupied QWS [Ret08, Kir08a, Kir10]. The excess energy in the electronic system relaxes on a timescale up to 3 ps through electron-phonon (e-ph) coupling and is transfered to the phononic system, leading to substantial lattice heating at these excitation densities. This results in a thermal expansion of the Pb film and induces an additional slow shift of the binding energy after the recovery of the initial peak shift at $t > 1$ ps in figure 4.8, which was not observed at lower excitation densities (compare figure 4.4) and persists up to 3 ps.

The transient binding energy of hoQWS as determined by fitting of the peak position is depicted in figure 4.8 (b) together with a polynomial background function. On top of the pronounced shift of the peak position which was discussed in the previous part, we see a weak periodic modulation of the peak position with a period of ~ 500 fs. To analyze the oscillating contribution to the peak shift, the incoherent background determined by the polynomial fit is subtracted, yielding the coherent oscillatory part of the peak shift, ΔE_osc, which is shown in the lower panel of figure 4.8 (b). Remarkably, the high dynamic range and good signal-to-noise (S/N) ratio in trARPES intensity of $> 10^5 : 1$ combined with the systematic analysis of fitting the peak position enables the observation of very small relative energy variations of only ~ 1 meV, which is significantly below the experimental energy resolution of 50 meV. A fit of a sine function to the data, shown as thin red line, yields a frequency of $\nu = 1.97(6)$ THz and an initial oscillation phase of $\phi = 0.4(2)\,\pi$, as indicated by the dashed extrapolation of the fit to zero pump-probe delay. A fast Fourier transformation (FFT) of ΔE_osc exhibits a sharp peak at a frequency of 2.0(1) THz that corroborates the results of the sine fit.

This brings up the question of the origin of the binding energy oscillation. The frequency of the oscillations of a few THz is in the range of acoustic or low-energy optical phonon modes of typical metals. Indeed, the optical excitation of coherent lattice vibrations by fs laser pulses is a rather common phenomenon and has been intensely studied in various materials [Dek00, Has05, Has10, Ish10], see also chapter 2.1.3, chapter 5 and chapter 7. One prerequisite for this process is the existence of phonon modes with finite energy at the Brillouin zone (BZ) center ($q = 0$), typically optical phonon modes, because the optical excitation does not provide a finite momentum. However, the fcc unit cell of Pb supports only acoustic phonon branches with vanishing energy at the BZ center. The phonon spectrum of Pb shows a pronounced peak around 2 THz [Lan76, Row69] and the highest energy modes around 2.1 THz are found in the longitudinal phonon branch near the BZ boundary along the Γ-L direction [Sav96], which is perpendicular to the film direction. To provide the momentum necessary for optical excitation of such modes, the broken symmetry perpendicular to the film has to be considered, giving rise to new phonon modes at the BZ center. More recent calculations of lattice dynam-

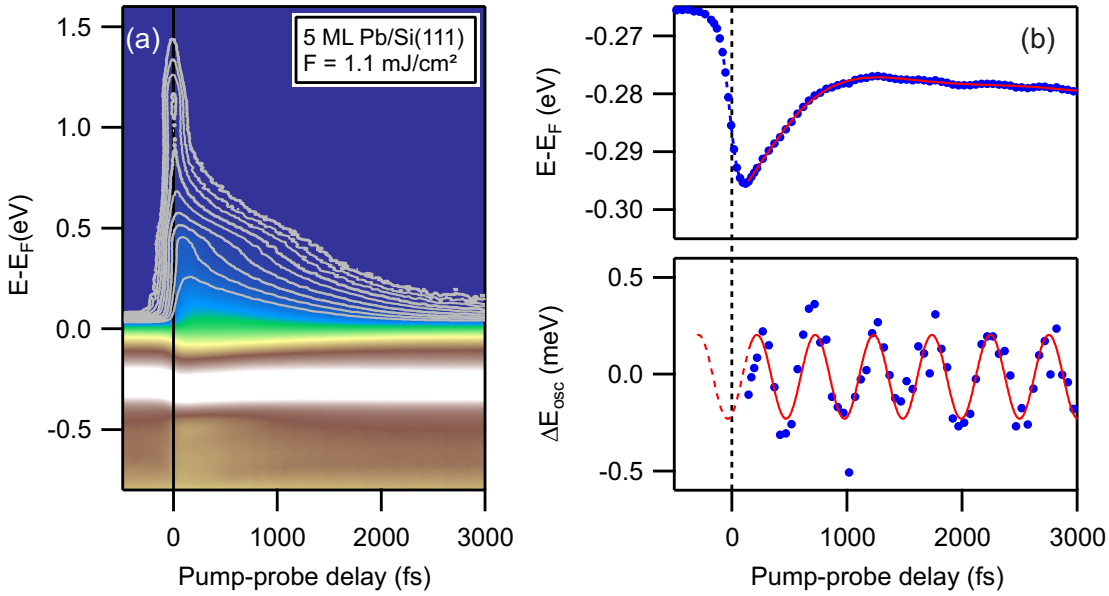

Figure 4.8: (a) Photoemission intensity as a function of $E - E_F$ and pump-probe delay for 5 ML Pb/Si(111) using an absorbed excitation fluence of $F = 1.1\,\mathrm{mJ/cm^2}$. Note the large amount of excited carriers above the Fermi level, highlighted by the contour lines. The state visible at $E - E_F = 1.1\,\mathrm{eV}$ (closed contour lines) is the lowest unoccupied QWS. (b) Upper panel: Peak position of the hoQWS determined from a fit as a function of pump probe delay, showing a transient coherent modulation after excitation. The red line is a fit to extract the incoherent contribution. Lower panel: relative peak shift after subtracting the incoherent contribution, highlighting the coherent oscillations. The red line is a sine-fit to the data.

ics in freestanding Pb slabs by Yndurain *et al.* [Ynd08] predicted longitudinal surface phonon modes at the BZ center with frequencies around 2 THz that show an oscillatory behavior of the phonon frequency with varying slab thickness and describe oscillations of the topmost atomic layers perpendicular to the surface [Ynd08]. The existence of such surface phonon modes with frequencies around 2.1 THz at $q = 0$ has been experimentally confirmed by He atom scattering on thin Pb films grown on Cu(111) [Bra09]. Thus, we consider the coherent excitation of a surface phonon mode as the origin of the periodic binding energy modulations. In addition, the observation of similar coherent oscillations in the hoQWS of 10 ML Pb/Si(111) with a slightly higher frequency of $\nu \approx 2.1$ THz [Kir08a] supports this assignment, as a modulation of the surface phonon frequency with the Pb film thickness has been predicted by the calculations [Ynd08].

Still, typical materials exhibiting coherent phonon excitations are semiconductors, semi-metals [Ish10] or rare-earth metals like Tb and Gd [Bov07]. Also, in some transition metals, excitation of coherent phonons has been observed [Has05]. In simple *sp*-metals like Pb, coherent phonon excitation has not been observed so far. A reason for this could be the efficient screening of excited carriers, resulting in a low excitation probability [Bov07]. Furthermore, the usually considered excitation of coherent phonons by displacive excitation of coherent phonons (DECP) requires a resonant interband transition at the pump photon energy [Has05], which was not directly observed here.

At surfaces, an ultrafast charge separation has been discussed as driving force for the excitation of coherent surface vibrations [Mel03]. Such a charge separation could be mediated in the Pb/Si quantum well system as discussed in the following. The ultrafast

excitation of a comparably large fraction of the valence electrons leads to a spatial redistribution of the electrons at the surface. This is a result of the vacuum potential, which presents a lower vacuum barrier for excited electrons at higher energies. Hence, their wave functions have a smaller damping outside the metal surface, leading to a larger electron density outside the film, the so-called electron spill-out. This leads to an electric dipole at the surface, which was already observed earlier in the modulation of the work function of Pb/Si(111) with Pb coverage due to the changing electron density near the Fermi level [Kir07, Kir08a]. This ultrafast modification of the surface dipole induces a driving force on the surface atoms perpendicular to the surface, leading to the excitation of a coherent surface phonon mode.

This brings up the question how the surface phonon mode modifies the binding energies of QWSs within the metal film. This can be understood from the strong sensitivity of the QWS binding energies to the width of the quantum well, i.e. the film thickness. If we consider the modification of the film thickness due to an oscillating topmost atomic layer, we can estimate the oscillation amplitude in real space from the phase accumulation model. From the amplitude of the coherent binding energy modulation of ~ 1 meV we found in the experiment, we estimate for the 5 ML film that already a modification of ~ 0.2 % of the interlayer distance, i.e. $< 10^{-2}$ Å, leads to the observed binding energy oscillations. This demonstrates that the high sensitivity of QWS binding energies to the film thickness provides a sensitive tool to study very small lattice dynamics in a well-defined low-dimensional system.

Summary

In summary, in this chapter we have investigated the ultrafast electron dynamics in the quantum well system Pb/Si(111) after intense optical excitation using time-resolved photoemission spectroscopy. We find a transient shift of the binding energies of quantum well states (QWSs) and interface states (ISs) to higher binding energies, i.e. an energetic stabilization, which occurs within the time resolution of the experiment. This peak shift is found independent of substrate doping and excitation wavelength relative to the band gap, demonstrating an effect located at the interface between Si substrate and metal film. By analyzing the peak shift for various film thicknesses and QWSs at different positions relative to the substrate band gap, we identify a transient ultrafast shift of the band gap relative to the metal Fermi level as the origin of the peak shift, mediated by a photo-induced charge depletion of metal-induced gap states. This scenario is corroborated by a simulation within the phase accumulation model, which reproduces the energy-dependent peak shift of QWSs.

Thereby our experiments demonstrate an ultrafast modification of the Fermi level pinning position and hence the Schottky barrier height, which is a technologically important property for metal-semiconductor interfaces. Ultimately, this might lead the way towards electro-optical switching devices, at the interface of optical and electronic circuitry. Furthermore, the transient modification of the confinement condition of QWSs and the resulting influence on the QWS line shape and position demonstrates in a descriptive manner the influence of the quantum confinement on QWS wave functions in a prototypical quantum system. Therefore, it would be instructive to investigate quantum well states on different substrates, e.g. QWSs in Pb/Cu(111) [Dil04, Mat10] or Pb/SiC [Dil07] or with different interface structures [Dil06, Slo11] in future experiments.

Using a much stronger excitation fluence of $F > 1$ mJ/cm^2, we observe in addition to this continuous shift a periodic modulation of the binding energy with a frequency of $\nu = 1.97(6)$ THz, which we attribute to a coherently excited phonon mode at the surface of the Pb film. We suggest the coherent excitation of such a surface vibrations through the ultrafast redistribution of carriers at the surface. The oscillation of the surface phonon's frequency with the film thickness predicted by Yndurain *et al.* [Ynd08] encourage further systematic thickness-dependent investigations. However, as the detection of the small oscillatory signal in the binding energy of $\Delta E_{\mathrm{osc}} \sim 1$ meV requires very sharp and well-defined QWSs, such an investigation has proven to be challenging for coverages without strongly confined QWSs within the Si band gap. Here, the analysis of unoccupied QWSs in Pb/Si(111) might enable such an investigation due to the stronger influence of the oscillations on the unoccupied bands predicted by the calculations [Ynd08].

5 trARPES of Iron Pnictides

With the discovery of the new class of iron-based high-T_c superconductors (HTSCs) in early 2008 [Kam08, Maz08], a new era of research on HTSCs has begun. Their discovery triggered a tremendous amount of research on the Fe pnictide superconductors and their parent compounds. Almost instantaneously, the highly sophisticated experimental and theoretical tools developed over the decades of experiments on cuprate HTSCs started to unravel the fundamental properties of this rich material class. One key observation was, like in the cuprates, the presence of antiferromagnetic (AFM) order in proximity to the superconducting (SC) state in the phase diagram [Maz10], where suppression of AFM ordering by doping or pressure leads to the emergence of superconductivity. In addition, the specific semi-metallic Fermi surface (FS) common to most Fe pnictides, as observed with angle-resolved photoemission spectroscopy (ARPES) seems to play an important role in the superconducting properties. However, the complex interplay between electronic, magnetic and lattice degrees of freedom found in the Fe pnictides [Maz10] up to now defy a profound understanding of superconductivity in these materials.

Thus, unraveling the elementary excitations governing the semi-metallic ground state and understanding the role of the AFM order and the coupling between low energy excitations like spin fluctuations and lattice vibrations may be an important step towards the understanding of superconductivity in the HTSCs. One promising approach to study such interactions is to analyze the transient state of optically excited materials and its subsequent relaxation to quantify the respective coupling strengths [Bro90]. While a richness of information on the quasiparticle (QP) dynamics in cuprate HTSCs has been collected over the years using time-resolved optical and THz spectroscopy (see chapter 6 and references therein), only a few time-resolved studies of Fe pnictides have been reported so far [Man09, Mer09, Chi10, Man10, Mer10, Tor10, Tor11, Kim12]. In particular, no experiments using time- and angle-resolved photoemission spectroscopy (trARPES), which has been quite successful to analyze electron-phonon (e-ph) coupling and Cooper pair recombination in cuprate HTSCs [Per07, Cor11], were reported.

In this chapter we present first trARPES experiments on several FeAs compounds, revealing a variety of interesting aspects of the electron and lattice dynamics in these systems. The material properties, SC phase diagrams, and the electronic structure of the various compounds of the pnictide family are discussed in chapter 5.1. The equilibrium laser ARPES data of the investigated parent compounds $EuFe_2As_2$ and $BaFe_2As_2$ and the superconducting $BaFe_{1.85}Co_{0.15}As_2$ are compared to literature values. Chapter 5.2 discusses the k-dependent electron dynamics near the Γ-point in the AFM phase of $EuFe_2As_2$ and $BaFe_2As_2$, where a strong asymmetry of electron and hole excitations is found to depend on the AFM ordering. Coherently excited phonons found to transiently modify the chemical potential in all investigated compounds are discussed in chapter 5.3. The assignment of three coherent modes is discussed as well as their fluence and temperature dependence and their relaxation dynamics. trARPES experiments using a high-harmonic generation (HHG) light source performed in a collaboration with M. Bauer's research group at the University of Kiel are presented, providing access to the whole Brillouin zone (BZ) and allowing to determine the influence of the coherent phonon excitations on the electronic states at the BZ center and corner, respectively. Finally, the determination of the average e-ph coupling constant λ, which is a key parameter in the Bardeen-Cooper-Schrieffer (BCS) theory of conventional superconductivity,

is discussed in chapter 5.5. Here, three different methods to determine λ are compared, which all yield a small $\lambda < 0.15$ for all three investigated compounds.

Part of the work presented in this chapter has already been published in Physical Review Letters [Ret12a] or has been submitted for publication [Avi12].

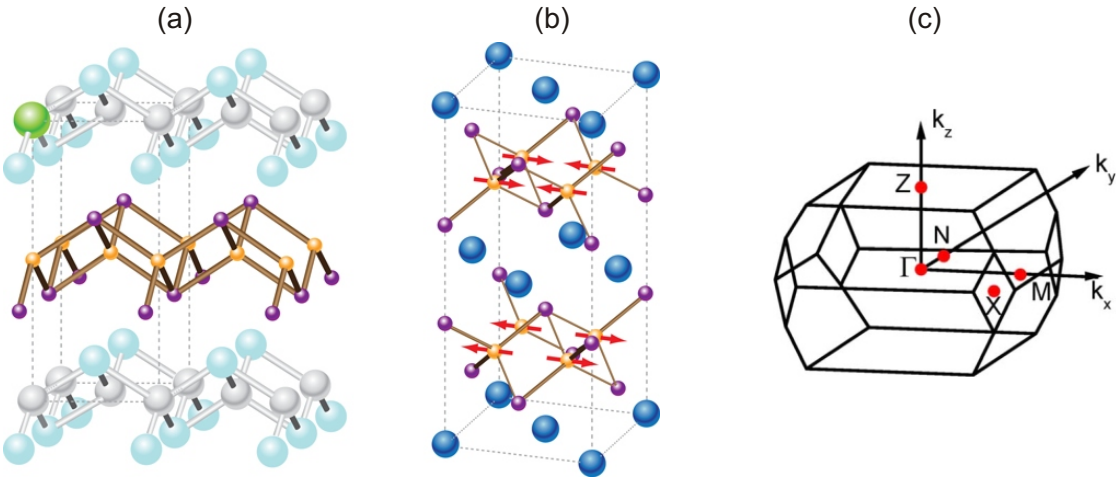

Figure 5.1: Crystal structure of FeAs compounds. (a) Crystal structure of the 1111 compounds, e.g $LaO_{1-x}F_xFeAs$. Doping replaces oxygen (gray) with fluorine (green), donating electrons to the FeAs layers. Other atoms shown are iron (yellow), arsenic (purple), and lanthanum (light blue). (b) Crystal structure of the 122 FeAs compounds, e.g. $BaFe_2As_2$. Here, blue atoms are barium. Common feature of all FeAs compounds are the buckled FeAs layers. The antiferromagnetic ordering of Fe magnetic moments is indicated. Taken from [Nor08]. (c) 3-dimensional Brillouin zone of the 122 compounds in the paramagnetic, tetragonal phase. High symmetry points are labeled. Taken from [Fin09].

5.1 FeAs high-T_c Superconductors

The FeAs HTSCs have many aspects in common with the other known class of HTSCs, the cuprates (see chapter 6). Like the cuprates, the Fe pnictides are complicated, quasi two-dimensional (2D) layered compounds with relatively large unit cells. In both material classes, the undoped parent compounds are not superconducting; the ground state of the undoped cuprates is a Mott insulating state [Dam03, Nor08], whereas the Fe pnictide parent compounds are bad paramagnetic metals [Nor08]. Like in the cuprates, superconductivity arises in the ferropnictides by doping of the parent compounds with either electrons or holes [Maz10, Joh10]. In addition, the pnictides also show superconductivity by applying external pressure to the system [Maz10, Joh10] and under isovalent substitution [Jia09, Sch09], which is not reported for the cuprate HTSCs.

The Fe based superconductors consist of several families with different compositions and crystal structures. Up to now, five different families of Fe pnictide compounds are known [Pag10]. Like the copper-oxide layers in the cuprates, the different families of the ferropnictides share a common building block, the buckled FeAs layers as sketched in figure 5.1 (a) and (b) exemplarily for two of the Fe pnictide families. The so-called '1111' crystals, named after their chemical composition, were the first to be discovered and show up to now the highest critical temperature of FeAs HTSCs, with $T_c = 55\,\mathrm{K}$ reached in $SmO_{1-x}F_xFeAs$ [Ren08]. In these compounds, the substitution of oxygen atoms by fluorine leads to electron doping into the FeAs layers and induces a suppression of the antiferromagnetic ordering of the parent compounds, leading eventually to superconductivity, as shown in the phase diagram in figure 5.2.

Another important class of FeAs HTSCs are the '122' compounds, which crystallize in the body-centered-tetragonal $ThCr_2Si_2$-type structure (space group $I4/mmm$). Most prominent member of this family is $BaFe_2As_2$, shown in figure 5.1 (b), with other

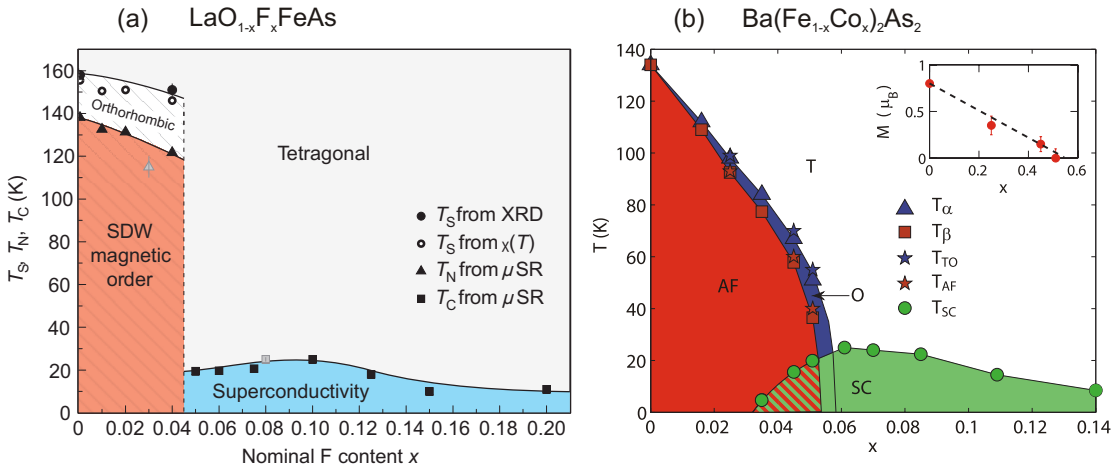

Figure 5.2: Phase diagrams of FeAs HTSCs. (a) Phase diagram of electron doped $LaO_{1-x}F_xFeAs$ as a function of the fluorine concentration x, showing a rapid, first order like transition from the antiferromagnetic SDW phase to superconductivity at $x > 0.04$ [Lue09]. The structural transition from tetragonal to orthorhombic structure at T_S precedes the antiferromagnetic transition at T_N by about 20 K even for the undoped compound. (b) Phase diagram for electron doped $Ba(Fe_{1-x}Co_x)_2As_2$, showing a slower, second order like transition from the antiferromagnetic to the SC phase, including coexistence of magnetic order and superconductivity in underdoped compounds [Les09]. Like in all 122 compounds, $T_S \equiv T_{TO}$ and $T_N \equiv T_{AF}$ coincide in the parent compounds and only slightly differ for weakly doped compounds.

compounds substituting Ba by e.g. Eu, Sr or Ca. The main advantage of the 122 pnictides is the high quality of single crystals available, with uniform sample sizes as large as $4 \times 4 \times 0.2\,mm^3$. Furthermore, the 122 family of Fe pnictides offers the opportunity of oxygen-free high-T_c superconductivity, which holds many advantages for technological applications. In $BaFe_2As_2$, superconductivity is reached by either hole doping through substituting Ba atoms with K, presenting the maximum $T_c = 38\,K$ for $Ba_{0.6}K_{0.4}Fe_2As_2$ [Rot08a], or by electron doping with Co substitution of Fe atoms reaching $T_c = 22\,K$ for $BaFe_{1.85}Co_{0.15}As_2$ [Sef08, Chu09]. In addition, for isovalent substitution of As with P, superconductivity at $T_c = 30\,K$ in $BaFe_2(As_{0.68}P_{0.32})_2$ is reported [Jia09].

The phase diagram of typical 1111 and 122 compounds upon electron doping is shown in figure 5.2 (a) and (b), respectively. Like already mentioned before, the parent compounds are bad paramagnetic metals at high temperatures and undergo a transition to an AFM phase, where Fe spins show a spin density wave (SDW)-like ordering, as shown in figure 5.1 (b). Simultaneously with or slightly preceding the magnetic transition in temperature, the compounds exhibit a structural transition from high-temperature tetragonal to low-temperature orthorhombic crystal structure (space-group Fmmm). With increasing doping, the structural and AFM transition temperatures are suppressed, and eventually superconductivity within the so-called "superconducting dome" sets in. While an abrupt transition from the AFM to the SC state is found in many 1111 compounds [Hua08b, Lue09], most 122 compounds, as well as some 1111 compounds exhibit coexistence of antiferromagnetism and superconductivity in the underdoped compounds [Rot08a, Che09, Dre09].

The parent compounds of the Fe pnictides are semi-metals, presenting a complicated

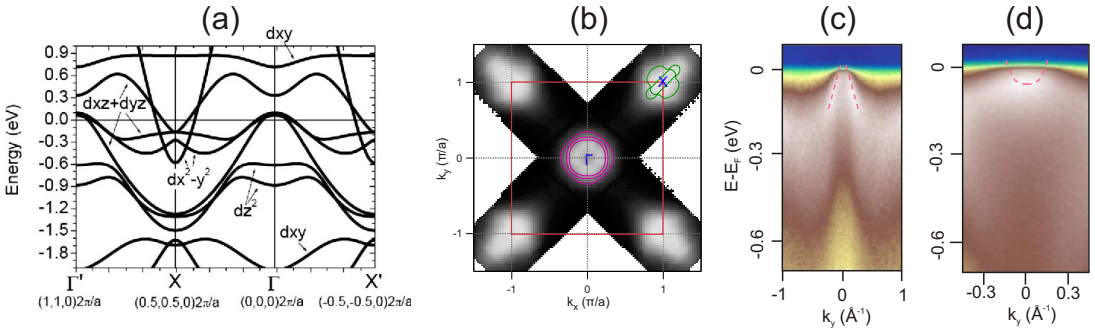

Figure 5.3: Electronic band structure of $BaFe_2As_2$. (a) Electronic DFT band structure calculation along the $\Gamma - X$ direction in the paramagnetic, tetragonal phase of $BaFe_2As_2$ [Fin09]. The orbital character of various bands is indicated. (b) Experimental Fermi surface of $BaFe_2As_2$ measured with ARPES [Yi09b]. The red square is the first BZ. The outlines of hole and electron pockets at the Γ and X-points, respectively, are indicated by thin lines. (c, d) ARPES dispersions along the $\Gamma - X$ direction near the Γ- and the X-point [Fin09]. The dispersion of one hole and electron pocket, respectively, is indicated by the purple lines.

electronic structure with multi-band nature. Common features of the electronic bands forming the FS and determining the low-energy excitations in all FeAs compounds are a number of hole pockets (i.e. bands that are almost completely filled and show a dispersion with negative effective electron masses) at the center of the BZ (Γ-point) and electron pockets (i.e. bands that are almost completely empty and show a dispersion with positive effective electron masses) at the zone corner (X-point in the paramagnetic, body-centered tetragonal BZ, see figure 5.1 (c)), as derived in theoretical calculations [Nek08, Ran09, Maz10, Dag10, Ma10, Wan10, Gra10b] and experimentally seen by ARPES [Din08, Liu08, Sin08, Nor08, Fin09, Yi09b, Maz10, Ric11]. Figure 5.3 shows the band structure calculation and experimental FS of $BaFe_2As_2$, which is the FeAs compound most intensely studied with ARPES and one of the compounds investigated in this thesis. The density functional theory (DFT) calculation in panel (a) exhibits three hole pockets at the Γ-point crossing the Fermi level and two electron pockets at the X-point, derived mostly from five Fe-3d orbitals, hybridized with As-4p orbitals [Wan10]. In addition, various lower-lying occupied and a number of unoccupied bands are found. The measured FS shown in (b) clearly exhibits two main FS sheets at Γ and at X, where the purple and green contours indicate the outline of the various hole and electron pockets, respectively. The ARPES cuts in (c) and (d) show the hole and electron character of the bands at the Γ- and X-point, respectively. Note that due to the broad range of momenta shown in panel (c), only one hole pocket is visible. A second, weaker hole pocket is seen in a momentum distribution curve (MDC) analysis [Fin09].

In undoped and weakly doped compounds, the electron and hole FS pockets are strongly nested by the nesting wave vector $\mathbf{q}_n \equiv \mathbf{q}_{SDW} = (\pi/a, \pi/a)$, in the two-dimensional BZ of the FeAs layers (see figure 5.4 (a)). This leads at sufficiently low temperatures below the Néel temperature T_N to AFM ordering of Fe magnetic moments and to the formation of a commensurate, stripe-like SDW [Hua08a, dlC08], as shown in figure 5.1 (b). This magnetic transition is accompanied or preceded in temperature by a structural transition from tetragonal to orthorhombic structure, with antiferromagnetic ordering along the slightly longer a-axis and ferromagnetic alignment along the shorter

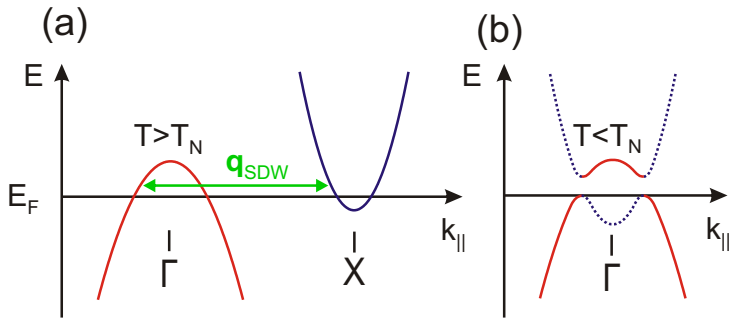

Figure 5.4: Band structure reconstruction in the AFM phase. (a) Simplified electronic band structure along the $\Gamma - X$ direction, with one hole pocket at the BZ center and one electron pocket at the BZ corner. The nesting vector $\mathbf{q}_{\mathrm{SDW}}$ is indicated. (b) Below T_{N}, the AFM order leads to a backfolding of the electron band from X to Γ, where it hybridizes with the hole band and opens SDW energy gaps as indicated [Ere10]. In real materials, the multi-band character of electron and hole pockets leads to a more complicated reconstruction.

b-axis [dlC08, Hua08a, Xia09, Wil09, Koo10]. In the undoped 122 compounds, the structural and magnetic transitions occur simultaneously and gradually become distinct upon doping [Les09, Rot11], whereas in the 1111 compounds, the structural transition precedes the magnetic transition also in the undoped compounds. Experiments using inelastic x-ray diffraction and neutron diffraction demonstrated strong coupling between magnetic and structural transitions [Jes08, Les09, Xia09, Koo10]. Above T_{N}, Ising nematic order caused by spin fluctuations, which breaks the rotational symmetry without breaking translational symmetry, is discussed to be related to the structural transition [Fer12]. This is supported by ARPES measurements, that show a significant imprint on the electronic structure even above T_{N} due to the magnetic and orbital anisotropy [Yi11a, Yi11b, Zha12]. Further evidence for the presence of nematic order is given by recent measurements of the in-plane anisotropy of the resistivity in detwinned crystals [Fis11]. Below T_{N}, the AFM ordering leads to backfolding of electron bands to Γ, where they hybridize with the hole bands and open partial SDW energy gaps on the FS near Γ, as sketched in figure 5.4 (b) [Liu09, Yan09, Yi09a, Ere10, dJ10, Che11, FJ11, Yi11a, Yi11b, Zha12]. Such partial energy gaps are a direct imprint of AFM ordering on the electronic band structure and their size correlates with the AFM order parameter [Yi09a, dJ10].

A major challenge to investigate the electron dynamics in FeAs compounds with the trARPES setup using 6 eV probe photon energy is the small photoemission cross-section of Fe-derived states at low photon energies [Koi08, Man11] and the limited momentum range accessible at low kinetic energies. This limits our investigations to the hole pockets around the BZ center and induces a larger incoherent background in the ARPES spectra compared to synchrotron experiments at higher photon energies. Figure 5.5 (a-c) shows the measured laser ARPES intensity for the three compounds studied here, $EuFe_2As_2$, $BaFe_2As_2$ and $BaFe_{1.85}Co_{0.15}As_2$, in a false color representation. For better illustration, panel (d) depicts EDCs for the $BaFe_2As_2$ data. For all three compounds, we can clearly identify the dispersion of one hole pocket around Γ. The Fermi momenta k_{F}, derived from fitting of MDCs at the Fermi energy are indicated by the red arrows in panels (a-c). Whereas there is no big difference between the two parent compounds $EuFe_2As_2$ and $BaFe_2As_2$, k_{F} is clearly smaller in $BaFe_{1.85}Co_{0.15}As_2$. This can be readily understood by the electron doping due to the Co atoms in this compound, which rigidly shifts the Fermi

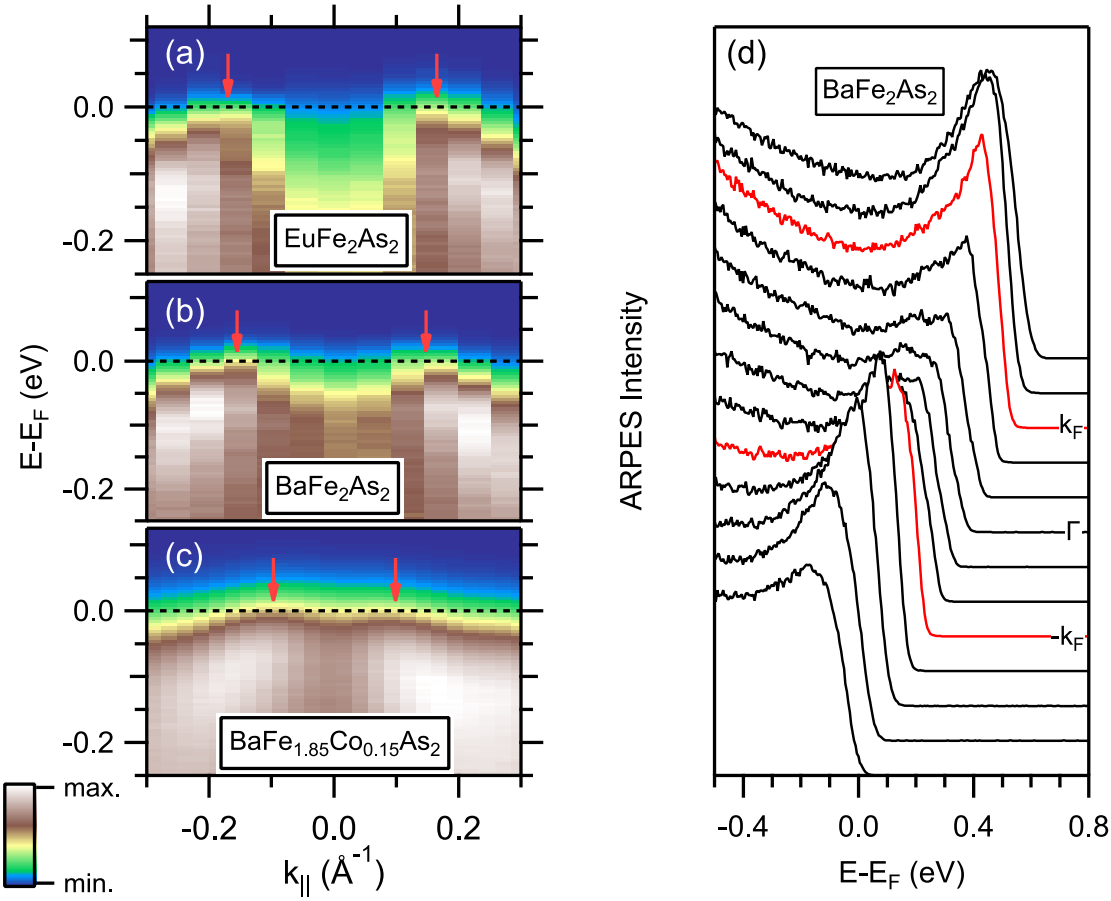

Figure 5.5: Laser ARPES spectra of various 122 FeAs compounds taken with a photon energy of $h\nu = 6.0\,\mathrm{eV}$ near the Γ-point as a function of binding energy $E - E_\mathrm{F}$ and parallel momentum $k_\parallel$ in a false color representation. (a, b) Spectra of $EuFe_2As_2$ and $BaFe_2As_2$, taken at $T = 30\,\mathrm{K}$ in the antiferromagnetic phase. (c) Spectra of Co doped $BaFe_{1.85}Co_{0.15}As_2$ at $T = 100\,\mathrm{K}$ in the normal state. The prominent dispersion of the main hole pocket is visible in all three compounds. Red arrows mark the Fermi surface momenta k_F. Note the shift of k_F to smaller values in (c), indicating the shift of the Fermi energy due to the electron doping. (d) EDCs of the data in (b). Spectra are vertically and horizontally offset for clarity and k_F spectra are shown in red.

level up and thus leads to a more filled hole pocket, consistent with literature [Bro09, Mal09, Sek09, Thi10, Man11].

In order to quantitatively compare our data to the literature, we have to take the 3-dimensionality of the 122 compounds into account. Due to the stronger coupling of neighboring FeAs layers in these compounds compared to the 1111 materials, the hole- and electron pockets exhibit a considerable dispersion along k_z, the direction perpendicular to the FeAs planes, resulting in a warping of the pocket sizes [Bro09, Mal09, Thi10, Man11]. Experimentally, in ARPES the momentum component perpendicular to the surface, $k_\perp$, is determined by the photon energy, assuming excitation into parabolic free-electron-like final states, see chapter 2.4. For the FeAs compounds, using an inner potential of $V_0 = 15\,\mathrm{eV}$ [Vil09], for normal emission and the kinetic energy of $E_{\mathrm{kin}} = 2.1\,\mathrm{eV}$ at $6\,\mathrm{eV}$, we get according to equation (2.38) $k_\perp = 2.1\,\mathrm{\AA}^{-1} = 4.4\,\mathrm{c}^*$, which is in between the Γ and the Z-point of the BZ (compare figure 5.1 (c)). However, recent laser based ARPES measurements using a photon energy of $7\,\mathrm{eV}$ in comparison to synchrotron measurements, concluded that such a low photon energy probes the region around the Z-point [Shi10, Shi11a, Shi11b]. This imposes some questions on the applicability of the free-electron final state approximation in these systems at low kinetic energies. Comparison of our data for $BaFe_2As_2$ with published data of the same compound taken with $h\nu = 7\,\mathrm{eV}$ [Shi10] indeed shows a good agreement of the dispersion of the hole pocket. Also, our data of $EuFe_2As_2$ compare well to data taken at higher photon energies close to the Z-point [dJ10]. For sake of simplicity, we will nevertheless refer to normal emission as the Γ-point in the following. Thus, having verified that we can investigate the equilibrium band structure, we can now safely proceed to the analysis of the ultrafast dynamical changes of the band structure after photoexcitation.

5.2 Momentum-dependent Electron Dynamics in antiferromagnetic $EuFe_2As_2$ and $BaFe_2As_2$

In the following, we will focus on the AFM state of $EuFe_2As_2$ and $BaFe_2As_2$ and the dynamics after optical excitation. Having identified the laser based ARPES band structure and in particular the hole pocket, we can study its modifications after optical excitation. Figure 5.6 (a) and (b) compare the trARPES intensity as a function of energy $E - E_F$ and momentum $k_\parallel$ before and at $t = 100\,\text{fs}$ after excitation, respectively. In order to better illustrate the changes induced by the optical excitation to the spectral weight $I(E,k)$, the pump induced changes $\Delta I(E,k,t) = I(E,k,t) - I_0(E,k)$ for $t = 100\,\text{fs}$ after excitation, i.e. the difference of intensity in panel (a) and (b), are shown in a color code in panel (c). Two distinct types of response are found: near the Γ-point within the hole pocket, an increase in spectral weight is observed (red), whereas we find a decrease for occupied states outside the hole pocket (blue). The asymmetry of the decrease for negative and positive $k_\parallel$ arises from the fact that by turning the sample we change the absorbed pumping fluence from $F = 70\,\mu\text{J/cm}^2$ at $k_\parallel = -0.3\,\text{Å}^{-1}$ to $F = 350\,\mu\text{J/cm}^2$ at $k_\parallel = 0.3\,\text{Å}^{-1}$. We can identify the increase (decrease) as additional excited electrons (holes) which originate from secondary electron-hole (e-h) pair excitations. These are created during the relaxation process of electrons initially excited by the pump photons, which relax their energy towards the Fermi level. This is mainly mediated through electron-electron (e-e) scattering with electrons within originally occupied states, e.g. of the hole-pocket bands, leading to the excitation of electrons from occupied states outside the hole pocket into unoccupied states inside the pocket. As we do not observe clear indications of the occupation of unoccupied states in the trARPES spectra and as the e-h pair distribution is established mostly within the pump pulse duration, we can conclude that the e-e scattering in iron pnictides is of considerable strength. This is further supported by the relatively fast thermalization time, which is discussed in chapter 5.5.

In order to get more insight into the origin of ΔI, figure 5.6 (d) and (e) compare EDCs before and after excitation at representative momenta for electron and hole excitations at Γ and at $k_\parallel = 0.25\,\text{Å}^{-1} > k_F$, respectively, and for various temperatures across the AFM transition. For states outside the hole pocket (figure 5.6 (d)) we see a transient excitation of e-h pairs symmetric to E_F, as expected for a single band metal [Fan92, Lis04b]. We find that this behavior is robust upon cooling below T_N[1], which is very reasonable as the magnetic order mainly affects states near Γ.

At Γ within the hole pocket the situation is qualitatively different (see figure 5.6 (e)). Above T_N, the system behaves like a metal with e-h excitations symmetric to E_F, similar to $k_\parallel = 0.25\,\text{Å}^{-1}$. With lowering $T < T_N$, however, we find a shift of the leading edge to lower energies before excitation, consistent with the opening of a SDW energy gap (see figure 5.4 (b)). Upon photoexcitation, this gap closes and is filled by electrons, evidenced by the shift of the leading edge and the strong increase of spectral weight at E_F (red area in figure 5.6 (e)). As this shift of the leading edge and the corresponding redistribution of spectral weight is only observed for $T < T_N$, we conclude that it is closely linked to the existence of AFM ordering. This suggests that analyzing the dynamics of the electron excitations at Γ enables us to investigate the collective dynamics related to the AFM order. Simultaneously, as will be shown in the following, the hole excitations at $k_\parallel > k_F$

[1] The dominance of hole excitations for higher temperatures can be understood from the experimental difficulty that due to a drift of the measurement position with temperature the effective emission angle at fixed sample angle changed slightly during measurements and thus the position of k_F. As a consequence, spectra at higher temperatures are measured at effectively larger $k_\parallel$ values.

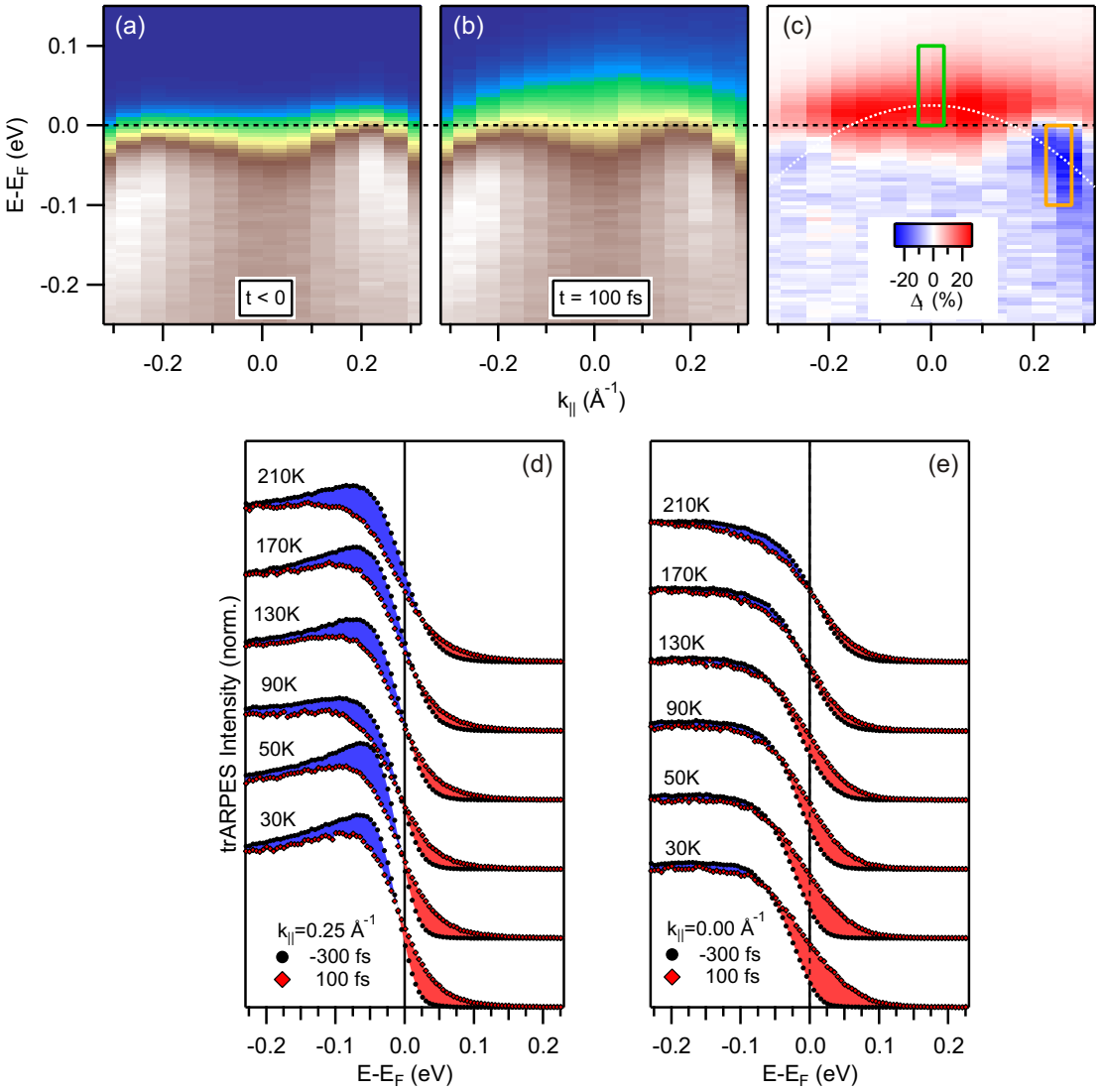

Figure 5.6: Time-dependent trARPES dispersion of $EuFe_2As_2$. (a) trARPES intensity near Γ before optical excitation at $T = 30$ K in a color coded intensity plot. (b) trARPES intensity at $t = 100$ fs after photoexcitation with an average absorbed fluence of $F = 280\,\mu J/cm^2$. Note the enhancement of intensity within the hole pocket and the depletion of occupied bands at $k > k_F$. (c) Pump-induced change of spectral weight ΔI in a false color map for $t = 100$ fs, showing the difference between the two spectra in (a) and (b). Blue color marks depletion of spectral weight (hole excitations), while red marks increased ΔI (electron excitations). Boxes represent integration areas for ΔI used in figure 5.7. The dispersion of the hole pocket is indicated by the white dashed parabola. (d) EDCs for $k_{||} = 0.25\,Å^{-1} > k_F$ before (black) and $t = 100$ fs after laser excitation (red) for various temperatures. Increase and depletion of spectral weight are marked by red and blue areas, respectively. Spectra are vertically offset for clarity. (e) EDCs for $k_{||} = 0.00\,Å^{-1}$ (Γ).

can serve as a measure for single-particle electron-phonon scattering dynamics, which determine the energy redistribution within the system.

To analyze the time evolution of the momentum-dependent e-h distribution, we integrate the data within representative intervals for electron and hole excitations, depicted in figure 5.6 (c). Thereby we determine the temporal evolution of pump-induced spectral weight for hole excitations ΔI_- (yellow box) and for electron excitations ΔI_+ (green box), depicted in figure 5.7 (a) for various T. The transient spectral weight of electrons, ΔI_+ shows an ultrafast increase within the pump-pulse duration and a relaxation in $1-2\,\mathrm{ps}$, whereas the transient ΔI_- of holes shows an ultrafast decrease within the same time window. In addition, we notice a strong variation with temperature in the pump-induced response for ΔI_+, while ΔI_- shows only minor variations. A closer look on the data reveals a transient oscillation of ΔI superimposed on the decay with a period of $\sim 200\,\mathrm{fs}$, the fingerprint of coherently excited phonon oscillations [Man09, Mer10]. These oscillations, however, do not influence the relaxation dynamics and will be discussed separately in section 5.3.

To further analyze the decay of electron and hole populations, $\Delta I_{+,-}$ are fitted with exponential decay functions, $\Delta I_{+,-}(t) = \pm A \exp(-t/\tau_{+,-}) + B$, convoluted with the temporal pump-probe envelope. Here, A is the excitation amplitude, τ the relaxation time constant and B accounts for an elevated lattice temperature after e-ph thermalization [Lis04b]. The fits are shown as solid lines in figure 5.7 (a) and the resulting relaxation constants $\tau_{+,-}$ as a function of T are depicted in figure 5.7 (b). For $T > T_\mathrm{N}$, both electron and hole populations relax within error bars on the same timescale of $\sim 400\,\mathrm{fs}$, governed by e-ph scattering (see below). By lowering T below T_N, however, we find a strong difference in τ between electron and hole relaxation. While the relaxation of excited holes shows a slight acceleration for lower T, the electron relaxation time at Γ strongly increases. At $T = 30\,\mathrm{K}$, holes decay more than four times faster ($\tau_- < 200\,\mathrm{fs}$) than electrons, which relax with $\tau_+ \sim 800\,\mathrm{fs}$.

We now discuss these peculiar temperature-dependent relaxation times τ_+ and τ_-. Hole excitations outside the hole pocket are barely influenced by the presence of AFM ordering. Their decay (τ_-) is governed by the energy transfer to the lattice through e-ph relaxation. This is supported by the slower relaxation with increasing T, which is understood from the slower energy transfer to the lattice at elevated temperatures due to the increased specific heat of the electronic system [Gro95]. In the limit of high temperatures, the e-ph relaxation time constant depends linearly on the temperature, which can be used to determine the e-ph coupling strength [Kab08, Sto10a, Gad10]. This is discussed in detail in chapter 5.5, where we find good agreement with published values, which further supports our assignment.

In contrast, electrons at Γ are strongly influenced by spin-dependent interactions in the AFM phase and thus the observed dynamics is linked to the transient change of the AFM order. Remarkably, the observed temperature dependence of τ_+ strikingly resembles the temperature dependence of the SDW order parameter in $EuFe_2As_2$ [Teg08, HM09, Xia09] and saturates at $\tau_+ = 800 \pm 100\,\mathrm{fs}$ below $100\,\mathrm{K}$, similar to the relaxation found in antiferromagnetic SmAsFeO by time-resolved optical spectroscopy [Mer10]. Qualitatively, we can understand the slower recovery dynamics of the AFM order (τ_+) compared to the e-ph relaxation (τ_-) by a reduced phase space available for e-e scattering across the energy gap and a spin-spin scattering bottleneck. With increasing temperature, thermal fluctuations of the spin order provide additional relaxation channels and thus decrease τ. Above T_N with the breakdown of spin order, the relaxation bottleneck is absent and the decay is governed by e-ph scattering on the same timescale as the hole

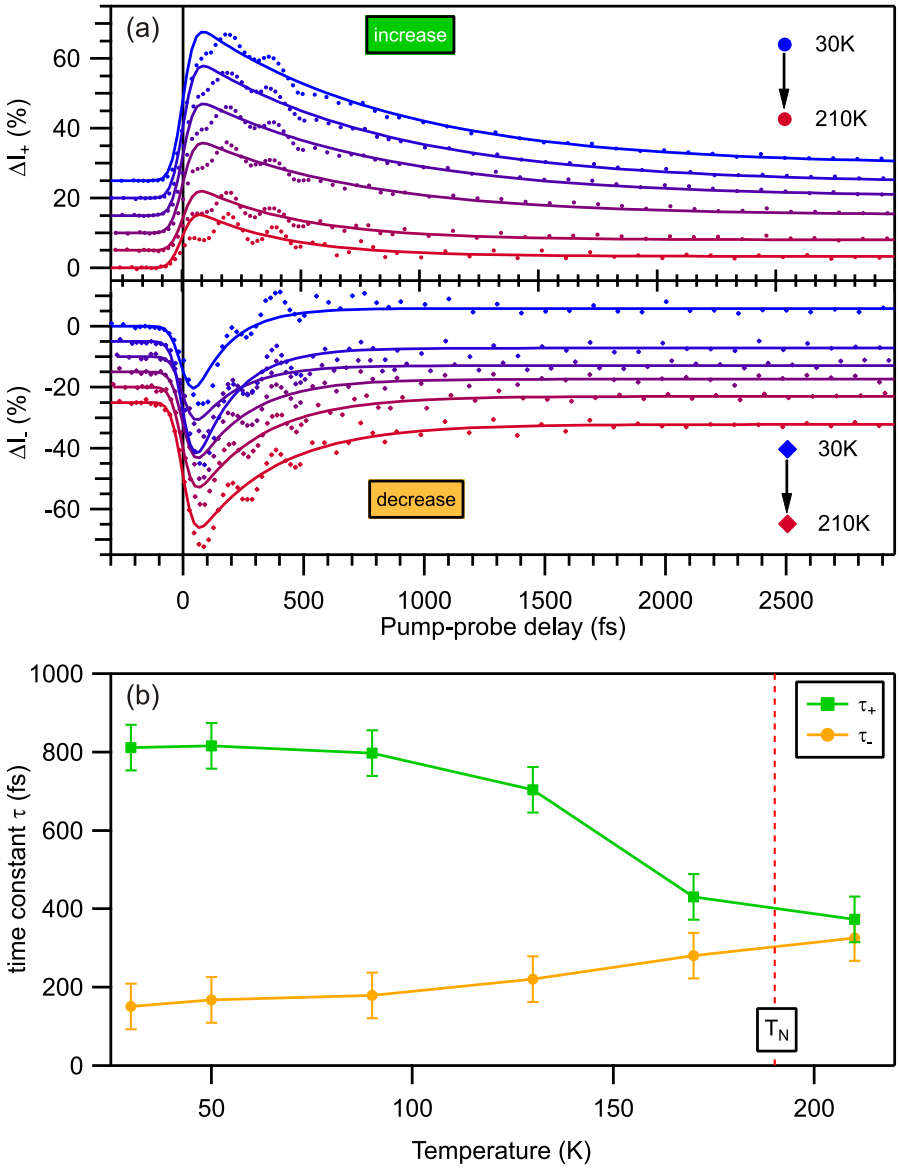

Figure 5.7: Temperature-dependent relaxation times in $EuFe_2As_2$. (a) Time-dependent spectral weight integrated within the energy-momentum intervals in figure 5.6 (c), at Γ (upper panel, increase) and $k_{\parallel} = 0.25\,\text{Å}^{-1}$ (lower panel, decrease) for various temperatures. Data are vertically offset for clarity. Solid lines are exponential fits, described in the text. (b) Relaxation time constants τ_+ and τ_- as a function of temperature obtained from the fits shown in (a). Error bars represent 99.7% confidence intervals. Note the strong difference of τ_+ and τ_- below the Néel transition temperature $T_N = 190\,\text{K}$.

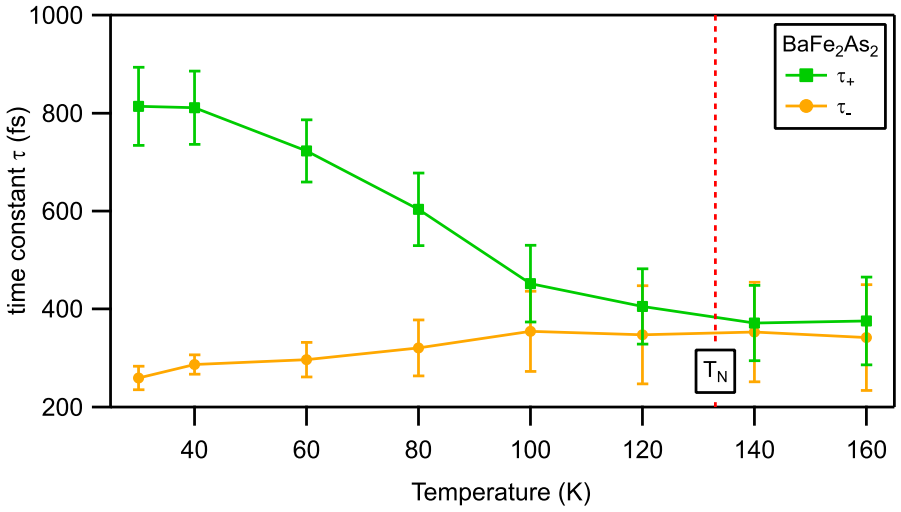

Figure 5.8: Temperature-dependent relaxation times in $BaFe_2As_2$. Similar data as shown in figure 5.7, but for $BaFe_2As_2$. Here, the Néel temperature is $T_N \sim 135$ K.

excitations.

Results of a similar analysis for data of undoped $BaFe_2As_2$ are depicted in figure 5.8, which has a Néel temperature of $T_N \sim 135$ K [Rot08b, Chu09, Wil09]. The general behavior compares well with the observations for $EuFe_2As_2$. The relaxation times found for temperatures above T_N are $\tau_- \sim \tau_+ \sim 400$ fs, identical with the values found in $EuFe_2As_2$ above T_N, although slightly higher than the hole relaxation times at the same temperatures in $EuFe_2As_2$ with $\tau_-^{Eu} \sim 300$ fs at 170 K. In addition, the decrease of the hole relaxation times is less pronounced in $BaFe_2As_2$, with $\tau_- \sim 250$ fs at 30 K. This indicates a slightly weaker e-ph interaction in $BaFe_2As_2$ than in $EuFe_2As_2$ and will be discussed in chapter 5.5. The electron relaxation times in $BaFe_2As_2$ show the same characteristic slowing down within the AFM phase and saturate for low T at $\tau_+ \sim 800$ fs, the same timescale found for τ_+ in $EuFe_2As_2$. However, in contrast to the $EuFe_2As_2$ data, in $BaFe_2As_2$ τ_+ only considerably increases below 100 K, which is significantly below T_N. A possible explanation for this is a residual Sn contamination in the $BaFe_2As_2$ samples, which is known to reduce the Néel temperature considerably [Ni08, Fin09, Su09]. Such residual Sn contamination is often found in samples grown by the Sn flux method [Ni08, Su09], which was used for the $BaFe_2As_2$ samples. Samples of $EuFe_2As_2$ have been grown with the Bridgman method [Jee08], which is a Sn free process. Thus, assuming an effective Néel temperature of $T_N \sim 100$ K for the particular sample, we find a good qualitative agreement to the data of $EuFe_2As_2$. Unfortunately, no characterization and independent determination of T_N has been available for the sample used for these measurements to support this conclusion.

Excitation Dynamics of the SDW Gap

In the next part, we will address the photo-induced perturbation of spin order by analyzing the shift of the leading edge midpoint (LEM) induced by the SDW energy gap at Γ. Figure 5.9 (a) and (b) show the trARPES intensities at the Γ point as a function of energy and pump-probe delay for $T = 210$ K and $T = 30$ K, respectively. Before excitation, we notice a shift of the leading edge of the trARPES spectra away from E_F, which can be quantized by extracting the LEM from the data, as shown by the red dots. As already mentioned earlier in the context of figure 5.6, this shift of the position of the

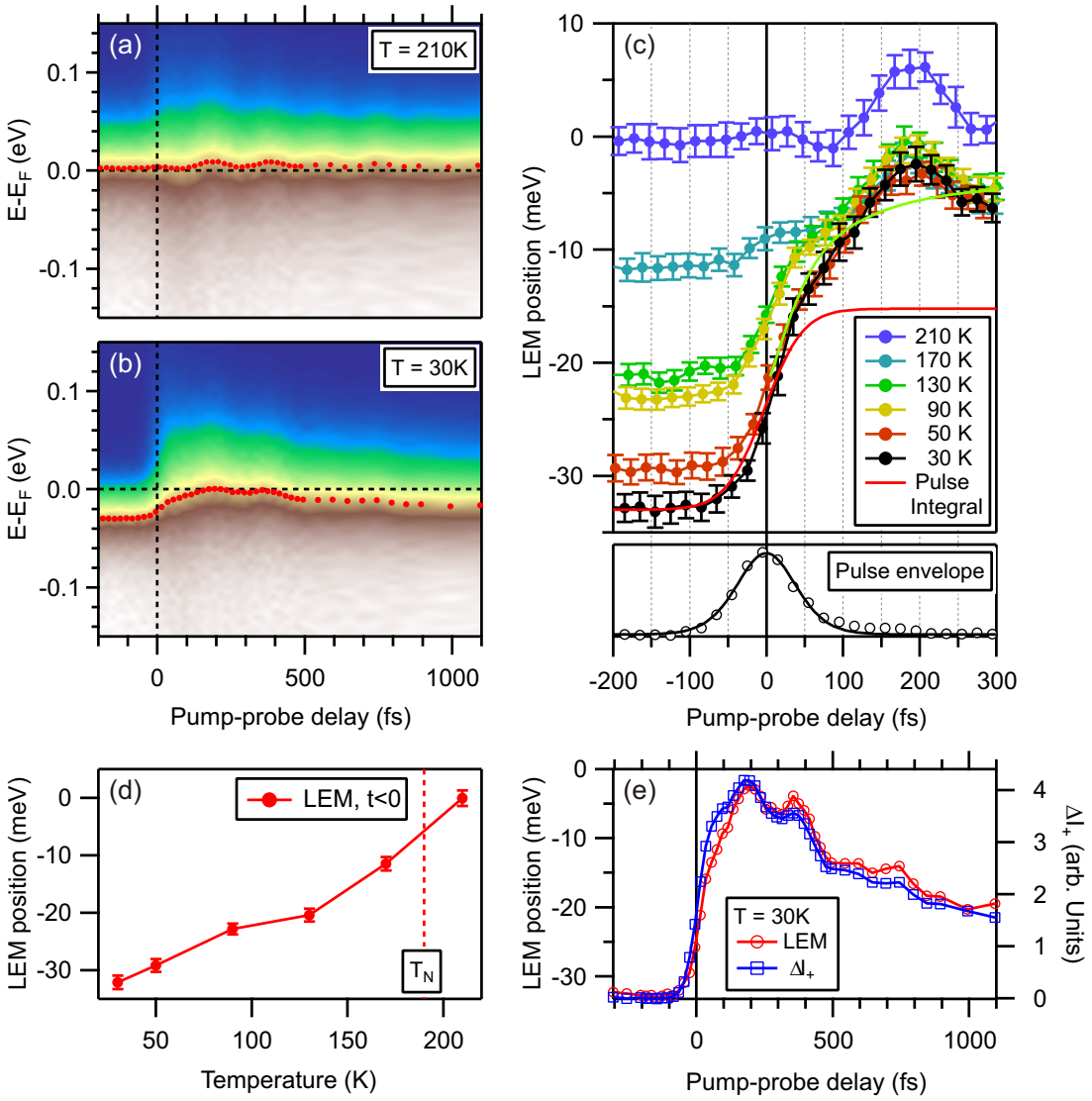

Figure 5.9: Excitation dynamics and closing of the SDW gap. (a), (b): Color coded intensity plot of the trARPES intensity at Γ for $T = 210\,\mathrm{K}$ and $T = 30\,\mathrm{K}$, respectively. The red dots mark the position of the leading edge midpoint (LEM) of the spectra. (c) Upper panel: Position of the LEM around zero pump-probe delay for various temperatures. The integral of the pump-probe pulse cross correlation (XC), scaled to the data at $T = 30\,\mathrm{K}$, is shown as red solid line, and the green line is an exponential fit (see text). Lower panel: Pump-probe pulse XC, determined from highly excited, short lived electrons at $E - E_\mathrm{F} > 1\,\mathrm{eV}$. The solid line is a Gaussian fit function, yielding a FWHM of $\tau_\mathrm{XC} = 94(5)\,\mathrm{fs}$. (d) LEM position before excitation as a function of temperature. (e) Comparison of the LEM position and the electron signal ΔI_+ at $T = 30\,\mathrm{K}$.

LEM to lower energies is induced by the SDW energy gap. The size of the shift before excitation is shown in figure 5.9 (d), which can serve a marker for the size of the SDW energy gap. The maximal shift of the LEM of ~ -30 meV is found for $T = 30$ K, which is comparable to values of the SDW energy gap of $2\Delta \sim 90$ meV measured by optical spectroscopy [Wu09]. To investigate the response of the SDW gap to the optical excitation in more detail, the LEM is shown in figure 5.9 (c) as a function of pump-probe delay and at various temperatures. At $T = 210$ K, above T_N, the LEM matches the Fermi level E_F and shows no significant modification within the first 100 fs around time zero. After ~ 100 fs, the coherent oscillations already observed in figure 5.7, most importantly the coherent A_{1g} phonon mode (see chapter 5.3) start modulating the LEM by ~ 5 meV.

In the AFM phase below T_N, we find a strong upshift of the LEM towards the high-temperature value upon excitation, i.e. a closing of the SDW gap. We can interpret this shift as a measure of the transient SDW energy gap and thus the AFM order parameter, which facilitates a quantitative analysis of its dynamics. For all $T < T_N$, the excitation leads to a nearly complete reduction of the LEM shift at ~ 200 fs, where the position of the LEM coincides for all temperatures[2]. The fact that the LEM nearly reaches the high-temperature value for all temperatures indicates a major loss of AFM order and a nearly complete transition to a transient paramagnetic state.

We identify two regimes in the excitation process: First, until $t = 50$ fs, we find a very fast shift of the LEM, which follows the pump-probe pulse integral, shown as a red solid line, scaled to match the data at 30 K at zero pump-probe delay. For later times, the LEM continues to shift on a slower timescale of $\tau \sim 100$ fs, as indicated by the green, solid line. The position of the LEM peaks at 200 fs when it has nearly reached the high-temperature value and likewise starts to become modulated by the coherent phonon modes. The subsequent decay towards the initial value is determined by the slow recovery of the AFM state, which was discussed in the previous part. This is evident from the comparison of the LEM with ΔI_+, which is shown in figure 5.9 (e).

The occurrence of two timescales in the initial shift of the LEM indicates that more than one process is involved in the photo-induced transition into a transient paramagnetic state. In collective phenomena involving lattice motion, e.g. in charge density wave (CDW) materials (see chapter 7), the response of the system is retarded with respect to the excitation due to the lattice inertia [Sch08a] and the limiting time constant is about 1/4 of the period of the characteristic lattice vibration associated with the transition [Sch11a, Roh11]. In contrast, purely electronic phenomena like Mott [Per06, Pet11, Wal11] and SDW transitions happen on much faster timescales. Indeed, in the Fe pnictides, the AFM transition is coupled to the structural transition from tetragonal to orthorhombic structure [dlC08, Hua08a], which is supposed to be induced by an Ising nematic order [Fer12], where short-ranged magnetic ordering is present but long-range order is suppressed by thermal fluctuations. Hence, the observation of two timescales in the pnictides could be explained by an ultrafast decoupling of the coupled AFM and structural transitions. First, the initial fast shift of the LEM shows the ultrafast reduction of long-range AFM ordering, whereas local Ising nematic ordering persists longer and is destroyed by the structural reorientation on the timescale of 100 fs. Here, future fluence-dependent studies might help to shed more light on the detailed processes involved in the transition and the coupled or competing character of the underlying fluctuations.

[2]Strikingly, the position of the LEM at 210 K is clearly offset in comparison to all other T. Whether this offset is a real physical effect related with the absence of AFM order or if this is an experimental artifact, due to e.g. an instability in the bias voltage or a small change in the distance between sample and spectrometer entrance is unclear.

5.3 Excitation of Coherent Phonon Modes

In the following part we will analyze and discuss the coherent oscillations which were already identified in figure 5.7. Such oscillations are found in all three FeAs compounds studied in this thesis. To investigate the oscillations in more detail, stronger excitation fluences F have been used. The trARPES intensity of $BaFe_{1.85}Co_{0.15}As_2$ at the Γ-point for $F = 1.42\,\mathrm{mJ/cm^2}$ is shown in figure 5.10 (a) in a color coded intensity plot as a function of pump-probe delay and binding energy. After the optical excitation, pronounced oscillations start to modulate the photoemission signal around E_F. The oscillations show a period close to 200 fs and persist up to several picoseconds.

Before we proceed with a detailed analysis of the oscillation frequencies, we want to determine the actual influence of the oscillations on the transient spectral weight measured by trARPES. For this purpose, figure 5.10 (b) compares spectra taken at $t = 100\,\mathrm{fs}$ and $t = 200\,\mathrm{fs}$, corresponding roughly to the first minimum and maximum of the oscillations, with a spectrum taken before excitation. Apart from the strong change in slope of the Fermi cutoff function after excitation, which evidences the high temperature of the electronic system [Lis04b], we find a rigid shift of the cutoff-position induced by the oscillation. To analyze this effect in more detail, spectra have been fitted with a Fermi-Dirac distribution function, multiplied with a phenomenological density of states (DOS), as shown by solid lines in figure 5.10 (b). The red and green arrows mark the position of the transient Fermi level determined by this fitting procedure, for $t = 100\,\mathrm{fs}$ and $t = 200\,\mathrm{fs}$, respectively. We find a strong modulation of E_F, shown as markers in figure 5.10 (a), whereas the DOS and the slope of the Fermi function, corresponding to the electronic temperature, show only minor or no oscillations. Thus, we conclude that the distribution function itself is modulated by the coherent oscillations, leading to a transient shift of its position. This direct influence of coherent excitations on the transient electron distribution demonstrates substantial coupling of the underlying low-energy excitations to electronic states at E_F. Possible origins and consequences of this transient modulation of the chemical potential will be discussed in section 5.4.

To analyze the coherent oscillations in more detail for various excitation conditions and compounds in the following part, we consider the integrated spectral weight, $\Delta I(t)$, for energies $E > E_F$, which provides a sensitive probe for the oscillations due to the high contrast at the Fermi cutoff. This procedure allows for a better signal-to-noise (S/N) ratio in the oscillations than analyzing the spectral cutoff by a fitting function, as has been checked by comparison of fast Fourier transformation (FFT) spectra. The time-dependent ΔI is depicted in figure 5.11 (a) for various fluences. The spectra show a steep rise after the optical excitation and an incoherent decay governed by e-ph relaxation within several picoseconds, superimposed with the coherent oscillations (compare figure 5.7).

In order to further analyze the coherent part of the signal by means of FFT, we have to determine and subtract the incoherent contribution, which produces a steep rising background in the FFT spectra at low frequencies. While for low excitation densities used for the analysis of the momentum-dependent relaxation in the previous part a single-exponential decay function was adequate to describe the incoherent decay processes, for higher excitation densities this procedure does not provide a satisfying background determination. Instead, we adopt a method of fitting a smooth spline function to the data, which was originally developed for the analysis of extended x-ray absorption fine structure (EXAFS) [Lee81] and was recently adopted to extract the coherent oscillations of the CDW amplitude mode in $TbTe_3$ [Sch11a], see also chapter 7.

Spline functions are piecewise polynomial functions (of usually 3^{rd} order, B-splines),

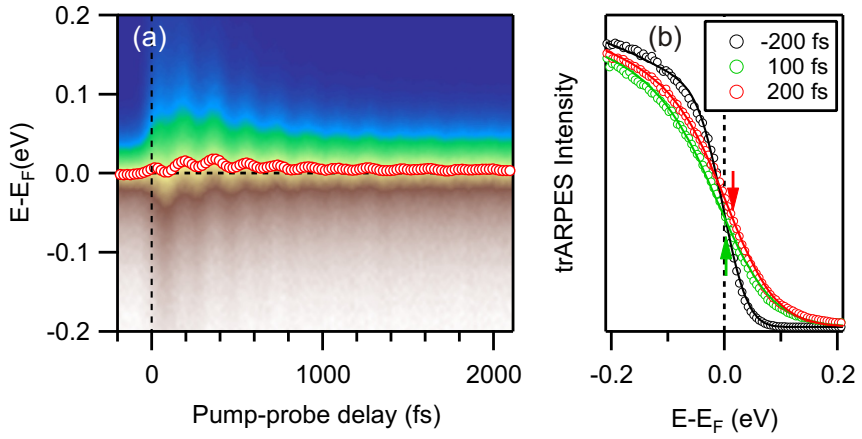

Figure 5.10: Coherent oscillations of spectral weight in $BaFe_{1.85}Co_{0.15}As_2$. (a) trARPES intensity in a color coded intensity plot as a function of energy and pump-probe delay taken at Γ with an incident pumping fluence $F = 1.42\,\mathrm{mJ/cm^2}$ and at $T = 100\,\mathrm{K}$. The strong oscillations of the spectral weight occurring after zero pump-probe delay are highlighted by the red markers, which represent the transient position of the Fermi level obtained from a fit to the spectra. (b) trARPES spectra before excitation (black), at the first minimum (green) and the first maximum (red) of the oscillations. The solid lines are fits to the data. The extracted position of the Fermi level E_F is indicated by the red and green arrows, showing a modulation of the transient E_F by the coherent modes.

which are continuously and differentiably connected at the interval boundaries and thus are completely determined by these conditions. To determine the smooth incoherent background, such B-spline functions where fitted to the data for $t > 200\,\mathrm{fs}$ for evenly spaced nodes within the fitted time interval by varying the vertical position of the nodes and applying a χ^2 criterion. The spacing of the nodes has to be carefully chosen, as a too large spacing will not be able to adequately reproduce the incoherent background, while a too small spacing will pick up some part of the oscillations in the background. An estimate for the highest frequency that will be picked up by the background for a given node spacing is the Nyquist frequency [Nyq28] $F_\mathrm{Nyquist} = \frac{1}{2\Delta t}$. The node spacing was carefully adjusted for our data and we found that a spacing of $\Delta t \sim 300\,\mathrm{fs}$ sufficiently suppresses frequencies $< 2\,\mathrm{THz}$, where no significant coherent contribution was found, while keeping higher frequencies mostly unaffected. The fitted spline functions and their defining nodes are shown as dashed lines and circles in figure 5.11 (a). In addition, we compared the results of this method for the background determination with a more sophisticated method based on polynomial smoothing and fitting to oscillator functions in combination with an autocorrelation criterion [Mel08], which gave essentially the same resulting oscillatory component ΔI_osc. However, as this method induces further degrees of complexity to the data analysis while not revealing additional information, we used the spline fitted background for further analysis.

Figure 5.11 (b) shows the coherent component ΔI_osc after subtracting the incoherent background contribution. Within the first 2 ps after excitation, we identify a strong oscillation mode with a period close to 200 fs corresponding to $\sim 5\,\mathrm{THz}$. For $t > 1\,\mathrm{ps}$, an interference pattern is observed, which indicates the presence of further frequency components. Next, the corresponding frequencies are determined by FFT, as shown in panel (c) for the fluence-dependent data in panel (b). We identify three distinct modes that contribute to the oscillations, a sharp and intense peak at $\omega_1 = 5.6(2)\,\mathrm{THz}$

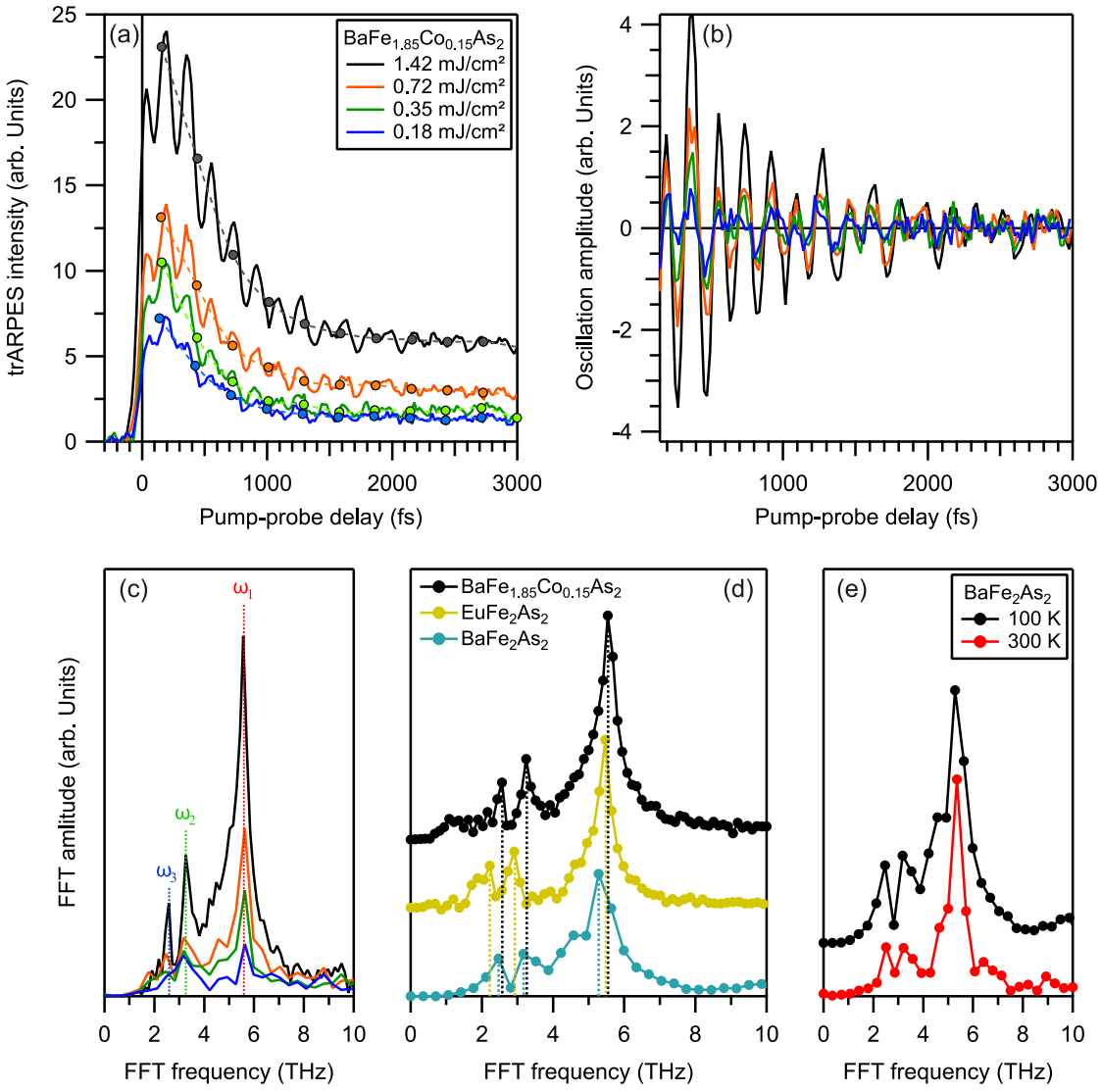

Figure 5.11: Analysis of coherent oscillations. (a) Integrated trARPES intensity $\Delta I(t)$ within a windows of $0 - 1.5$ eV above E_F, for $BaFe_{1.85}Co_{0.15}As_2$ at $T = 100$ K for various fluences. The dashed lines and markers are spline fits and their anchor points, respectively, used to determine the incoherent background (see text). (b) Coherent part ΔI_{osc} after subtracting the incoherent contribution. (c) Fast Fourier transformation (FFT) of the data in panel (b), showing three coherent modes at $\omega_1 = 5.6$ THz, $\omega_2 = 3.3$ THz and $\omega_3 = 2.6$ THz. (d) Comparison of FFTs for $BaFe_{1.85}Co_{0.15}As_2$, $EuFe_2As_2$ and $BaFe_2As_2$. (e) Comparison of FFTs of $BaFe_2As_2$ at $T = 100$ K and $T = 300$ K. All three modes are found independent of T.

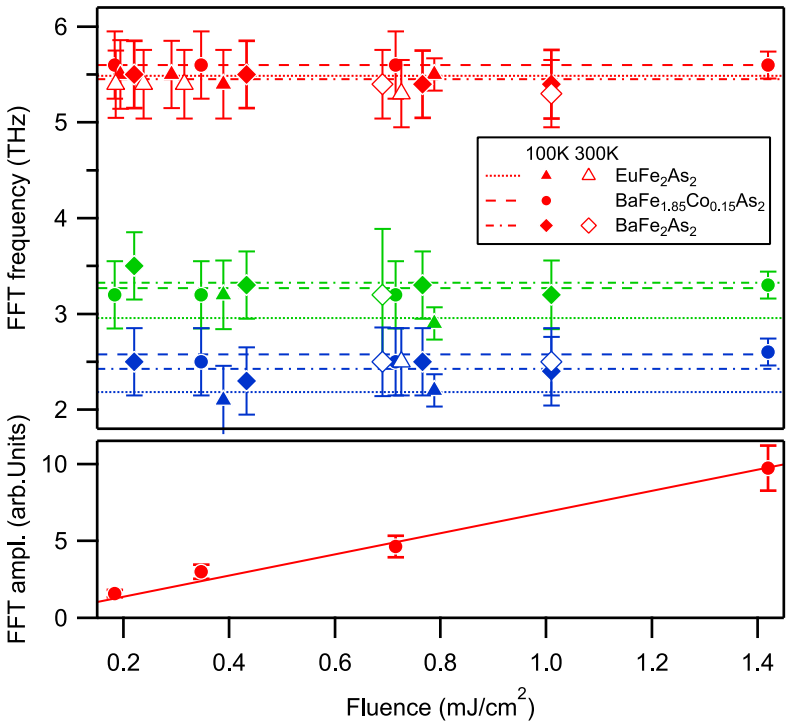

Figure 5.12: Fluence dependence of the coherent modes. Upper Panel: FFT frequencies as a function of excitation fluence F for $EuFe_2As_2$ (triangles), $BaFe_{1.85}Co_{0.15}As_2$ (circles) and $BaFe_2As_2$ (diamonds). Open and closed symbols represent data taken at $T = 300\,\mathrm{K}$ and $T = 100\,\mathrm{K}$, respectively. Error bars are defined by the inter-point spacing of the FFT. Horizontal lines mark the error weighted mean value of the three modes and compounds for data taken at $T = 100\,\mathrm{K}$. Line types are small dashed for $EuFe_2As_2$, large dashed for $BaFe_{1.85}Co_{0.15}As_2$ and dash-dotted for $BaFe_2As_2$. The three modes ω_1 (red), ω_2 (green) and ω_3 (blue) are distinguished by their color. Lower Panel: FFT amplitude of ω_1 for $BaFe_{1.85}Co_{0.15}As_2$ as a function of incident pumping fluence. The line is a linear fit to the data.

($\hbar\omega_1 = 23(1)\,\mathrm{meV}$) and two weaker modes at $\omega_2 = 3.3(2)\,\mathrm{THz}$ ($\hbar\omega_2 = 14(1)\,\mathrm{meV}$) and $\omega_3 = 2.6(2)\,\mathrm{THz}$ ($\hbar\omega_3 = 11(1)\,\mathrm{meV}$). Here, the experimental errors are determined by the point spacing of the FFT which depends on the extend of the respective data set in the time domain. No fluence dependence of the frequencies within error bars are found in panel (c). In panel (d), we compare data of $BaFe_{1.85}Co_{0.15}As_2$, $EuFe_2As_2$ and undoped $BaFe_2As_2$ samples for similar excitation conditions as the highest in panel (c). All three modes are found in all compounds at similar frequencies. Furthermore, all three modes are found independent of temperature, as shown in panel (e) for data of $BaFe_2As_2$ at $T = 100\,\mathrm{K}$ and $T = 300\,\mathrm{K}$.

Figure 5.12 summarizes the frequencies determined by FFT for the three compounds studied and various fluences as a function of incident pumping fluence. Open and closed symbols denote data taken at $T = 300\,\mathrm{K}$ and $T = 100\,\mathrm{K}$, respectively. The dashed lines mark the weighted mean frequencies of the three modes at $T = 100\,\mathrm{K}$ for the three compounds, which are summarized in table 5.1. While the mode ω_1 is identical for all three compounds within error bars, the modes ω_2 and ω_3 appear to be at slightly lower frequencies in $EuFe_2As_2$. However this is based on few data points only and thus might not be significant. The FFT amplitude for the highest mode ω_1 in $BaFe_{1.85}Co_{0.15}As_2$ shown in the lower panel of figure 5.12 is well described by a linear dependence with

mode	$BaFe_{1.85}Co_{0.15}As_2$	$BaFe_2As_2$	$EuFe_2As_2$	Raman[1]	Theory[2]
ω_1	5.60(12) THz	5.45(18) THz	5.49(14) THz	5.5 THz	5.8 THz
ω_2	3.27(12) THz	3.33(18) THz	2.95(16) THz	3.7 THz	3.8 THz
ω_3	2.58(12) THz	2.43(18) THz	2.18(16) THz	–	2.5 THz

[1] $BaFe_2As_2$, Ref. [Cha09]
[2] $BaFe_2As_2$, Ref. [Boe10b, Boe10a]

Table 5.1: Frequencies of coherent oscillations. Weighted mean frequencies of the coherent modes for $BaFe_{1.85}Co_{0.15}As_2$, $BaFe_2As_2$ and $EuFe_2As_2$. Reference values from Raman spectroscopy and a theoretical study are given.

fluence. In combination with the fluence-independent frequencies, this points to a linear regime of the coherent excitations, showing no indication for anharmonicity within our accuracy [Has02].

To determine geometry and character of the coherent modes, we compare our data with Raman scattering data [Cho08, Lit08, Cha09, Sug10, Cha11, Kum11] and a theoretical study [Boe10b, Boe10a]. Figure 5.13, left depicts the calculated phonon dispersion of $BaFe_2As_2$ in the paramagnetic, tetragonal phase for the Γ-X direction. We can clearly identify the mode ω_1 at 23 meV with the Raman active As A_{1g} phonon mode, corresponding to a displacement of the As atoms perpendicular to the FeAs layers, as sketched in figure 5.13, center. This mode was found in Raman scattering studies of various pnictide 122 compounds [Cho08, Lit08, Cha09, Sug10, Cha11, Kum11], including $BaFe_2As_2$. In addition, the coherent excitation of this mode has also been observed in time-resolved optical reflectivity measurements in Co doped $BaFe_2As_2$ [Man09] where the frequency was determined to be 5.56 THz, in agreement with our observation. A more recent study found a coherent excitation of the A_{1g} mode also in SmFeAsO [Mer10], which suggests, that the coherent excitation of this mode is a general phenomenon in the Fe pnictides. However, the other two modes were not observed with time-resolved optical spectroscopy.

Thus, the assignment of the other two modes is less clear. For the excitation of coherent phonons, traditionally two models have been established [Has05, Ish10], the displacive excitation of coherent phonons (DECP) [Zei92] and the impulsive stimulated Raman scattering (ISRS) [Yan85], see chapter 2.1.3. While the DECP mechanism is supposed to be the main excitation mechanism in opaque media like metals and semimetals and allows to first order only the excitation of fully symmetric A_1 modes [Zei92], the ISRS is commonly accepted as the excitation process in transparent media like insulators and some semiconductors and allows for the excitation of all Raman active modes [Has05, Man09]. Later, it was shown that DECP can be understood as a special case of resonant stimulated Raman scattering, which however still only allows for the excitation of Raman active modes at the BZ center [Gar96]. Coherent excitations of non fully symmetric modes have also been detected in the bulk [Has05] and at surfaces [Mel08] of metals, which was attributed to a combination of resonant ISRS and DECP in the former and an excitation mechanism based on spin separation in the latter study. Another ingredient for the observation of coherently excited phonons in trARPES is a strong coupling of the coherent vibrations to electronic states, as we measure the imprint of the coherent modes on the electronic system. Indeed, the calculation of the e-ph coupling strength shown in figure 5.13 [Boe10a] predicts strong coupling for the

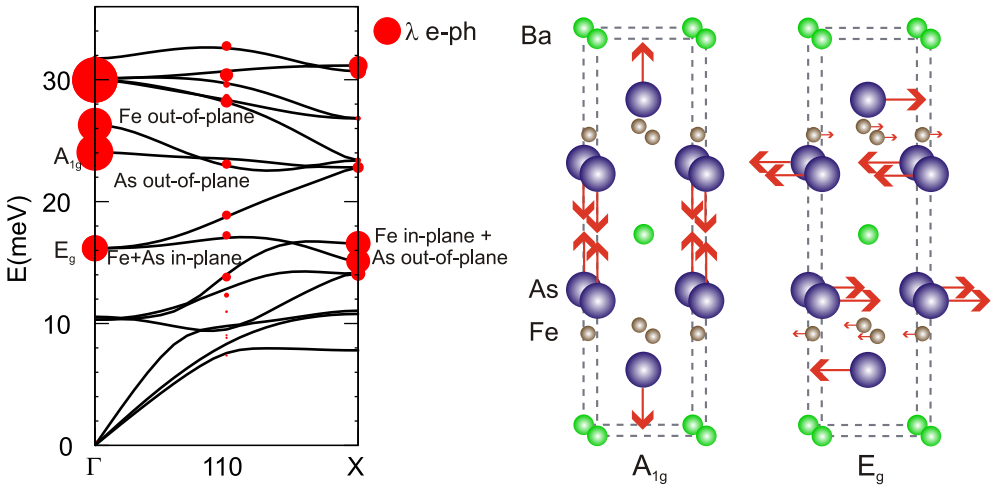

Figure 5.13: Phonon dispersion of $BaFe_2As_2$. Left: Calculated phonon dispersion along the $\Gamma - X$ direction in the paramagnetic phase by L. Boeri [Boe10a]. The size of the red markers provides a measure for the e-ph coupling strength λ. The character of specific modes is indicated. Center: Oscillation pattern of the Raman active out-of-plane As A_{1g} mode. Right: Oscillation pattern of the in-plane E_g mode, involving motions of Fe and As atoms.

A_{1g} mode.

Comparing our frequencies with the calculated phonon dispersion in figure 5.13, a possible candidate for the mode ω_2 could be the E_g mode, corresponding to a shear vibration of As and Fe atoms within the FeAs layers [Lit08] (figure 5.13, right). On the one hand, this Raman active mode is found at 16 meV corresponding to 3.8 THz, which is considerably higher than the mode ω_2 in our experiment, and this frequency for the E_g mode is consistent with Raman observations of this mode in $BaFe_2As_2$ [Cha09]. On the other hand, a Raman scattering study on $CaFe_2As_2$ reported the observation of a mode at 3.35 THz close to our mode ω_2, which was attributed to the E_g mode [Lit11]. In addition, a recent study of Co doped $BaFe_2As_2$ using inelastic x-ray scattering found modes close to the BZ center with an energy of $\sim$ 13 meV [Rez09], corresponding to $\sim$ 3.1 THz. Another possible candidate in the phonon dispersion of figure 5.13 for the ω_2 mode could be the mode at the X-point around 13 meV, which shows combined in-plane and out-of-plane oscillations with $q = q_N$ and enhanced e-ph coupling according to the calculations. On the one hand, the coherent excitation of phonon modes with finite momenta is usually prohibited, as the exciting photons allow only vertical transitions due to their negligible momentum. On the other hand, a specific momentum-dependent optical excitation probability involving optical resonances could in principle also excite boson modes with finite momenta [Sai01]. Furthermore, contributions of surface phonons or spin excitations [Mel08, Ino10], which do not show up in the calculations or in Raman spectroscopy, cannot be ruled out.

Regarding the ω_3 mode, we find a mode at the zone-center around 10 meV in the calculation in figure 5.13, which is, however, not Raman active. Furthermore, according to the calculation, this mode couples only weakly to the electronic system and thus would not be observable in trARPES.

Interestingly, as already mentioned before, the modes ω_2 and ω_3 are found at slightly smaller frequencies in $EuFe_2As_2$ than in the Ba based compounds. This points to a possible involvement of motions of the heavier Eu and lighter Ba atoms in these modes.

Considering the ratio of atomic masses of Eu and Ba, a frequency difference by a factor of

$$\frac{f_{\mathrm{Eu}}}{f_{\mathrm{Ba}}} = \sqrt{\frac{m_{\mathrm{Ba}}}{m_{\mathrm{Eu}}}} = 0.95$$

would be expected. Indeed, this is comparable to the experimentally found ratios $\frac{f_{\mathrm{Eu}}}{f_{\mathrm{Ba}}} \approx 0.9$ found for the modes ω_2 and ω_3. This point could be clarified by studying different FeAs 122 compounds, e.g. the lighter $CaFe_2As_2$ or $SrFe_2As_2$, where the ratio of atomic masses is significantly different. In addition, the involvement of As motions can be quantified by substituting P on the As sites [Thi11]. Thus, while the mode ω_1 is clearly identified with the As A_{1g} mode, additional work is required in order to unambiguously clarify the geometry and character of the modes ω_2 and ω_3.

A possible connection of the coherent phonons with the AFM or structural transitions discussed in the previous section, like e.g. the excitation of the SDW amplitude mode (see chapter 2.3.2 and chapter chapter 7), might be considered as well. This scenario, however, is very unlikely as no significant influence of the temperature on the coherent modes was found and all modes are present in the superconducting compound as well, which does not show any long-range spin ordering.

Having determined the spectrum of the coherent excitations, we now turn to a closer analysis of the relaxation dynamics of the oscillations. From the FFT shown in figure 5.12 (c) we recognize that the mode ω_1 exhibits a considerably broader peak in the frequency domain than the other two modes ω_2 and ω_3. This indicates a faster relaxation of this mode in the time domain. In order to investigate the relaxation of the coherent modes in the time domain, we pursued two approaches. Here we concentrated on the $BaFe_{1.85}Co_{0.15}As_2$ data using the highest pumping fluence of $F = 1.42\,\mu\mathrm{J/cm^2}$: First, we applied a corresponding fitting model to the data in the time domain to directly model the oscillations, which, however bears several complications. The second approach is a so-called sliding window fast Fourier transformation (swFFT), which results in a time-dependent frequency analysis (spectrogram) by Fourier transform data within a time window, that is moved along the data.

To fit the time domain data of the oscillations, ΔI_{osc}, we used a fitting model consisting of damped cosine functions of the form

$$\Delta I_{\mathrm{osc}}(t) = A \exp(-t/\tau) \cos(2\pi f t + \phi) \quad ,$$

convoluted with the pulse XC. Here, A is the initial amplitude of the oscillation, τ the decay constant, f the frequency and ϕ the initital phase of the oscillation. For the sake of simplicity of the model, we did not allow the frequency to change with time (a so-called chirp). Efforts to fit all three modes simultaneously to the data unfortunately were not stable, as this results in a fit with too many unknown and partly interdependent variables. To avoid these problems, we proceeded in a two-step fitting procedure, where we first fitted the dominating ω_1 mode and then fitted the two modes ω_2 and ω_3 to the residual of the first fit. Results of this procedure are show in Figure 5.14. The upper panel shows the background subtracted ΔI_{osc} together with the fit of the dominating ω_1 mode. Below, the residual of this fit is shown together with the fit to the other two modes. The beating behavior of these two modes is clearly visible and fits well to the beating observed in the data. The remaining residual of this second fit, shown in the bottom, shows mostly noise. Some remaining oscillations, mainly of the mode ω_1, show the limitations of the model to describe the data. This indicates that the single-exponential decay is insufficient to describe the relaxation of the mode ω_1.

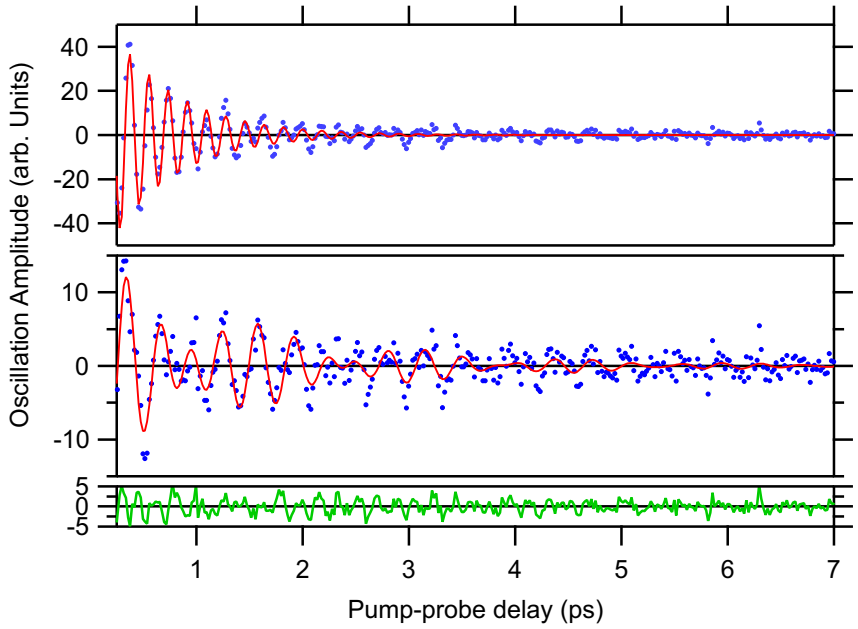

Figure 5.14: Fitting procedure of the coherent oscillations. Top: Oscillation signal ΔI_{osc} of $BaFe_{1.85}Co_{0.15}As_2$ (dots) together with a fit of one damped cosine function to the data (solid line). Middle: Residual from the fit in the top panel, containing mostly the modes ω_2 and ω_3. The data are fitted with two damped cosine functions. Bottom: Residual from the fit in the middle panel, still showing some oscillations not captured in the two fitting steps.

mode	A (arb. Units)	τ (ps)	f (THz)	ϕ (rad/π)
ω_1	200(30)	0.63(7)	5.54(3)	-0.09(4)
ω_2	16(3)	1.3(3)	3.19(3)	-0.11(6)
ω_3	6(2)	2.1(7)	2.52(3)	0.11(9)

Table 5.2: Fitting results of the coherent oscillations.

The results of this fitting procedure are shown in table 5.2. The frequencies of the oscillations fit well with the values extracted from the FFT and even allow a more accurate determination of f within the model assumptions. More interestingly, we find the relaxation of the mode ω_1 to be two times faster than for the other two modes. The initial phase of all three modes is very close to 0, i.e. they are close to the cosine function. This is in agreement with the DECP excitation mechanism, where the abrupt change of the ion potentials starts the oscillation in the displaced configuration [Zei92].

To get an independent cross-check for the relaxation of the modes and to detect possible non exponential decays or time-dependent shifts of the frequencies, one can separate the time-domain data into smaller fragments of the original data length, that cover only a certain time interval and analyze the frequency components within such time windows by FFT. By sliding the position of the window across the original data, one gets the evolution of frequencies with time. This is the principle of the sliding window fast Fourier transformation (swFFT). However, due to the reciprocity of time and frequency, such kind of analysis will always be a compromise between time and

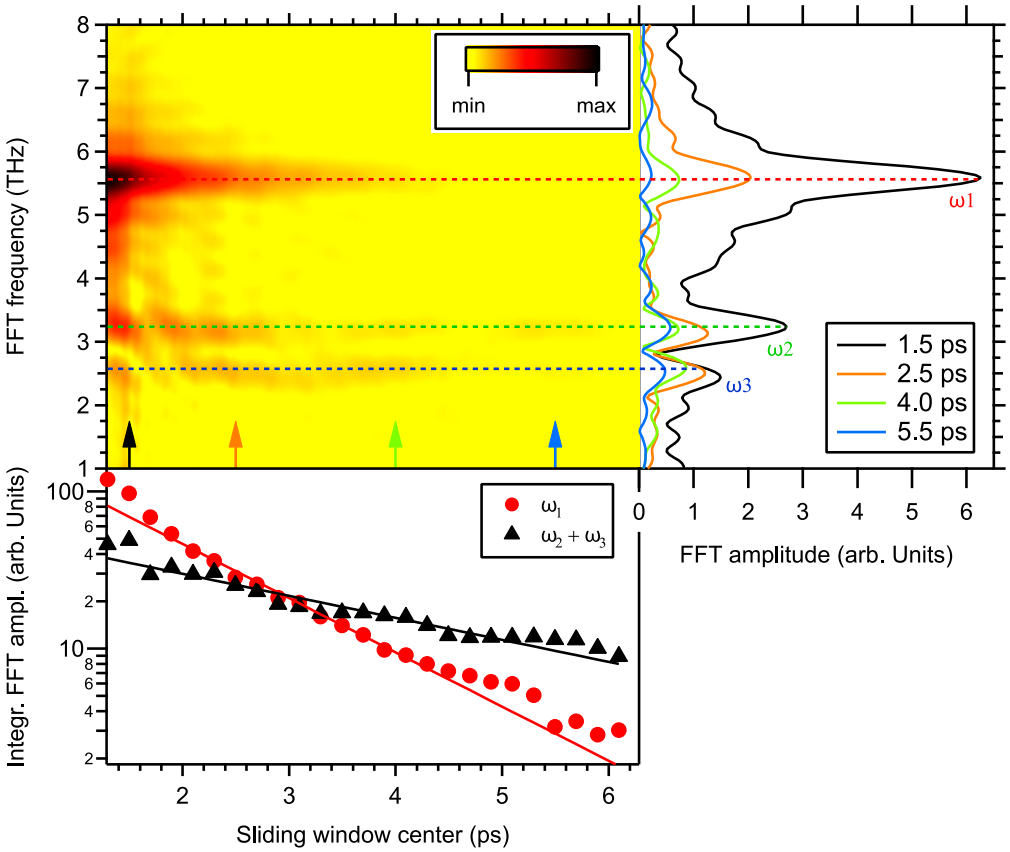

Figure 5.15: Sliding-window FFT amplitude with a window size of 2.4 ps as a function of the sliding window center (time delay) and the FFT frequency in a color coded intensity plot. The three modes are clearly identified. Right panel: Vertical cuts through the data in the main panel at various time delays marked by colored arrows. The highest mode ω_1 shows a faster relaxation than the other two modes. No variation of the mode frequencies with time delay (chirp) is observed. Bottom: FFT intensity integrated about the ω_1 mode (red) and both ω_2 and ω_3 modes (black) as a function of time delay on a logarithmic intensity scale. Solid lines are exponential fits to the data.

frequency resolution. For the swFFT spectrum shown in figure 5.15 in a color intensity plot as a function of sliding window center and FFT frequency, we used a window size of 2.4 ps, which allows a frequency resolution of ~ 0.5 THz, sufficient to resolve the two modes ω_2 and ω_3. By comparing the FFT spectra shown in the right panel for various time delays, we clearly identify the faster relaxation of the ω_1 mode with respect to the other two modes. For instance at 4 ps (green curve), the FFT amplitude of the mode ω_1 is already smaller than of ω_2 and ω_3.

In order to analyze the decay of the modes, we integrated the FFT amplitude around the frequencies of the modes, shown in the lower panel as a function of the window position on a logarithmic intensity scale. Due to interference effects between the two lower-lying modes, we integrated over both modes ω_2 and ω_3. By fitting exponential decay functions to the amplitude relaxation, we determine $\tau_1 = 1.2(1)$ ps and $\tau_{2+3} = 3.1(4)$ ps, both values clearly larger than found in the fitting. This is another sign for the non-exponential decay of the coherent excitation, which is clearly visible in the relaxation of the mode ω_1, which deviates from the exponential fit for $t < 2$ ps. As the amplitude in the time domain is largest for early times, a faster relaxation behavior there

will be found in the fitting, because this will produce the largest contributions to χ^2. Indeed, if we restrict the fitting to $t > 1$ ps in figure 5.14, the relaxation time increases considerably to $\tau \sim 1.2$ ps, consistent with the decay found in the swFFT analysis. No variation of the frequencies with time was found, which is consistent with the harmonic regime of the oscillations already concluded from the linear fluence dependence of the FFT amplitude found in figure 5.12. This is also a justification for the chosen fitting model, which neglects a possible chirp of frequencies.

We will now discuss the different relaxation times for the mode ω_1 and the modes ω_2 and ω_3. The relaxation of coherently excited phonons occurs both through dephasing and population decay of the excited modes. While the dephasing occurs mainly by scattering at crystal defects and e-ph interaction, the population decay is governed by anharmonic phonon-phonon (ph-ph) interaction [Has10]. The scattering with crystal impurities is unlikely to explain the different decay behavior of different modes within the same crystal, assuming a homogeneous excitation density of these modes. However, this could be different e.g. for surface vibrations. The other two relaxation processes can be distinguished by their temperature and fluence dependence. On the one hand, the relaxation by anharmonic ph-ph decay into two acoustic phonons shows an increase in decay rate with increasing temperature [Has05, Has10]. This is not observed in our case, as can be seen from the FFT spectra in figure 5.11 (e), where we find no apparent variation of the width of the A_{1g} mode with temperature. On the other hand, the scattering of coherent phonons with excited carriers by e-ph coupling is highly dependent on the density of excited carriers and thus on the excitation density, which leads to a faster decay at higher fluences [Has02, Has10]. This is indeed observed in the data in figure 5.11 (b), where we find a decrease from $\tau \sim 1000$ fs to $\tau \sim 600$ fs with increasing the fluence from $F = 0.18\,\mathrm{mJ/cm^2}$ to $F = 1.42\,\mathrm{mJ/cm^2}$, as determined by the fitting procedure. Thus, we can conclude that the dominating relaxation channel for the coherent oscillations is the coupling to excited carriers by e-ph scattering. The shorter lifetime of the mode ω_1 compared to the other two modes thus demonstrates a stronger coupling to the electronic system for the A_{1g} mode. This is consistent with the smaller amplitude of the other two modes, as e-ph coupling is the key parameter for both the generation and the detection of coherent phonons in trARPES and thus the amplitude of coherent modes scales with the coupling strength.

Interestingly, the relaxation found for the A_{1g} mode ω_1 is clearly faster than in time-resolved optical reflectivity measurements, where the A_{1g} mode was found to relax with a time-constant $\tau_{A_{1g}} \sim 2.5$ ps [Man09]. This might be explained by a difference in crystal quality, exhibiting less crystal defects in the optical pump-probe experiments. Another possibility might be the different detection technique used. Whereas the optical reflectivity probes the entire region of the optical penetration depth of several tens of nanometers, trARPES is a rather surface sensitive technique (see chapter 2.4). Thus, the coherent phonons in the sub-surface region might exhibit a faster relaxation than in the bulk of the lattice.

5.4 Electron Dynamics at the Γ- and X-Point

The observation of the modulation of the chemical potential at the Γ-point by the coherent excitations evidences a strong modification of the electronic bands and their occupation at the center of the BZ. Such a shift can be understood from the significant variation of the electronic DOS near E_F in the pnictide band structure [Zbi09], where charge neutrality might require a transient readjustment of the chemical potential at Γ and X. Thus, for a more complete understanding of the ultrafast processes after photoexcitation, the semi-metallic band structure of the Fe pnictides has to be considered and information on the electron pockets at the BZ corner are necessary to complement the information gained at the Γ-point. Especially the investigation of the influence of the coherent A_{1g} phonon on the hole and electron pockets at Γ and X could provide valuable information on the detailed nature of e-ph coupling in the FeAs multi-band structure.

Here, two scenarios of the imprint of the coherent oscillations on the electronic bands are discussed. First, we consider a rigid band shift in the opposite direction of the hole and electron pockets at Γ and X, respectively. This scenario is sketched in figure 5.16 (a), where the hole pocket (red line) including the *local* Fermi level is shifted up in energy, leading to excess electrons at Γ (red area). This is accompanied by an opposite shift to lower energies of the electron bands (blue lines) at X, leading to a depletion of spectral weight there (blue area). The corresponding DOS, shown on the right side, is shifted along with the bands. Such a scenario of opposite band shifts is also considered for the case of the A_1 mode in the small bandgap semiconductor Te [Kim03], which even undergoes a semi-conductor to semi-metal transition at high excitation densities [Kim03]. In addition, the corresponding modification of the band-overlap of electron and hole pockets influences the nesting condition between Γ and X, which is directly connected to magnetic ordering and possibly superconductivity in the Fe pnictides.

An alternative scenario is the modification of the DOS by the coherent oscillations through e.g. contraction or expansion of the FeAs tetrahedra. The corresponding change in Fe magnetic moment [Yin08] can e.g. modify the effective masses of Fe-derived bands. This is sketched in figure 5.16 (b), where an enhancement of the effective masses of electron and hole pockets is shown by the dashed parabolas. Consequently, the DOS in each band is modified, leading to a global adjustment of the chemical potential, because the total number of electrons remains constant. In this case, the *global* chemical potential adjusts and an in-phase oscillation of E_F in the whole BZ is expected. A strong dependence of the DOS at the Fermi level on the A_{1g} mode has indeed been predicted by Zbiri *et al.* [Zbi09], corroborating this scenario. Additional support for this scenario comes from calculations of the influence of the A_{1g} phonon excitation on the electronic band structure in $LaFeAsO_{1-x}F_x$, which found a simultaneous band shift for the electron and hole pocket bands [Ynd11] and from a report on recent time-resolved THz experiments of $BaFe_2As_2$, which discusses a similar scenario [Kim12].

In order to investigate the electron dynamics across the BZ, trARPES experiments at the Γ and at the X-point have been performed. As the photon energy of $h\nu = 6.0\,\text{eV}$ at the trARPES setup in Berlin does not allow to access momenta at the BZ boundary, trARPES measurements were performed using extreme ultraviolet (XUV) radiation from a high-harmonic generation (HHG)-based source in the university of Kiel, which is described in chapter 3.2. This experimental setup provides XUV pulses at the 27^{th} harmonic of a titan sapphire amplifier system at $h\nu = 43\,\text{eV}$ with a pulse duration of $< 10\,\text{fs}$ [Mat07, Roh11] and is equipped with a hemispherical imaging analyzer for electron detection, which allows feasible access to the whole BZ of the Fe pnictides.

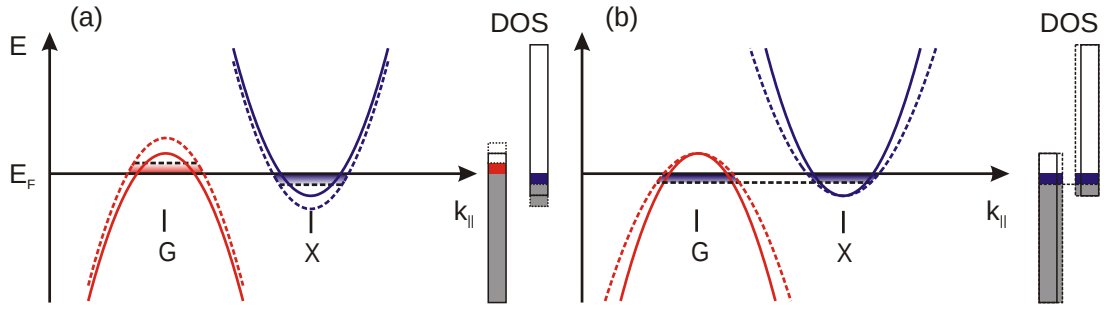

Figure 5.16: Possible influence of the coherent oscillations and electron redistribution in the BZ. (a) Rigid band shift and modification of the band overlap: The electron and hole bands are shifted in energy by the coherent oscillations (dashed parabolas), leading to a change of the band overlap and the local chemical potentials at Γ and X. This leads to an opposite phase of the oscillations, where electron excitations at Γ (red) correspond to hole excitation at X (blue). The modified local DOS at Γ and X is indicated on the right side. (b) Change of the band dispersion: The modification of the unit cell by the coherent oscillations can lead to a change in the band dispersions (dashed parabolas, shown for an increased effective mass), leading to a change in the DOS, shown on the right side. To accommodate for the constant total number of electrons, the chemical potential adjusts globally, resulting in an in-phase oscillation of E_F at Γ and X.

ARPES data of $BaFe_2As_2$ before optical excitation taken at $T \sim 120\,K$ along the $\Gamma - X$ direction near the Γ- and the X-point are shown in figure 5.17 (a) and (b), respectively. Despite the limited energy resolution of ~ 700 meV due to the bandwidth of the XUV pulses, a comparison to data taken at similar photon energies at the synchrotron shown in figure 5.3 reveals clear signatures of the hole pockets at Γ and the electron pockets at X. After optical excitation by the pump pulse at $h\nu = 1.6$ eV with a fluence of $F \sim 3\,mJcm^{-2}$, we observe a considerable change of spectral weight, which is shown as a color coded intensity plot of MDC transients integrated in a window of ± 0.5 eV around E_F in figure 5.17 (c) and (d) for Γ and X, respectively[3]. The most prominent effect is a transient depletion of spectral weight (blue and deep-blue color), which is strongest at the position of the hole and electron bands at Γ and X, respectively. On top of this depletion, we find again the modulation of the spectral weight by the coherently excited modes, which was discussed before. Directly at Γ, within the hole pocket, we also see a weak increase of intensity in the high oscillation phases, indicated by the red color.

Next, in order to investigate the spectral transients in more detail, the trARPES intensity is integrated within representative momentum intervals shown as color bars in figure 5.17 (c) and (d). The resulting transients are depicted in figure 5.18 (a) and (b) for data near Γ and X, respectively. At Γ, we find a strong depletion at $k_{||} < -0.2\,Å^{-1}$ and $k_{||} > 0.2\,Å^{-1}$, where the bands of the hole pockets are located. At $k_{||} \sim 0.0\,Å^{-1}$, we find after an initial depletion an oscillation between spectral depletion and gain, like already concluded from the MDC transients in figure 5.17 (c). In contrast, at the X-point we find the strongest depletion directly at the BZ corner, where the occupied part of the electron pocket is located, whereas the depletion is smaller away from the X-point. Apart from these small differences, we can clearly identify that the effect of the coherent

[3]To reduce noise induced by the HHG source and to enhance the visibility of the transient changes, the data have been smoothed along the momentum axis.

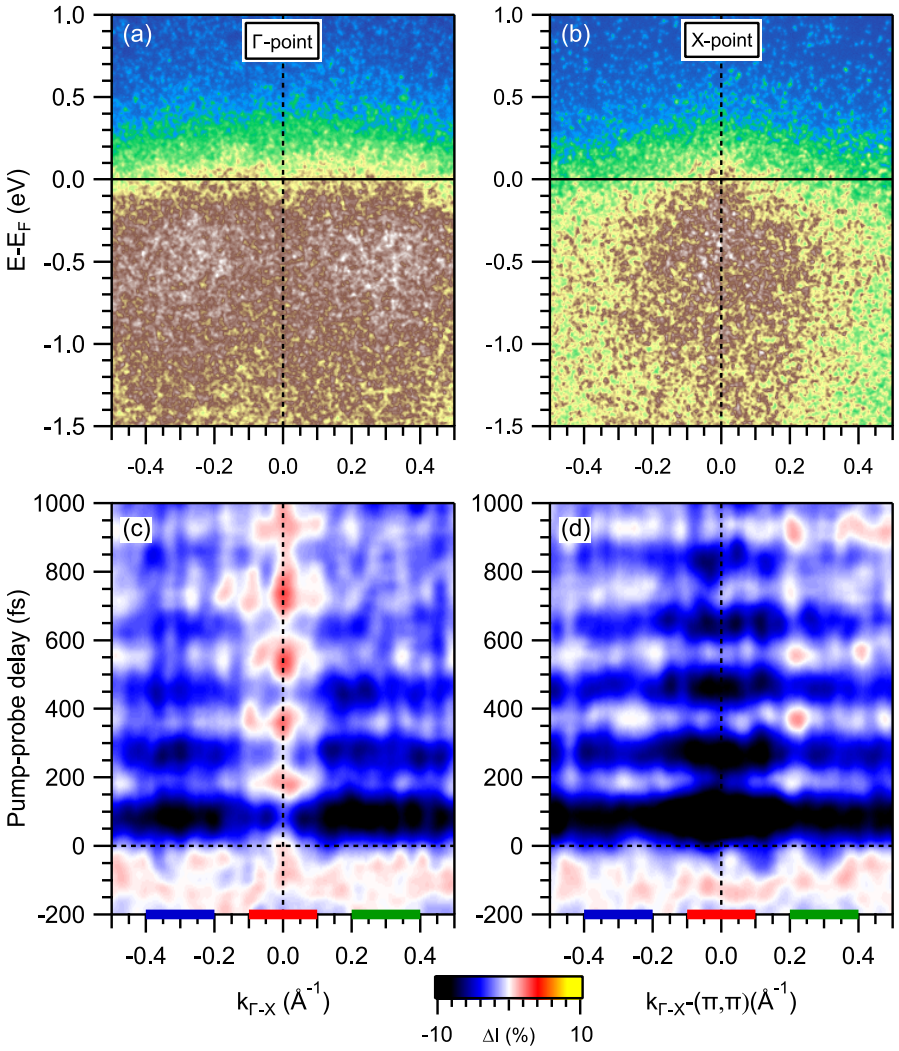

Figure 5.17: trARPES data at the Γ- and X-point using the HHG XUV pulses. ARPES intensity before optical excitation as a function of energy $E-E_\mathrm{F}$ and parallel momentum along the $\Gamma - X$ direction $k_{\Gamma-X}$ around the Γ-point (a) and the X-point (b) in a false color representation. Despite the low energy resolution, the hole pocket at Γ and the electron pocket at X are visible. MDC transients of the pump-induced intensity change $\Delta I(k,t)$, integrated in a window of ± 0.5 eV around the Fermi level are shown in panels (c) and (d) as a function of $k_{\Gamma-X}$ and pump-probe delay for Γ and X, respectively. The strongest depletion (deep blue) is located at the respective bands. Color bars represent integration areas used for the transients in figure 5.18.

oscillation is very similar at the Γ and the X-point. In both figure 5.18 (a) and (b), the first minimum of spectral intensity occurs at ~ 90 fs and the first maximum at ~ 180 fs, which indicates that the spectral weight oscillates in phase at Γ and X, which would represent a global shift of the chemical potential throughout the BZ. Integrating the whole spectral intensity for $-0.6\,\text{Å}^{-1} < k_\parallel < 0.6\,\text{Å}^{-1}$ reveals a net depletion of spectral weight for both Γ and X.

To investigate this more systematically, the transient Fermi level, which has been determined by fitting of the Fermi edge of the spectra, is shown in figure 5.19 (a) and (b) for Γ and X, respectively. The red solid lines represent fits with a cosine function

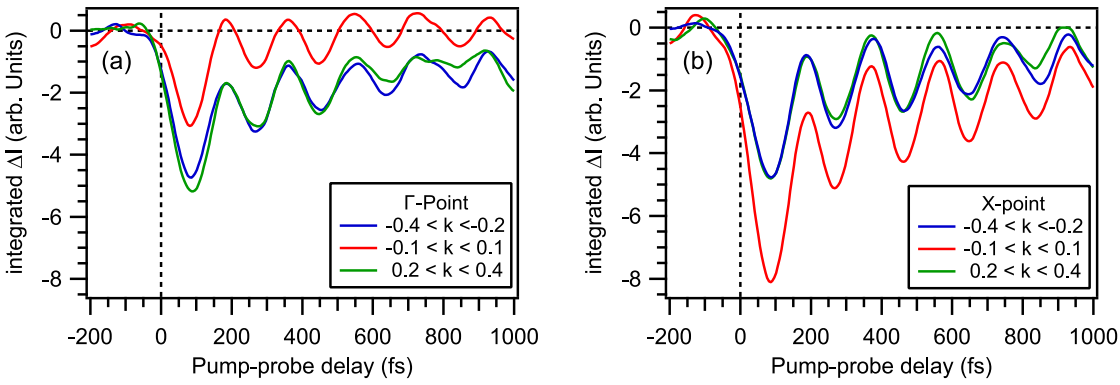

Figure 5.18: Transient trARPES intensity, integrated ±0.5 eV about the Fermi level and within the momentum intervals depicted in figure 5.17 (c) and (d) as a function of pump-probe delay at Γ (a) and X (b). A strong depletion of signal is found at the bands of the hole and electron pocket (blue/green curve in (a) and red curve in (b)). The coherent oscillations modulate the intensity at Γ and X with the same phase.

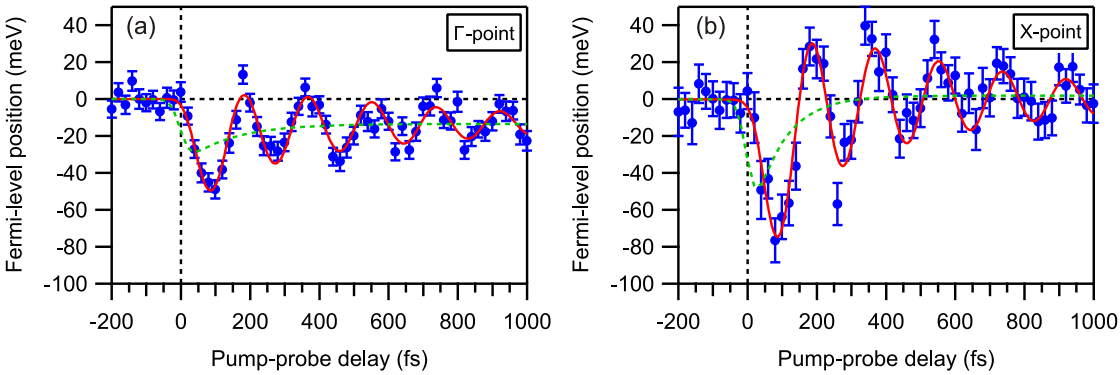

Figure 5.19: Transient position of the Fermi level at Γ (a) and X (b), determined by fitting of angle-integrated EDCs. Red lines are fits of oscillation functions to the data, on top of an exponential decay, given by the dashed green lines. The in-phase oscillations of the Fermi level at the center and corner of the BZ demonstrate a modification of the global chemical potential.

on top of a transient exponential decay, which is shown as dashed green lines. The Fit yields an initial phase of $\phi_\Gamma = +0.02(9)\,\pi$ and $\phi_X = -0.03(9)\,\pi$, which confirms the in-phase modulation of the chemical potential at Γ and X.

The observation of an in-phase oscillation at the center and corner of the BZ clearly favors the second scenario of a transient modification of the DOS, discussed in figure 5.16 (b). In addition, the observation of a net depletion of spectral weight around the Fermi level indicates a global change of the energy reference and not just a redistribution of electrons in the BZ. Still, a redistribution along the k_z direction perpendicular to the FeAs planes might be considered. Such a behavior would lead to a different oscillation phase for different photon energies, which probe the Γ and Z-point of the three-dimensional (3D) BZ. However, the experimentally available XUV photon energy of $h\nu = 43$ eV corresponds to a vertical momentum component of $k_z = 7.76\,\mathrm{c}^*$, which is close to the Γ-point, whereas $h\nu = 6$ eV probes states close to Z [Shi11a]. Considering the same oscillation phase close to a cosine found for both photon energies at Γ, such a scenario remains highly unlikely as well.

5.5 Determination of the Electron-Phonon Coupling Constant

The observation of coherent phonon modes in trARPES demonstrates substantial e-ph coupling at least for specific modes, as we detect their imprint on electronic states near E_F. As the e-ph coupling is a key parameter responsible for superconductivity in the BCS theory of conventional superconductors and one potential candidate for the pairing interaction in the HTSCs, the quantitative determination of the e-ph coupling strength is of particular interest. To quantify the e-ph coupling strength, we can make use of the energy resolution provided by trARPES. Several methods to determine the e-ph coupling strength have been established in the literature and successfully used in various studies. In the energy domain, ARPES analyzes the renormalization of the single-particle spectral function by the electronic self energy (see chapter 2.4), which includes the e-ph coupling. However, such type of analysis requires very high sample and data quality, which is difficult to obtain in the Fe pnictides and only few ARPES studies of FeAs compounds were able to determine effects of the electron self-energy [Wra08, Ric09, Koi09]. In addition, usually only information on specific modes that couple to QPs close to the Fermi level are obtained and a separation of different contributions to the electron self energy is often difficult.

In contrast, fs time-resolved spectroscopies allow to separate e-ph scattering from other relaxation channels like e.g. e-e scattering or heat diffusion, which can be distinguished from their different timescales out of thermal equilibrium. Conventionally, the e-ph relaxation in metals has been successfully described using the two-temperature model (TTM) [Ani74, All87, DF00, Ret02, Lis04b, Lis05a, Per07], which is discussed in chapter 2.1.2. This model describes a system of two coupled heat baths for electrons and phonons with temperatures T_e and T_l by coupled rate equations for T_e and T_l, respectively. One key assumption of this model is that e-e and ph-ph scattering occurs on a much faster timescale than the e-ph coupling, leading to a thermal distribution within each subsystem. However, in correlated electron systems like the Fe pnictides, e-ph scattering might occur on similar timescales, which imposes some questions on the applicability of the TTM for these materials and care has to be taken. Nevertheless, we will analyze our data in terms of a specific version of the TTM and will compare the results with other methods for the determination of the e-ph coupling strength.

5.5.1 Analysis of e-ph Coupling within the TTM

The temperature of the thermalized part of the electronic subsystem T_e can be extracted from the trARPES data by fitting Fermi-Dirac distribution functions,

$$f(E - E_F, T_e) = \left[1 + \exp(\frac{E - E_F}{k_B T_e})\right]^{-1} \quad ,$$

to the high energy cutoff of the transient data, multiplied by a phenomenological DOS function and convoluted with an instrumental resolution function, where k_B is the Boltzmann constant [Lis04b, Per07]. Exemplary fits to the data of $EuFe_2As_2$ at an excitation fluence of $F = 0.8\,\mathrm{mJ/cm^2}$ and at $T = 100\,\mathrm{K}$ are shown in figure 5.20 (a) for various pump-probe delays on a logarithmic scale. At least for the first few hundred fs, we encounter significant deviations from a thermal Fermi-Dirac distribution, evident from the nonexponential behavior of the electron distribution. However, already for $t > 250\,\mathrm{fs}$, this deviation is less than 1% of the population and thus should not have significant

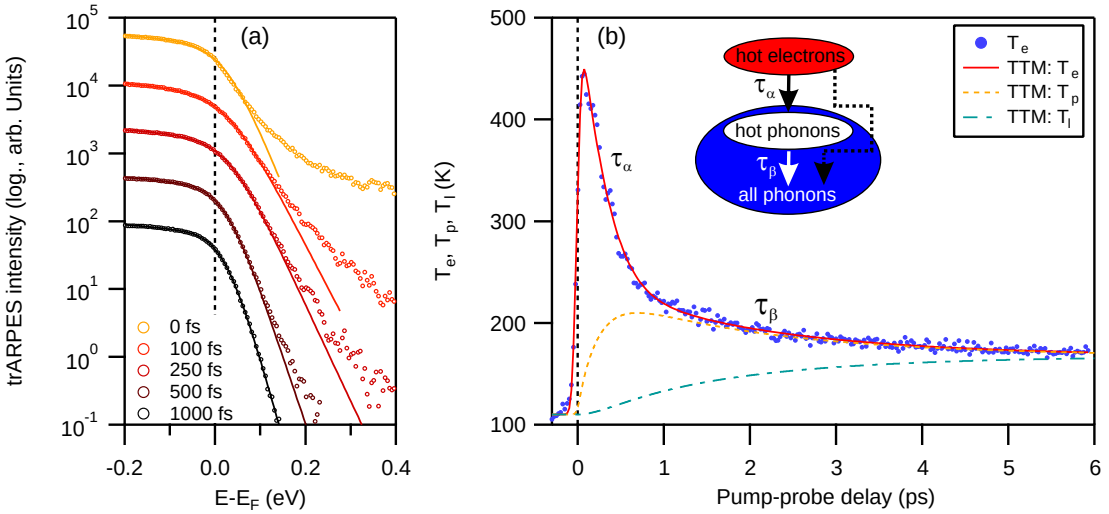

Figure 5.20: Analysis within the two-temperature model (TTM). (a) trARPES spectra of $EuFe_2As_2$ at $T = 100\,\mathrm{K}$ and for $F = 0.8\,\mathrm{mJ/cm^2}$ for various pump-probe delays on a logarithmic intensity scale. Solid lines are fits to Fermi-Dirac distribution functions. Note the deviation from the thermal distribution for $t < 250\,\mathrm{fs}$, indicating a nonthermal contribution. Spectra are vertically offset for clarity. (b) Electronic temperature T_e and a fit to the extended TTM described by the sketch in the inset [Per07]. Hot electrons couple selectively to a subset of hot phonons on a timescale τ_α. These hot phonons couple to the rest of the phonon modes on a slower timescale τ_β. Temperatures of the hot phonons (T_p) and the other phonons (T_l) are shown as dashed and dash-dotted lines, respectively.

influence anymore. Furthermore, for smaller excitation fluences, the thermalization of excited electrons occurs even on a faster timescale. It should be noted here that extended versions of the TTM exist, that partially account for the non-thermal part of the transient electron distribution [Lis04b, Lis05a].

The electronic temperature determined by the fitting is shown in figure 5.20 (b) as a function of pump-probe delay. After the steep rise of the electronic temperature at t_0, we find a relaxation on two distinct timescales τ_α and τ_β. As has been shown for the cuprate HTSC $Bi_2Sr_2CaCu_2O_{8+\delta}$ [Per07], such a behavior indicates the selective coupling of hot electrons to a subset of strongly coupled phonon modes on the faster timescale τ_α. Subsequently these hot phonons then transfer their energy to the rest of the phonons by anharmonic ph-ph coupling, determined by τ_β. For this situation, an extended version of the TTM (sometimes also called three-temperature model) has been proposed and successfully applied by Perfetti and coworkers [Per07]. Indeed, such a behavior has already been found previously for Fe pnictides by time-resolved optical reflectivity measurements and has been interpreted within the same extended TTM [Man10].

The extended TTM introduces a third coupled rate equation for the temperature of the hot phonon distribution T_p to the two equations for the electron and lattice temperatures T_e and T_l (see chapter 2.1.2), leading to the following set of coupled rate

equations:

$$\frac{\mathrm{d}T_e}{\mathrm{d}t} = -H(T_e,T_p) + \frac{S}{C_e} \tag{5.1}$$

$$\frac{\mathrm{d}T_p}{\mathrm{d}t} = +\frac{C_e}{C_p}H(T_e,T_p) - \frac{T_p - T_l}{\tau_\beta} \tag{5.2}$$

$$\frac{\mathrm{d}T_l}{\mathrm{d}t} = +\frac{C_p}{C_l}\frac{T_p - T_l}{\tau_\beta} \quad . \tag{5.3}$$

The source term S is a Gaussian excitation pulse with a FWHM of 50 fs and an energy density determined by the absorbed fluence distributed over the optical penetration depth λ_{opt}. The specific heat of electrons is determined by $C_e = \gamma_e T_e$, with the electronic specific heat coefficient γ_e. For the specific heat of the hot phonons and the rest of the phonons, the Einstein model with a mode ω_0 is used, $C_p = 3f\hbar\omega_0 \left.\frac{\partial n}{\partial T}\right|_{T_p}$ and $C_l = 3(1-f)\hbar\omega_0 \left.\frac{\partial n}{\partial T}\right|_{T_l}$, where $n = (e^{\hbar\omega_0/k_BT} - 1)^{-1}$ is the Bose-Einstein distribution function. The parameter f is the fraction of modes that are more strongly coupled to the electrons, and the anharmonic decay of phonons is described by τ_β. For the energy transfer from the electrons to the more strongly coupled phonons, the formula derived by Allen [All87] is used:

$$H(T_e,T_p) = \gamma_T(T_e - T_p) = \frac{3\hbar\lambda\left\langle\omega^2\right\rangle}{\pi k_B}\frac{T_e - T_p}{T_e} \quad , \tag{5.4}$$

where $\lambda\left\langle\omega^2\right\rangle$ is the second moment of the Eliashberg e-ph coupling function $\alpha^2F(\omega)$ (see chapter 2.1). Electron-phonon coupling to the fraction $(1-f)$ of the lattice modes that are less coupled only weakly influences the evolution of T_e and has therefore been neglected. Electronic diffusion processes have been neglected as well in this model as the electric and thermal conductivity is strongly reduced along the longer c-axis due to the layered, quasi-2D structure of the Fe-pnictides [Tan09, Rei10].

Naturally, the description of the phonon system with a simple Einstein mode is a strong simplification and a proper choice of the mode energy influences the result of the simulations. To provide an estimate for the frequency ω_0, we consider the phonon spectrum of the 122 FeAs compounds. The calculated phonon spectrum extends up to $\sim$ 35 meV as derived in several calculations [Hah09, Zbi09, Rez09, Mit09b, Boe10b, Boe10a] (see also figure 5.13) and supported by experiments [Zbi09, Hah09, Mit09a] with the strongest contributions to $\alpha^2F(\omega)$ between $10 - 30$ meV [Boe10b]. Another estimate can be made from the lattice specific heat capacity C_l measured in $BaFe_2As_2$ [Sto10b, Kan10, Rot10], which is well approximated for $T > 100$ K by $\omega_0 \sim 18 - 20$ meV, consistent with the Debye temperature of $\Theta_D \sim 275 - 300$ K [Wel09, Rot10].

The proper choice of the electronic heat capacity, $C_e = \gamma_e T_e$ bears even more uncertainties. While for undoped $BaFe_2As_2$ values between $\gamma_e \sim 4 - 40\,\mathrm{mJK^{-2}mole^{-1}}$ [Don08, Sef09, Har10, Kan10, Rot10] have been reported, a strong dependence of γ_e on the doping level due to the sensitivity of the DOS at the Fermi level from doping [Sin08] is found in $BaFe_{2-x}Co_xAs_2$ [Gof10, Har10]. In addition, the experimental excitation density bears some uncertainties due to the unknown value of the optical penetration depth λ_{opt}. However, reasonable agreement was found for values around $\lambda_{\mathrm{opt}} \sim 30$ nm, in agreement with $\lambda_{\mathrm{opt}} = 26$ nm reported for optimally doped $Ba_{1-x}K_xFe_2As_2$ [Tor11].

In order to account for these unknown parameters in the model, we fitted the extended TTM for various values of ω_0 between $10 - 30$ meV, while leaving γ_e as a free fitting parameter. The resulting values for the parameters of the model are summarized in table 5.3 for the investigated compounds. For γ_e, f and $\lambda\left\langle\omega^2\right\rangle$, the left and right

compound	γ_e ($\mathrm{mJK^{-2}mole^{-1}}$)	f	$\lambda\langle\omega^2\rangle$ ($\mathrm{meV^2}$)	τ_β (ps)
$EuFe_2As_2$	$58-36$	$0.43-0.38$	$56-65$	2.9(3)
$BaFe_{1.85}Co_{0.15}As_2$	$48-28$	$0.48-0.43$	$46-55$	3.3(5)
$BaFe_2As_2$	$80-41$	~ 0.45	$30-46$	~ 3.5

Table 5.3: Fitting parameters of the extended TTM. Left and right values for γ_e, f and $\lambda\langle\omega^2\rangle$ are for a choice of $\omega_0 = 10\,\mathrm{meV}$ and 30 meV, respectively. For $BaFe_2As_2$, only data up to 4 ps pump-probe delay were available, which did not allow a reliable determination of f and τ_β, thus similar values as found for $BaFe_{1.85}Co_{0.15}As_2$ have been used.

values are for a choice of $\omega_0 = 10\,\mathrm{meV}$ and 30 meV, respectively. An exemplary fit of the electronic temperature T_e using $\omega_0 = 18\,\mathrm{meV}$ is shown in figure 5.20 (b) as solid line, which shows excellent agreement with the measured data. For other choices of ω_0, similar agreement to the data is found. The temperatures of hot phonons (T_p) and other phonons (T_l) derived from the model are shown as dashed and dash-dotted lines, respectively.

The values determined for $\lambda\langle\omega^2\rangle$ can be compared to recently published values for the e-ph coupling strength determined from optical pump-probe experiments. Mansart *et al.* [Man10] report values of $\lambda\langle\omega^2\rangle \approx 64\,\mathrm{meV^2}$ for Co doped $BaFe_2As_2$, which is determined by the extended TTM. Stojchevska *et al.* [Sto10a] derived a somewhat higher value of $\lambda\langle\omega^2\rangle = 110(10)\,\mathrm{meV^2}$ in $SrFe_2As_2$ from the temperature dependence of QP relaxation time constants, and for $SmFeAsO_{1-x}F_x$ an even larger value of $\lambda\langle\omega^2\rangle = 135(10)\,\mathrm{meV^2}$ is reported [Mer10]. In general, our results are compatible with the weak e-ph coupling found in the Fe pnictides and indicate even weaker coupling for Ba-based compounds than in $EuFe_2As_2$. However, one has to bear in mind that the thermalization of non-thermal hot electrons leads to an additional heating of the thermalized electron distribution, which counteracts the energy transfer to the lattice and leads to a slower energy relaxation of the thermalized electrons. Thus, the analysis of only the thermalized part of the electronic distribution might considerably underestimate e-ph coupling especially at early times [Gad10].

The fraction $f \sim 0.4$ of preferentially coupled modes is in agreement with the observations of Mansart *et al.* [Man10], and is considerably higher than $f \sim 0.2$ found in the cuprate HTSC $Bi_2Sr_2CaCu_2O_{8+\delta}$ [Per07]. This stronger selectivity of e-ph coupling in the cuprates might be explained by the stronger 2D character of the cuprates, which might favor the selective coupling to specific modes. The Fe pnictides and especially Co doped 122 compounds are characterized by a stronger interlayer coupling and a more 3D character [Vil09], which might lead to a less selective e-ph coupling [Man10]. The equilibration time τ_β of the hot phonon distribution with the rest of the lattice modes is considerably faster here than in the optical reflectivity measurements in reference [Man10], who report $\tau_\beta \sim 5-7\,\mathrm{ps}$. This faster relaxation of excited phonon modes observed in trARPES measurements compared to optical reflectivity is consistent with the faster relaxation of the coherently excited phonon modes discussed in chapter 5.3 and indicates a different phonon relaxation behavior in the bulk and the subsurface region, respectively. In addition, the excitation densities in the experiments by Mansart *et al.* where a factor of two to three larger than here, and an increase of τ_β with fluence was observed [Man10], which might also help to explain this discrepancy.

5.5.2 Analysis of non-thermal Electrons

The previous analysis within the TTM was based on the energy relaxation within the thermalized part of the transient electronic distribution function. In addition, also the non-thermal, highly excited electrons can provide information about the strength of e-ph coupling. This aspect will be discussed in the following by analyzing the energy relaxation of non-thermal, excited electrons.

The scattering rate of electrons excited at energy $\epsilon = E - E_\mathrm{F}$ above the Fermi level is in the self-energy formulation of many-body theory determined by $\Gamma = \hbar\tau^{-1} = 2\mathrm{Im}\Sigma(\epsilon)$, where $\mathrm{Im}\Sigma$ is the imaginary part of the electronic self energy [Ech00]. Important energy-dependent contributions to Γ arise from e-e and e-ph scattering[4]. Electron-electron scattering is considered to follow the quadratic energy scaling of the Fermi liquid theory [Pin66], $\Gamma_{e-e} = 2\beta\left[(\pi k_B T)^2 + \epsilon^2\right]$ (see figure 5.21 (a)). As the proportionality coefficient β is rather small in typical metals (in the order of $10^{-2}\,\mathrm{eV}^{-1}$ to $10^{-1}\,\mathrm{eV}^{-1}$) [McD95, Val99], this contribution is negligible compared to the e-ph scattering at low excitation energies. The latter increases up to the maximal phonon energy $\hbar\omega_{max}$ and is constant above (see figure 5.21 (a)). For $\epsilon > \hbar\omega_{max}$ and $T = 0\,\mathrm{K}$, Γ_{e-ph} results for an Einstein mode ω_0 to [Eng63]

$$\Gamma_{e-ph} = \pi\hbar\lambda\omega_0 \quad , \tag{5.5}$$

where λ is the e-ph coupling constant. Within the energy window between $\hbar\omega_{max}$ and the crossover regime, where Γ_{e-e} becomes dominant (shaded area in figure 5.21 (a)), the rate of energy dissipation of an electron due to the emission of a phonon with energy $\hbar\omega_0$ is given by

$$\frac{\mathrm{d}E}{\mathrm{d}t} = \frac{\hbar\omega_0}{\tau} = \pi\hbar\lambda\omega_0^2 \quad , \tag{5.6}$$

which leads to a linear relaxation of the electron energy [Gus98].

The rate of energy relaxation of excited electrons can be extracted from the experimental trARPES intensity $I(\epsilon, t)$ by analyzing the mean excess energy,

$$\langle\Delta E(t)\rangle = \frac{\int_{\epsilon_0}^{\epsilon_1} \epsilon\Delta I(\epsilon, t)\mathrm{d}\epsilon}{\int_{\epsilon_0}^{\epsilon_1} \Delta I(\epsilon, t)\mathrm{d}\epsilon} \quad . \tag{5.7}$$

However, this integral represents the mean excess energy within a selected partition of a transient distribution function and not the energy relaxation of single individual electrons. Thus, special care has to be taken with the determination of the integration boundaries, ϵ_0 and ϵ_1. For the lower integration boundary, on the one hand a too small value will lead to slower relaxation and an underestimation of e-ph scattering, as the e-ph scattering rate decreases for low ϵ and the influence of the thermalized part of the distribution leads to slower relaxation. A too high value for ϵ_0 on the other hand will increase the influence of e-e scattering and lead to an overestimation of Γ_{e-ph}. This also holds true for the upper boundary ϵ_1. In addition, electrons that are excited above ϵ_1 scatter into the integration window and thus lead to a slowing down of the energy relaxation. This favors a higher value of ϵ_1, where this effect is minimized. A careful investigation of the dependence of the values found for $\lambda\langle\omega^2\rangle$ from the integration boundaries and the excitation fluence reveals that the influence of the e-ph interaction cannot be totally separated from other influences by this evaluation.

[4] Defect mediated scattering is usually considered to be energy conserving and is thus neglected here.

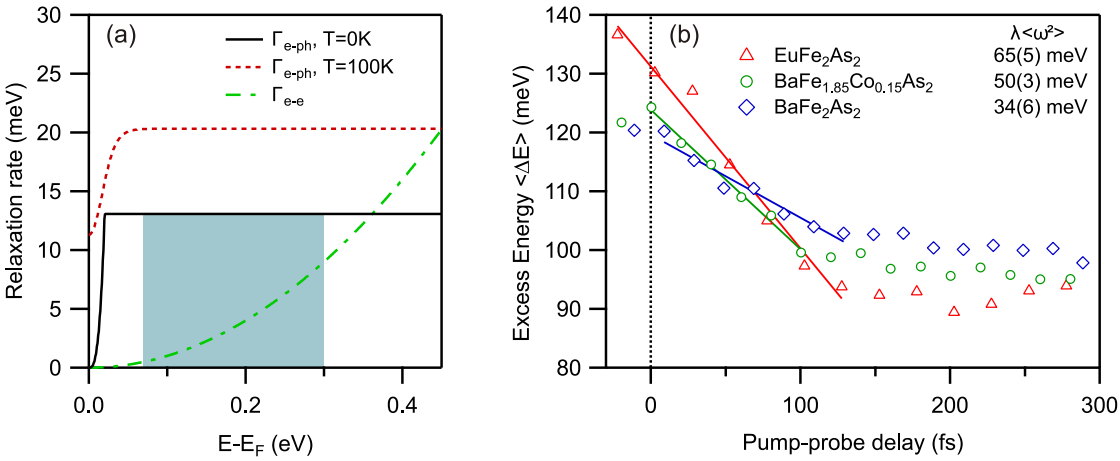

Figure 5.21: Analysis of excess energy relaxation. (a) Electron-phonon (e-ph) and electron-electron (e-e) contributions to the electron decay rate Γ. The e-ph contribution Γ_{e-ph} calculated in the Debye model with $\hbar\omega_D = 20\,\text{meV}$ and $\lambda = 0.3$ at $T = 0\,\text{K}$ and $T = 100\,\text{K}$ increases up to $\sim \omega_D$ and is constant above. The electronic contribution Γ_{e-e} calculated for $\beta = 0.1\,\text{eV}^{-1}$ exceeds γ_{e-ph} only at higher energies. The shaded area marks the energy where e-ph scattering dominates. (b) Electron mean excess energy extracted from trARPES data at $T = 100\,\text{K}$ near k_F within the energy window $0.07\,\text{eV} < \epsilon < 0.3\,\text{eV}$ marked in (a). Solid lines are fits to equation (5.6).

However, a reasonable choice of $\epsilon_0 = 70\,\text{meV}$ and $\epsilon_1 = 300\,\text{meV}$ for the boundaries allows to give a rough estimate of the e-ph coupling strength.

Experimental data of $EuFe_2As_2$, $BaFe_{1.85}Co_{0.15}As_2$ and $BaFe_2As_2$ near k_F and at $T = 100\,\text{K}$ are shown in figure 5.21 (b). To minimize lattice heating and the influence of the hot thermalized electron distribution, low excitation fluences of $F \sim 50\,\mu\text{Jcm}^{-2}$ have been used. The linear fits according to equation (5.6) within the first $\sim 100\,\text{fs}$ yield values of $\lambda\langle\omega^2\rangle = 65(5)\,\text{meV}^2$ for $EuFe_2As_2$, $\lambda\langle\omega^2\rangle = 50(3)\,\text{meV}^2$ for $BaFe_{1.85}Co_{0.15}As_2$ and $\lambda\langle\omega^2\rangle = 34(6)\,\text{meV}^2$ for $BaFe_2As_2$. Here, error bars represent the numerical uncertainties of the linear fits. Due to the influence of the integration boundaries discussed above and of the elevated lattice temperature, the absolute errors are considered substantially larger. Nevertheless, we find a good agreement with the values found in the TTM simulations and a considerably higher e-ph coupling in $EuFe_2As_2$ than in $BaFe_{1.85}Co_{0.15}As_2$ and even lower $\lambda\langle\omega^2\rangle$ in $BaFe_2As_2$.

5.5.3 Evaluation of the temperature-dependent Relaxation

Finally, another estimate of the e-ph coupling strength can be gained from the temperature dependence of QP relaxation rates [All87, Kab08, Sto10a, Gad10]. A recent theoretical investigation of the Boltzmann equation for e-e and e-ph interaction found an analytic solution for the temperature dependence of the QP relaxation rate τ [Kab08]. In the limit of a bad metal at elevated temperatures, τ depends linearly on T [Kab08, Sto10a, Gad10]:

$$\tau = \frac{2\pi k_B T}{3\hbar\lambda\langle\omega^2\rangle} \quad . \tag{5.8}$$

This relation allows for an independent determination of the e-ph coupling strength $\lambda\langle\omega^2\rangle$.

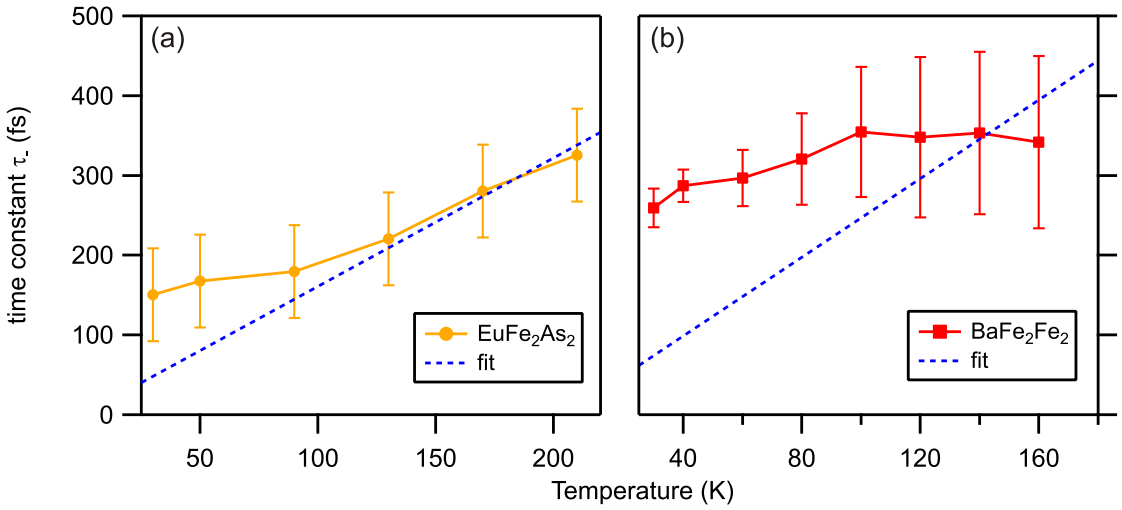

Figure 5.22: Evaluation of the temperature dependence of relaxation rates in $EuFe_2As_2$ (a) and $BaFe_2As_2$ (b). The dashed lines are linear fits to equation (5.8) in the temperature range $T > 100\,\mathrm{K}$.

Experimentally, we use the temperature-dependent hole relaxation times τ_-, determined in chapter 5.2, which are found to be independent from the AFM transition. τ_- for $EuFe_2As_2$ and $BaFe_2As_2$ are shown in figure 5.22 together with linear fits to equation (5.8) to the data for $T > 100\,\mathrm{K}$. For $EuFe_2As_2$, we find good agreement to the linear behavior and derive a value of $\lambda\left\langle\omega^2\right\rangle_{\mathrm{Eu}} = 90(30)\,\mathrm{meV}^2$, where the error represents a confidence interval of 80% due to the few points entering the fit. This value, albeit considerably higher than the values found in the TTM and in the evaluation of the excess energy, is in agreement with the other evaluations within error bars. For $BaFe_2As_2$, the linear increase of τ_- with temperature is less apparent from the data, which might be due to the limited temperature range of the data. Nevertheless, the linear fit for $BaFe_2As_2$ yiels a smaller value of $\lambda\left\langle\omega^2\right\rangle_{\mathrm{Ba}} = 50(30)\,\mathrm{meV}^2$, in agreement with our other results.

Based on our results of $\lambda\left\langle\omega^2\right\rangle$ we can estimate the value of the e-ph coupling constant λ for a particular value of ω. Considering the coherently excited A_{1g} mode at 23 meV, which showed enhanced e-ph coupling in calculations, we find $\lambda < 0.15$ for all compounds. This estimate is in agreement with calculations of various Fe-pnictide compounds, which report average values of $\lambda < 0.35$ [Boe08, Boe10b]. Taking the mean of the phonon DOS as reference, λ gets even smaller, in agreement with other publications [Man10, Sto10a]. Even if we consider the lowest coupled modes around 12 meV to be most important for e-ph coupling, λ does not exceed a value of 0.5. Similar small values for λ have been found in the cuprate HTSCs [Per07], which suggests limited importance of e-ph coupling for the pairing mechanism in both classes of materials.

These values for the e-ph coupling constant λ allow to estimate the superconducting (SC) critical temperature T_c, assuming a conventional BCS-type of pairing based on e-ph coupling. Here, the SC critical temperature T_c in isotropic systems and in a strong coupling regime is given by McMillan's formula [McM68], modified by Allen and Dynes [All75],

$$T_c = \frac{\omega_{\log}}{1.20}\exp\left(-\frac{1.04(1+\lambda)}{\lambda-\mu^*-0.62\lambda\mu^*}\right) \tag{5.9}$$

where μ^* is the effective Coulomb repulsion and $\omega_{\log}$ is the logarithmic average of the

phonon spectrum. Taking $\mu^* = 0$ and $\omega_{\log} = 205\,\mathrm{K}$ [Boe08], which provides an upper limit for T_c, we find $T_c = 0.06\,\mathrm{K}$ and $T_c = 7.5\,\mathrm{K}$ for $\lambda = 0.15$ and $\lambda = 0.5$, respectively.

While these low values of T_c cannot explain the high critical temperatures found in the pnictide HTSCs by a conventional BCS pairing scenario, e-ph coupling might still play an important role in the Cooper pair formation in the Fe pnictides. For instance, a very strong sensitivity of the Fe magnetic moment on the As height in the FeAs tetrahedra was found in DFT band structure calculations [Yin08], with a rate of $6.8\,\mu_\mathrm{B}/\text{Å}$. Inelastic x-ray scattering experiments on $CaFe_2As_2$ concluded on strong coupling of phonons to magnetic excitations even in the high-temperature paramagnetic phase [Hah09]. Furthermore, a strong sensitivity of the maximum critical temperature on the pnictogen height was found [Joh10]. On the basis of these findings a strong magneto-phonon coupling in these compounds was proposed and, e.g. the strongly coupled A_{1g} mode perpendicular to the Fe layers, which modulates the pnictogen height, could mediate superconductivity in the Fe-pnictides [Ega10]. Such a scenario is supported by the strong coupling of this particular mode to electronic states directly at the Fermi level observed in this thesis through the coherent phonon oscillations.

Summary

In summary, we studied the time- and angle-resolved response of the electronic structure of various Fe pnictide compounds to optical excitation. In antiferromagnetic $EuFe_2As_2$ and $BaFe_2As_2$, an asymmetry in the relaxation times of excited electrons and holes inside and outside the hole pocket was found. This striking difference in relaxation behavior, which we were able to separate due to the momentum resolution provided by time- and angle-resolved photoemission spectroscopy (trARPES), is induced by the antiferromagnetic (AFM) order and allows to separate the collective dynamics of the recovery of the AFM phase from single-particle dynamics like electron-phonon (e-ph) scattering. In the AFM phase, the restricted phase space for relaxation of electrons at Γ and a spin-relaxation bottleneck lead to a slow recovery of AFM ordering with $\tau = 800\,\mathrm{fs}$, while e-ph scattering is more than four times faster. The ultrafast initial closing of the spin density wave (SDW) gap found in the analysis of the leading edge midpoint of trARPES spectra suggests that the initial loss of spin order is dominated by purely electronic processes, followed by a structural reorientation on a slower timescale of $\tau \sim 100\,\mathrm{fs}$, which might be related to remnant local Ising nematic order.

Furthermore, we analyzed coherent oscillations in the transient trARPES signal close to the Fermi level. We identified three coherent modes that modulate the transient position of E_F and are present in all investigated compounds independent of temperature. A comparison with calculations and Raman scattering data identifies the strongest mode with the Raman active As A_{1g} phonon mode. The assignment of the other two lower frequency excitations is less obvious and possible candidates are discussed. The relaxation of the coherent oscillations in the time domain and the relative amplitudes of the oscillations indicate stronger e-ph coupling for the A_{1g} mode than for the other two modes. Future studies as a function of doping might provide more insight into the origin of the changes in the chemical potential as well as the material specificity of all observed coherent phonon modes.

The oscillation of the transient chemical potential induced by the coherent phonon modes is investigated using a high-harmonic generation (HHG)-based trARPES setup providing extreme ultraviolet (XUV) radiation, allowing to reach the X-point at the Brillouin zone (BZ) corner. We find an in-phase oscillation of the chemical potential both at Γ and at X, which exhibits a cosine-like oscillation phase, corresponding to an in-phase oscillation of the global Fermi level in the system. The results are discussed on the basis of changes in the electronic density of states.

Three different approaches are compared to determine the e-ph coupling constant λ, which is of importance in the Bardeen-Cooper-Schrieffer (BCS) theory of conventional superconductivity, and their limitations and applicability are discussed. Values determined by all three methods agree and are comparable to literature values. We determine small values for the second moment of the Eliashberg coupling function $\lambda\langle\omega^2\rangle < 100\,\mathrm{meV}^2$, corresponding to $\lambda < 0.15$ for a reasonable choice of $\langle\omega^2\rangle$, and e-ph coupling is found to be even smaller in $BaFe_{1.85}Co_{0.15}As_2$ and $BaFe_2As_2$ than in $EuFe_2As_2$. The small values of λ are discussed to be insufficient to explain the high $T_c = 38\,\mathrm{K}$ found in K doped Ba 122 compounds with a conventional paring scenario based on e-ph coupling.

6 trARPES of superconducting $Bi_2Sr_2CaCu_2O_{8+\delta}$

With the discovery of superconductivity at $T > 30\,\mathrm{K}$ in LaBaCuO in 1986 by Bednorz and Müller [Bed86], a new era of research on superconductors had begun, which rapidly produced very high critical temperatures of up to more than 90 K in $YBa_2Cu_30_{7-\delta}$ by 1987 [Wu87]. However, despite the experimental progress in producing higher critical temperatures with the record of $T_c = 133.5\,\mathrm{K}$ found in $HgBa_2Ca_2Cu_3O_{8+x}$ [Sch93], a microscopic understanding of the phenomenon of high-T_c superconductivity is still missing. Thus, even after more than two decades of intense research and the recent discovery of the pnictide high-T_c superconductors (HTSCs) (see chapter 5), the complete understanding of the phenomenon of high-T_c superconductivity remains one of the most challenging problems of current Solid State Physics. In this context, angle-resolved photoemission spectroscopy (ARPES) has proven to be a very powerful experimental technique, providing information on the single-particle spectral function of these materials with a very high energy and momentum resolution [Dam03]. However, it gives limited information on the coupling of single particle states with collective excitations, which seems to be essential to understand the ground state of the HTSCs [Dam03, Kor06b].

Additional information can be obtained from femtosecond time-resolved optical and THz techniques [Han90, Dem99, Ged04, Kus05, Kai05, Ged05, Kus08, Liu08, Gia09, DC12], which allow studying the quasiparticle (QP) interactions responsible for the relaxation of a photoexcited non-equilibrium state. Applied to the HTSCs, such time-resolved techniques have investigated the microscopic processes that take part in photoexcited QP recombination into Cooper pairs (CPs). In fact, earlier optical works attributed the observed time scales to such QP recombination [Dem99, Ged04, Kus05, Kai05, Kus08, Liu08, Gia09] and pursued efforts to disentangle the electronic and phononic contributions to the superconducting (SC) glue [DC12]. But they have also lead to several controversies [How04, Ged04, Kai05, Ged05, Kab05, Kus08] due to the inherent lack of momentum resolution of these experiments, which only allows relating them to the electronic band structure in an indirect way.

Complementary to ARPES and all optical time-resolved techniques, femtosecond time- and angle-resolved photoemission spectroscopy (trARPES) allows overcoming these limitations as it provides both momentum- and energy-resolved information on the single particle spectral function in combination with its temporal evolution. This facilitates a direct investigation of the QP relaxation along the Fermi surface (FS) just above the superconducting gap. However, first investigations on cuprate superconductors by trARPES only investigated the dynamics along the nodal direction [Per07, Gra11] where the SC gap vanishes and under strong excitation condition, where superconductivity is immediately destroyed ($F \gg 100\,\mu\mathrm{J/cm^2}$) [Per07], and thus could not directly observe the dynamics related to the SC state. Here, we overcome these limitations by investigating regions of the FS with finite SC gaps at very high emission angles and using very weak pump fluences down to $F \sim 6\,\mu\mathrm{J/cm^2}$, which enables to directly monitor the dynamics of the SC condensate density in a weakly perturbed system. In addition, the use of smaller pump fluences allows us to work with a laser repetition rate of 300 KHz without introducing average sample heating[1], which enables the detection of the very

[1] In the experiments by Perfetti *et al.* [Per07], the repetition rate had to be reduced to 30 KHz to

small changes induced by the weak pumping fluences.

In this chapter, we investigate the ultrafast electron dynamics in superconducting $Bi_2Sr_2CaCu_2O_{8+\delta}$ (BSCCO) at different points of its FS, from the nodal towards the antinodal point. First, in chapter 6.2, we discuss the dynamics at weak excitation conditions within the SC state. We find, that the density of non-equilibrium QPs created by photoinduced breaking of CPs is momentum dependent and related to the size of the superconducting gap. In contrast, the observed recombination rate of these QPs exhibits no sign of momentum dependence. In a second part, we discuss the momentum-dependent dynamics in the normal state for $T > T_c$ in chapter 6.3, where we find a pronounced momentum dependence of the relaxation rates. These results are discussed and compared to a fast relaxation component found also in the SC state for higher excitation fluences $F \gtrsim 100\,\mu\mathrm{J/cm^2}$.

Part of the results presented in this chapter have already been published during this thesis in Physical Review Letters [Cor11].

avoid accumulating sample heating between two successive pump pulses.

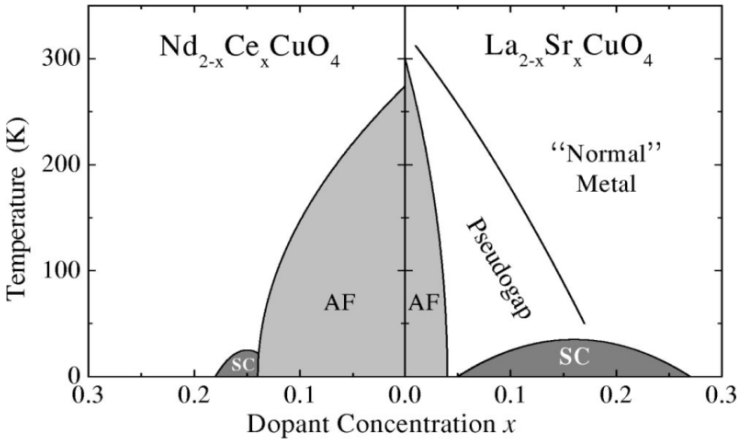

Figure 6.1: Schematic phase diagram of the cuprate HTSCs. The undoped cuprates are antiferromagnetic (AFM) Mott-insulators. After suppression of the AFM phase by either hole (right) or electron (left) doping, superconductivity emerges in the "superconducting dome". The nature of the pseudogap phase is still under debate. After [Dam03].

6.1 The Cuprate high-T_c Superconductors

The parent compounds of the cuprate HTSCs are layered, quasi-two-dimensional (2D) ceramic copper oxides, that are antiferromagnetic (AFM) Mott-Hubbard insulators due to the very strong electron-electron (e-e) correlations (i.e. large Coulomb repulsion U) found in these materials [Dam03]. A prototypical phase diagram of the cuprates for electron and hole doping is depicted in figure 6.1. For both electron and hole doping, the insulating AFM phase is rapidly suppressed and replaced on the hole-doped side by the so-called pseudogap phase. At higher doping levels, superconductivity emerges in the so-called "superconducting dome", with the highest T_c at a hole or electron concentration of $x \sim 0.15$ electrons or holes/Cu. There exist several families of cuprate HTSCs, which differ by their exact chemical composition and within each family, compounds are characterized by the number of CuO layers per unit cell, which are the common building block of all cuprate HTSCs. A selection of the most intensely studied compounds includes e.g. $La_{2-x}Sr_xCuO_4$ (LSCO), $Nd_{2-x}Ce_xCuO_4$ (NCCO), $YBa_2Cu_30_{7-\delta}$ (YBCO) and $Bi_2Sr_2CaCu_2O_{8+\delta}$ (BSCCO). In BSCCO, the compound studied in this thesis, a maximal $T_c \sim 91$ K is reached at a hole concentration per Cu site of $x \sim 0.15$ [Eis04].

BSCCO is the cuprate HTSC most intensely studied with ARPES due to its excellent cleaving behavior and the availability of very large ($\sim 3 \times 3 \times 0.5\,\mathrm{mm}^3$) and homogeneous single crystals. These properties make BSCCO especially suited for ARPES experiments, which revealed a lot of details of its electronic structure, see [Dam03] and references therein. The relatively large tetragonal unit cell of BSCCO ($a = 3.817$ Å, $c = 30.5$ Å, space group $I4/mmm$ [Tar88, Pic89]) is depicted in figure 6.2 (a). The two CuO layers in the center of the unit cell are most important for the electronic structure in the vicinity of the Fermi level. The BiO and SrCaO layers serve as buffer layers, and substitution of atoms in these layers or variation of the oxygen content in the CuO layers can be used for charge doping, which leads to superconductivity (see figure 6.1). The simplified, normal state FS and QP dispersion of overdoped BSCCO is sketched in figure 6.2 (b) (bottom and center). The QP bands close to the Fermi level are derived from Cu $3d_{x^2-y^2}$ and O $2p_x$ and $2p_y$ orbitals and consist of hole-like pockets centered at

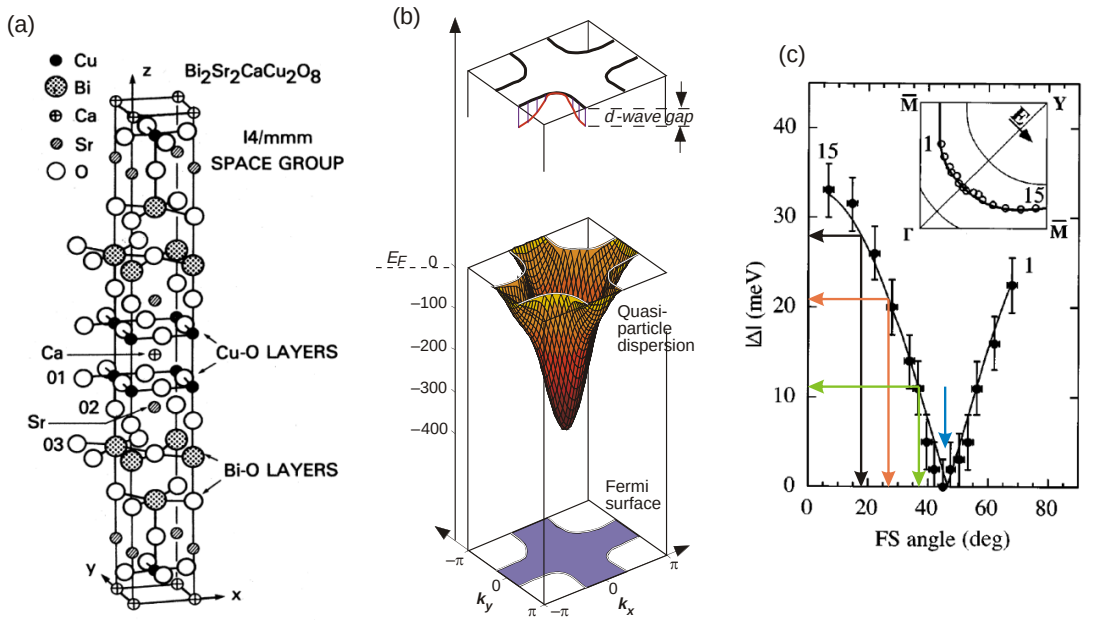

Figure 6.2: (a) Crystal structure of BSCCO. The CuO layers are indicated, which are the common building block of all cuprate HTSCs and host the superconducting condensate [Pic89]. (b) QP dispersion and schematic FS of overdoped BSCCO. The distribution of the *d*-wave gap is indicated at the top [Ron98]. (c) Size of the *d*-wave gap measured in BSCCO as a function of the FS angle [Din96]. The FS angles studied in this thesis are marked by colored arrows.

the Brillouin zone (BZ) corners (π/a,π/a) [Dam03]. As a complication, the large unit cell and superstructures found in BSCCO lead to photoelectron diffraction and weak replica of the main FS found in ARPES, such as *shadow* and *umklapp* bands [Dam03]. Most important modification may be the bilayer splitting of bands into a pair of bonding and antibonding bands due to the two adjacent CuO layers found in BSCCO (see figure 6.2 (a)). However, with the limited momentum and energy resolution in the present investigation, this splitting cannot be resolved and one main FS as sketched in figure 6.2 (b) is observed.

The SC gap in most cuprate HTSCs is now established and commonly accepted to be anisotropic and of $d_{x^2-y^2}$ symmetry [Din96, Dam03, Has11], as sketched in the top of figure 6.2 (b). The consequence of such a pairing symmetry is that the SC gap function exhibits nodes in the momentum space, where the SC gap vanishes. Such nodes are found in BSCCO along the BZ diagonal ((0,0)-(π/a,π/a)), the so-called nodal line. The experimental gap size of optimally doped BSCCO determined by ARPES is shown in figure 6.2 (c) as a function of the FS angle ϕ, defined as

$$\phi = \arctan\left(\frac{\pi/a - k_x}{\pi/a - k_y}\right) \quad ,$$

see also figure 6.3 (a). The gap vanishes at $\phi = 45°$, the nodal line, and is at a maximum at $\phi = 0°$, the antinodal region. FS angles and corresponding gap sizes investigated in this thesis are marked with colored arrows.

The nature of the pseudogap phase, which is found in underdoped and optimally doped cuprates for $T_c < T < T^*$ is still under debate. It has been discussed as either

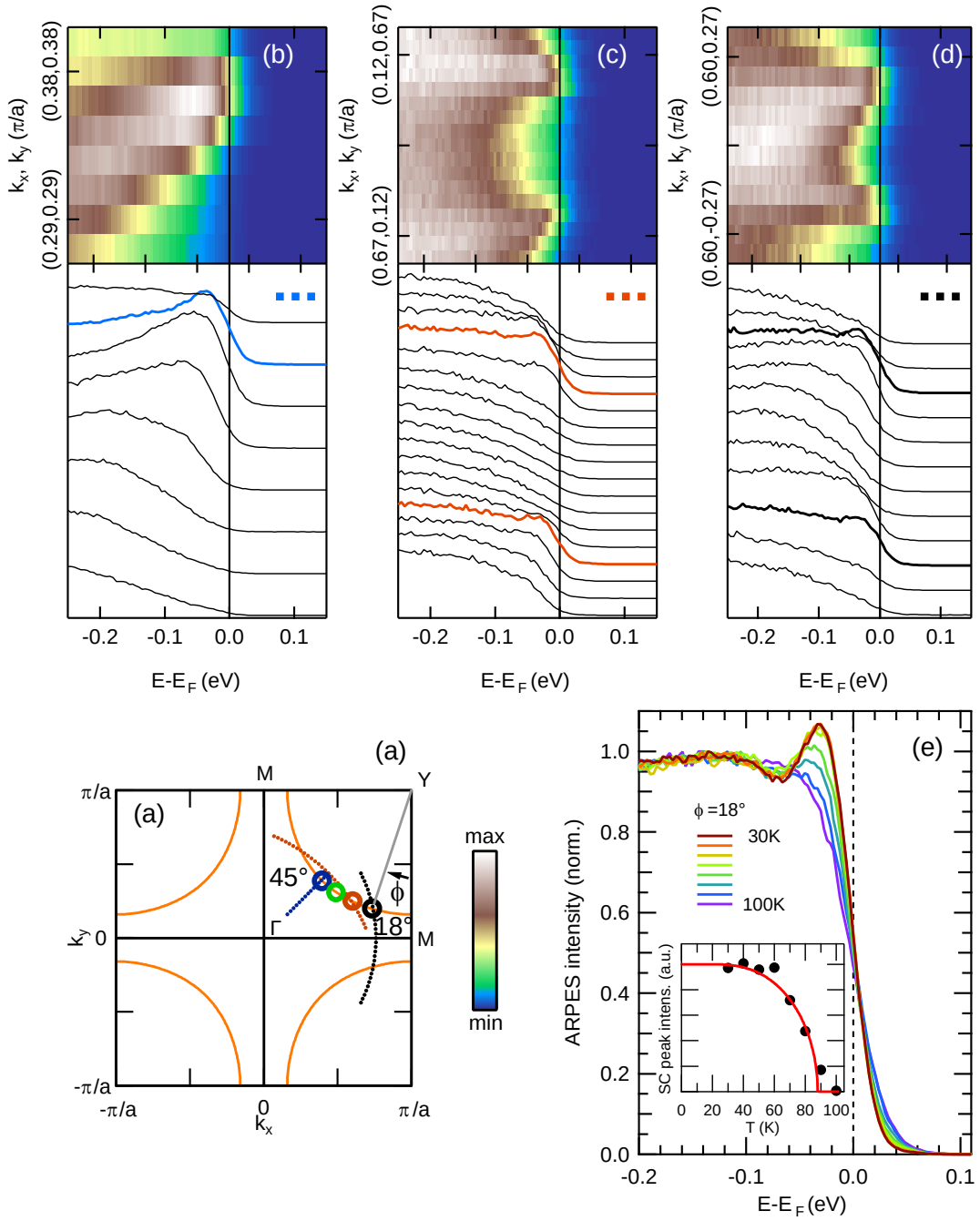

Figure 6.3: (a) Sketch of the normal state FS of BSCCO. Circles mark the FS angles, $\phi = 18°, 27°, 37°$ and $45°$, considered in this work. Some of the arcs cutting the FS along which the ARPES spectra were taken are also shown. (b) ARPES spectra and their representation as a false color plot, measured along the nodal line ($\phi = 45°$, blue cut in (a)). The spectrum at the FS is highlighted with a thick blue line. (c) ARPES spectra along the red arc in (a), cutting the FS at $\phi = 27°$ and $\phi = 63°$. (d) ARPES spectral along the black arc in (a), reaching $\phi = 18°$ close to the antinodal point. (c) Normalized ARPES spectra measured at $\phi = 18°$ for various temperatures. The inset shows the integrated intensity of the SC peak as a function of temperature, which nicely fits the temperature dependence of the SC gap in the BCS theory (solid line).

a precursor of superconductivity with preformed CPs, but without macroscopic phase coherence of the SC condensate [Tim99] or as a different ground state order parameter, competing with superconductivity [Tim99, Sto08]. In ARPES data, the pseudogap manifests as additional energy gaps at the Fermi level that persist above T_c and show a similar k-dependence as the SC gap [Dam03, Sto08]. It is also reported that the pseudogap phase extends into the slightly overdoped region [Tim99, Dam03, Sto08].

The BSCCO samples studied in this work were nearly optimally doped single crystals with a transition temperature $T_c = 88\,\mathrm{K}$. With the work function of BSCCO of $\Phi \approx 4.1\,\mathrm{eV}$ and the low photon energy of 6.0 eV of the probe pulses, it is challenging to reach the FS towards the antinodal region where the SC gap opens, as very large emission angles are necessary to reach these momenta. By means of a slanted sample holder (see chapter 3.1.4) it was possible to reach points along the FS corresponding to FS angles between $\phi = 45°$ (nodal line) and $\phi = 18°$ (close to the antinodal point), using different cuts through the reciprocal space as shown in figure 6.3 (a). The corresponding laser ARPES data for three exemplary k-space cuts are shown in panel (b-d), cutting the normal state FS at $\phi = 45°$ ((b), blue cut), $\phi = 27°$ ((c), red cut) and $\phi = 18°$ ((d), black cut). The nodal spectra (panel (b)) show the sharp dispersion of nodal QPs, consistent with earlier results [Per07, Gra11]. In the spectra measured off the nodal line, a sharp peak is observed at the FS, which is known to be a direct consequence of the superconducting state [Nor98, Fen00, Din01, Dam03]. The temperature dependence of this coherent SC peak is shown for $\phi = 18°$ in figure 6.3 (e). The spectral weight of this SC peak depicted in the inset as a function of temperature is found to closely follow the temperature dependence of the SC gap in the BCS theory (see chapter 2.2.1) and disappears above T_c, corroborating its relation with superconductivity. Although we do not see a clear indication of a SC gap in the leading edge of the spectra, this coherent SC peak can serve as an unambiguous marker for the SC state and its spectral weight is proportional to the SC gap. The absence of a clear shift of the leading edge of the spectra in the investigated temperature range could be due to the effect of the pseudogap phase, which is known to induce a gap in the leading edge near the antinode in optimally doped BSCCO even above T_c [Nor05][2].

[2]The detection of a SC gap in the spectra using laser ARPES and a time-of-flight (TOF) spectrometer is hindered due to the ambiguity in the absolute energy reference. Using hemispherical analyzers, the energy position of the Fermi level is usually obtained from polycrystalline noble metal reference samples. In a TOF spectrometer, the energy reference depends on the distance of the illuminated sample spot to the spectrometer entrance, which is difficult to maintain constant between the superconductor and a reference sample, especially using emission angles $> 60°$. Thus, the energy reference for each measurement series is obtained experimentally from individual spectra by considering the Fermi cutoff, which, however, defies the detection of absolute gaps. In addition, small changes of the photon energy on a day-to-day basis and space charge effects [Gra10a] complicate such an analysis.

6.2 Momentum-dependent Dynamics of the superconducting State

The excitation of the sample by the 1.5 eV pump pulse produces a depletion of the SC peak, as well as an increase of the spectral weight above the Fermi level E_F (figure 6.4 (a) and (b)) which persist for several picoseconds and which are different than the ones produced by a mere increase of the temperature, which becomes apparent when comparing figure 6.3 (c) and figure 6.4 (b). Especially, the position of the Fermi cutoff is shifted upon photoexcitation, compatible with the closing of an SC gap, whereas we did not observe such a shift upon increase of the temperature. This indicates the absence of a pseudogap in the transient state found after photoexcitation. We find that both quantities have the same evolution with the pump-probe delay, as shown in figure 6.4 (c). This shows that the increase of the spectral weight at $E > E_F$ corresponds to the creation of a non-equilibrium density of QPs by breaking CPs and the decrease of that spectral weight can be attributed to the recombination of these QPs. Thus, our observations demonstrate that the time-dependent spectral weight above E_F directly reflects the dynamics of the recovery of the superconducting condensate after photoexcitation. This result provides experimental justification for the description of the dynamics of the superconducting state in terms of the photoinduced QP density assumed in fs time-resolved optical and THz works [Ged04, Kab05, Kai05, Kus08, Gia09]. We proceed now by a momentum-dependent analysis of the evolution of that spectral weight at $E > E_F$.

trARPES spectra were measured at four points of the FS (see figure 6.3 (a)), for four different pump fluences, (see figure 6.5 (b)). Next, the normalized trARPES intensity change with respect to the intensity before the arrival of the pump pulse, $\Delta I(t)/I$, was determined for $E > E_F$, as shown in figure 6.5. Here, the intensity above E_F before the arrival of the pump pulse is mainly due to the finite energy resolution of ~ 50 meV, which is larger than the thermal broadening at $T = 30$ K and the size of the superconducting gap at any ϕ (see figure 6.2 (c)). The decay of $\Delta I(t)/I$ in the measurements with $F \leq 32\ \mu\mathrm{J/cm^2}$ was fitted to a single-component exponential decay function,

$$\Delta I(t)/I = A \exp(-t/\tau) + B \quad ,$$

convoluted with a 100 fs width Gaussian accounting for the temporal resolution. Here, A is the excitation amplitude, τ is the relaxation time of the non-equilibrium QPs and B accounts for heat diffusion effects [Sch87]. Exemplary fits are shown in figure 6.5 for different FS angles (a) and fluences at fixed FS angle (b). For larger $F \gtrsim 100\ \mu\mathrm{J/cm^2}$, an additional decay component with smaller τ is observed in $\Delta I(t)/I$ as seen in the inset of figure 6.5 (b). We fit these data by a biexponential decay, accounting for the slow and fast components τ_{slow} and τ_{fast}, respectively.

First we focus on the slower contribution τ_{slow} and its momentum dependence. Figure 6.6 shows the momentum-dependent amplitudes A and decay times τ obtained by fitting $\Delta I(t)/I$. All the fluences considered here show (within error bars) a constant $\tau \sim 2.5$ ps, see panel (a), and a pronounced decrease in A with increasing ϕ, panel (b)[3]. Albeit the error bars of τ increase for larger ϕ due to the simultaneous reduction in A, we can exclude that a similarly strong variation as in A occurs for τ. We rather find that τ depends only very weakly or is even independent on the FS angle. In particular the data for $F = 32\ \mu\mathrm{J/cm^2}$ support this conclusion.

[3]The incident pump fluence was kept constant, which lead in the angle-dependent studies to a variation of the absorbed fluence F due to changes in the reflectivity and the effective pump polarization, see chapter 3.1.2. To compensate for this effect, the amplitudes were were corrected accordingly by linear interpolation to the same F at all FS angles.

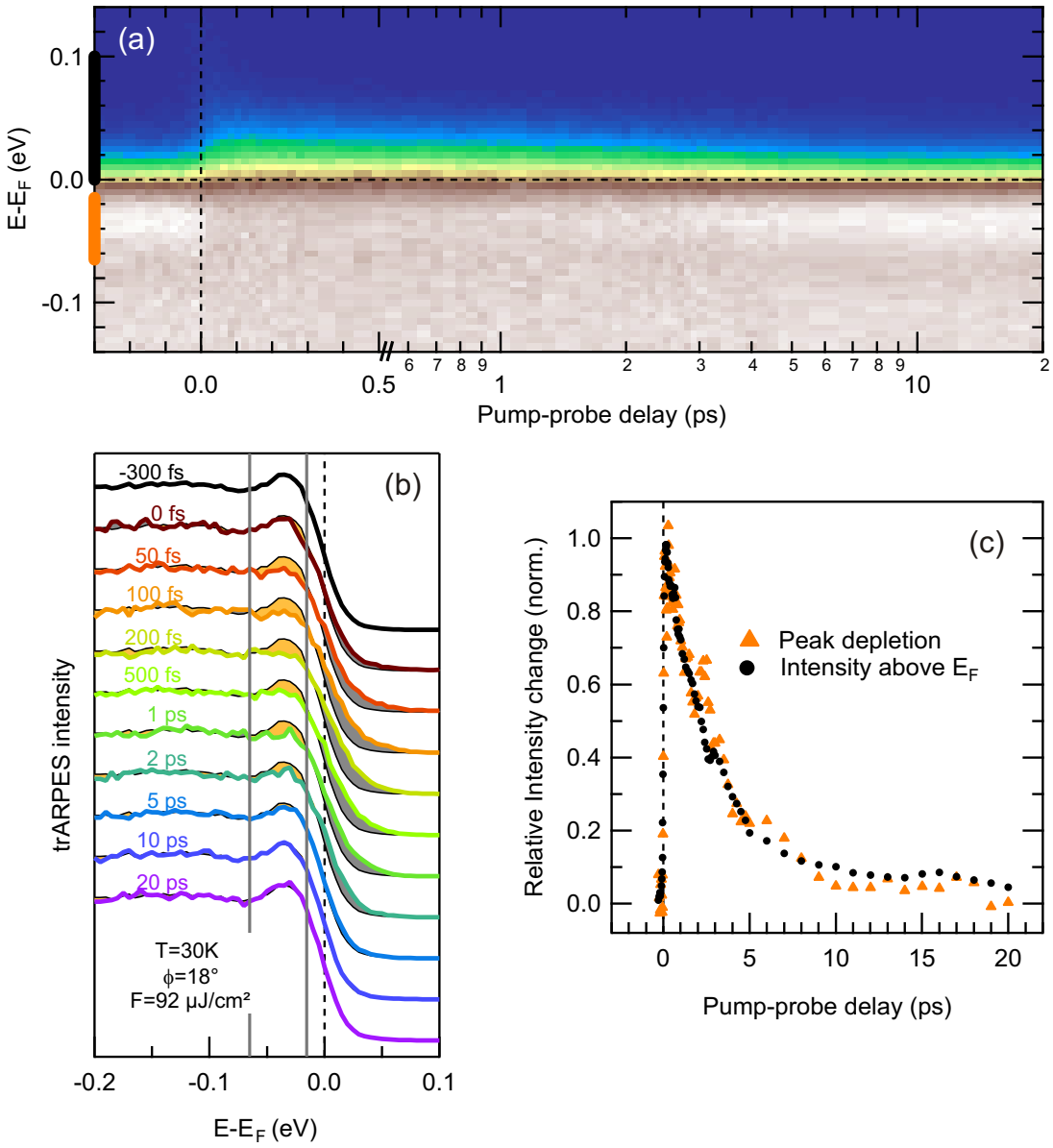

Figure 6.4: Time-dependent trARPES spectra of BSCCO near the antinodal point. (a) trARPES intensity at $\phi = 18°$ as a function of energy and pump-probe delay. After t_0, the SC peak (orange marker) disappears and an increase of intensity is found for $E > E_F$ (black marker), which relaxes within several picoseconds. (b) trARPES spectra from (a), at various pump-probe delays. The depletion of the SC peak and the increase of spectral weight above the Fermi level, in relation to the spectrum measured before optical excitation, are shaded in yellow and gray, respectively. (c) Depletion of the SC peak (yellow area between the vertical gray lines in (b)) and increase of the intensity above E_F (gray area in (b)) as a function of the pump-probe delay.

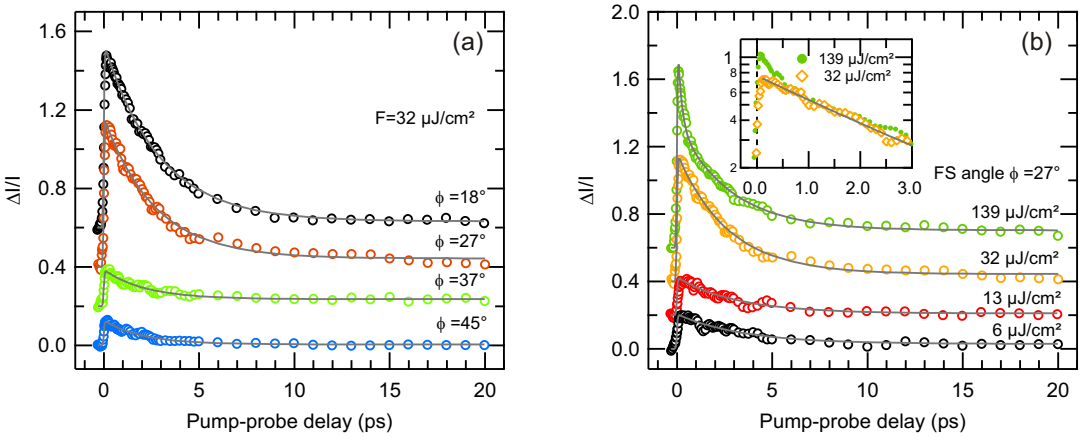

Figure 6.5: Relative trARPES intensity change above E_F, $\Delta I(t)/I$, measured at different FS angles ϕ, using a pump fluence $F = 32$ μJ/cm^2 (a) and measured at $\phi = 27°$, using different pump fluences (b). A zoom of the spectra measured at $\phi = 27°$ with $F = 139$ μJ/cm^2 and $F = 32$ μJ/cm^2, using a logarithmic vertical scale, is shown as an inset in (b). Exponential fits to the data (see text) are shown as thin gray lines. In the inset, only the fitting of the spectrum measured at 32 μJ/cm^2 to a single-component exponential decay function for $t > 100$ fs is shown. To fit the data at 139 μJ/cm^2 an additional component is needed.

Here, A represents the density of photoexcited quasiparticles, which shows a momentum dependence strikingly similar to the gap function of a d-wave superconductor (see figure 6.2 (c)). This suggests that the photoexcitation process promotes a fraction of CPs (their density is proportional to the SC gap size and decreases for larger ϕ towards the node) by CP breaking to unoccupied QP states just above the SC gap, maintaining the initial momentum. In more detail, QPs are initially excited to energies up to the order of the pump photon energy and then relax within the first few hundred femtoseconds [Nes98] by inelastic scattering processes, exciting new QPs to states just above the gap. In the following we discuss the decay processes of this low energy photoexcited state. Looking at our data we find that the amplitudes A are larger far off the node, while the decay is simply described for all momenta by a single exponential decay exhibiting constant τ. Therefore, we find no indication of preferential scattering between different points of the FS. Intuitively, one might think that QPs just above the gap in the antinodal region could gain energy through e-e scattering toward the node, where the SC gap is small and hence their energy would be reduced (process (1) sketched in figure 6.6 (c)). However, this would result in an accumulation of excited QPs at the node, which is not observed, implying that this relaxation channel is blocked. The reason might be the lack of the scattering partners required by momentum and energy conservation, due to the presence of the d-wave superconducting gap, see figure 6.6 (c). As a consequence, QPs off the node become transiently stabilized, in agreement with the conclusions of theoretical investigations by Howell *et al.* [How04] and Gedik *et al.* [Ged04], which were up to now difficult to prove experimentally.

Having excluded scattering towards the node as an active relaxation channel for the QP population above the gap, we focus now on the observed momentum-independent decay time of $\tau \sim 2.5$ ps (figure 6.6 (a)). This value compares well to reports of earlier optical investigations of BSCCO [Dem99, Kai05, Liu08, Gia09]. We recall that on this very same time scale the recovery of the SC peak was observed (figure 6.4) and thus

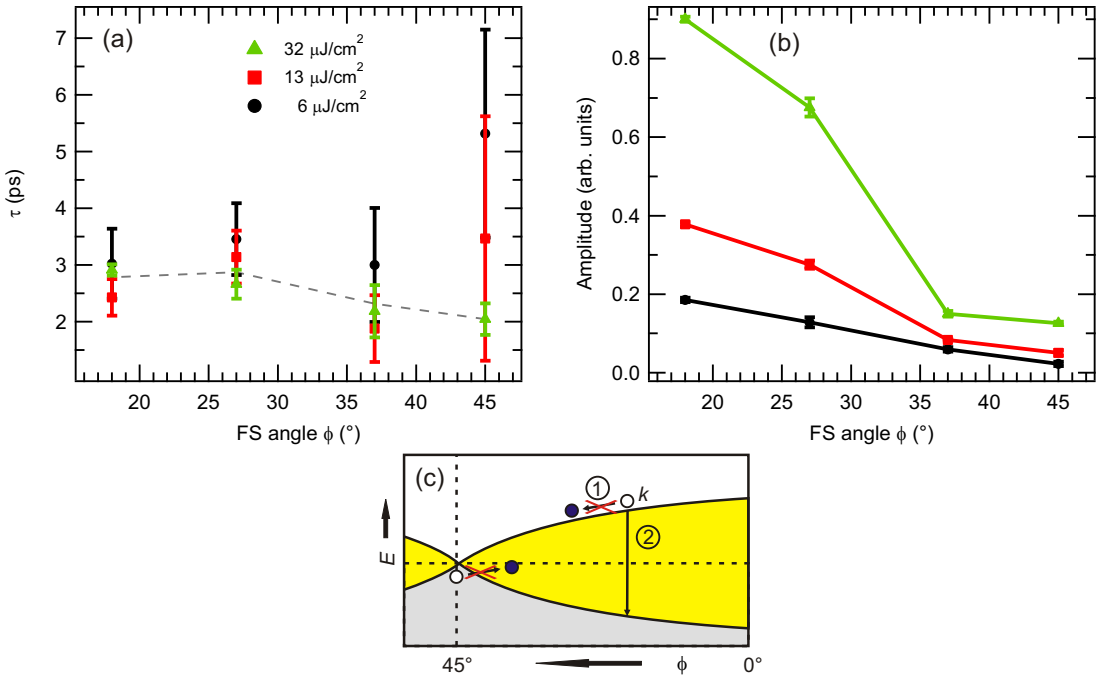

Figure 6.6: Relaxation time τ (a) and excitation amplitude A (b), obtained from the fitting to exponential decay functions (see text), as a function of the FS angle, ϕ. Lines are guides to the eye. (c) Sketch of potential decay processes of photoexcited quasiparticles discussed in the text.

we can safely identify the decay of the QPs with recombination into CPs (process (2) in figure 6.6 (c)). This requires coupling of a QP with momentum $\hbar\vec{k}$ with one at $-\hbar\vec{k}$ and a boson with twice the gap energy. Still, the momentum independence of the decay times is intriguing. The increase in the gap function for smaller ϕ should favor higher energy gain near the antinode, increasing the decay rate. Also the momentum-dependence in the spin-fluctuation-mediated pairing interaction [Dah09] and in electron-phonon (e-ph) coupling [Boh03] suggests a variation of τ with ϕ. However, in a d-wave superconductor, the interaction of k-dependent QP recombination, CP breaking by the bosons emitted during the recombination, and the relaxation rate of those bosons might result in a compensating effect, leading to the observed momentum independence of τ. This scenario might be the one of the so called boson bottleneck regime, which appears in the context of the phenomenological Rothwarf-Taylor equations (RTE) [Rot67] (see chapter 2.2.3).

The RTE are widely used to analyze QP recombination in fs time-resolved optical and THz studies [Kab05, Kai05, Ged04, Gia09, Kus08]. At low T where the photoexcited QP density, n^*, is considerably larger than the thermal one, n_T, i.e. $n^* \gg n_T$, the relaxation of the low energy photoexcited QPs is governed by the probability to find a recombination partner leading to a recombination rate with a quadratic dependence on the QP density (second-order kinetics) [Kai05, Kab05]. At higher $T < T_c$, in the boson bottleneck regime, an exponential decay is predicted and experimentally observed [Dem99, Kus05, Liu08]. It arises from the competition between QP recombination emitting a boson with twice the gap energy and CP breaking by that boson. In this regime, the relaxation is determined by the decay rate of these bosons and thus it is independent of the excitation density. Alternatively, the exponential decay observed at higher T, where $n_T > n^*$, has

also been explained by means of the RTE not as due to a boson bottleneck but due to the recombination of the photoexcited QPs with the thermal ones into CPs [Kai05]. The decay that we find at $T = 30\,\mathrm{K}$ is well described by a single exponential function exhibiting momentum and pump fluence-independent decay times. However, it cannot be explained considering only recombination with thermal QPs. CP pair formation requires the two QPs involved in the process to have opposite momenta and, as most of the thermally excited QPs are in the nodal region, this would imply that the photoexcited QPs scatter toward the node before they recombine with the thermal ones, contrary to our observation. Therefore only the existence of a boson bottleneck can explain all our results and we can conclude that optimally doped BSCCO is in the strong bottleneck regime. This challenges the conclusion of previous optical studies [Kai05, Ged05] about the absence of a bottleneck, based on the observation of a second-order kinetics. However, such a dynamics can also be found in a strong bottleneck regime, as pointed out by an analytic solution of the RTE [Kab05].

Although a compensating effect in the boson bottleneck regime might explain the observed momentum-independent decay times, this regime is a specific case of the RTE. The RTE are the most suitable theoretical framework currently available to discuss these trARPES results, but they do not take into account momentum degrees of freedom, which are very relevant in this case. Therefore, the development of a more sophisticated theoretical description beyond the RTE, taking the symmetry of the order parameter into account, would be necessary.

6.3 Normal State Dynamics

Now, we will come back to the second and faster component τ_{fast} observed in the decay of $\Delta I(t)/I$ for $F \gtrsim 100\,\mu\text{J/cm}^2$. The relaxation constants τ_{fast} of this faster component at early times are shown in figure 6.7 (b) as blue diamonds as a function of FS angle ϕ. In the data of $\phi = 18°$, we did not observe such a fast component; however, here the highest fluence was $F = 92\,\mu\text{J/cm}^2$. The appearance of a second, faster relaxation component above a certain excitation threshold was also observed recently with transient reflectivity in underdoped and optimally doped LSCO [Kus08] and also in underdoped BSCCO [Gia09], exhibiting a relaxation time similar to the timescale found above T_c, which was attributed to the transient evaporation of the SC condensate and a transition to the normal state after photoexcitation [Kus08, Gia09]. Indeed, we also find a saturation behavior of the amplitudes of the slow component for higher fluences, which is compatible with such a scenario (see the inset of figure 6.5 (b)). Interestingly, we find a clear increase of the relaxation time of this faster component for FS angles off the node.

In order to understand this momentum-dependent relaxation constants of the fast component, the transient QP dynamics in the normal state at $T = 100\,\text{K} > T_c$ is investigated. Figure 6.7 (a) compares the transient $\Delta I(t)/I$ at $T = 30\,\text{K}$ and $T = 100\,\text{K}$ for $\phi = 45°$ and $\phi = 18°$. For both FS angles, we find a much faster relaxation behavior at $T = 100\,\text{K}$ than in the SC state. While the excitation amplitude at the node is similar in the SC and normal state, near the antinode the amplitude is more than twice as large in the SC state. Relaxation times and amplitudes at $T = 100\,\text{K}$ are shown in figure 6.7 (b) and (c), respectively, for two different fluences as a function of the FS angle[4]. We find, similar to the SC phase, an increase of A towards the antinode, which shows for all FS angles a linear fluence dependence. The fluence-independent decay times, however, show a strong increase from $\tau \sim 300\,\text{fs}$ at the nodal line to $\tau \sim 800\,\text{fs}$ near the antinode, in contrast to the FS angle-independent decay times found in the SC state. This is very similar to the increase of the fast relaxation τ_{fast} found in the SC state, indicating that the same relaxation channel might be responsible in both cases.

We will now discuss this FS angle-dependent QP relaxation found for $T > T_c$ and in the fast relaxation in the SC state. At the first glance, this behavior is very surprising, as in the normal, metallic state the QP relaxation is governed by e-ph relaxation [Bro90, Per07], which is usually assumed to be momentum independent. However, theoretical investigations reported a momentum dependence of e-ph coupling in cuprate HTSCs [Boh03]. Assuming such a momentum-dependent e-ph coupling constant, the slower relaxation found for smaller ϕ indicates a decrease of the e-ph coupling strength towards the antinode. However, the momentum-dependent increase in the excitation amplitude is still difficult to explain by assuming a momentum-dependent e-ph coupling constant.

An alternative explanation for the momentum-dependent relaxation times and amplitudes would be the relaxation of QPs across the pseudogap near the antinode. Indeed, similar relaxation times found in optical reflectivity experiments for $T > T_c$ have been interpreted as carrier recombination across the pseudogap [Kab99, Dem99, Dvo02, Kus05, Kus08, Liu08]. Furthermore, a shift in the leading edge of trARPES spectra is also found in the normal state for $\phi = 18°$, compatible with the closing of a pseudogap. Such a scenario would explain the increasing excitation amplitude, as similar to the SC gap, the size of the pseudogap increases towards the antinode [Nor05]. Here, the slower relaxation towards the antinode might be explained by a relaxation bottleneck due to the presence

[4]For $\phi = 27°$ no reliable data are available.

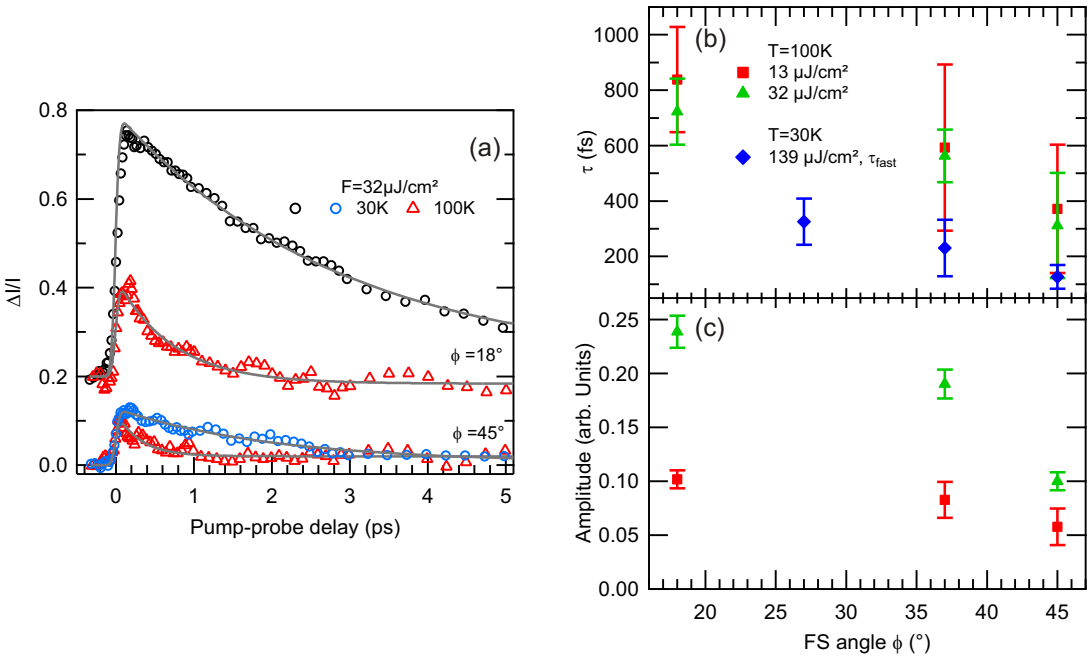

Figure 6.7: Momentum-dependent relaxation in the normal state. (a) Relative trARPES intensity $\Delta I(t)/I$ for $F = 32\,\mu\mathrm{J/cm^2}$ and for $T = 30\,\mathrm{K}$ (circles) and $T = 100\,\mathrm{K} > T_c$ (triangles) as a function of pump-probe delay. Shown FS angles $\phi = 45°$ and $\phi = 18°$ are indicated. Lines are exponential fits (see text). Panel (b) and (c) show the relaxation times and the excitation amplitudes, respectively, for $T = 100\,\mathrm{K}$ for $F = 32\,\mu\mathrm{J/cm^2}$ (green triangles) and $F = 13\,\mu\mathrm{J/cm^2}$ (red squares) as a function of FS angle ϕ[4]. Blue diamonds represent the fast relaxation constant τ_{fast} found in the SC state at $F \gtrsim 100\,\mu\mathrm{J/cm^2}$.

of the pseudogap for smaller ϕ.

To further investigate this momentum-dependent relaxation and to determine the influence of the pseudogap, experiments on the evolution of relaxation times with temperature and/or pump fluence would be necessary. In addition, studies in overdoped samples without a pseudogap phase could provide further input. In this way, the momentum-dependence of e-ph coupling in the normal state could be studied along the FS using trARPES [Per07, Gad10] without the complication of a pseudogap.

Summary

In summary, we presented in this chapter the analysis of the momentum dependence of the transient population and decay times of photoexcited quasiparticles (QPs) in the cuprate high-T_c superconductor $Bi_2Sr_2CaCu_2O_{8+\delta}$ (BSCCO) below and above T_c. In the superconducting (SC) state, we demonstrate the direct observation of the ultrafast depletion of the superconducting (SC) condensate after optical excitation through the disappearance of the SC peak near the antinodal point. The momentum dependence of the transient QP distribution demonstrates a transient stabilization of the photoexcited QPs near the antinode, which is explained by blocking of electron-electron (e-e) scattering away from the node due to the SC d-wave gap. The decay of these QPs is dominated by recombination into Cooper pairs (CPs) and, in the low fluence limit, is well described by a single exponential function with momentum- and pump fluence-independent decay time. A discussion in terms of the phenomenological Rothwarf-Taylor equations allows to conclude that BSCCO is in the boson bottleneck regime, where the QP recombination is governed by the decay of gap-energy bosons. The relaxation times found in the normal state for $T > T_c$ are found to depend on the Fermi surface (FS) angle and increase towards the antinode, similar to the fast relaxation component observed for high fluences in the SC state. These momentum-dependent relaxation constants are discussed in terms of momentum-dependent electron-phonon (e-ph) coupling and the influence of the pseudogap phase.

A more quantitative analysis of the transient evolution of the SC state could be enabled by analysis of the spectral shape of the coherent SC peak [Nor98, Fen00, Din01, Dam03] and the shift of the leading edge [Din96, Dam03] by fitting of transient time- and angle-resolved photoemission spectroscopy (trARPES) spectra with a model function. As such an analysis is complicated through to the limited energy resolution of the trARPES data, which was always larger than the SC gap, attempts to fit the data with corresponding models gave no reliable results and thus, such an analysis remains out of the scope of the current investigation. However, a recent analysis of resolution effects on the determination of SC gap size [Evt09] indicate that such an analysis should be possible despite the low resolution. In addition, further experiments with a better energy resolution compromising temporal resolution [Gra11, Sob12] could simplify a model description of transient trARPES spectra. A question which could be answered from such an analysis would be the appropriate description of the non-equilibrium SC state. Here, traditionally two limiting cases have been discussed in the literature, the T^* and the μ^* model [Owe72, Par75, Nic03, Gia09], which describe the excited superconductor by a transient temperature T^* and chemical potential μ^*, respectively. The transient trARPES spectra, enabling the direct observation of the transient electron distribution should in principle be able to separate between these two models.

7 trARPES of the CDW Material RTe_3

The emerging microscopic cooperative effects in low-dimensional materials represent a fascinating topic of condensed matter research. Self-coordination and collectivity can lead to instabilities of the underlying coupled degrees of freedom like e.g. the electronic and lattice excitations, which can have macroscopic impacts on the material properties like phase transitions. The low-temperature broken-symmetry phases such as e.g. superconducting, charge density wave (CDW) or magnetically ordered states present fascinating emergent properties that are of both fundamental and technological interest. As a model system of emergent order, the formation of the CDW ground state found in many materials of reduced dimensionality is one of the well-established and intensely studied examples that are at the heart of our understanding of quantum many-body physics [Grü94] . Among such systems, RTe_3 (R = rare-earth element) has been identified to be a quasi-one-dimensional (1D) model system, well suited to study the Fermi surface (FS) nesting driven CDW formation [DiM95, Gwe98, Bro04, Mal05, Kim06, Ru06, Fan07, Bro08, Ru08, Moo10], which allows even to study the effect of two perpendicular CDW distortions. The electronic structure and FS of RTe_3, which has been intensely studied via angle-resolved photoemission spectroscopy (ARPES), is modified by large energy gaps of several 100 meV in the CDW phase [Gwe98, Bro04, Bro08, Moo10], making RTe_3 an ideal candidate to study the dynamics intrinsically linked to the CDW state using time- and angle-resolved photoemission spectroscopy (trARPES).

Starting point for the experiments on RTe_3 reported in this thesis were our first experiments using trARPES on $TbTe_3$ in 2007, which are discussed in detail in previous publications [Sch08a, Sch11a] and thesis work [Kir08a, Sch11b]. In these experiments, we observed the ultrafast transition of $TbTe_3$ into a transient metallic state after strong optical perturbation, which was based on the analysis of the transient dispersion of the gapped CDW band close to E_F. In addition, a coherent oscillation of $f \sim 2.5$ THz found in the CDW band was attributed to the coherent excitation of the CDW amplitude mode oscillation based on its exclusive occurrence close to k_F and in the gapped region of the Brillouin zone (BZ) in the CDW phase. The goals of the experiments conducted during this thesis were (i) to investigate the closing of the CDW gap in more detail and as a function of position on the FS, (ii) to further investigate the influence of the amplitude mode oscillation on the gapped CDW band structure and (iii) to investigate the temperature dependence of the amplitude mode oscillations. In addition, the excellent crystal quality and cleanliness of ARPES data achievable with RTe_3 made it an ideal test case for our recently developed position-sensitive time-of-flight (pTOF) spectrometer [Kir08b, Kir08a], which allows to observe the transient trARPES intensity simultaneously within a contiguous area of the reciprocal space and thus to monitor the transformation of the gapped FS into a transient, ungapped metallic band. These experiments were conducted as part of a vivid collaboration with the research groups of Prof. Z.-X. Shen and Prof. I. R. Fisher at the Stanford University, where also the static laser-based ARPES data of $HoTe_3$ were obtained.

In this chapter, we investigate various aspects of the model system for CDW formation RTe_3 in three compounds of the series, namely $HoTe_3$, $DyTe_3$ and $TbTe_3$. First, we summarize the material properties and the basic electronic structure derived from a Tight-Binding (TB) model in chapter 7.1, which is compared to high-resolution laser ARPES data of the occupied band structure of $HoTe_3$ in chapter 7.2. We observe the

successive occurrence of two perpendicular CDW transitions and discuss agreement and deviations of ARPES data from the TB model calculations. In chapter 7.3, we present the spectroscopy of the unoccupied band structure using trARPES employing the pTOF spectrometer and discuss the distribution of the CDW gap along the FS, as seen from ARPES and trARPES. Chapter 7.4 discusses the transient dynamics of the FS and the CDW gap after strong optical excitation in $DyTe_3$. We present the first time-resolved FS mapping and determine the transient gap size for various fluences along the FS. An asymmetry in the closing of the gap, depending on the relative position of the gap with respect to the Fermi level is discussed. Finally, in chapter 7.5 we investigate the coherent oscillations of the amplitude mode observed at low excitation fluences and determine its influence on the transient CDW gap. The temperature dependence of the amplitude mode oscillations in the three compounds is compared to literature and the coherent control and selective excitation of the involved frequencies is demonstrated.

7.1 The Family of Rare-Earth Tritellurides

The family of rare-earth tritellurides RTe_3 (R being a member of the lanthanide family) presents an excellent low-dimensional model system to study the effect of FS nesting-driven CDW formation. The rare-earth tritellurides exhibit a layered and weakly orthorhombic crystal structure, with the underlying space group $Cmcm$. The unit cell, depicted in figure 7.2 (a) consists of a pair of square-planar Te layers, which form a quasi two-dimensional (2D) square net in the plane of the a/c-axis ($a \approx c \approx 4.3 - 4.5$ Å). They are stacked with buckled RTe slabs along the longer b-axis ($b \approx 26$ Å), which is in the usual convention of the $Cmcm$ space group oriented perpendicular to the Te planes. The rare-earth tritellurides and their CDW formation have been intensely studied using e.g. structural [DiM95, Kim06, Ru08], optical [Sac06, Sac07] and transport methods [Ru08]. Due to the very high quality of available single crystals and their good cleaving behavior, RTe_3 is especially suited for ARPES studies [Gwe98, Kom04, Bro04, Bro08, Moo10], which has revealed a great deal of information about the electronic structure and CDW formation in RTe_3. In particular, the strong modifications of the electronic bands close to the Fermi level induced by the CDW transition, opening large energy gaps of several 100 meV, render RTe_3 an excellent model system for the study of FS nesting driven CDW formation.

Another advantage of the system is the tunability of the CDW properties by choosing different members of the lanthanide series, as depicted in figure 7.1. As the lanthanide atoms do not significantly contribute to the electronic structure near the Fermi level [Bro08], their influence is mostly due to exertion of chemical pressure (the incorporation of larger or smaller ions into the lattice, expanding or contracting the crystal) on the lattice [DiM95, Ru08]. By moving through the series from La towards Yb, the increasing occupation of the $4f$ orbitals leads to a decrease of the ion radii and in turn to a decrease of the chemical pressure and the in-plane lattice parameter, as depicted in figure 7.1 (a). Tuning the chemical pressure through substitution of various lanthanide atoms directly influences the CDW transition temperature T_{c1}, where a large chemical pressure and lattice constant increases the onset of unidirectional CDW ordering in the light members of the series [Ru08]. To visualize this relation, the CDW transition temperatures for various RTe_3 are shown as a function of in-plane lattice constant in figure 7.1 (b). For the heavier members of the series starting at $DyTe_3$, a second, perpendicular CDW transition is observed at a lower transition temperature T_{c2}, which increases as T_{c1} decreases, accompanied by a decrease of orthorhombicity [Ru08, Moo10]. In addition, the CDW energy gap as measured by ARPES increases with increasing chemical pressure and CDW transition temperature, as evidenced by the dependence of the CDW gap size from lattice constant shown in figure 7.1 (c). In this thesis, we investigate the compounds $TbTe_3$ with $T_{c1} \approx 335$ K, $DyTe_3$ with $T_{c1} \approx 305$ K and $T_{c2} \approx 50$ K and $HoTe_3$ with $T_{c1} \approx 285$ K and $T_{c2} \approx 125$ K which allows to analyze the effect of the onset of the second CDW on the dynamics of the CDW transition.

The two building blocks of the particular structure of RTe_3 determine two different unit cells as depicted in figure 7.2 (a) and (b). The larger 3D unit cell (green) is defined by the R atoms of the RTe slab, while the square net of the Te layers define a smaller 2D unit cell (purple) that is rotated by 45° with respect to the 3D unit cell. The electronic band structure close to the Fermi level in RTe_3 is mostly determined by the square Te layers, giving rise to a highly anisotropic band structure. An ab-initio band structure calculation using the linear muffin-tin orbital (LMTO) method [Lav05, Bro08] revealed that from the 18 bands that are found in the calculation only 4 bands cross the Fermi level. These strongly dispersing bands, which are derived from the Te-$5p$ orbitals that lie

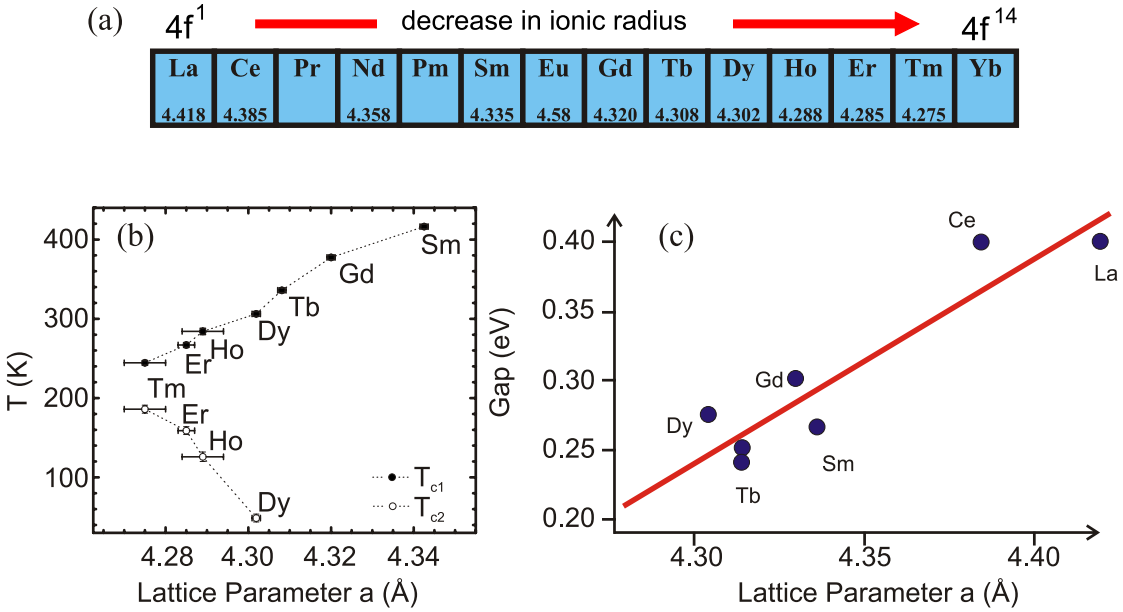

Figure 7.1: Family of rare-earth tritellurides: (a) Lattice constants of RTe_3 for the series of lanthanide atoms R. With increasing occupation of the $4f$ orbitals, the ionic radius and the lattice constant decrease. (b) CDW transition temperatures as a function of lattice parameter for selected RTe_3 [Ru08]. The heavier compounds exhibit two successive CDW transitions at T_{c1} and T_{c2}. (c) CDW gap size measured by ARPES for various RTe_3, showing a larger gap for the lighter R atoms [Bro08].

in the Te plane, are well approximated by a simplified TB model that only considers an isolated Te plane in the 2D unit cell, as sketched in figure 7.2 (b). The system is modeled by two linear chains of Te-$5p_x$ (red) and $5p_z$ (blue) orbitals, that exhibit coupling along and perpendicular to the chains, $t_\parallel$ and $t_\perp$, respectively, giving rise to the following band dispersion [Bro08]:

$$E_{p_x}(k_x,k_z) = -2t_\parallel \cos([k_x+k_z]\cdot a/2) - 2t_\perp \cos([k_x-k_z]\cdot a/2) - E_\mathrm{F} \quad , \tag{7.1}$$

$$E_{p_z}(k_x,k_z) = -2t_\parallel \cos([k_x-k_z]\cdot a/2) - 2t_\perp \cos([k_x+k_z]\cdot a/2) - E_\mathrm{F} \quad , \tag{7.2}$$

where k_x and k_z are defined along the reciprocal lattice vectors $a^* = 2\pi/a$ and $c^* = 2\pi/c$ of the 3D unit cell. The Fermi level E_F is fixed by considering that p_x and p_z each contain 1.25 electrons, i.e. $E_\mathrm{F} = -2t_\parallel \sin(\pi/8)$, assuming a trivalent R atom which donates 0.5 valence electrons per Te plane [Bro08]. The parameters of the TB model are adjusted to match the calculated and measured band structure. For values of $t_\parallel \approx -1.9$ and $t_\perp \approx 0.35$, an almost perfect agreement to the LMTO bands close to E_F is found. This excellent description by this simple model indicates a very weak influence of the RTe slabs, which is indeed supported by the anisotropy in electronic transport [Ru08]. The resulting TB FS is depicted in figure 7.2 (c), where p_x and p_z bands are shown as red and blue lines, respectively. The bands gain a small curvature proportional to the ratio $t_\perp/t_\parallel$ which leads to a diamond shaped FS in the reduced 3D BZ (green) corresponding to the larger 3D unit cell. The extended 2D BZ (purple) of the Te planes is also indicated.

This underlying 3D symmetry, which is not contained in the simple TB model, leads to the backfolding of the extended 2D BZ to the reduced 3D BZ, which produces folded replica of the p_x and p_z bands, as depicted in figure 7.3 (a) as dashed lines. The 3D

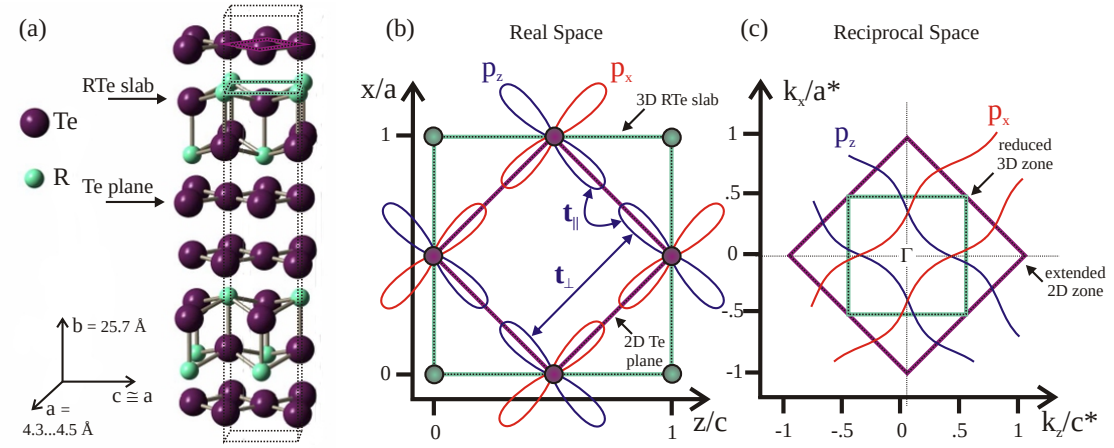

Figure 7.2: Crystal structure and Tight-Binding (TB) model of RTe_3. (a) 3-dimensional orthorhombic unit cell of RTe_3 consisting of flat, square Te planes in the a-c axis direction sandwiched between buckled RTe slabs along the longer b-axis. The crystals cleave between two Te layers. (b) Square net of Te atoms (purple) in the Te planes, described in a reduced 2D unit cell (purple square). The extended 3D unit cell (green) is defined by the R atoms (green) in the RTe slabs. For the electronic states close to E_F, a TB model of a square net of independent chains of Te $5p_x$ and $5p_z$ orbitals is considered. Coupling terms parallel ($t_\parallel$) and perpendicular ($t_\perp$) to the chains are indicated. (c) Reduced 3D (green) and extended 2D (purple) BZ of RTe_3. The diamond-shaped Fermi surface of the TB model is constructed from the Te $5p_x$ and $5p_z$ bands, shown as red and blue lines, respectively.

coupling leads to a transfer of spectral weight from the main p_x and p_z bands to the folded bands, which appear as weak bands in the outer BZ in ARPES measurements [Bro08]. In addition, the interaction of p_x and p_z orbitals, which is not included in the TB model, leads to an avoided crossing at the diamond tips and separates the FS into an inner square part and an outer FS.

Below T_{c1}, RTe_3 exhibits an incommensurate periodic lattice distortion along the slightly longer c-axis, which is characterized by a single in-plane CDW wave vector of approximately $q^{3D}_{CDW_1} \approx 2/7c^*$, as determined by structural [DiM95, Ru08] methods and tunneling microscopy [Fan07]. However, for the FS nesting properties, the nesting vector as defined in the extended 2D BZ, $q^{2D}_{CDW_1} = c^* - q^{3D}_{CDW_1} \approx 5/7c^*$, is more convenient, which will be used in this thesis. The corresponding nesting vector is shown in figure 7.3 (b). The scattering of electron wave functions off the corresponding periodic superlattice leads to a transfer of spectral weight to electronic bands that are translated by $\pm q_{CDW_1}$, the so-called CDW shadow bands, as depicted in figure 7.3 (b) as dash-dotted lines. The particular shape of the FS and the size of the CDW wave vector q_{CDW_1} lead to a perfect overlap of main and shadow bands, i.e. a perfect nesting of the FS near the diamond tips. Here, due to the influence of the CDW and the interaction of main and shadow bands, large CDW energy gaps open centered at the Fermi level, and lead to a disappearance of large portions of the FS, marked by the gray shaded areas. Due to the different curvature of main and shadow bands, the FS nesting gradually becomes imperfect, as the crossing of main and shadow bands moves above E_F. This leads to residual fragments of the FS that are maintained, the so-called metallic pockets. These nesting properties will be explained in more detail in the next section.

For the heavier members of RTe_3 a successive second CDW transition is observed

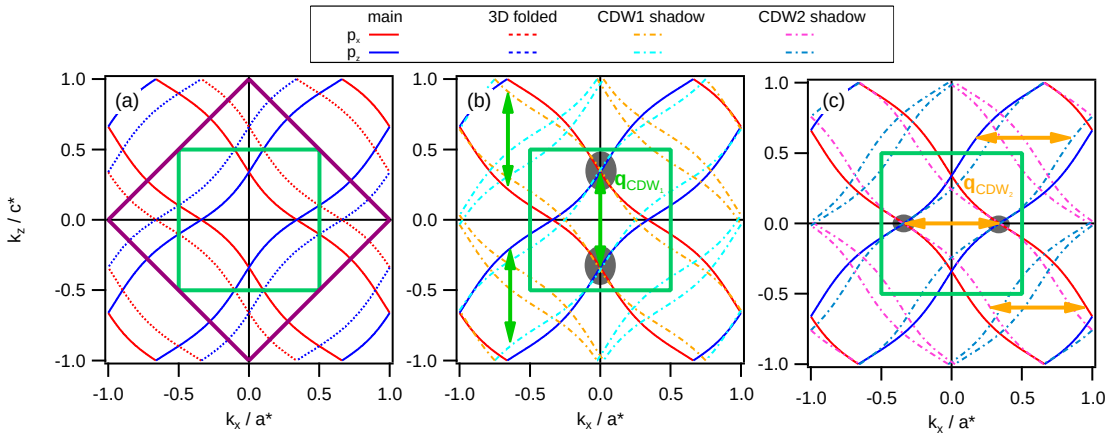

Figure 7.3: Modifications to the Tight-Binding model. (a) The folding of the extend 2D BZ to the reduced 3D BZ leads to the formation of 3D folded bands in the outer BZ as indicated with dashed red and blue lines. These bands are, however, not of importance here, as they are not accessible with the employed low photon energies. (b) The formation of the CDW along the k_z direction leads to the translation of TB bands by $\pm q_{\mathrm{CDW}_1}$ into CDW shadow bands, shown as orange and turquoise dash-dotted lines. Where these bands align on the FS, i.e. are nested by q_{CDW_1}, energy gaps open and gap out large regions of the FS (gray areas). Away from these regions, imperfect nesting leads to transfer of spectral weight into the shadow bands. (c) For the heavier members of RTe_3 (R=Dy, Ho, Er, Tm), a successive second CDW forms at lower T along the k_x direction, forming shadow bands translated along $\pm q_{\mathrm{CDW}_2}$ (magenta and cyan dash-dotted lines) and opening smaller energy gaps along k_x.

below T_{c2}, as discussed previously. This second CDW transition is characterized by a similar CDW nesting vector q_{CDW_2} which is aligned along the a-axis, as depicted in figure 7.3 (c). Similarly, this leads to the emergence of another set of shadow bands translated by $\pm q_{\mathrm{CDW}_2}$ and of the opening of a smaller CDW energy gap along the k_x axis, depicted by the gray areas in figure 7.3 (c).

In order to investigate the effect of the CDW on the TB bands, an interacting TB model is constructed. The coupling between bare bands $|k\rangle$ and shadow bands $|k \pm q_{\mathrm{CDW}_1}\rangle$ of strength V_1, where V_1 depends on the strength of electron-phonon (e-ph) coupling and the CDW modulation amplitude [Voi00, Bro08, Moo10], is taken into account by considering the following wave function which allows for the coupling of states $|k\rangle$ and $|k \pm q_{\mathrm{CDW}_1}\rangle$:

$$|\Psi_k\rangle = u_{k-q_{\mathrm{CDW}_1}} |k - q_{\mathrm{CDW}_1}\rangle + u_k |k\rangle + u_{k+q_{\mathrm{CDW}_1}} |k + q_{\mathrm{CDW}_1}\rangle \quad , \tag{7.3}$$

where the coefficients are determined as the solutions of the coupling matrix [Bro08]:

$$M = \begin{pmatrix} \epsilon_{p_{x/z}}(k - q_{\mathrm{CDW}_1}) & V_1 & 0 \\ V_1 & \epsilon_{p_{x/z}}(k) & V_1 \\ 0 & V_1 & \epsilon_{p_{x/z}}(k + q_{\mathrm{CDW}_1}) \end{pmatrix} \quad . \tag{7.4}$$

In this manner, the energy dispersion of the i^{th} interacting band is given by the eigenvalues $\epsilon_i(k)$ of the interaction matrix M. The corresponding spectral weight, which is proportional to the observed ARPES intensity is determined by the square of the projection of the respective eigenvector $\vec{r}_i$, corresponding to the eigenvalue ϵ_i, onto the

$p_{x/z}$ orbitals, i.e. $|r_{i,1}|^2$ [Voi00]. In the same manner, the coupling of the p_x and p_z bands and of the 3D folded bands can be taken into account with coupling strengths V_{xz} and V_{3D}, respectively, leading to the following interaction matrix:

(7.5)

$$\begin{pmatrix}
\epsilon_{p_x}(k) & V_{xz} & V_{3D} & & V_1 & & V_1 & \\
V_{xz} & \epsilon_{p_z}(k) & & V_{3D} & & V_1 & & V_1 \\
V_{3D} & & \epsilon_{p_x}(k+a^*) & V_{xz} & & & & \\
 & V_{3D} & V_{xz} & \epsilon_{p_z}(k+c^*) & & & & \\
V_1 & & & & \epsilon_{p_x}(k-q) & V_{xz} & & \\
 & V_1 & & & V_{xz} & \epsilon_{p_z}(k-q) & & \\
V_1 & & & & & & \epsilon_{p_x}(k+q) & V_{xz} \\
 & V_1 & & & & & V_{xz} & \epsilon_{p_z}(k+q)
\end{pmatrix}$$

In a similar manner, the effect of the second CDW transition can be incorporated, determined by the nesting vector q_{CDW_2} and the coupling strength V_2.

7.2 Spectroscopy of the occupied Band Structure

The properties of this interacting TB model are discussed in figure 7.4 in comparison to high-resolution ARPES data of $HoTe_3$ obtained with the 7 eV laser ARPES system at the Stanford University, which is described in chapter 3.3. We start the discussion with the ungapped FS obtained at $T = 300\,\mathrm{K} > T_{c1}$ shown in figure 7.4 (a1). The continuous FS of the inner diamond-shaped part is well described by the TB p_x and p_z bands shown in red and blue, respectively. At the tips of the diamond, the avoided crossing of the bands induced by the interaction V_{xz} separates inner and outer part of the FS, where we can see a small part of the latter for $k_x > 0.5\,\mathrm{Å}^{-1}$. The selected energy/momentum cuts shown in figure 7.4 (b1-f1) show the nearly linear dispersion of the bands crossing the Fermi level at all momenta, in excellent agreement with the predictions of the TB model, where the model parameters $t_{\parallel} = -1.9$ and $t_{\perp} = 0.35$ where chosen to match the experimental FS. The interacting TB model ($V_{xz} = 0.4\,\mathrm{eV}$, $V_{3\mathrm{D}} = 0.1\,\mathrm{eV}$), shown as red symbols, where the symbol size represents the spectral weight, essentially follows the bare bands, except near the diamond tip (panel (b1)), where the p_x/p_z interaction leads to the observed dispersion. The band of high intensity appearing in panel (e1) and (f1) at $E - E_{\mathrm{F}} \approx -0.4\,\mathrm{eV}$ is identified as a Te-derived band which is not captured in the simple TB model, but does not participate in the CDW transition [Sch08a]. The asymmetry in intensity observed for bands with p_x and p_z character can be explained by different photoemission matrix elements with respect to the laser light polarization.

By cooling down to $T = 180\,\mathrm{K} < T_{c1}$, the first CDW gap opens along k_z and the FS is gapped out for $k_z > 0.2\,\mathrm{Å}^{-1}$ by the nesting between main and CDW1 shadow bands, as shown in figure 7.4 (a2). The energy momentum cuts (b2-d2) showing the band dispersion in the gapped region illustrate how the linear dispersion found for $T > T_{c1}$ is replaced by a gapped dispersion where the bands are bent away from the Fermi level in a characteristic manner, in excellent agreement with the interacting TB model shown as red markers. The CDW interaction induces a CDW gap of $\Delta_1 = 2V_1 = 0.4\,\mathrm{eV}$ in the electronic structure and splits the band into two parts, which we refer to as the lower and upper CDW band in the following. This gap is nearly symmetrical around the crossing of the main p_x (red line) and the CDW shadow band (orange dash-dotted line), which is translated by $q_{\mathrm{CDW}_1} = 0.695\,\mathrm{c}^*$. Simultaneously, the spectral weight reduces very quickly away from the crossing, transferring only a small fraction of spectral weight into the shadow bands. Near the diamond tip, where the bands are nested almost perfectly at the Fermi level (b2), the gap is mostly situated below E_{F}, allowing for an efficient gain in electron energy, which stabilizes the CDW. Moving away from the diamond tip, the nesting of the FS reduces gradually, as the crossing point of main and shadow band moves above E_{F}. This leads to a shift of the center of the CDW band gap to higher energies, reducing the gapped part of the occupied band structure. Eventually, the whole band gap moves above the Fermi level, leading to the residual metallic pocket, as shown in the cut (f2). Here, the presence of the CDW still leads to a notable transfer of spectral weight into the shadow band, which appears as new feature on the Fermi surface and in the energy dispersion.

Cooling further down to $T = 15\,\mathrm{K} < T_{c2}$, the FS shown in figure 7.4 (a3) exhibits in addition to the large gap along k_z induced by q_{CDW_1} a second gap opening on the residual FS in the metallic pockets, near the diamond tip along k_x. This additional gap, induced by the perpendicular $q_{\mathrm{CDW}_2} = 0.685\,\mathrm{a}^*$ along k_x is seen in cut (f3), well described by the interacting TB model using two perpendicular gaps [Moo10]. Simultaneously, new shadow bands, associated with q_{CDW_2} (cyan dash-dotted lines), appear near the

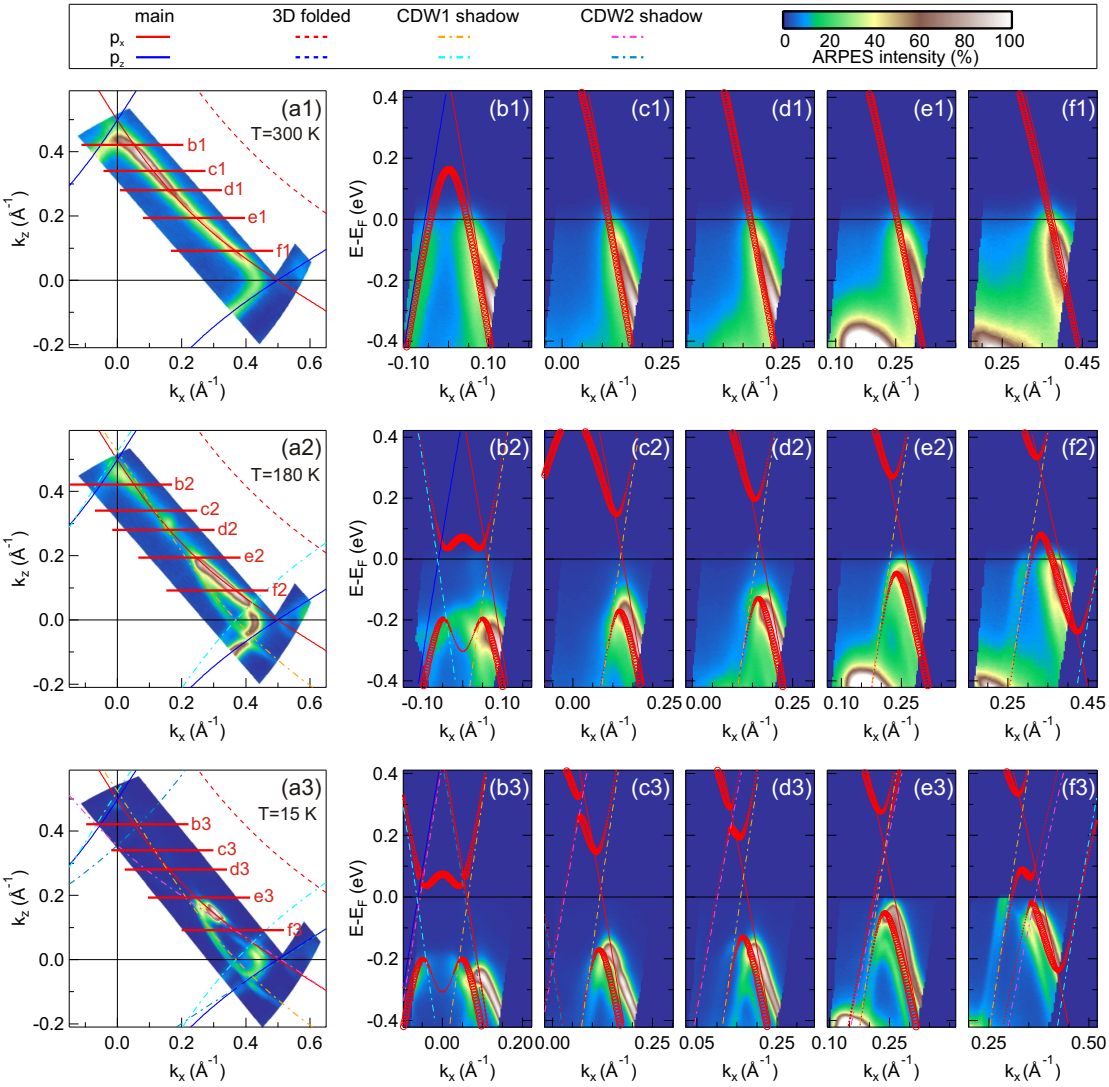

Figure 7.4: Temperature-dependent low-energy electronic structure of $HoTe_3$ obtained with 7 eV high-resolution laser ARPES. (a1-a3) Fermi surface maps of the inner diamond shaped part of the FS obtained by integrating the ARPES intensity at ± 10 meV about the Fermi level for $T = 300$ K, $T = 180$ K and $T = 15$ K, respectively. TB bands for no CDW (300 K), 1 CDW (180 K) and 2 CDWs (15 K) are indicated and red lines are the positions of the energy-momentum cuts shown in (b1-b3) to (f1-f3). (b1-f1) ARPES intensity maps along momentum cuts shown in (a1) for $T = 300$ K. Lines mark positions of the main TB bands. Open symbols mark the position of the interacting TB model without CDW, where the marker size corresponds to the spectral weight. (b2-f2) ARPES intensity maps as in (b1-f1) for $T = 180$ K. The symbols mark the interacting TB model with one CDW along k_z. (b3-f3) Same as in (b1-f1) and (b2-f2) but for $T = 15$ K. The TB symbols are for two CDWs along k_z (large gap) and k_x (small gap).

large gapped FS, visible e.g. in cut (d3). Notably, the size of the second CDW gap $\Delta_2 = 2V_2 = 0.1\,\text{eV}$ along k_x is much smaller than the gap along k_z, consistent with the lower transition temperature and the weaker shadow band intensity [Moo10].

7.2.1 Bilayer Splitting

Despite the excellent description of the general band structure and the CDW band gap by the interacting TB model, especially the data taken at low temperatures presented in figure 7.4 (a3-f3) allow, due to the remarkable energy and momentum resolution of the 7 eV laser ARPES setup and strongly reduced thermal broadening, to identify a variety of additional details in the experimental data, that are not captured in the TB model. First, we identify a fine splitting of all bands crossing the Fermi level in the FS at $T = 15\,\text{K}$, which leads to a double structure of all bands. This splitting, called bilayer splitting [Bro08] arises from the fact, that the unit cell of RTe_3 contains two equivalent neighboring Te layers, see figure 7.2 (a), whereas the TB model only considers an isolated Te square layer. Such a bilayer splitting into bonding and antibonding bands is a common phenomenon in systems with equivalent multilayer structures and has been observed e.g. in bilayer cuprate superconductors [Dam03].

In order to investigate the bilayer splitting of bands in more detail, a cut along k_z (see the FS of figure 7.6 (a)) through the remaining part of the metallic pocket is shown in figure 7.5 (a). We identify three dispersing bands: the main p_x band on the right, a less intense split-off band with a steeper slope that does not cross the Fermi level (middle) and the CDW shadow band with the opposite dispersion on the left. A closer look reveals that the main and the shadow band exhibit a bilayer splitting into a pair of lines, while the third band does not present such a splitting within the limits of our resolution. In order to quantify the splitting, momentum distribution curve (MDC) spectra as shown in figure 7.5 (b) are fitted with five Lorentzian lines to follow the peak dispersions. The peak positions obtained from the fit are indicated by red markers. The amount of splitting in the main and shadow band is shown in units of the reciprocal lattice vector c^* in figure 7.5 (c) as a function of energy. While the main band shows an increase of the bilayer splitting towards the Fermi level, the splitting is relatively constant within the shadow band. At the Fermi level, the splitting amounts to $\delta \sim 0.012\,\text{c}^*$.

The bilayer splitting of bands in RTe_3 has already been previously discussed both in the context of experimental data [Gwe98, Bro04, Bro08] and in the context of LMTO calculations [Lav05, Bro08]. The calculations predict a splitting of bands into a pair of parallel bands over a large energy interval around the Fermi level. The amount of bilayer splitting is found to differ from the square to the outer part of the BZ and amounts to $\delta \sim 0.04\,\text{c}^*$ on the square and $\delta \sim 0.01\,\text{c}^*$ on the outer part. Experimentally, the third, weaker band found in figure 7.5 was assigned to the bilayer split band. However, these measurements where not able to detect the fine splitting of main and shadow band into two parallel replica due to their limited momentum resolution, prohibiting to investigate structures smaller than $\sim 0.02\,\text{c}^*$ [Bro08]. Here, we could benefit from the very high momentum resolution available with laser-based ARPES to detect the additional splitting that provides a much more natural candidate for the bilayer splitting, as discussed below.

Despite the fact that the splitting of bands we found here is much smaller than the prediction of the LMTO calculations, we believe that the fine splitting of p_x and shadow band represents the real bilayer splitting of the system. The bilayer split bands exhibit an almost parallel dispersion and equal intensities, in agreement with the LMTO calculations, whereas the dispersion of the split-off band shows a steeper dispersion than

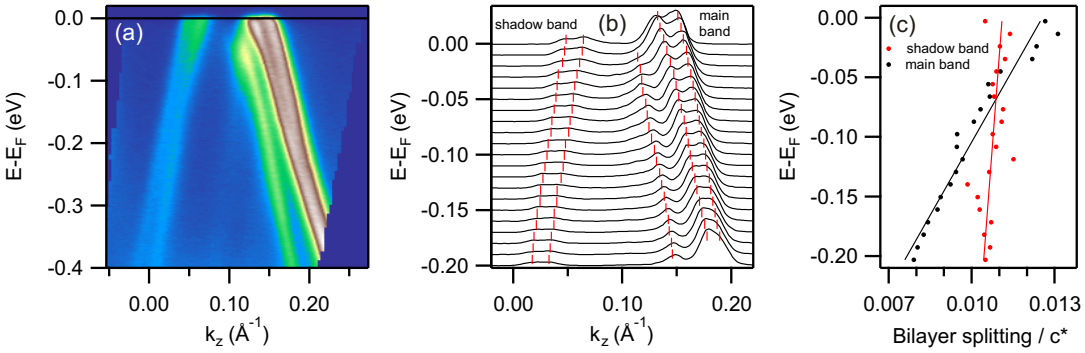

Figure 7.5: Bilayer splitting in $HoTe_3$. (a) ARPES intensity map along k_z at $k_x = 0.31\,\text{Å}^{-1}$ at the tip of the metallic pocket, showing the bilayer split main band (right) and shadow band (left). (b) MDCs of the data in (a) with peak positions marked by red lines. (c) Amount of bilayer splitting for the main and shadow band. Lines are guides to the eyes.

the main k_x band and has a much weaker intensity. In addition, the split-off band does not reach the Fermi level, but disappears just below E_F. A closer look reveals that the split-off band actually shows a characteristic bending just below the Fermi level, corresponding to a gapping of the band. In addition, a very weak shadow band can be identified. If we look at the cuts along k_x shown in figure 7.4 (b3-f3), we can identify this split-off band at all momenta, which shows an even stronger shift in momentum in the gapped region and always weaker intensities than the main p_x band. Near $k_x = 0$, the momentum shift amounts to $\delta \sim 0.085\,\text{c}^*$ at $E - E_F = -0.35\,\text{eV}$, which seems a very large value for the bilayers splitting. If we recall that the amount of bilayer splitting at E_F found in the calculation was larger on the square part of the FS than on the outer part [Bro08], we expect to find a smaller bilayer splitting on the shadow band, as this band is translated from the outer part of the FS (compare figure 7.3). Indeed, this is reproduced at least qualitatively in figure 7.5 (c), where the bilayer splitting at the Fermi level is larger in the main p_x band than in the shadow band.

A possible explanation for these split-off bands might be their relation to the surface layer. RTe_3 has its cleavage plane just between two neighboring Te layers [Fan07], where the topmost surface layer consists of a single, isolated Te layer. As the band structure is mainly determined by the *in*-plane orbitals, an electronic structure in the topmost layer similar to the double layers present in the bulk of the crystal is expected. This assumption is supported by the observation of the same CDW ordering on the surface as in the bulk, which has been observed in scanning tunneling microscopy (STM) investigations [Fan07]. However, due to the different coordination of the surface layer, the orbital overlap of the intra-plane orbitals might be considerably altered, leading to a renormalized band structure for the surface layer, which would naturally explain the different slope found in the split-off band. Indeed, most of the weak, split-off bands originally assigned to the bilayer splitting can be well accounted for by a TB model where the energy dispersion has been renormalized by a factor of $\sim 1.5 - 2.5$ [Moo12a]. In addition, a variation of the split-off bands with photon energy was reported, where a maximum of intensity in these bands was observed at $h\nu = 35\,\text{eV}$ [Bro08]. Indeed, at such photon energies, the surface sensitivity of ARPES is most pronounced, as the mean free path of electrons shows its minimum around $30 - 40\,\text{eV}$ [Sea79, Zan88], see chapter 2.4. At the small photon energy of 7 eV used for the measurements presented

here, the mean free path is much larger and hence the relative intensity of the surface derived bands is expected to be weaker. Additional support for this assignment comes from the absence of bilayer splitting *within* the split-off band (see figure 7.5), which would be naturally explained by the isolated Te layer at the surface. To test this scenario, the investigation of ultrathin epitaxial films of RTe_3 containing only a few Te layers as a function of the film thickness could provide further inside and might even allow to study a single isolated Te layer. The preparation of ultrathin films of complex materials by means of molecular beam epitaxy (MBE) is quite established e.g. for cuprate high-T_c superconductors (HTSCs) [Web87, Bol11] and might become available for RTe_3 in the near future [Sch11b, Moo12a], allowing for such investigations.

7.2.2 Distribution of the CDW Gap along the FS

A closer look at the gap distribution along the FS reveals another deviation from the TB model. As already apparent from comparing the cuts shown in figure 7.4 (c3) and (d3), a region exists where the lower edge of the gap stays constant or even moves down in energy again when going towards the metallic pocket along the FS. This becomes apparent if one compares the top of the ARPES band to the TB dispersion, which lies below the ARPES band in panel (c3) and above the ARPES data in panel (d3). In addition, panel (c3) reveals an interesting intensity modulation of the gapped band dispersion. To analyze this in more detail, respective energy momentum cuts along the normal state FS as shown in figure 7.6 (a) are analyzed. Panel (b) shows the gap distribution in the region of the large gap, where the maximum of intensity originates from the top of the gapped dispersion. The respective band position of the interacting TB model is shown as solid and dashed lines for the lower and upper band edges, respectively. Starting from the metallic pocket, where the lower CDW band crosses the Fermi level, the lower band edge shifts down in energy as the nesting condition improves for decreasing k_x, in agreement with the TB model.

Around $k_x = 0.15\,\text{Å}^{-1}$, however, the lower band edge moves down in energy very rapidly and simultaneously the spectral weight is transferred to a second band where the lower band edge is higher in energy. Thus, the band edge exhibits a discontinuity, which is not captured in the TB model. A closer look at the situation at $T = 220\,\text{K}$, shown in panel (c), where the data have been divided by the temperature-dependent Fermi-Dirac distribution function to visualize part of the unoccupied states above E_F [Lee07, Moo10], reveals intensity from the upper band edge approaching the Fermi level at the same k-point. This unoccupied band is also found in investigations of the unoccupied electronic band structure of $TbTe_3$ using trARPES, presented in chapter 7.3, where this splitting of the CDW gap will be discussed in more detail.

Following the dispersion of the lower band edge further towards $k_x = 0$, the shift of the gap position saturates as predicted by the TB model. Here, at $T = 220\,\text{K}$, intensity from the upper band edge is visible again near $k_k = 0.09\,\text{Å}^{-1}$, allowing to determine the center of the gap and thus the absolute gap value. For illustration, EDCs divided by the Fermi-Dirac distribution function at the position of the red arrows in panels (b-d) are shown in panel (e) for various temperatures, where the center of the gap is located at $\sim 50\,\text{meV}$ below E_F. At $T = 300\,\text{K} > T_{c1}$ (panel (d)), no sign of the gap persists, as already discussed in figure 7.4. To determine the temperature-dependent size of the gap, the leading edge midpoint (LEM) of the temperature-dependent EDCs with respect to the gap center is considered, which can serve as a measure for half the width of the gap, $\Delta_1/2 = V_1 \approx 170\,\text{meV}$ at $T = 15\,\text{K}$, as indicated in panel (e). However, at this k-point, the total size of the gap is already reduced due to the proximity to the diamond tip,

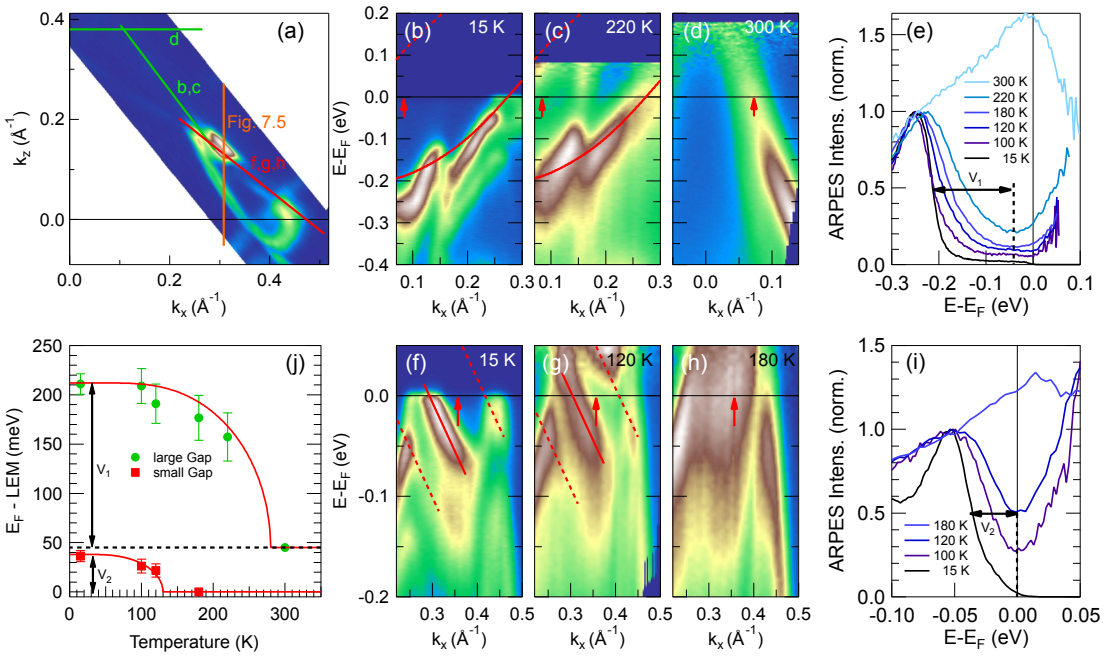

Figure 7.6: Temperature-dependent gap sizes in $HoTe_3$. (a) partial FS map of $HoTe_3$ at $T = 15\,\mathrm{K}$ indicating cuts along the normal state FS shown in panels (b-c) and (f-h). (b) ARPES intensity map along the main FS where the large gap opens, showing the distribution of the gap along the FS. Here, the k_x position is used as implicit coordinate for the position on the FS. Red solid and dashed lines are interacting TB band positions of occupied and unoccupied band edges, respectively. The red arrow marks the position of EDCs shown in (e). (c) Same as in (b) but for $T = 220\,\mathrm{K}$ and divided by the temperature-dependent Fermi function. Note the thermal population of the upper band edge for $k_x < 0.1\,\mathrm{Å}^{-1}$. (d) ARPES cut along k_x for $T = 300\,\mathrm{K}$ divided by the Fermi function, showing the completely closed gap. (e) Temperature-dependent normalized EDCs at $k_x = 0.09\,\mathrm{Å}^{-1}$ at the FS for various T across the CDW transition. (f-h) Cuts along the main FS at the small gap for various T. Red lines are guides to the eye. Arrows mark the position of EDCs shown in (i). (i) EDCs at various T at the position shown in (f-h). (j) Position of the leading edge midpoint (LEM) as a function of temperature determined from the spectra in (e) and (i) for the large and small gap, respectively. Solid lines mark the expected mean-field behavior referenced to the respective center of the gaps. Error bars are determined from the width of the leading edges (40%-60% width).

where the p_x/p_z interaction leads to a reduction of the band separation. This manifests itself in the saturation of the lower band edge shift, visible in panel (b) and (c). Thus, the determined gap value underestimates the real magnitude of the CDW gap and access to the unoccupied band structure at larger k_x values is required to determine the full value of the gap, as will be discussed in chapter 7.3.

A similar analysis is performed for the small gap, as shown in panels (f-i). The small gap crosses the Fermi level close to the position where the large gap moves above E_F, and its center decreases in energy for larger k_x, as indicated by the solid and dashed red lines, which indicate lower and upper band edge of the small gap. Due to the smaller gap magnitude, the upper band edge of the small gap is well observed in the Fermi-Dirac divided spectra at $T = 120\,\mathrm{K}$ shown in panel (g). In addition, a gap of similar magnitude opens between lower edge of the large gap and lower edge of the small gap, as indicted by the lower dashed line in panel (i). This gap is clearly connected to the second CDW transition, as it is absent above T_{c2} (panel (h)) and arises most likely from the interaction of the shadow bands of both CDWs, which cross at this position. The gap evolution as a function of temperature is, like in the case of the large gap, derived from the temperature-dependent EDCs shown in panel (i) and yields $\Delta_2/2 = V_2 \approx 40\,\mathrm{meV}$ at $T = 15\,\mathrm{K}$.

The gap size as a function of temperature is shown for both gaps in panel (j) of figure 7.6. The general trend of both gaps follows the Bardeen-Cooper-Schrieffer (BCS)-like behavior expected from mean-field theory in the weak coupling regime [Grü94, Moo10] according to equation (2.14), which is shown as red solid lines. For the large gap, however, the gap size decreases more quickly than predicted by mean-field theory and deviates from the BCS value, as was already discussed for the case of $ErTe_3$ [Moo10]. Interestingly, the distinct deviation from the mean-field behavior of $V_1(T)$ develops for temperatures, where V_2 is already considerably reduced (see figure 7.6 (j)). Thus, a possible scenario to explain this deviation might be an additional stabilization of the first CDW due to the presence of the second CDW. However, as the two perpendicular CDW distortions lie within one Te plane and hence couple to the same atoms [Moo10], one would rather expect a competing interaction of the two CDWs. To analyze this in more detail, further experimental and theoretical input is necessary.

7.3 Spectroscopy of the unoccupied Band Structure

So far, we investigated the occupied band structure of RTe_3 using conventional laser-based angle-resolved photoemission spectroscopy, which revealed a detailed picture of the occupied states below E_F with excellent energy and momentum resolution. By making use of the thermal occupation and dividing by the Fermi-Dirac distribution function, limited access to unoccupied states within several meV above the Fermi level can be gained [Dam03, Hüf03, Lee07, Moo10]. However, a more complete access to the unoccupied band structure exceeding a few meV above E_F is highly desirable to investigate further aspects of the electronic properties. For instance, optical properties are determined by optical interband transitions between occupied and unoccupied bands. In the case of RTe_3, the exact position of the CDW gap along the FS and its exact magnitude bear several uncertainties by only considering the occupied part of the gapped band structure [Bro08, Moo10]. Even though thermal occupation allows to determine the gap center at certain momenta near the diamond tip (see previous chapter and e.g. [Moo10]), in this region the p_x/p_z interaction prevents the detection of the full gap magnitude. Furthermore, the good description by the relatively simple TB model found for the occupied states makes RTe_3 an ideal candidate to test the applicability of theoretical band structure calculations such as the TB model also for the unoccupied band dispersion.

Traditionally, several methods fascilitate the spectroscopy of unoccupied electronic states. Scanning tunneling spectroscopy (STS) is widely used to investigate both occupied and unoccupied electronic states of e.g. adsorbate systems [Fra11] or metallic overlayers [Jia07, Bru09, Hon09] and optical spectroscopy is sensitive to direct transitions in the electronic structure and thus can provide limited, indirect access to the unoccupied band structure. However, these methods are not k-resolved and integrate over the whole BZ. Therefore, the interpretation of such data is difficult in electronically anisotropic systems such as RTe_3 and allows e.g. only for the detection of a k-averaged value for the CDW gap [Sac06, Sac07, Fan07]. Inverse photoemission (IPE) is in principle a k-resolved method, which detects unoccupied states above E_F by using monochromatized and directed electron beams. This technique, however, suffers from a very low detection yield and poor statistics and provides only limited energy and momentum resolution [Bud07].

Another approach is the use of non-equilibrium probes, where unoccupied states are transiently populated with ultrashort laser pulses and can be subsequently analyzed. A common scheme is the two-photon photoemission (2PPE), which enables the k-resolved detection of unoccupied states between the Fermi and the vacuum level and which has been widely used to investigate e.g. image potential states at noble metal surfaces [Kno96, Wol97, Pet97, Wei02b, Roh05, Güd07]. However, in the standard configuration, where the probe photon energy $h\nu_{\mathrm{probe}}$ is smaller than the sample work function Φ, a k-resolved detection of unoccupied states close to the Fermi level is prohibited, as their kinetic energy close to zero does not allow to reach finite k-values even at large emission angles (see chapter 2.4).

Here, we establish trARPES as a powerful technique to simultaneously investigate electronic states below *and* above E_F in a k-resolved manner. Electronic states up to $E - E_F = 1.5\,\mathrm{eV}$ are transiently populated by the infrared (IR) pump pulse. Subsequently, the probe photon energy $h\nu_{\mathrm{probe}} = 6.0\,\mathrm{eV} > \Phi$ is used to detect occupied and transiently populated unoccupied electronic states in an angle-resolved manner. This way, the kinetic energy of unoccupied states is larger and allows for a k-resolved study of states even directly above the Fermi level. Here, we demonstrate trARPES

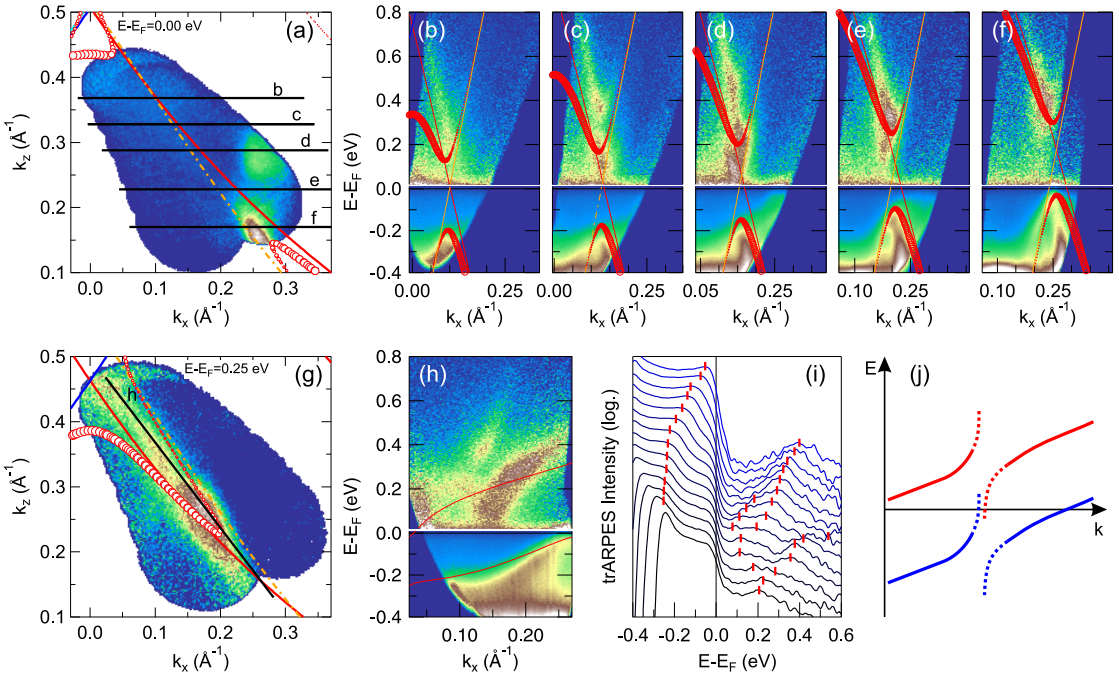

Figure 7.7: trARPES dispersion of occupied and unoccupied states in $TbTe_3$ obtained with the pTOF spectrometer. The delay between the weak pump beam ($F = 150 - 250\,\mu J/cm^2$) and the probe beam was fixed at $t = 50\,fs$. (a) FS map of $TbTe_3$ at $T = 30\,K$ obtained with the pTOF spectrometer, integrated at $\pm 25\,meV$ about E_F. Lines and symbols mark bare and interacting TB bands, respectively. Cuts shown in (b-f) are indicated. (b-f) trARPES intensity along cuts shown in (a). Lines and symbols denote bare and interacting TB bands, respectively. Intensity at $E > E_F$ is enhanced by a factor $\times 100$. (g) Constant energy map at $E - E_F = 0.25\,eV$. Note the pocket of the unoccupied band. (h) trARPES intensity along a cut parallel to the FS shown in (g). Solid lines are interacting TB bands. Note the splitting of unoccupied bands at $k_x = 0.15\,Å^{-1}$. (i) EDCs of the data shown in (h). Peak positions are indicated. (j) Sketch of the interrupted dispersions of occupied (blue) and unoccupied (red) band edges along the FS.

with a newly developed position-sensitive time-of-flight spectrometer [Kir08c] (pTOF, see chapter 3.1.5), which has been successfully employed in this thesis for the first time and enables the simultaneous detection of a contiguous area of the reciprocal space within a single measurement. This technique allows to efficiently map a large fraction of the occupied and unoccupied band dispersion. However, one has to bear in mind that this technique optically excites the sample and thus probes the excited electronic system, which could in principle be different from the ground state. For systems like RTe_3, where most dynamics of the electronic system is lattice-driven [Sch08a], the use of moderate pumping fluences and small pump-probe delays helps to minimize the effect of the pump pulse on the electronic structure and to investigate the populated, quasi-unperturbed electronic band structure above E_F.

Figure 7.7 shows trARPES data of $TbTe_3$ taken at $T = 30\,K$ along the FS, where the delay between the pump pulse with a moderate incident pumping fluence[1] of $F = 150 - 250\,\mu J/cm^2$ and the probe pulse is set to $t = 50\,fs$. That way, almost the complete pump pulse has been absorbed and the occupation of unoccupied states is maximal, while still no significant modifications of the CDW ground state and the gap size are detected (see chapter 7.4). The data set shown here has been combined from different sample orientations, spanning a large fraction of the FS, which is shown in panel (a). The FS compares well to the data of $HoTe_3$ shown in figure 7.4 and to the TB model. Energy/momentum cuts indicated in panel (a) are shown in panels (b-f) in a false color representation. Here, the unoccupied states $E > E_F$ have been enhanced by a factor of $\times 100$, which indicates an excitation density of $\sim 1\%$ of the valence electrons near E_F. Apart from the dispersion of occupied states, that was already discussed before, we can clearly identify the gapped dispersion of the unoccupied part of the band gap, which follows the dispersion of the interacting TB model. Starting from the diamond tip, where the gap is almost completely below E_F, both occupied and unoccupied band edges move up in energy, as the crossing of main and shadow band moves above E_F. Near the metallic pocket (panel (f)), the unoccupied band is found at $\approx 0.4\,eV$ above E_F. A constant energy map at $E - E_F = 0.25\,eV$ shown in panel (g) illustrates how the unoccupied band extends from the diamond tip and turns into the shadow band near $k_x = 0.2\,Å^{-1}$, similar to the situation at the metallic pocket on the FS.

The dispersion of the gap along the cut parallel to the FS indicated in (g) is shown in panel (h). In the occupied part of the spectrum, we find the continuous shift of the band edge to lower energies, as already discussed for the case of $HoTe_3$. However, here we do not observe the splitting of the gap that we found in $HoTe_3$. This is most likely due to the incoherent photoemission background at $E - E_F < 0.2\,eV$, which makes the detection of the occupied band edge difficult. However, looking at the unoccupied states, we find a similar discontinuity of the unoccupied band edge precisely at the same momentum as in $HoTe_3$ (see figure 7.6 (b)). Starting from the metallic pocket at $k_x = 0.25\,Å^{-1}$, both occupied and unoccupied CDW bands move down in energy towards smaller k_x, in agreement with the TB model. At $k_x \approx 0.15\,Å^{-1}$, however, the upper band edge is bent down more quickly and almost reaches the Fermi level. Intensity from this band was also observed close to E_F in the data of $HoTe_3$ divided by the Fermi function shown in figure 7.6 (c). At the same time, a second unoccupied band appears above the first one, gains in intensity and subsequently follows the dispersion of the TB band up to the diamond tip. This band splitting is also apparent in the cuts shown in panel (c) and (d), which resemble very much the situation of the occupied dispersion in $HoTe_3$ (see figure 7.4 (c3)).

[1] The pumping fluence differs slightly due to the different angles of incidence during sample rotation.

To further investigate this splitting, MDCs of the data in (h) are shown in panel (i) on a logarithmic intensity scale, where peak positions are indicated by red markers. From the peak separation at the metallic pocket, we can determine the CDW gap value to $\Delta_{\mathrm{CDW}} \approx 0.46\,\mathrm{eV}$, which is almost twice the value of $\Delta_{\mathrm{CDW}} \approx 0.24\,\mathrm{eV}$ reported for $TbTe_3$ using conventional ARPES [Bro08]. This gap at first shifts consistently to lower energies until the unoccupied band dispersion turns towards the Fermi level and reduces the CDW gap to $\Delta \sim 0.25\,\mathrm{eV}$. Simultaneously, a splitting into the new unoccupied band and at certain momenta even an additional splitting into three bands is observed. At the bottommost spectra, we observe once more a uniform gap of $\Delta_{\mathrm{CDW}} \sim 0.46\,\mathrm{eV}$.

This observation indicates that the size of the CDW gap is considerably reduced around $k_x = 0.15\,\mathrm{\AA}^{-1}$. To explain this behavior, three scenarios are considered here: (i) the gap size $\Delta_{\mathrm{CDW}} = 2V_1$ has to become momentum dependent, (ii) multiple nesting vectors or (iii) interaction between more than two bands are involved in the CDW transition. The first scenario would involve a k-dependent coupling term $V_1(k)$, which is not compatible with a FS nesting driven CDW formation, where the gap distribution is solely determined by the nesting properties of the nested bands and the nesting vector [Grü94]. Furthermore, this scenario could not explain the observed band splitting. A nesting with multiple nesting vectors which are close to each other seems very unlikely as well, as these different periodicities would compete with each other and lead to strong fluctuations that would lower the critical temperature and the energy gain of the system. In addition, only a single CDW modulation vector has been found in x-ray scattering [Ru08] and STM [Fan07] experiments.

In contrast, the interaction of multiple bands is a natural consequence of the bilayer splitting of the bands. Combining the observations in figure 7.6 and figure 7.7 leads to the following picture, sketched in figure 7.7 (j): Starting from the metallic pocket at large k_x, where the CDW gap lies completely above E_{F}, the gap shifts continuously down in energy. Near $k_x = 0.15\,\mathrm{\AA}^{-1}$ the gap moves quickly down in energy until the upper band edge almost reaches the Fermi level. Simultaneously, the spectral weight is transfered to another gapped band dispersion, where the gap center is located roughly at E_{F}, leading to the band split observed in figure 7.6 (b) and 7.7 (h). These new bands now continue the original dispersion of the gap position towards the diamond tip at small k_x.

The observation of such a splitting of the gapped CDW dispersion has not been reported previously. However, the fact that we observe this effect in two different samples ($HoTe_3$ vs. $TbTe_3$) and in both occupied and unoccupied states indicates that this observation is a general feature of the CDW formation in RTe_3. To determine whether this behavior is really a consequence of the bilayer splitting or if further bands have to be considered and what implications on the CDW formation follow from such a band splitting, however, requires further theoretical investigations and remains outside the scope of this theses.

Additional trARPES data of occupied and unoccupied states in $DyTe_3$ showing the dispersion of states within the metallic pocket and at the metallic tip of the diamond-shaped FS can be found in appendix A.1, demonstrating a high contrast in the spectroscopy of states up to $\sim 1.5\,\mathrm{eV}$ above E_{F}.

7.4 Collapse of the CDW Gap along the Fermi Surface

By varying the pump-probe delay, trARPES allows to investigate the dynamics of the CDW state in response to strong optical excitation, as was already demonstrated earlier for the case of $TbTe_3$, where an ultrafast transition to a transient metallic state was found [Sch08a, Kir08a, Sch11a]. However, these experiments only investigated the dynamics on one fixed k-position on the FS and the limited momentum resolution of the conventional time-of-flight spectrometer used for these experiments defied a precise analysis of the CDW gap dynamics. Here, we make use of the superior momentum resolution provided by the pTOF spectrometer and its capability to map out a contiguous region of the reciprocal space to investigate the transient collapse of the CDW gap along the FS of $DyTe_3$. Using this technique, we present here for the first time a time-resolved Fermi surface mapping, which enables to investigate the detailed modifications of the FS topology upon optical excitation and its transformation from the gapped CDW state to a transient metallic state, where the continuous FS is recovered. Such an analysis is highly non-trivial using standard scanning techniques with 2D hemispherical analyzers, as the spatial and temporal overlap and the stability of the laser system have to be verified throughout a series of scans. In addition, the change of the sample orientation in such a scan will modify the projection of the pump beam onto the sample and thus change the effective pumping fluence throughout the scan, which complicates the comparability of the results (see also chapter 5). Most of these caveats can be overcome by the advantages provided by the pTOF spectrometer. Still, time-resolved measurements using the pTOF are challenging as the available count rate is distributed over the four-dimensional (4D) parameter space of energy, k_x, k_z and pump-probe delay, and measurements as presented in the following comprise measurement times of > 11 h and a total data volume of ~ 450 GBytes.

Several snapshots of the temporal evolution of the transient energy dispersion and FS of $DyTe_3$ in the gapped region near the metallic pocket are shown in figure 7.8, where panels (a-c) show the transient FS map, panels (d-f) a constant energy map at $E - E_F = -0.125$ eV and panel (g-j) the energy dispersion along the cut indicated in panels (a) and (d). Before excitation (panel (a)), most of the visible FS is gapped out, and the residual FS of the metallic pocket is seen in the lower right corner[2], well described by the interacting TB model (blue line). The constant energy map in panel (d) illustrates the bending of the band dispersion due to the CDW interaction and the transfer of spectral weight from the main p_x band (solid black line) to the CDW shadow band (green dashed line). The energy/momentum cut shown in panel (g) exhibits the gapped dispersion of the CDW state and the characteristic bending of the main band into the shadow band, well described by the TB model (circles).

Directly at the pump-probe overlap, no apparent changes of the occupied bands are observed, as shown in panel (h), leaving the constant energy cut and the FS essentially unchanged (not shown). However, we find a considerable occupation of the unoccupied CDW band, which is in good agreement with the prediction of the TB model. With increasing pump-probe delay, the occupied and unoccupied bands start to move towards each other, as the CDW state melts and the band gap closes. At $t = 100$ fs, the lower band already touches the Fermi level, as shown in panel (i). This closing of the gap leads to the reformation of the normal state FS starting from the metallic pocket, as seen in panel (b). Simultaneously, spectral weight is transfered from the shadow band

[2]The weak intensity observed in the upper left corner originates from the residual FS of twinned domains of the sample where the gap opens along k_x.

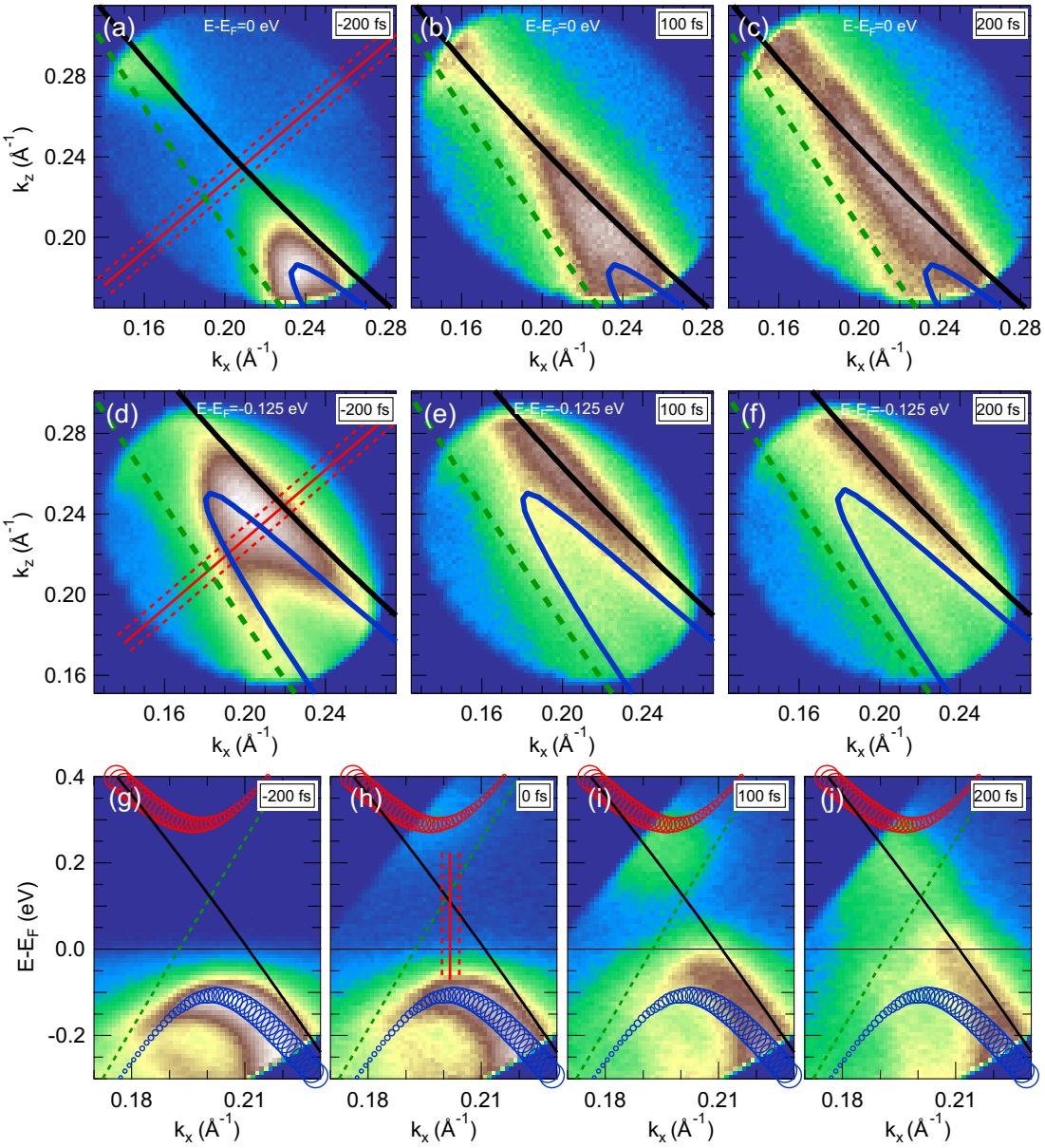

Figure 7.8: Time-resolved Fermi surface of $DyTe_3$ at $T = 30\,\mathrm{K}$ near the metallic pocket. The incident excitation fluence was $F = 1.1\,\mathrm{mJ/cm^2}$. (a-c) FS maps integrated at $\pm 25\,\mathrm{meV}$ about E_F before excitation, at $t = 100\,\mathrm{fs}$ and at $t = 200\,\mathrm{fs}$ after excitation. The excitation leads to an extension of the metallic pocket and eventually to a complete closing of the FS at $t = 200\,\mathrm{fs}$, where the normal state FS indicated by the black p_x TB band is recovered. (d-f) constant energy maps for $E - E_\mathrm{F} = -0.125\,\mathrm{eV}$ as in (a-c). Note the disappearance of the shadow band, indicated by the green dashed line. (g-j) Transient trARPES energy/momentum maps integrated along the cut perpendicular to the FS shown in panels (a) and (d) for various pump-probe delays. Note how the gapped dispersion of the interacting TB model (blue and red markers) visible at $t = 0\,\mathrm{fs}$ is replaced by the quasi-linear dispersion of the bare, ungapped p_x TB band (black line) within 200 fs. The red lines in (h) indicate the integration area of EDCs shown in figure 7.9.

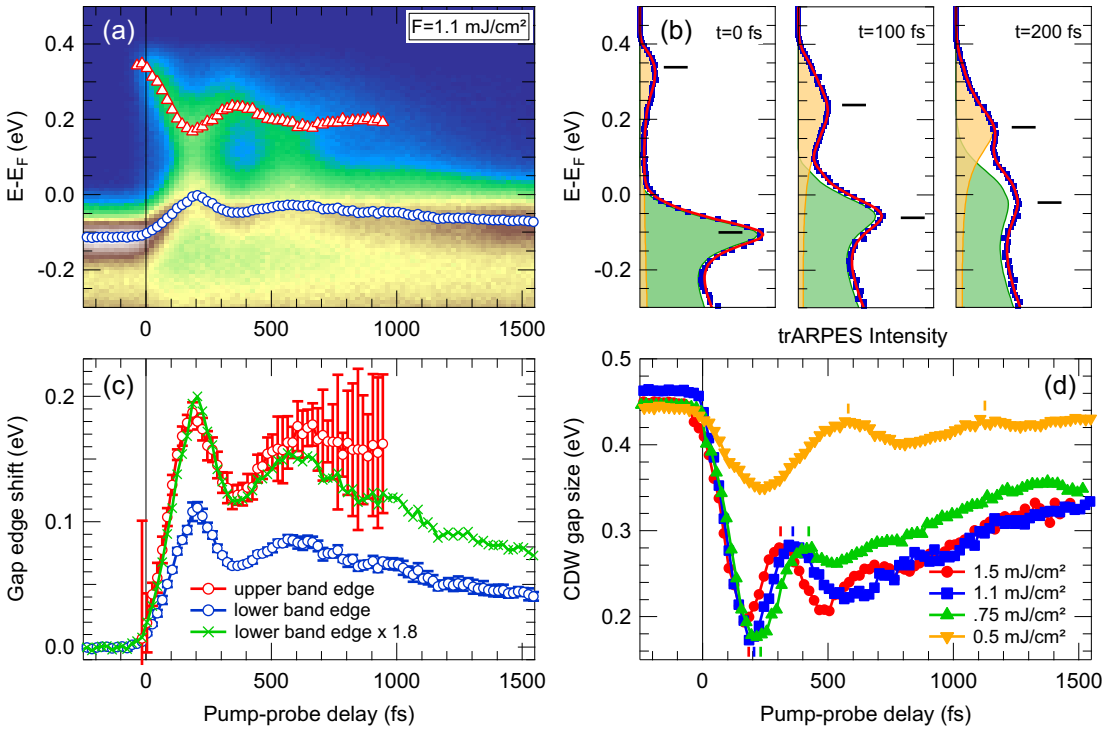

Figure 7.9: Temporal evolution of the transient CDW gap size. (a) Transient EDCs integrated between the dashed lines shown in figure 7.8 (h) in a false-color representation as a function of pump-probe delay. The transient positions of the lower and upper gap edges determined by a fitting procedure are shown as blue and red markers, respectively. (b) EDCs at representative pump-probe delays together with the fitting functions (see text). The black markers indicate the peak position determined from the second derivative of the spectra. (c) Relative shift of the band edges with respect to the equilibrium value. Note the stronger shift of the upper band edge. For comparison, the lower band edge shift is also drawn scaled by a factor of $\times 1.8$. (d) Transient gap sizes for various fluences as determined from the distance of lower and upper band edge. Note the slowing down of the transient oscillations of the gap size with lower fluence.

back into the main p_x band, which is well observed in panel (e), where the characteristic bending of the band is already almost absent and the shadow band intensity is strongly reduced. At $t = 200$ fs, the band dispersion in panel (j) is well described by the nearly linear dispersion of the main p_x band, indicating the transient melting of the CDW. At this delay time, the gap on the FS is completely absent and the continuous dispersion of the high-temperature phase is recovered (panel (c)). In addition, the shadow band in panel (f) has almost completely vanished, indicating the strong suppression of the CDW modulation q_{CDW}.

7.4.1 Transient Evolution of the CDW Gap Size

In order to quantify the temporal evolution of the CDW gap, EDCs integrated around the center of the CDW gap as indicated by red lines in figure 7.8 (h) are shown in figure 7.9 (a) as a function of pump-probe delay in a color coded intensity plot. Before excitation, the occupied CDW band is situated at $E - E_{\mathrm{F}} = 0.12(1)$ eV (blue markers). With the arrival of the pump pulse at $t = 0$ fs, we identify the optical excitation of carriers into

the unoccupied CDW band at $E-E_F = 0.34(3)$ eV (red markers), indicating a CDW gap of $\Delta_{CDW} \sim 0.46$ eV. With increasing pump-probe delay, both occupied and unoccupied CDW bands shift towards E_F and peak at $t \approx 200$ fs, where the CDW gap is smallest. Subsequently, the bands shift *away* from E_F again and the gap size *increases* again, followed by damped oscillations of the gap size. A large population of excited carriers in the unoccupied CDW band persists up to > 1 ps, indicating a strongly perturbed and highly non-thermal electron system up to very long pump-probe delays.

Next, the position of the CDW bands are determined by fitting the transient EDCs, as shown for exemplary pump-probe delays in figure 7.9 (b). To account for the highly non-thermal distribution of electrons within the first picosecond, a fitting model composed of two independent parts for the occupied and unoccupied band structure was considered, shown as green and yellow areas, respectively. Each part consists of a linear background and a Lorentzian peak function, multiplied with a Fermi-Dirac distribution. Here, the position of the Fermi-Dirac distribution of the unoccupied bands was used as an auxiliary parameter to mimic the cut-off at high energies due to the dispersion of the acceptance angle of the pTOF (see the high-energy intensity cutoff in figure 7.8 (h)). We find an excellent description of the data by the fits for all pump-probe delays. Due to the highly non-thermal electron system after excitation, even the Fermi-Dirac distribution used for the formally occupied part of the spectrum needs to be considered as an auxiliary parameter, as no Fermi level can be defined any more in the spectrum e.g. at $t = 200$ fs. In order to crosscheck the results of the fitting procedure, peak positions are compared to the extrema in the second derivative of the data with respect to energy, as commonly used in ARPES [Dam03], confirming the results of the fitting procedure (black markers in figure 7.9 (b)).

The peak positions of the occupied and unoccupied CDW band edges determined by this fitting procedure are shown as blue and red markers in panel (a), respectively. We immediately recognize, that even at $t = 200$ fs, the gap is not completely closed, although the metallic FS is recovered at this delay and the peak dispersion found in figure 7.8 (j) resembles the nearly linear high-temperature dispersion. This becomes evident from the data in figure 7.9 (b), where still two distinct peaks are found at $t = 200$ fs, indicating a residual CDW gap of $\Delta_{CDW}^{min} \approx 0.17$ eV. In addition, we find a considerably larger shift of the unoccupied CDW peak, which indicates an asymmetric closing of the CDW gap.

In order to quantify the asymmetry of the collapse of the CDW gap and the transient gap size, the relative peak shift of the two bands is shown in panel (c). We find a maximal shift of ≈ 190 meV for the unoccupied band (red), whereas we find only a shift of ≈ 110 meV for the occupied band (blue) at $t = 200$ fs. This asymmetry in the closing of the gap is surprising, because in the simple band-crossing picture of the interacting TB model, the center of the gap is determined by the crossing of main and shadow band. Thus, the asymmetric closing of the CDW gap indicates a transient modification of the band curvature or the nesting condition, which determine the relative position of the bands, as will be discussed in more detail in section 7.4.2.

Due to the progressing thermalization of the electronic system, the position of the unoccupied CDW band becomes hard to determine on top of the background of the hot thermalized electron distribution for $t > 500$ fs and is indistinguishable from the background for delays $t > 1000$ fs. In order to determine the transient gap size for all pump-probe delays, we compare the occupied band shift scaled by a factor of $\times 1.8$, shown as green markers, to the unoccupied band shift. We find a close agreement for $t < 500$ fs, indicating a constant asymmetry of the gap closing with pump-probe delay. The deviations towards larger band shift of the unoccupied band found for $t > 500$ fs

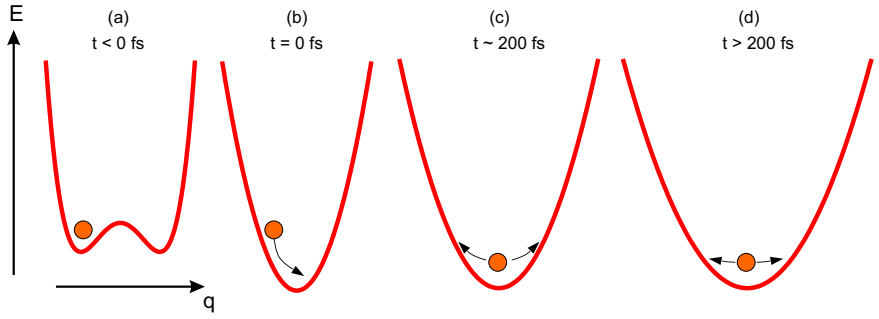

Figure 7.10: Sketch of the transient CDW potential. Before excitation, the system, described by the lattice distortion coordinate q, is located in a minimum of a double-well potential (a). With the optical excitation at t_0, the system moves in a new steep potential towards the undistorted position and starts oscillating (b). Simultaneously, the transient potential starts to soften, leading to a slowing down of the oscillations (c,d).

correspond to a systematic underestimation of the peak energy, which can be explained by the asymmetric peak shape due to the exponential background of the hot electron distribution and manifests in the large error bars. Thus, for delays $t > 500$ fs, where no reliable determination of the unoccupied peak position is possible, we extrapolate the unoccupied peak shift by the scaled occupied peak shift, assuming a constant proportion of occupied and unoccupied peak shift.

The transients of the gap values determined from the peak distance of occupied and unoccupied CDW peak are shown in panel (d) for various fluences. We find a strong dependence on the pumping fluence F: For low $F \leq 0.5\,\mathrm{mJ/cm^2}$ (yellow), we find a small decrease of Δ_{CDW} after t_0, followed by a periodic coherent oscillation of Δ_{CDW} around the initial value of the gap with a frequency of $f \sim 2$ THz, as indicated by the color ticks at the first and second maximum of the oscillation. These coherent oscillations last for several picoseconds and correspond to the excitation of the amplitude mode of the CDW order parameter [Grü94, Sch08a] and will be discussed in more detail in chapter 7.5.

For higher F, we find an ultrafast quench of Δ_{CDW} within ~ 200 fs, followed by a slower recovery of Δ_{CDW} overlaid by strongly anharmonic and damped oscillations. These oscillations as well as the initial collapse of the CDW gap exhibit an acceleration with increasing fluence, as can be seen from the ticks that mark the first minimum and maximum of Δ_{CDW}. Interestingly, the minimal value of the gap $\Delta^{\mathrm{min}}_{\mathrm{CDW}} \sim \frac{1}{3}\Delta^{0}_{\mathrm{CDW}}$ does not depend on the excitation fluence, and also the recovery of the CDW state is very similar for all fluences.

We now discuss the fluence-dependent gap dynamics as presented in figure 7.9 (d). The anharmonic and strongly damped oscillations present in the transient order parameter, which are induced by the transient movements of the ion cores in the CDW potential, demonstrate the importance of the lattice dynamics for the transition to a transient metallic state. The movement of ions towards their equilibrium position is governed by the transient potential energy surface of electronic states, as sketched in figure 7.10. Before excitation, the broken-symmetry state of the system can be described as a double-well potential [Grü94, Yus10], where the distorted lattice occupies the potential minimum with $|q| \neq 0$. With the sufficiently strong excitation of the electronic system, the double-well potential energy surface is replaced by a potential with only one minimum at the undistorted lattice position on an ultrafast timescale. This causes the ions to move in that potential landscape towards the new potential minimum, which

corresponds to a reduction of the periodic lattice distortion, followed by an oscillation around the new equilibrium position. As the amplitude of the lattice distortion is directly connected with the CDW order parameter, the observed reduction and oscillations of the gap magnitude are a direct measure of the transient CDW order. This implies, that important information on the transient potential energy surface can be gained from the transient slowing down of the oscillations. A common explanation of such a "chirp", i.e. a transient change of the central frequency of coherent phonon oscillations, considers the anharmonicity of the energy potential, which results in a dependence of the frequency on the oscillation amplitude [Has02, Mat06]. However, this can be ruled out here, as an anharmonicity of the potential yields lower frequencies for higher oscillation amplitudes present at early times and thus results in a *blueshift* of the frequency with the decay of the oscillation amplitude for longer pump-probe delays [Has02]. Thus, the observed *redshift* of the oscillations evidences a transient softening of the potential in which the ions move, as sketched in figure 7.10 (c) and (d), which yields valuable information about the transition to a transient metallic state. This goes clearly beyond the limits of the Born-Oppenheimer approximation [Bor27], and demands for a simultaneous description of the coupled ionic and electronic motions. Such a description might be possible in the context of the Ginzburg-Landau theory [Grü94, Yus10] and might help to disentangle the dynamical evolution of the electronic and ionic system.

In this context, the increase of the oscillation frequencies with fluence (see figure 7.9 (d)) gives further insight into the transient energy potential. The faster oscillations indicate a stronger initial driving force for the ion oscillations with increasing fluence, which corresponds to a steeper initial energy potential. This can be qualitatively understood in a simple picture of the screened ion potential: With increasing fluence, more and more electrons are excited from the cold Fermi sea, which can lead to a modification of the screening of the ion cores, also known as photo-doping. This modified screening can lead to a stronger attraction of electrons and ion cores, which corresponds to an enhancement of lattice bonding strengths and hence to a steeper potential for lattice distortions. Such a scenario is compatible with the transient hardening of lattice bonds predicted for soft materials [Rec06] such as RTe_3, which has been experimentally observed recently in Au under intense laser excitation [Ern08]. Finally, the observation of a decrease of the closing time of the CDW gap, determined by the first minimum of the transient gap size is consistent with a stronger driving force for the CDW melting. This melting time is intrinsically governed by the timescale of the lattice dynamics and the amplitude mode frequency f, where at least a time $\tau \sim \frac{1}{4f}$ is necessary for the melting of lattice order [Sch11a]. This highlights the intimate coupling of electronic and lattice degrees of freedom in the CDW system RTe_3, which ultimately sets the limiting time scale for the transition to a transient metallic state. This separates the CDW formation from other broken-symmetry ground states, such as spin density wave (SDW) or Mott-Hubbard physics, where the lattice is not involved and hence faster response times are found [Per08, Hel10, Wal11, Pet11, Roh11, Ret12a].

The incomplete closing of the CDW gap observed even for fluences up to $F = 1.5\,\mathrm{mJ/cm^2}$ is surprising, as a complete transition to a transient metallic state and a melting of the CDW order was reported for fluences exceeding $F \sim 1\,\mathrm{mJ/cm^2}$ for $TbTe_3$ using trARPES [Sch08a, Sch11a]. This analysis was based on the reformation of a quasi-linear dispersion of the metallic phase. In this study, however, the transient gap size could not be determined directly due to the limited resolution and the large background of non-thermal electrons. Indeed, the transient dispersion of $DyTe_3$ at $t = 200\,\mathrm{fs}$ (figure 7.8 (j)) is described remarkably well by the quasi-linear dispersion of the bare p_x

band, and we do not find any characteristic bending of bands in MDC fits, indicating a complete closing of the gap. This is in contrast to the intensity along the band dispersion, which still shows a distinct minimum at the gap center, as discussed in figure 7.9 (b). Thus, while we find a metallic peak dispersion at $t = 200\,\mathrm{fs}$, the intensity distribution within the band still shows the existence of a remaining CDW gap. Furthermore, the apparent fluence independence of the remaining gap magnitude is puzzling. In recent experiments using time-resolved resonant soft x-ray scattering [Moo12b], which monitored the lattice part of the CDW distortion, also an incomplete reduction of the CDW diffraction peak for even higher fluences $F \sim 3\,\mathrm{mJ/cm^2}$ was observed, indicating an incomplete closing of the gap even at these fluences. However, this effect could also be explained by the larger penetration depth of the x-ray beam into the sample than the IR pump beam in these experiments [Moo12b]. In addition, a recent theoretical investigation of the problem of an ultrafast excitation of a CDW system concluded on an ultrafast decoupling of the electronic and the lattice part of the order parameter, leading to a partial suppression of the CDW gap [She12]. However, in that work, it was argued that the lattice part of the CDW order is not or only weakly influenced by the optical excitation [She12], which is inconsistent with the strong reduction of the lattice order parameter observed in transient x-ray scattering [Moo12b] and with our observation of transient ion oscillations. An alternative explanation for the residual gap in the transient state of RTe_3 after photoexcitation might be the occurrence of remnant *local* order, whereas the *macroscopic* correlation is destroyed by the fluctuations induced by the pump pulse. Likewise, despite the strong excitation of the electronic system evident from the transient trARPES spectra, a small CDW gap might still be favorable for the system, as the potential energy of the occupied states is still reduced in the partially gapped state.

7.4.2 Momentum-dependent Asymmetry of the CDW Band Shift

Now we turn back to the asymmetric band shift that we observed in figure 7.9. In order to investigate the closing of the gap at different k-positions, figure 7.11 (a-c) shows the transient trARPES intensity along a cut parallel to the FS at $t = 0\,\mathrm{fs}$, $t = 100\,\mathrm{fs}$ and $t = 200\,\mathrm{fs}$. Here, k_x is used as implicit coordinate for the FS position. The peak position of occupied and unoccupied CDW bands determined by fits are shown as blue and red symbols, respectively, demonstrating a continuous reduction of the gap size at all momenta. Due to the limits of the k-region investigated in this measurement, the fitting of occupied and unoccupied peaks is restricted to regions, where the respective peak is discernible for all pump-probe delays. The peak positions for $t = 0\,\mathrm{fs}$ and $t = 200\,\mathrm{fs}$ are depicted in figure 7.11 (d), which allows comparison of the maximal shift of the band edges as a function of FS position. The data reveal an increase of the peak shift of the unoccupied band for increasing k_x, which leads to a decrease of the slope of the band edge after excitation (see the different sizes of the black arrows shown in figure 7.11 (d)). In contrast, the lower band edge shows a reduction of the band shift for larger k_x, leading to an increase of the asymmetry of the gap closing for larger k_x. This behavior also leads to a decrease of the transient shift of the gap center with k_x (green triangles), defined as $E_{\mathrm{center}} = (E_{\mathrm{upper}} + E_{\mathrm{lower}})/2$, where E_{upper} and E_{lower} are the positions of upper and lower band edges, respectively. Independent of pump-probe delay, extrapolating the center of the gap towards smaller k_x (solid green line) yields $k_x \sim 0.17\,\mathrm{\AA}^{-1}$ for the zero-crossing of the gap center, i.e. the situation where the gap is centered at E_{F} (green arrow).

The relative band shift as depicted in figure 7.11 (e) confirms this observation. In

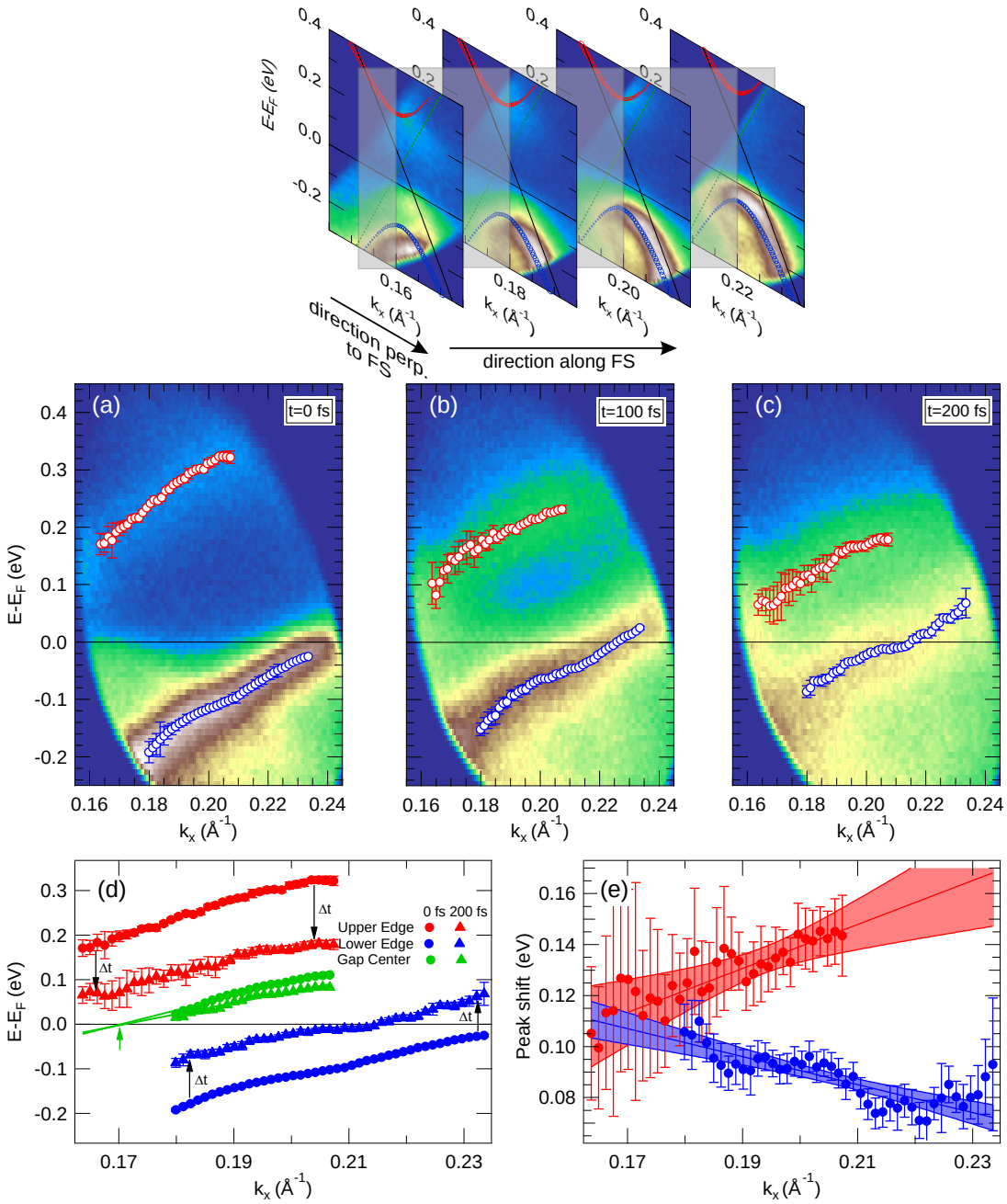

Figure 7.11: Momentum dependence of the CDW gap collapse. Top: Various Energy/momentum cuts perpendicular to the FS as a function of the direction along the FS. The gray plane indicates the integration area used for cuts parallel to the FS. (a-c) Energy/momentum maps corresponding to a cut along the FS for selected pump-probe delays. The k_x position is used as implicit coordinate. The position of lower and upper band edges along the FS determined from peak fits are indicated by blue and red markers, respectively. (d) Comparison of the position of the band edges for 0 fs and 200 fs. Note the change in slope of both upper and lower band edge with pump-probe delay and the asymmetry in shift magnitude. The center of the gap, shown as green symbols also shows a momentum-dependent shift. The solid green lines are linear fits of the gap center. (e) Momentum-dependent peak shift at $t = 200$ fs of lower and upper band edges. Solid lines and shaded areas are linear fits and 95% confidence bands, respectively.

the unoccupied band, we find an increase of the transient band shift[3] from 110 meV at $k_x = 0.165$ Å^{-1} to 145 meV at $k_x = 0.205$ Å^{-1}. A linear fit to the data yields a slope of $s_{\text{upper}} = 0.9(6)$ eVÅ. In the occupied band, we find the opposite behavior with a peak shift decreasing from 105 meV at $k_x = 0.18$ Å^{-1} to 80 meV at $k_x = 0.23$ Å^{-1}. Here, the fit yields a slope of $s_{\text{lower}} = -0.5(2)$ eVÅ, within error bars identical to the value of the unoccupied band, but of opposite sign. If we extrapolate the lower peak shift to small momenta, we find that the peak shift of both bands becomes comparable for $k_x \sim 0.17$ Å^{-1}, corresponding to a symmetric closing of the CDW gap around its center. Interestingly, this value perfectly coincides with the position where we found the gap centered at E_{F}.

This result indicates a correlation of the asymmetry in the closing of the gap with the distance of the gap center from the Fermi level, i.e. that the amount of peak shift depends on the position of the peak with respect to E_{F}. As already mentioned before, such a k-dependence of the closing of the gap is not encountered in the TB model, assuming only a time-dependent interaction strength V_1. Even more, the slightly stronger curvature of the bands for higher energies leads to a slightly smaller shift of the upper band [Moo12a]. Thus, the observed asymmetric gap closing indicates a transient modification of the nesting condition in addition to the transient reduction of the interaction strength. A possible scenario might be the modification of the TB coupling terms $t_{\parallel}$ and $t_{\perp}$, which influence the slope and curvature of the bands and hence the deviation from perfect nesting along the FS. In more detail, the shift of the gap center along the FS is determined by the curvature of the diamond-shaped FS, which is proportional to $k_{\perp}/k_{\parallel}$ [Bro08] and which vanishes in the limit of 1D bands, where $k_{\perp} = 0$ and perfect nesting of the whole FS is achieved. Thus, this scenario can also naturally explain the observed symmetric gap closing at the point of perfect nesting, i.e. where the gap is symmetric to E_{F}. Such a modification of the orbital overlap and hence the bonding strength is likely to occur under strong optical excitation due to the modifications of the screening potential by transiently excited electron-hole (e-h) pairs, which was also considered in the discussion of the faster gap collapse with increasing F. Indeed both softening and hardening of lattice electronic bonds haven been investigated theoretically and experimentally in various materials [Rec06, Ram08, Ern08, Ern09]. Thus, in this picture, the observation of the transient, k-dependent asymmetric gap shift allows to quantify the transient modification of the fundamental interactions like the orbital overlap in the system. Future experiments concentrating on larger areas of the FS and on the high-temperature, metallic phase might even observe a change in the band curvature directly on the FS. A transient modification of the CDW modulation vector q_{CDW} seems unlikely, as this would involve the formation of a different long-range periodic order in the system after optical excitation, which usually is associated with *disorder*. In addition, no significant change of the position of the CDW diffraction peak has been observed in recent experiments using time-resolved resonant soft x-ray diffraction [Moo12b].

As a final remark, the scenario of the transient modification of the band dispersion by the photo-doping should lead to a fluence dependence of the observed momentum-dependent asymmetry in the closing of the gap. Future evaluations of the fluence-dependent gap closing along the FS could thus provide further evidence for this scenario.

[3] The slightly smaller shift found here compared to the evaluation of figure 7.9 can be explained by a small shift already present at $t = 0$ fs and a slightly different k-space position analyzed here.

7.5 Coherent Excitation of the CDW Amplitude Mode

As we already recognized in figure 7.9 (d), at low excitation fluences $F \lesssim 0.5\,\mathrm{mJ/cm^2}$, the CDW band performs a coherent oscillation of the band position, which has a period of $\sim 500\,\mathrm{fs}$ and persists for several picoseconds. This oscillation was observed previously in our trARPES experiments on $TbTe_3$ and was assigned to the amplitude mode of the CDW order parameter at $f \sim 2.5\,\mathrm{THz}$ [Sch08a, Sch11a]. This assignment was based on the selective observation of this mode in the CDW band near k_F in the gapped region of the FS and its absence for higher temperatures, where the CDW was almost absent. Moreover, a coherently excited phonon mode at $f = 2.2\,\mathrm{THz}$ was found in measurements of the transient optical reflectivity in $TbTe_3$, $DyTe_3$ and $HoTe_3$, which showed a characteristic softening with temperature [Yus08]. A mode at $f \sim 2.2\,\mathrm{THz}$ showing a similar softening was also observed by Raman scattering in $DyTe_3$ and $LaTe_3$ [Lit08]. The softening of the mode was found in both studies to follow the predictions of mean-field theory [Grü94] close to T_CDW, on the basis of which the mode was assigned to the amplitude mode of the CDW, in agreement with our assignment [Sch08a].

In order to gain further insight into the nature of the amplitude mode oscillation and its precise manifestation in the electronic structure and the CDW gap, information on its influence on the occupied and unoccupied CDW band is of strong interest. As was already concluded earlier [Sch08a, Sch11a], the amplitude mode leads to an oscillation of the peak position of the occupied CDW band, as well as its amplitude and spectral width. In addition, at early times a strong downshift of the unoccupied band was observed, leading to an initial drop of the gap size [Sch11a] (see also figure 7.9). However, the occupation of the upper CDW band quickly decays and for $t > 300\,\mathrm{fs}$, only the oscillations of the occupied band can be observed[4]. In order to overcome this limitation and to investigate the temporal evolution of the unoccupied CDW band, a three-pulse experiment was designed, as depicted schematically in figure 7.12 (a). After excitation of the amplitude mode by the pump pulse $h\nu_\mathrm{Pump} = 1.5\,\mathrm{eV}$, a second pump pulse, termed population pulse $h\nu_\mathrm{Pop} = 1.5\,\mathrm{eV}$ repopulates the unoccupied CDW band, which is subsequently probed by the probe pulse $h\nu_\mathrm{Probe} = 6.0\,\mathrm{eV}$. Here, the delay of population and probe pulses was fixed at $t = 100\,\mathrm{fs}$ where the population of the upper CDW band is maximal and the pump-probe delay is measured between pump and probe pulses. In order to minimize the influence of the population pulse on the amplitude mode oscillation, a much weaker fluence $F_\mathrm{Pop} \ll F_\mathrm{Pump}$ was used. This way, the transient dynamics of both occupied and unoccupied CDW band can be observed.

Figure 7.12 (c) depicts the transient three-pulse-trARPES intensity as a function of pump-probe delay and energy $E - E_\mathrm{F}$, below and above E_F. Here, the intensity scale is enhanced by a factor $\times 30$ above E_F. After t_0, we find the characteristic oscillations of the amplitude mode in position of the occupied peak, where the dashed lines mark the maxima of the oscillations. In the unoccupied band, we find a weak intensity modulation with the amplitude mode, which is highlighted by the gray contour lines. Looking at the transient trARPES spectra shown on the right side for a maximum (blue) and minimum (green) of the oscillations in the lower band, we also recognize a shift in the band position of the unoccupied band, which exhibits an opposite sign with respect to the occupied band.

In order to analyze this in more detail, the peak positions of the occupied and unoccupied band are determined by Lorentzian line fits and the results are depicted in

[4] The transient gap size depicted in figure 7.9 (d) reflects the oscillation of the occupied band for $t > 300\,\mathrm{fs}$.

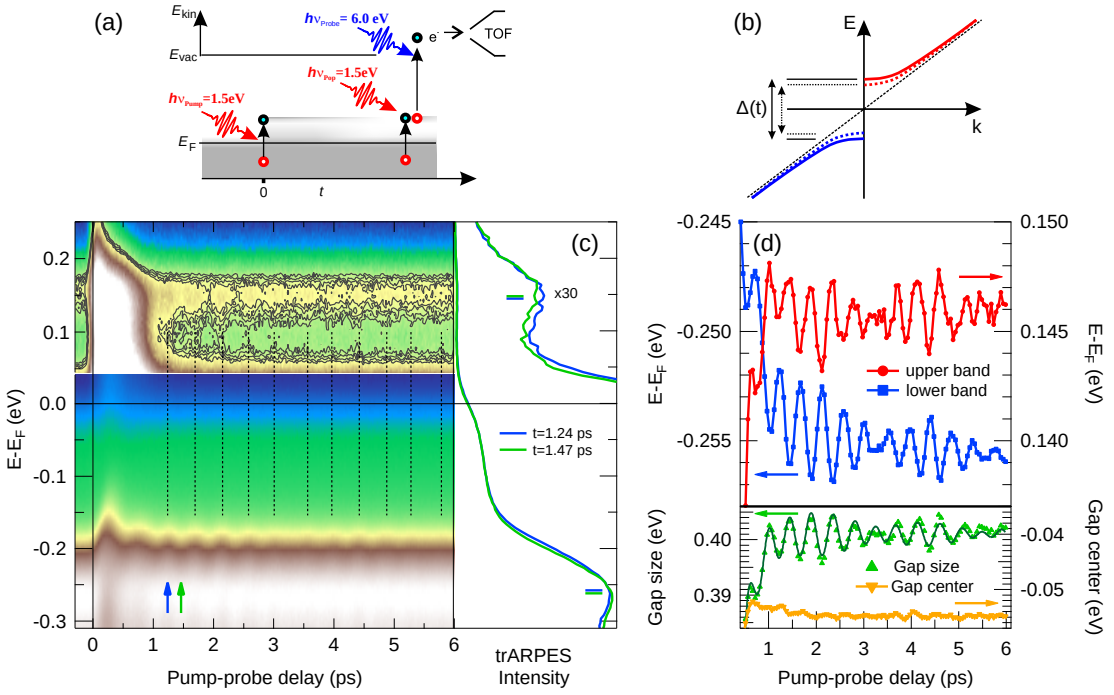

Figure 7.12: CDW gap modulation by the amplitude mode. (a) Sketch of the three-pulse experiment: After excitation of the amplitude mode oscillation by the pump pulse $h\nu_{\mathrm{Pump}}$ ($F = 240\,\mu\mathrm{J/cm^2}$), a second weaker pump pulse $h\nu_{\mathrm{Pop}}$ ($F = 90\,\mu\mathrm{J/cm^2}$) set at a fixed delay of $t_{\mathrm{Pop}} = 100\,\mathrm{fs}$ with respect to the probe pulse repopulates the unoccupied CDW band. The probe pulse $h\nu_{\mathrm{Probe}}$ monitors both occupied and unoccupied bands. (b) Sketch of the effect of the amplitude mode on the gapped dispersion of the CDW state, which transiently modulates the gap size (dashed curves). (c) Left: Three-pulse trARPES intensity of $TbTe_3$ as a function of pump-probe delay and energy $E - E_{\mathrm{F}}$ in a false color representation. The upper color scale is enhanced by a factor of $\times 30$. Dashed lines mark the positions of maxima of the lower peak position and contour lines highlight intensity oscillations in the upper band. Right: trARPES spectra at $t = 1.24\,\mathrm{ps}$ (blue) and $t = 1.47\,\mathrm{ps}$ (green) after excitation, corresponding to a maximum and minimum of the lower peak, respectively. (d) Top: Peak positions of lower (blue) and upper (red) CDW band edge determined by fitting of trARPES spectra. Both traces show an antipodal oscillation with the characteristic frequency of the amplitude mode, corresponding to a transient oscillation of the gap size. Bottom: Transient CDW gap size, $E_{\mathrm{upper}} - E_{\mathrm{lower}}$ and transient gap center $(E_{\mathrm{upper}} + E_{\mathrm{lower}})/2$. The solid line is a fit to the data (see text).

the upper panel of figure 7.12 (d). We clearly find oscillations of the same magnitude in the position of both bands with a frequency of $f \sim 2.2$ THz, which show a beating pattern with a period of $t \sim 3$ ps, indicating the presence of more than one mode. Most remarkable, the oscillations are clearly anti-correlated, where a maximum in the lower band corresponds to a minimum in the upper band and vice versa. This behavior corresponds to a transient oscillation of the gap size $\Delta_{\mathrm{CDW}} = E_{\mathrm{upper}} - E_{\mathrm{lower}}$, as depicted in the lower panel (green)[5]. In contrast, the gap center $E_{\mathrm{center}} = (E_{\mathrm{upper}} + E_{\mathrm{lower}})/2$ (yellow) shows virtually no oscillations.

A sketch of a simple linear band model shown in figure 7.12 (b) illustrates the effect of the amplitude mode: The linear dispersing band (dashed black line) is modified by the opening of a CDW gap of magnitude Δ_{CDW} at E_{F}, which is proportional to the CDW order parameter, and is split into lower and upper CDW band (solid blue and red lines). The excitation of the amplitude mode now modifies the magnitude of the gap, leading to a shift of both lower and upper CDW bands towards E_{F} (dashed lines) and to a transient gap size $\Delta(t)$. This is indeed the expected behavior for the influence of the amplitude mode of the CDW order parameter, which is the collective excitation of the amplitude of the complex order parameter $\Delta = |\Delta| \exp(i\phi)$ [Grü94] and hence the CDW gap size (see chapter 2.3.2). This result provides additional, very strong evidence that the oscillations observed in the lower CDW band indeed correspond to the amplitude mode oscillation.

The frequencies of the amplitude mode are analyzed by fitting the transient gap size with two damped oscillators and an exponential background function, depicted as dark green line in figure 7.12 (d). The fit, which shows a good agreement with the oscillations and the beating pattern, yields central frequencies of $f_1 = 2.230(6)$ THz and $f_2 = 1.77(2)$ THz, which agree very well with the frequencies observed in $TbTe_3$ with transient optical reflectivity [Yus08]. In our previous measurements, the 1.75 THz mode was not observed due to the limited scan range of these measurements [Sch11a], that did not allow to resolve the beating pattern. Also the ratio of amplitudes, $A_1/A_2 \sim 6$ agrees well with the observations of optical reflectivity [Yus08], indicating that indeed both methods are susceptible to the same coherent excitations. However, trARPES can provide additional inside by investigating the precise influence of the coherent excitation on the electronic band structure.

7.5.1 Temperature Dependence of the Amplitude Mode

The observation of the 1.75 THz mode in the amplitude oscillations of the CDW gap raises the question of its influence on the formation of the CDW state. To this end, the temperature dependence of the oscillations of the order parameter can provide additional information. Experiments using transient optical reflectivity [Yus08] and temperature-dependent Raman scattering data [Lit08] concluded on a resonant coupling of the amplitude mode, which follows a mean-field like softening with temperature, to the mode at 1.75 THz, which results in a mode mixing near the crossing of the two modes and a splitting of the modes, where the symmetries of amplitude and 1.75 THz mode are exchanged.

In order to establish a connection of the results obtained with transient reflectivity and Raman scattering experiments with the oscillations of the gap magnitude found in trARPES, the temperature dependence of the amplitude mode oscillations in trARPES

[5] The slightly smaller gap found here in comparison to the data presented in figure 7.7 can be explained by the fact, that the BZ position investigated here is closer to the diamond tip, where the total gap size is reduced due to the p_x/p_z interaction.

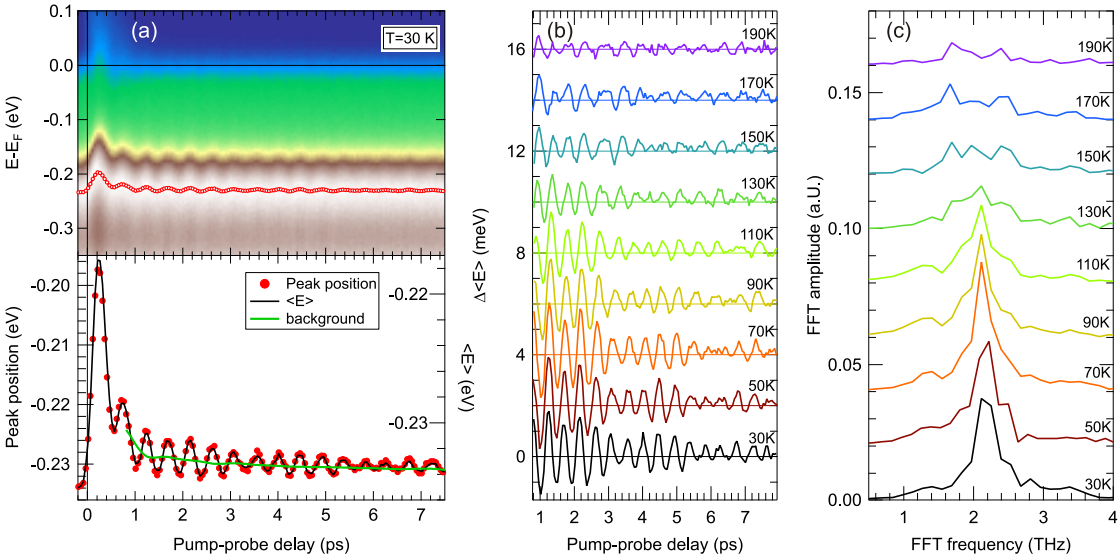

Figure 7.13: Evaluation of the amplitude mode oscillations. (a) Top: Transient trARPES intensity of $TbTe_3$ in false color representation. The red markers depict the transient position of the lower CDW peak determined by a peak fit. Bottom: Comparison of the fitted peak position (red markers, left axis) with the first moment $\langle E \rangle$ of trARPES spectral weight (black line, right axis). The oscillations are well represented by $\langle E \rangle (t)$. The green curve shows a fitted background function used to subtract the incoherent contribution. (b) Transient coherent shift $\Delta \langle E \rangle$ as a function of pump-probe delay for various temperatures. Traces are vertically offset for clarity. (c) Fast Fourier transformation (FFT) spectra for the data shown in (b).

is analyzed. As the close relation of the oscillation of the peak position of occupied and unoccupied CDW bands established above demonstrates a symmetric oscillation of the gap magnitude Δ_{CDW}, for the temperature-dependent measurements only the oscillation of the occupied band position is considered. The transient peak position of the occupied CDW peak as determined by line fitting from trARPES spectra of $TbTe_3$ at $T = 30\,\mathrm{K}$ is depicted in figure 7.13 (a) as red symbols. As the spectral shape deviates from a Lorentzian line shape for higher T and we want to avoid the model-based description by line fitting, an analysis based on the center-of-mass of trARPES spectra is performed [Sch11a]. The first moment of the spectral weight $I(E,t)$ in the proximity of the CDW peak, $\langle E(t) \rangle = \int_{E_0}^{E_1} I(E,t) E \,\mathrm{d}E / \int_{E_0}^{E_1} I(E,t) \,\mathrm{d}E$ is shown in the lower panel of figure 7.13 (a) as black line. We find a close agreement of the transient evolution of $\langle E(t) \rangle$ with the transient peak position, where especially the oscillations of the amplitude mode are nicely reproduced. The absolute shift of $\langle E(t) \rangle$ is considerably smaller than of the peak position, which however does not influence the determination of oscillation frequencies. For the removal of the incoherent contribution to the peak shift, which arises from the relaxation of the excited electronic system, a smooth background determined by cubic spline fitting is subtracted [Sch11a], as shown by the green line. Details of this background determination were discussed in chapter 5.3. The separation of the spline nodes for the background determination was chosen such that a satisfying suppression of frequencies $< 0.5\,\mathrm{THz}$ was achieved.

The resulting $\Delta \langle E(t) \rangle$ is shown for various temperatures in figure 7.13 (b), which demonstrates a drastic reduction of the oscillation amplitude with increasing T. In addition, a more complicated oscillation pattern is found for $T \gtrsim 130\,\mathrm{K}$, which complicates

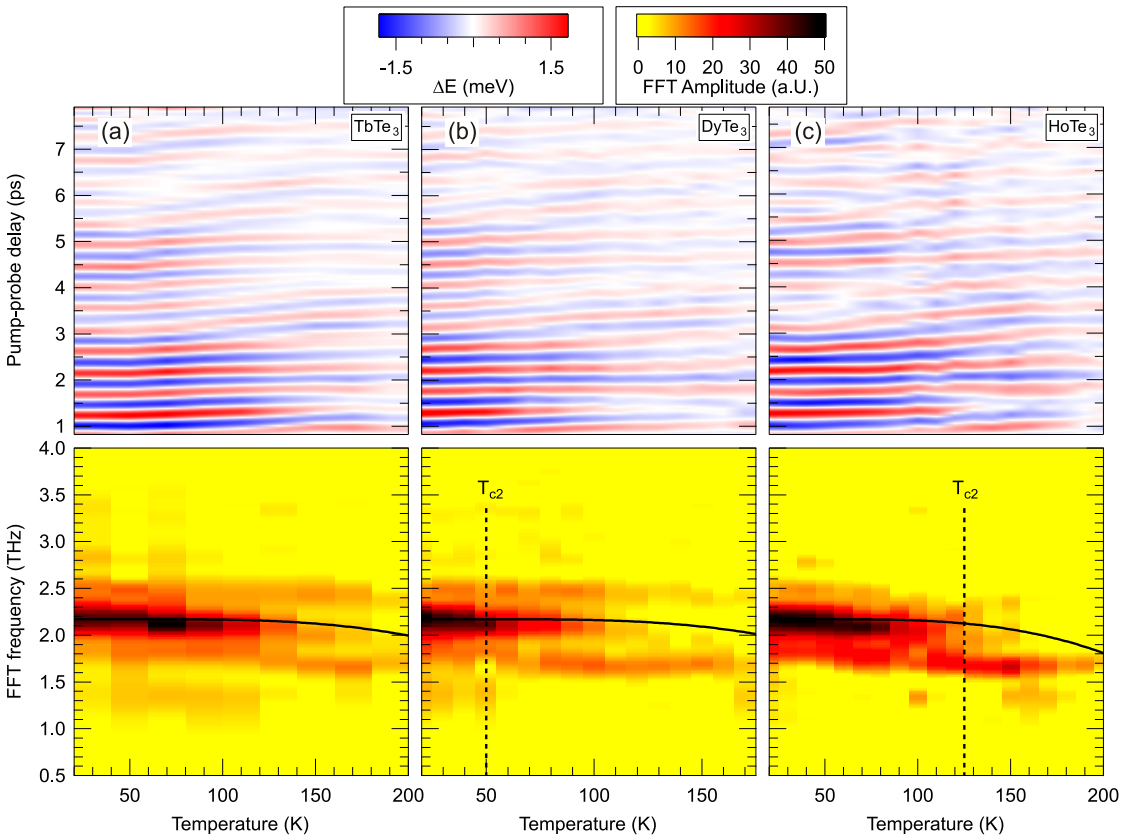

Figure 7.14: Temperature dependence of the amplitude mode oscillations. Top: Time- and temperature-dependent amplitude of the coherent oscillations of $\Delta \langle E(t) \rangle$ in (a) $TbTe_3$, (b) $DyTe_3$ and (c) $HoTe_3$ as a function of temperature and pump-probe delay in a false color representation. Bottom: Color coded FFT amplitude of (a) $TbTe_3$, (b) $DyTe_3$ and (c) $HoTe_3$ as a function of temperature and FFT frequency. The black lines denote the expected mean-field softening of the amplitude mode. For $DyTe_3$ and $HoTe_3$, T_{c2} is also indicated.

an analysis by fitting of sinusoidal functions. Instead, frequencies are determined by fast Fourier transformation (FFT), as depicted in figure 7.13 (c). While at lower T, the prominent peak of the amplitude mode at $f = 2.2\,\mathrm{THz}$ dominates the spectrum, this mode softens and decreases in intensity with T. At the same time, the 1.75 THz mode, which is only a weak shoulder at $T = 30\,\mathrm{K}$, becomes more intense and softens as well. In addition, we find weak modes at $f \sim 1.3\,\mathrm{THz}$ and $f \sim 2.6\,\mathrm{THz}$ which are also present in the optical reflectivity data [Yus08].

The representation of the oscillation amplitudes and FFT spectra as false-color maps shown in the upper and lower panels of figure 7.14 for $TbTe_3$, $DyTe_3$ and $HoTe_3$ as a function of temperature allows for a comparison of the temperature evolution of the oscillations in the three compounds. For sake of clarity, a band pass filter has been applied to the oscillation amplitudes to further remove low frequency components ($f < 0.5\,\mathrm{THz}$ and high-frequency noise ($f > 4.5\,\mathrm{THz}$). The temporal shift of the oscillation phases with temperature visible in the temperature- and time-dependent oscillation amplitudes evidences the softening of the main mode in all three compounds, in addition to the decrease of oscillation amplitude for higher T. In the FFTs presented in the lower panels, the black lines depict the expected behavior for a soft mode in the mean-field

theory [Grü94], which closely follows the temperature dependence of the order parameter, see chapter 2.3. Within the investigated temperature range, we find qualitative agreement with the mean-field behavior. However, especially in $TbTe_3$, the experimental data show even stronger softening than predicted by the mean-field theory. This could be explained by the effect of the pump fluence $F \sim 250\,\mu J/cm^2$, which leads to a higher effective temperature in the experiment due to transient sample heating. This effect is expected to be stronger when approaching T_{CDW}, as the applied fluence might drive the system closer to the melting threshold of the CDW phase at higher T, where the CDW condensate density is weaker. Such a behavior is indeed observed in the fluence dependence at higher T, where the softening of modes is partly reduced when lowering the pumping fluence.

While we do not observe the crossing of the amplitude mode and the 1.75 THz mode explicitly in our data due to the limited temperature range, we clearly find the latter mode also in trARPES and find its typical mode softening, indicating the presence of mode mixing with the amplitude mode. This corroborates the strong coupling of this mode to the CDW order parameter and hence its importance for the CDW formation in RTe_3. The softening of the mode at 2.6 THz also indicates the coupling of this mode to the CDW formation, in agreement with [Yus08]. Similar to this study, we do not observe any clear indication for the influence of the second CDW transition on the coherent oscillations. This is, however, probably understood from the fact, that we probe the amplitude mode at the *large* gap, whereas a possible amplitude mode of the second CDW would couple to the *small* gap. In principle, trARPES provides the tool to selectively investigate the small gap, and first measurements in $HoTe_3$ indicate an oscillation of similar frequency that modulates the small gap. However, further investigations are necessary to unambiguously clarify this point.

7.5.2 Coherent Control

The observation of both the 2.2 THz and the 1.75 THz mode in the transient oscillations of the order parameter raises the question, how far these modes are mutually coupled and influence each other or whether they independently modulate the CDW gap. The mode crossing of the two modes observed in transient reflectivity and Raman scattering indeed suggests a substantial coupling, especially near the crossing point of the modes. Additional insight into this coupling can be gained from coherent control experiments, where a second time-delayed pump pulse is employed to control the oscillation of a coherent phonon excited by the first pump pulse. Such coherent control of coherent phonon oscillations has been demonstrated in a number of materials [Dek93, Has96, DeC01, Roe04, Mur05, Ono07, Mis07a, Mis07b], including the selective excitation of certain vibrational modes [Tak09, Oka11] and asymmetric control schemes exploring collective dynamics in correlated material systems [Yus10, Kus11]. A sketch of the coherent control experiment is shown in figure 7.15 (a). In this three-pulse experiment, two excitation pulses $h\nu_{Pump1}$ and $h\nu_{Pump2}$ of equal fluence $F \sim 250\,\mu J/cm^2$ separated by the pump-pump delay t_{12} were used. The first pump pulse excites the amplitude mode oscillation at t_0, and the second pump pulse is used for coherent control of the oscillations, coherently enhancing or suppressing the oscillations depending on t_{12}. The resulting oscillations are observed by the probe pulse after the pump-probe delay t. Here, for each scan, t_{12} was held fix and multiple scans for various t_{12} were performed.

The three-pulse trARPES intensities for a pump-pump delay of $t_{12} = 0.67$ ps and $t_{12} = 0.93$ ps are shown in figure 7.15 (b) and (c), corresponding to a coherent suppression and enhancement of the amplitude mode oscillation, respectively. The XCs of

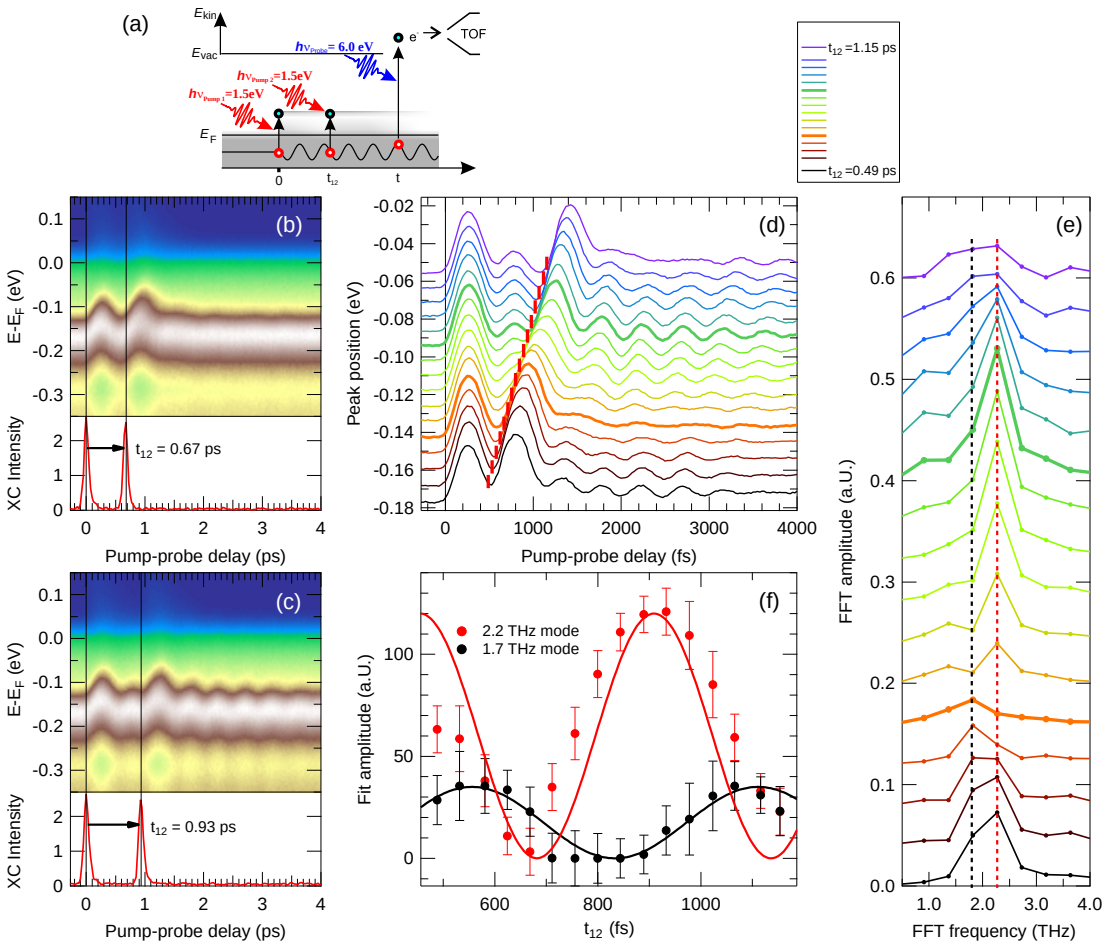

Figure 7.15: Coherent control of the amplitude mode. (a) Experimental scheme of the 3-pulse setup used for the coherent control experiments. The separation of the two pump pulses, t_{12} was set fixed for each experiment. (b) trARPES intensity of $DyTe_3$ for a pump-pulse separation $t_{12} = 0.68$ ps, corresponding to a coherent quench of the amplitude mode oscillation (out-of-phase). The lower panel shows the XC trace of the two pump pulses with the probe pulse obtained from electrons with $E - E_F > 1.3$ eV. (c) trARPES intensity for a pump-pulse separation $t_{12} = 0.93$ ps, corresponding to a coherent enhancement of the amplitude mode oscillation (in-phase). (d) Transient peak position of the lower CDW peak as a function of pump-probe delay for various pump-pulse separations t_{12}, indicated by red markers. The data corresponding to the situation in (b) and (c) are highlighted by thick orange and green lines, respectively. Traces are vertically offset for clarity. (e) FFT amplitude for various t_{12}. Positions of the 1.75 THz and 2.2 THz mode are marked with black and red vertical lines, respectively. (f) Fitted FFT amplitude of the 1.75 THz (black) and 2.2 THz (red) mode as a function of pump-pulse separation t_{12}. Solid lines are fits to equation (7.6).

the two pump pulses with the probe pulse are depicted in the lower panels, showing the positions and equal excitation amplitudes of both pump pulses. We clearly recognize the efficient suppression of the amplitude mode oscillation at $f = 2.2\,\mathrm{THz}$ in (b), whereas the oscillation is enhanced in (c). The transient peak position of the lower CDW peak determined by line fits is shown for various pump-pump delays t_{12} in panel (d), where the arrival of the control pulse is indicated by the red markers. After the initial shift of the peak position associated with the arrival of each pump pulse, the coherent oscillations are well resolved in all cases. Traces of out-of-phase and in-phase excitation, corresponding to (b) and (c) are highlighted by thick orange and green lines, respectively.

In order to quantify the coherent control of the amplitude mode, FFT traces obtained from the transient peak position after background subtraction for $t > 2\,\mathrm{ps}$ are shown in figure 7.15 (e). The position of the two modes at $f = 2.2\,\mathrm{THz}$ and $f = 1.75\,\mathrm{THz}$ are marked by red and black dashed lines, respectively. While both peaks are present at $t_{12} = 0.49\,\mathrm{ps}$ (bottommost curve), at $t_{12} = 0.68\,\mathrm{ps}$ (orange curve), the intensity of the amplitude mode is almost completely suppressed, and only the weak mode at 1.75 THz remains. Similarly, at $t_{12} = 0.93\,\mathrm{ps}$, only the enhanced oscillation of the amplitude mode is observed and the 1.75 THz mode is absent. A fit of two Lorentzian line shapes centered at $f = 1.75\,\mathrm{THz}$ and $f = 2.2\,\mathrm{THz}$ to the FFT spectra is used to determine the FFT amplitudes, which are shown in figure 7.15 (f) as a function of pump-pump delay t_{12} as black and red symbols, respectively. Neglecting the decay of the coherent oscillations between the two pump pulses, the coherent oscillation amplitude $A(t_{12})$ of independent modes can be described by [Ono07]

$$A(t_{12}) = \frac{A_0}{2}\left[1 + \cos(f \cdot t_{12} \cdot 2\pi)\right] \quad , \tag{7.6}$$

where f is the frequency of the oscillation and A_0 is the maximal amplitude for resonant excitation with both pump pulses. Fits to equation (7.6) are shown as solid black and red lines in figure 7.15 (f) for the 1.75 THz and 2.2 THz mode, respectively.

While the description with this model captures the general behavior of both modes and especially their different periods with t_{12} very well, and hence indicates the applicability of the model, certain deviations especially for the amplitude mode at $f = 2.2\,\mathrm{THz}$ are found and worthwhile to be discussed. Whereas we find a large amplitude of the 2.2 THz mode of $A_{2.2\,\mathrm{THz}} \sim 120$ for $t_{12} \approx 930\,\mathrm{fs}$, corresponding to an in-phase excitation after two periods of this mode, at $t_{12} \approx 480\,\mathrm{fs}$ (in-phase excitation after one oscillation period) the amplitude reaches only half that value. This is indeed remarkable as the decay of the coherent excitation by the first pulse, neglected in the model would lead to a higher amplitude at smaller t_{12}. Interestingly, the amplitude of the 1.75 THz mode is almost maximal at $t_{12} \approx 480\,\mathrm{fs}$, whereas this mode is almost absent at $t_{12} \approx 930\,\mathrm{fs}$. Thus, a possible competing interaction of the two modes might explain the observed difference in amplitudes. As these modes both modulate the amplitude of the CDW order parameter, they couple to the same degrees of freedom. Recent time-resolved resonant soft x-ray scattering results for $TbTe_3$ indicate that the 1.75 THz mode might be connected to out-of plane motions of Te towards the Tb atoms, as this mode is most prominently detected for resonant transitions at the Tb sites [Moo12b]. Thus, the presence of such motions might limit the remaining degrees of freedom for in-plane oscillations of Te atoms and hence explain the reduction of the 2.2 THz oscillation amplitude at $t_{12} \approx 480\,\mathrm{fs}$.

Another deviation of the amplitude of the 2.2 THz mode from the simple model is found in the rising and falling edges of the resonance at $t_{12} \approx 930\,\mathrm{fs}$. Here, we find a quicker increase of $A_{2.2\,\mathrm{THz}}(t_{12})$ than predicted and a slower decrease, leading to an apparent stabilization of the mode amplitude even for slightly off-resonant conditions.

In this case, the presence or absence of the 1.75 THz mode cannot explain the observed deviations, as it is absent at the rising edge and almost maximal at the falling edge, respectively. Thus, a higher signal at the rising edge and a lower signal at the falling edge would be expected. This effect could be an artifact due to the phase shift occurring to the oscillations when crossing the resonance condition, which leads to a deviation of the FFT spectra from Lorentzian line shapes. Here, a systematic analysis in the time domain including the phases of the oscillations might provide deeper insight. However, the measured range up to 4 ps might be too short to unambiguously determine at least eight free parameters in the model (two damped oscillators with amplitude, frequency, damping constant and phase each, compare figure 7.12 (d)). Another possible explanation might be a nonlinearity in the dependence of the oscillation amplitude from the excitation fluence, which would result in a saturation of the oscillation amplitude, compatible with the experimental observation. A detailed fluence dependence of the (single excitation pulse) oscillation amplitude might help to reveal such nonlinearities.

Furthermore, additional insight into the collective nature of the amplitude mode oscillations can be gained from the coherent control experiments. The concept of the collective nature of the CDW amplitude mode oscillation represents a coherent *macroscopic* oscillation of the charge and lattice order in the system. This, in combination with the very large coherence length in the μm range, three to four orders of magnitude larger than the lattice constant [Ru08] raises the question if this coherence is maintained after optical excitation or whether the observed modes rather correspond to local excitations of the amplitude mode and the large-scale coherence is lost after excitation. Traditionally, the amplitude mode oscillations are considered as delocalized oscillations of the atomic displacement $\delta U(t)$ [Grü94], as depicted in figure 7.16 (a), top. All displaced atoms of a linear chain with a Peirls instability oscillate in-phase towards their undistorted positions, leading to a coherent oscillation of the charge density. The coherent control of the system leads to the enhancement or attenuation of the amplitude of the delocalized oscillation, and a complete quench of the amplitude mode oscillation leads to a global suppression of the oscillations in the displacement $\delta U(t)$ (bottom).

Alternatively, one might consider a large number of localized oscillators $\delta u(t)$, where only some oscillators are initially excited by the pump pulse, as depicted in figure 7.16 (b), top. Now, the control pulse would lead to the excitation of a different subset of oscillators $\delta u(t)$, with an oscillation phase corresponding to the pump-pump separation t_{12}. In case of a complete quench of the oscillations as depicted in the bottom part, this corresponds to an out-of-phase oscillation of initially excited oscillators (red) and oscillators excited by the control pulse (green). Such a scenario was suggested by Lobad *et al.* for coherent excitations in the cuprate HTSC $YBa_2Cu_3O_{7-\delta}$ [Lob01].

Measurements of the transient optical reflectivity, as traditionally employed for the study of coherent phonons [Dek00, Ish10] cannot distinguish between the two scenarios, as the coherent superposition of many localized oscillators generates the same transient signal as one delocalized phonon field. Especially in the case of a complete coherent quench, a suppression of the delocalized oscillations produces the same transient reflectivity signal as an equal number of localized oscillators oscillating exactly out-of-phase. In contrast, the spectral resolution provided by trARPES enables the detection of the specific influence of the oscillating modes on the electronic structure on an absolute energy scale. Thus, trARPES allows for a distinction of the two cases of coherent control of a delocalized oscillator or superimposed oscillations of localized oscillators by analyzing the transient oscillations of the peak shift, as will be discussed in the following.

In order to illustrate the effect of the two scenarios discussed above on the transient

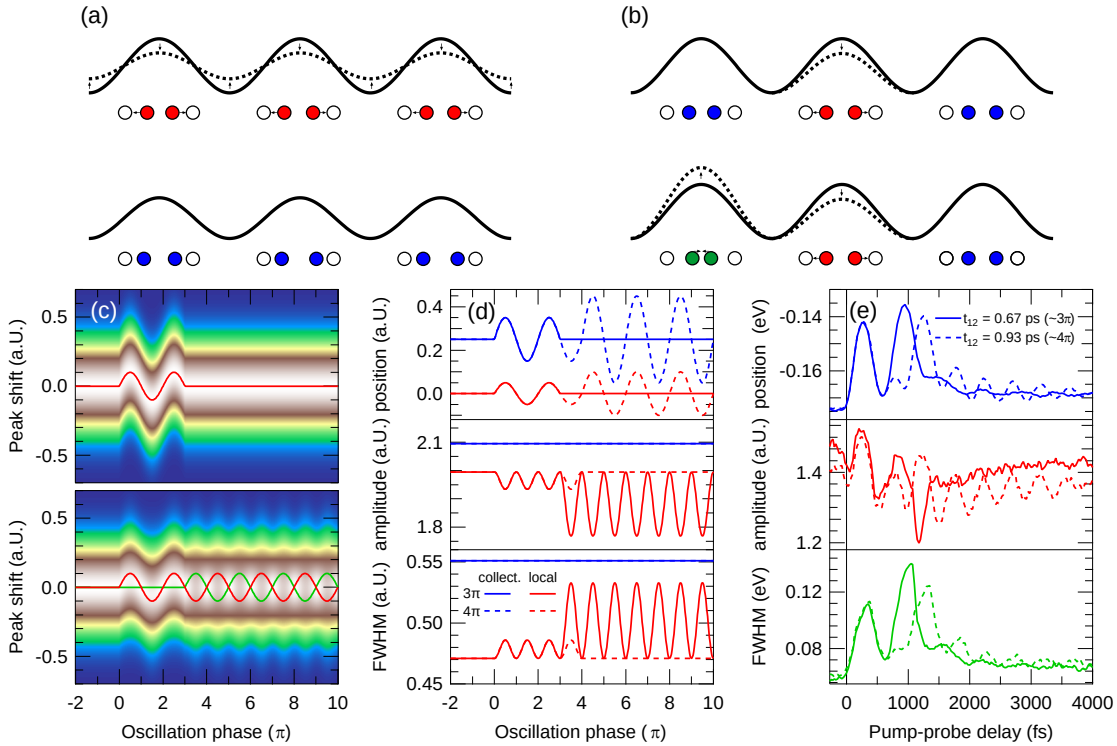

Figure 7.16: Effect of the coherent control. (a) Sketch of the coherent quench of the amplitude mode. Top: Before the quench, all atoms oscillate in a delocalized, collective mode around their equilibrium position. The atomic motions and the modification of the charge density is indicated. Bottom: After the quench, the delocalized coherent motion is stopped and all atoms rest at their equilibrium position. (b) Sketch of the coherent quench of a localized coherent mode. Top: Before the quench, only a fraction of atoms oscillate around their equilibrium position (red), while others remain still (blue). Bottom: The quench pulse excites another fraction of atoms (green) to an oscillation which is out-of-phase with the atoms excited by the first pump pulse (red). (c) Simulation of the transient spectral weight for an oscillating peak position, for the scenario shown in (a) (top) and (b) (bottom) as a function of oscillation phase Φ. The peak position of the two oscillating subsets is indicated with red and green lines. The quench occurs at $\Phi = 3\,\pi$. (d) Peak position (top), peak amplitude (middle) and peak width (FWHM, bottom) determined from the simulation for the scenario shown in (a) (blue) and (b) (red). Traces are vertically offset for clarity. Solid and dashed lines show the situation for an out-of-phase ($\Phi = 3\,\pi$) and in-phase ($\Phi = 4\,\pi$) situation, respectively. (e) Experimental peak position (top), peak amplitude (middle) and peak FWHM (bottom). Solid and dashed lines represent a pump-pulse separation of $t_{12} = 0.67$ ps and $t_{12} = 0.93$ ps, corresponding to $\Phi = 3\,\pi$ and $\Phi = 4\,\pi$, respectively.

trARPES signal, a simulation of transient trARPES traces is performed, as shown in figure 7.16 (c). In the case of the coherent control of a delocalized mode, we consider a Gaussian line shape in the energy domain,

$$I_{\text{collective}}(E,t) \propto \exp\left(-\frac{[E-E_c(t)]^2}{2\sigma}\right) \quad , \tag{7.7}$$

where the peak position $E_c(t)$ is modulated by the coherent phonon mode and σ defines the width of the peak. The resulting trARPES intensity for a coherent quench at $\Phi = 3\pi$ is shown in figure 7.16 (c), top as a function of the oscillation phase Φ and energy. The peak position of the oscillation is marked by the red line. After the quench, the coherent oscillation of the peak position is suppressed and the situation before excitation is recovered.

To simulate the effect of a superposition of local oscillators with opposite phases, two Gaussian peaks corresponding to the two subsets of oscillators are considered:

$$I_{\text{localized}}(E,t) \propto \exp\left(-\frac{\left[E-E_c^1(t)\right]^2}{2\sigma}\right) + \exp\left(-\frac{\left[E-E_c^2(t)\right]^2}{2\sigma}\right) \quad . \tag{7.8}$$

Here, the peak position of the two subsets $E_c^1(t)$ and $E_c^2(t)$ are modulated by the initial pump pulse and the control pulse, respectively. The simulated trARPES signal for the coherent quench at $\Phi = 3\pi$ is shown in figure 7.16 (c), bottom, where the red and green traces correspond to the two peak positions $E_c^1(t)$ and $E_c^2(t)$, respectively. Similar to the situation in the collective model, the oscillations of the peak position are suppressed after the coherent quench. However, now we recognize strong modulations of the peak amplitude and width with twice the oscillation frequency.

This effect is immediately obvious when comparing the peak position, amplitude and width of the two scenarios as determined by fitting of the simulated trARPES spectra, shown in figure 7.16 (d). Traces of the collective and localized model are shown as blue and red curves, and the situation of coherent quench ($\Phi = 3\pi$) and coherent enhancement ($\Phi = 4\pi$) corresponds to solid and dashed curves, respectively. While we cannot distinguish the two models from the oscillations of the peak position, a modification of the peak amplitude and width only occurs for the localized model. While this modification is very weak for the coherent enhancement and might be blurred by the strong oscillations in peak position in this case, oscillations of the width and amplitude in the case of a coherent quench are very pronounced and should be detectable in the experiment.

Figure 7.16 (e) shows the experimental peak position, amplitude and FWHM as determined from line fits to the data for the limiting cases of coherent quench ($t_{12} = 0.67\,\text{ps}$, $\Phi \sim 3\pi$, solid lines) and coherent enhancement ($t_{12} = 0.93\,\text{ps}$, $\Phi \sim 4\pi$, dashed lines). In the experimental data, we find coherent oscillations of the peak position, amplitude and width. The oscillations of the peak position nicely fit the expectations of both models, neglecting the initial rise of the peak position and the residual oscillations of the 1.75 THz mode after the quench. The oscillations found in the peak amplitude and width seem to favor the localized model on the first glance. However, a closer look reveals that the strength of these oscillations is correlated with the oscillation of the peak position and that they are strongest in the case of coherent enhancement (dashed curve), in contrast to the localized model prediction. In addition, the frequency of these oscillations is identical to the amplitude mode oscillations, whereas the modulations of width and amplitude in the localized model occur with twice the frequency. These

oscillations of peak amplitude and width are indeed also present with a single pulse excitation, and are intrinsic properties of the amplitude mode oscillations, that were not accounted for in the model. Thus, the absence of the oscillations with twice the amplitude mode frequency in the width and amplitude of the peaks is incompatible with the localized oscillator scenario.

In conclusion, the deviations of the experimental data from the predictions of the localized oscillator model demonstrate that the coherent oscillations of the amplitude mode represent delocalized *macroscopic* oscillations of the order parameter in RTe_3, as expected from the collective excitations in the mean-field theory and indicate that the coherent control of the mode indeed leads to enhancement or quench of the global amplitude of the oscillation and large scale phase coherence is maintained.

Summary

In summary, we investigated the occupied and unoccupied equilibrium band structure of the prototypical, low-dimensional charge density wave (CDW) model system RTe_3 and its response to optical excitation in the strong and weak perturbation regime. The laser-based angle-resolved photoemission spectroscopy (ARPES) data presented for $HoTe_3$ with two successive CDW transitions reveal a richness of details of the occupied band dispersion. The general trend is found to be well described by a simple Tight-Binding model of a single square net of Te atoms. The superior momentum and energy resolution of the laser ARPES setup allows for the first time to detect the real bilayer splitting of the material, and additional split-off bands, originally assigned to the bilayer splitting were discussed to originate from surface contributions to the ARPES spectra. The temperature dependence of the CDW gap size was found to deviate slightly from the mean-field theory for the large gap, which was discussed in terms of a possible interaction of the two CDW gaps.

Using time- and angle-resolved photoemission spectroscopy (trARPES) and employing a newly developed position-sensitive time-of-flight (pTOF) spectrometer, we were able to investigate the occupied and unoccupied electronic structure of $TbTe_3$ around the Fermi level, which allows us to determine the precise distribution of the CDW gap along the Fermi surface (FS) which was found to be well described by the scenario of FS nesting driven CDW formation used for the Tight-Binding (TB) model. In addition, this method enables to determine for the first time the real magnitude of the CDW gap $\Delta_{\mathrm{CDW}} \approx 0.46\,\mathrm{eV}$ in $TbTe_3$, which is difficult to measure by other, momentum-integrating methods. A discontinuity of the dispersion of the large CDW gap along the FS was observed both in the occupied and unoccupied states and several scenarios for its origin were discussed. The most likely explanation for this discontinuity is the bilayer splitting in the system, which separates the gapped dispersion of the CDW band into two gapped bands along the FS.

Furthermore, we presented the first fs time-resolved FS mapping enabled by the pTOF spectrometer. In the strongly perturbed regime, we observe an ultrafast collapse of the CDW gap, which leads to a recovery of the metallic normal-state FS and a depletion of spectral weight in the CDW shadow bands within $\approx 200\,\mathrm{fs}$. The gapped dispersion of lower and upper CDW bands is found to merge into a nearly linear, metallic dispersion within the same timescale. The good momentum resolution and access to the Brillouin zone (BZ) allow to determine the transient CDW gap size as a function of fluence, which is found to exhibit strongly anharmonic and damped oscillations. These oscillations are discussed to be induced by the atomic movements in the transient energy potential landscape of the collapsing CDW order, and their fluence-dependent acceleration points to a strong influence of the modification to the screening by the excited electronic system. A residual minimal gap size $\Delta^{\mathrm{min}}_{\mathrm{CDW}} \sim \frac{1}{3}\Delta^{0}_{\mathrm{CDW}}$, which is found to be fluence independent challenges the earlier conclusion on a complete collapse of the CDW gap and several explanations are discussed. In addition, we observe an asymmetric closing of the CDW gap, which depends on the relative position of the gap with respect to the Fermi level. This asymmetric closing of the gap, which is not found in the TB model, could be explained by a transient modification of the nesting conditions, possibly caused by a change of the transient orbital overlap within the Te planes. These results demonstrate the fundamental differences of the transient state after photoexcitation from the metallic high-temperature state, which are only accessible with a non-equilibrium probe such as trARPES and highlight the rich information on the non-equilibrium state that can be gained from such techniques.

In the limit of weak perturbation, we observe the coherent oscillations of the CDW amplitude mode. Using a three-pulse experiment, we are able to determine its precise influence on the gapped dispersion of the CDW bands. The oscillations are found to modulate the transient size of the CDW gap, which further strengthens their assignment to the CDW amplitude mode. The analysis of the frequencies of the oscillations reveals two main contributions at 2.2 THz and 1.75 THz, where the latter has not been detected in trARPES before. In addition, the temperature dependence of the amplitude mode oscillations is analyzed in $TbTe_3$, $DyTe_3$ and $HoTe_3$ and a softening of the modes as predicted by the mean-field theory is found, in agreement with observations in transient reflectivity and Raman scattering. Finally, the coherent control of both modes found in the coherent oscillations is demonstrated, indicating coupling between the 2.2 THz and 1.75 THz mode. The energy resolution of trARPES allows to distinguish the coherent control of collective delocalized oscillations from a superposition of many localized oscillators and demonstrates the collective nature of the amplitude mode oscillations.

8 Conclusions and Outlook

The present thesis investigated the ultrafast electron dynamics in correlated, low-dimensional model systems. In such materials, the strong electron-electron (e-e) correlations or coupling to other degrees of freedom such as the lattice within the complex many-body quantum system can give rise to new, emergent properties that are characterized by phase transitions into broken-symmetry ground states such as magnetic, superconducting or charge density wave (CDW) phases. The investigation of the dynamical processes related with order like transient phase changes, collective excitations or the energy relaxation within the system allows deeper insight into the complex physics governing the emergence of the broken-symmetry state. These fundamental questions have been addressed in a number of model systems for broken-symmetry ground states like high-T_c superconductors (HTSCs) or prototypical CDW materials using time- and angle-resolved photoemission spectroscopy (trARPES). In addition, the dynamical modification of the charge balance at interfaces in heterostructures was investigated.

Summarizing, in **epitaxial films of Pb on Si(111)** an ultrafast energy gain of occupied quantum well states (QWSs) and of states located at the Pb/Si interface is observed. From the coverage dependence of this energy gain, a sudden modification of the delicate charge balance at the Pb/Si interface in the heterostructure is identified as origin, which results in a shift of the energetic band alignment at the interface. The related change of the QWS confinement and the resulting modification of the QWS line shape and position demonstrates the influence of the quantum confinement on QWS wave functions in a descriptive manner. In addition, a coherent oscillation of the QWS binding energy around 2 THz is observed at high excitation densities, which is assigned to the excitation of a coherent surface phonon mode, mediated by the charge redistribution within the QWS system. This demonstrates how the broken symmetry along the film normal and the quantum confinement facilitate the generation and observation of coherent lattice vibrations in a simple *sp*-metal.

The sensitivity of the QWS confinement to the interfacial structure and energy alignment suggests future experiments on epitaxial metal films on different substrates, e.g. in Pb/Cu(111) [Dil04, Mat10] or Pb/SiC [Dil07], or with different interface structures [Dil06, Slo11]. In addition, angle-dependent measurements might provide additional information. A predicted oscillation of the surface phonon frequency with film thickness [Ynd08] could be investigated in future thickness-dependent experiments at high excitations fluences. Here, also an investigation of the oscillations in the unoccupied states using a three-pulse experiment might be of interest, as the influence of the surface phonon mode is predicted to be stronger in the unoccupied QWSs [Ynd08].

Experiments on the **Fe pnictides**, the recently discovered novel class of HTSCs, investigated a variety of interesting features. Temperature-dependent measurements on the parent compounds $EuFe_2As_2$ and $BaFe_2As_2$ revealed a strong asymmetry of electron and hole relaxation rates around the hole pocket at the Brillouin zone (BZ) center. In the antiferromagnetic (AFM) phase at low temperatures, the restricted phase space for relaxation of electrons at Γ and a spin-relaxation bottleneck lead to a slow recovery of AFM ordering with $\tau = 800$ fs, while relaxation of holes occurs via electron-phonon (e-ph) scattering and is more than four times faster. Two distinct timescales found in the initial collapse of the spin density wave (SDW) gap indicate the importance of coupling

between spin and lattice degrees of freedom. Furthermore, strong coherent oscillations of the photoelectron intensity observed also in electron doped $BaFe_{1.85}Co_{0.15}As_2$ are identified with the excitation of coherent phonon modes. Three distinct modes are found, where the strongest mode is identified with the As A_{1g} mode, which modifies the shape of the FeAs tetrahedra and might be relevant for superconductivity. The coherent modes are found to modulate the transient chemical potential throughout the BZ, corroborating their strong coupling to states at E_F. Three methods for determination of the average e-ph coupling constant λ are compared and a small value of $\lambda < 0.15$ is found, making the e-ph interaction in combination with a conventional pairing scenario an unlikely origin of superconductivity in the Fe pnictides.

Future experiments on the Fe pnictides will include experiments in the superconducting state and at low excitation densities, which will enable a direct comparison to the dynamics in the cuprate HTSCs. However, due to the comparably low transition temperatures, this requires an improvement of the sample cooling in the current setup. In addition, the nature of the coherent phonon modes could be determined in future studies by replacing the constituting atoms with isovalent counterparts with significantly different masses, such as P substitution at the As sites [Thi11] or by investigating e.g. $CaFe_2As_2$. In this respect, also experiments on 1111 or 111 compounds might be instructive.

The relaxation dynamics in the superconducting (SC) and normal state of the **cuprate HTSC $Bi_2Sr_2CaCu_2O_{8+\delta}$ (BSCCO)** was analyzed at various positions of the Fermi surface (FS). The coherent SC peak found for small FS angles near the antinodal region allows to directly monitor the suppression and reformation of the SC condensate. In the SC state, a momentum- and fluence-independent relaxation time $\tau \sim 2.5$ ps of excited quasiparticles (QPs) is found in a regime of weak excitation. Employing the momentum sensitivity of trARPES, we can exclude momentum scattering of QPs towards the nodal line and identify recombination of transiently stabilized QPs into Cooper pairs (CPs) as dominating relaxation channel. These results demonstrate the first observation of SC condensate dynamics using trARPES and are of relevance for the interpretation of transient optical reflectivity measurements, which lack the momentum resolution to distinguish these different relaxation channels. In addition, from the observed momentum dependence of the excitation amplitudes and decay times we conclude that BSCCO is in the strong bottleneck regime, where the reformation of the SC condensate is dominated by the decay of gap-energy bosons. In the normal state for $T > T_c$ and for higher excitation densities in the SC state, we find a considerably faster and and momentum-dependent relaxation with increasing relaxation times towards the antinode, which can be related to the relaxation across the pseudogap.

In order to clarify the influence of the pseudogap on the relaxation, an investigation of clearly overdoped samples without the occurrence of a pseudogap is suggestive. In addition, this might enable a more clear-cut analysis of the transient SC gap. In this regard, also future experiments with a better energy resolution compromising temporal resolution [Gra11, Sob12] could simplify a model description of transient trARPES spectra and establish a more profound understanding of the transient SC state. For an investigation of the influence of a thermal QP population on the QP recombination, additional detailed temperature-dependent studies are of interest. Furthermore, an excitation using THz radiation with photon energies in the order of or below the SC gap size could provide deeper insight into the nature of the d-wave gap.

Finally, the electronic structure and the dynamics of the **prototypical, quasi-one-dimensional CDW material RTe_3** (R = rare-earth) have been investigated. The occupied band structure of $HoTe_3$, which shows a remarkable agreement with a simplified Tight-Binding (TB) description, is investigated using high-resolution laser-based angle-resolved photoemission spectroscopy (ARPES), revealing a variety of details that go beyond the description by the TB model, such as the bilayer splitting of the material and additional split-off bands assigned to surface contributions. Employing a novel position-sensitive time-of-flight (pTOF) spectrometer, the unoccupied band structure of $TbTe_3$ is investigated by trARPES, allowing to verify the validity of the TB model also for the unoccupied states. In addition, our measurements allow to determine the full gap size in $TbTe_3$ of $\Delta_{CDW} \approx 0.46\,eV$. A discontinuity in the CDW gap distribution is observed in both occupied and unoccupied states and discussed on the basis of the bilayer splitting. The pTOF enables us to obtain the first time-resolved FS map, which allows to observe the ultrafast closing of the CDW gap and the reformation of a continuous, metallic FS within $< 200\,fs$ after sufficiently strong optical excitation. We determine the transient CDW gap size from the time-dependent position of the occupied and unoccupied CDW bands, which is a direct observation of the transient order parameter $\Delta(t)$ and bears important information on the excited energy potential landscape. We find an incomplete melting of the CDW order and a residual gap even for the strongest excitation fluences, which is discussed in terms of remnant local correlations. In addition, the contiguous access to the k-space provided by the pTOF reveals an asymmetric closing of the CDW gap, which depends on the position of the gap with respect to E_F and corresponds to a transient change of the nesting condition. This provides vital information on the transient modification of the band structure due to photo-doping. The coherent oscillations observed at weak excitation in the CDW band [Sch08a] are found to modulate the CDW gap size, providing further, unambiguous evidence for the assignment to the CDW amplitude mode. In addition to a dominating mode at 2.2 THz, a second distinct mode at 1.75 THz is found, which has not been observed in trARPES before [Sch08a], demonstrating the importance of both modes for the CDW transition. The temperature-dependent softening of these modes corroborates the interpretation of earlier optical investigations and indicates a strong coupling between the two modes. In addition, the coherent control of the amplitude mode oscillations demonstrates the collective nature of the oscillations of the order parameter amplitude and provides additional information on the coupling of the two modes.

In order to investigate the momentum-dependent asymmetry in the gap collapse in more detail, future experiments on different regions of the FS, where the gap center is located below E_F, are suggested. In addition, the modification of the nesting condition due to photo-doping suggests the evaluation of the fluence dependence of the asymmetric gap closing. For a deeper understanding of the transient gap dynamics after strong excitation, a theoretical description of the temporal evolution of the transient energy potential surface would be of importance. In addition, an investigation of the dynamics related with the small gap is suggested in materials with two successive CDW transitions. In particular, the detection of the amplitude mode of the small gap promises important information on the coupling of the two perpendicular CDWs. In this respect, an excitation wavelength in the mid-infrared (IR) in resonance with either of the CDW gaps could provide fundamentally new insight. Finally, we establish trARPES here as a powerful method for the investigation of the unoccupied electronic band structure, which encourages similar experiments in other materials [Sob12].

A Appendix

A.1 Unoccupied Band Structure of $DyTe_3$ near the Diamond Tip

Here, we show additional data of $DyTe_3$ to demonstrate the high potential of time- and angle-resolved photoemission spectroscopy (trARPES) for the spectroscopy of the electronic band structure from well below to far above the Fermi level in a large part of the reciprocal space and to discuss the applicability of the Tight-Binding (TB) model far above the Fermi level.

Data showing the occupied and unoccupied bands in $DyTe_3$ in the region of the diamond tip are shown in figure A.1, obtained with the position-sensitive time-of-flight (pTOF) spectrometer and the pump beam with $F = 90 - 135\,\mu\mathrm{J/cm^2}$ fixed at $t = 50\,\mathrm{fs}$. The experimental Fermi surface (FS) is shown in panel (a), where the metallic pocket is visible in the upper part (compare figure 7.4). As this sample exhibits a mixture of domains which are oriented at 90° to each other and where the charge density wave (CDW) gap opens along k_z and k_x, respectively, two traces of the TB model are shown. In the green bands, which describe the FS well, the CDW is oriented along k_z, whereas the red FS is gapped out in this region. Constant energy maps of the unoccupied states at higher energies are shown in the panels (b-d), where the unoccupied part of the gapped dispersion, corresponding to the red TB bands, is dominant.

The energy/momentum cuts along the k_x and k_z axis, presented in the panels (e-h) and (i-l), respectively, show the distribution of gapped and ungapped bands in the occupied and unoccupied band structure. Here, the intensities above E_F are enhanced by a factor of 10-20 for better visibility. In the occupied bands, signs of both domains are clearly observable; e.g. in panel (e) or panel (i), a band crossing E_F is well described by the green, ungapped dispersion, and the more intense, gapped dispersion is found at higher binding energies, reasonably well described by the red bands. The unoccupied states are observed up to $E - E_\mathrm{F} > 1.2\,\mathrm{eV}$ and are mostly described reasonably well by the gapped, red dispersion, as the CDW gap opens in the unoccupied band structure in the green bands. Close to E_F, also the unoccupied bands corresponding to this domain are visible e.g. in the panels (g), (i) and (j). An interesting discontinuity of the bands is observed for $E_\mathrm{F} > 0.8\,\mathrm{eV}$ in the panels (d), and (l). As becomes apparent from the cuts along k_x shown in the panels (g) and (h), this discontinuity corresponds to a splitting of the unoccupied band into up to three bands in this direction. As origin of this splitting, an influence of the small gap, which is not included in the calculations, can be ruled out, as the same splitting is observed at $T = 60\,\mathrm{K} > T_{c2}$. A possible explanation could be the bilayer splitting, however, the splitting is with $> 0.15\,\mathrm{a^*}$ very large and is not present in the lower-lying bands. Thus, the origin of this splitting remains unclear and points to the limitations of the TB description. Here, also final state effects could play a role.

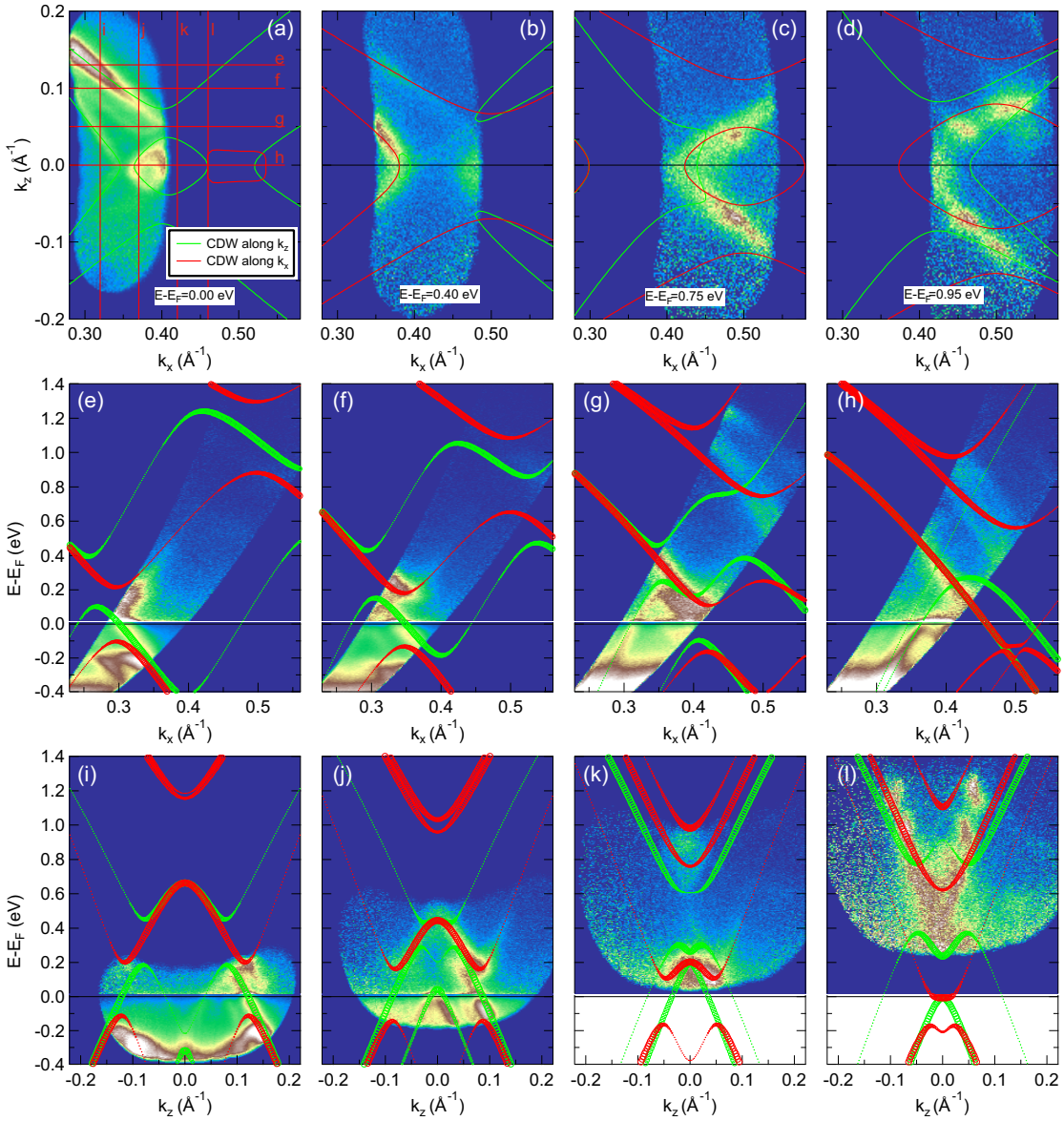

Figure A.1: trARPES dispersion near the diamond tip in $DyTe_3$ at $T = 30\,\mathrm{K}$, obtained with the pTOF spectrometer (pump beam at $F = 90 - 135\,\mu\mathrm{J/cm^2}$ fixed at $t = 50\,\mathrm{fs}$). Red and green lines and symbols mark interacting TB bands (one CDW) with the CDW gap opening along k_x and k_z, respectively. (a-d) Constant energy maps at various energies as indicated. The positions of cuts shown in (e-h) and (i-l) are indicated in (a). (e-h) trARPES intensity maps of cuts along k_x as indicated in (a). Intensity at $E > E_\mathrm{F}$ is enhanced by a factor of $\sim 10 - 20$. (i-l) trARPES intensity maps of cuts along k_z as indicated in (a).

Bibliography

[Aes00] M. Aeschlimann, M. Bauer, S. Pawlik, R. Knorren, G. Bouzerar, & K. H. Bennemann. *Transport and dynamics of optically excited electrons in metals.* Applied Physics A **71**, 5, 485 (2000). DOI: 10.1007/s003390000704. 57

[All75] P. B. Allen & R. C. Dynes. *Transition temperature of strong-coupled superconductors reanalyzed.* Physical Review B **12**, 905 (1975). DOI: 10.1103/PhysRevB.12.905. 108

[All87] P. B. Allen. *Theory of thermal relaxation of electrons in metals.* Physical Review Letters **59**, 1460 (1987). DOI: 10.1103/PhysRevLett.59.1460. 10, 63, 102, 104, 107

[Alo90] M. Alonso, R. Cimino, & K. Horn. *Surface Photovoltage Effects in Photoemission from Metal-Gap (110) Interfaces: Importance for Band Bending Evaluation.* Physical Review Letters **64**, 16, 1947 (1990). DOI: 10.1103/PhysRevLett.64.1947. 59

[Ani74] S. I. Anisimov, B. L. Kapeliovich, & T. L. Perelman. *Electron Emission from Metal Surfaces Exposed to Ultrashort Laser Pulses.* Soviet Physics JETP-USSR **39**, 375 (1974). 10, 63, 102

[Ash76] N. W. Ashcroft & N. D. Mermin. *Solid State Physics.* Thomson Learning (1976). 3, 8

[Avi12] I. Avigo, R. Cortés, L. Rettig, S. Thirupathaiah, H. S. Jeevans, P. Gegenvart, T. Wolf, M. Ligges, M. Wolf, J. Fink, & U. Bovensiepen. *Coherent excitations and electron phonon coupling in 122 FeAs compounds investigated by time-resolved ARPES.* submitted to: Journal of Physics: Condensed Matter (2012). 74

[Bar57a] J. Bardeen, L. N. Cooper, & J. R. Schrieffer. *Microscopic Theory of Superconductivity.* Physical Review **106**, 1, 162 (1957). DOI: 10.1103/PhysRev.106.162. 13

[Bar57b] J. Bardeen, L. N. Cooper, & J. R. Schrieffer. *Theory of Superconductivity.* Physical Review **108**, 5, 1175 (1957). DOI: 10.1103/PhysRev.108.1175. 13

[Bas11] D. N. Basov & A. V. Chubukov. *Manifesto for a higher T_c.* Nature Physics **7**, 4, 272 (2011). DOI: 10.1038/nphys1975. 16, 17

[Bed86] J. G. Bednorz & K. A. Müller. *Possible High-T_c Superconductivity In the Ba-La-Cu-O System.* Zeitschrift für Physik B - Condensed Matter **64**, 2, 189 (1986). DOI: 10.1007/BF01303701. 16, 111

[Ben08] K. H. Bennemann & L. B. Ketterson. *Superconductivity - Conventional and Unconventional Superconductors.* Springer Berlin (2008). 14, 15, 17

[Ber64a] C. N. Berglund & W. E. Spicer. *Photoemission Studies of Copper + Silver - Experiment.* Physical Review A **136**, 4A, 1044 (1964). DOI: 10.1103/PhysRev.136.A1044. 26

[Ber64b] C. N. Berglund & W. E. Spicer. *Photoemission Studies of Copper + Silver - Theory.* Physical Review A **136**, 4A, 1030 (1964). DOI: 10.1103/PhysRev.136.A1030. 26

[Boe08] L. Boeri, O. V. Dolgov, & A. A. Golubov. *Is $LaFeAsO_{1-x}F_x$ an electron-phonon superconductor?* Physical Review Letters **101**, 026403 (2008). DOI: 10.1103/PhysRevLett.101.026403. 108, 109

[Boe10a] L. Boeri. *private communication* (2010). Max-Planck-Institut für Festkörperforschung, Stuttgart, Germany. 92, 93, 104

[Boe10b] L. Boeri, M. Calandra, I. I. Mazin, O. V. Dolgov, & F. Mauri. *Effects of magnetism and doping on the electron-phonon coupling in $BaFe_2As_2$.* Physical Review B **82**, 020506 (2010). DOI: 10.1103/PhysRevB.82.020506. 92, 104, 108

[Boh03] K.-P. Bohnen, R. Heid, & M. Krauss. *Phonon dispersion and electron-phonon interaction for $YBa_2Cu_3O_7$ from first-principles calculations.* Europhysics Letters **64**, 1, 104 (2003). DOI: 10.1209/epl/i2003-00143-x. 120, 122

[Bol11] A. T. Bollinger, G. Dubuis, J. Yoon, D. Pavuna, J. Misewich, & I. Bozovic. *Superconductor-insulator transition in $La_{2-x}Sr_xCuO_4$ at the pair quantum resistance.* Nature **472**, 7344, 458 (2011). DOI: 10.1038/nature09998. 136

[Bor27] M. Born & R. Oppenheimer. *Zur Quantentheorie der Molekeln.* Annalen der Physik **389**, 457 (1927). DOI: 10.1002/andp.19273892002. 148

[Bor10] R. Bormann, M. Gulde, A. Weismann, S. V. Yalunin, & C. Ropers. *Tip-Enhanced Strong-Field Photoemission.* Physical Review Le **105**, 147601 (2010). DOI: 10.1103/PhysRevLett.105.147601. 55

[Bov04] U. Bovensiepen, A. Melnikov, I. Radu, O. Krupin, K. Starke, M. Wolf, & E. Matthias. *Coherent Surface and Bulk Vibrations Induced by Femtosecond Laser Excitation of the Gd(0001) Surface State.* Physical Review B **69**, 23, 235417 (2004). DOI: 10.1103/PhysRevB.69.235417. 11, 30

[Bov07] U. Bovensiepen. *Coherent and Incoherent Excitations of the Gd(0001) Surface on Ultrafast Timescales.* Journal of Physics: Condensed Matter **19**, 8, 083201 (2007). DOI: 10.1088/0953-8984/19/8/083201. 3, 12, 70

[Boy92] R. W. Boyd. *Nonlinear Optics.* Academic Press, San Diego, USA (1992). 34

[Bra09] J. Braun, P. Ruggerone, G. Zhang, J. P. Toennies, & G. Benedek. *Surface phonon dispersion curves of thin Pb films on Cu(111).* Physical Review B **79**, 205423 (2009). DOI: 10.1103/PhysRevB.79.205423. 70

[Bro90] S. D. Brorson, A. Kazeroonian, J. S. Moodera, D. W. Face, T. K. Cheng, E. P. Ippen, M. S. Dresselhaus, & G. Dresselhaus. *Femtosecond Room-Temperature Measurement of the Electron-Phonon Coupling Constant Γ in Metallic Superconductors.* Physical Review Letters **64**, 18, 2172 (1990). DOI: 10.1103/PhysRevLett.64.2172. 73, 122

[Bro04] V. Brouet, W. L. Yang, X. J. Zhou, Z. Hussain, N. Ru, K. Y. Shin, I. R. Fisher, & Z.-X. Shen. *Fermi Surface Reconstruction in the CDW State of $CeTe_3$ Observed by Photoemission.* Physical Review Letters **93**, 126405 (2004). DOI: 10.1103/PhysRevLett.93.126405. 125, 127, 134

[Bro08] V. Brouet, W. L. Yang, X. J. Zhou, Z. Hussain, R. G. Moore, R. He, D. H. Lu, Z.-X. Shen, J. Laverock, S. B. Dugdale, N. Ru, & I. R. Fisher. *Angle-resolved photoemission study of the evolution of band structure and charge density wave properties in RTe_3 (R = Y, La, Ce, Sm, Gd, Tb, and Dy).* Physical Review B **77**, 235104 (2008). DOI: 10.1103/PhysRevB.77.235104. 125, 127, 128, 129, 130, 134, 135, 139, 142, 151

[Bro09] V. Brouet, M. Marsi, B. Mansart, A. Nicolaou, A. Taleb-Ibrahimi, P. Le Fevre, F. Bertran, F. Rullier-Albenque, A. Forget, & D. Colson. *Nesting between hole and electron pockets in $Ba(Fe_{1-x}Co_x)_2As_2$ (x=0-0.3) observed with angle-resolved photoemission.* Physical Review B **80**, 16, 165115 (2009). DOI: 10.1103/PhysRevB.80.165115. 80

[Bru09] C. Brun, I-P. Hong, F. Patthey, I. Yu. Sklyadneva, R. Heid, P. M. Echenique, K. P. Bohnen, E. V. Chulkov, & W.-D. Schneider. *Reduction of the Superconducting Gap of Ultrathin Pb Islands Grown on Si(111).* Physical Review Letters **102**, 207002 (2009). DOI: 10.1103/PhysRevLett.102.207002. 4, 57, 139

[Bud07] M. Budke, V. Renken, H. Liebl, G. Rangelov, & M. Donath. *Inverse photoemission with energy resolution better than 200 meV.* Review of Scientific Instruments **78**, 8, 083903 (2007). DOI: 10.1063/1.2771096. 139

[Cao98] J. Cao, Y. Gao, H. E. Elsayed-Ali, R. J. D. Miller, & D. A. Mantell. *Femtosecond Photoemission Study of Ultrafast Electron Dynamics in Single-Crystal Au(111) Films.* Physical Review B **58**, 16, 10948 (1998). DOI: 10.1103/PhysRevB.58.10948. 57

[Car92] J. A. Carlisle, T. Miller, & T.-C. Chiang. *Photoemission Study of the Growth, Desorption, Schottky-Barrier Formation, and Atomic Structure of Pb on Si(111).* Physical Review B **45**, 7, 3400 (1992). DOI: 10.1103/PhysRevB.45.3400. 57

[Cha09] L. Chauvière, Y. Gallais, M. Cazayous, A. Sacuto, M. A. Méasson, D. Colson, & A. Forget. *Doping dependence of the lattice dynamics in $Ba(Fe_{1-x}Co_x)_2As_2$ studied by Raman spectroscopy.* Physical Review B **80**, 9, 094504 (2009). DOI: 10.1103/PhysRevB.80.094504. 92, 93

[Cha11] L. Chauvière, Y. Gallais, M. Cazayous, M. A. Méasson, A. Sacuto, D. Colson, & A. Forget. *Raman scattering study of spin-density-wave order and electron-phonon coupling in $Ba(Fe_{1-x}Co_x)_2As_2$.* Physical Review B **84**, 104508 (2011). DOI: 10.1103/PhysRevB.84.104508. 92

[Che90] T. K. Cheng, S. D. Brorson, A. S. Kazeroonian, J. S. Moodera, G. Dresselhaus, M. S. Dresselhaus, & E. P. Ippen. *Impulsive excitation of coherent phonons observed in reflection in bismuth and antimony.* Applied Physics Letters **57**, 10, 1004 (1990). DOI: 10.1063/1.104090. 11

[Che91] T. K. Cheng, J. Vidal, H. J. Zeiger, G. Dresselhaus, M. S. Dresselhaus, & E. P. Ippen. *Mechanism for Displacive Excitation of Coherent Phonons in Sb, Bi, Te, and Ti_2O_3.* Applied Physics Letters **59**, 16, 1923 (1991). DOI: 10.1063/1.106187. 11

[Che96] C. Chen, Z. Xu, D. Deng, J. Zhang, G. K. L. Wong, B. Wu, N. Ye, & D. Tang. *The vacuum ultraviolet phase-matching characteristics of nonlinear optical $KBe_2BO_3F_2$ crystal*. Applied Physics Letters **68**, 21, 2930 (1996). DOI: 10.1063/1.116358. 52

[Che09] H. Chen, Y. Ren, Y. Qiu, W. Bao, R. H. Liu, G. Wu, T. Wu, Y. L. Xie, X. F. Wang, Q. Huang, & X. H. Chen. *Coexistence of the spin-density wave and superconductivity in $Ba_{1-x}K_xFe_2As_2$*. Europhysics Letters **85**, 1, 17006 (2009). DOI: 10.1209/0295-5075/85/17006. 76

[Che11] F. Chen, Y. Zhang, J. Wei, B. Zhou, L. Yang, F. Wu, G. Wu, X.H. Chen, & D.L. Feng. *Electronic structure reconstruction of $CaFe_2As_2$ in the spin density wave state*. Journal of Physics and Chemistry of Solids **72**, 5, 469 (2011). DOI: 10.1016/j.jpcs.2010.10.076. 78

[Chi00] T.-C. Chiang. *Photoemission Studies of Quantum Well States in Thin Films*. Surface Science Reports **39**, 7-8, 181 (2000). DOI: 10.1016/S0167-5729(00)00006-6. 57

[Chi10] E. E. M. Chia, D. Talbayev, J.-X. Zhu, H. Q. Yuan, T. Park, J. D. Thompson, C. Panagopoulos, G. F. Chen, J. L. Luo, N. L. Wang, & A. J. Taylor. *Ultrafast Pump-Probe Study of Phase Separation and Competing Orders in the Underdoped (Ba,K)Fe_2As_2 Superconductor*. Physical Review Letters **104**, 027003 (2010). DOI: 10.1103/PhysRevLett.104.027003. 73

[Cho90] G. C. Cho, W. Kütt, & H. Kurz. *Subpicosecond Time-Resolved Coherent-Phonon Oscillations in GaAs*. Physical Review Letters **65**, 6, 764 (1990). DOI: 10.1103/PhysRevLett.65.764. 11

[Cho08] K.-Y. Choi, D. Wulferding, P. Lemmens, N. Ni, S. L. Bud'ko, & P. C. Canfield. *Lattice and electronic anomalies of $CaFe_2As_2$ studied by Raman spectroscopy*. Physical Review B **78**, 21, 212503 (2008). DOI: 10.1103/PhysRevB.78.212503. 92

[Chu06] E. V. Chulkov, A. G. Borisov, J. P. Gauyacq, D. Sanchez-Portal, V. M. Silkin, V. P. Zhukov, & P. M. Echenique. *Electronic Excitations in Metals and at Metal Surfaces*. Chemical Reviews **106**, 10, 4160 (2006). DOI: 10.1021/cr050166o. 2

[Chu09] J.-H. Chu, J. G. Analytis, C. Kucharczyk, & I. R. Fisher. *Determination of the phase diagram of the electron-doped superconductor $Ba(Fe_{1-x}Co_x)_2As_2$*. Physical Review B **79**, 014506 (2009). DOI: 10.1103/PhysRevB.79.014506. 76, 85

[Chw90] J. M. Chwalek, C. Uher, J. F. Whitaker, G. A. Mourou, J. Agostinelli, & M. Lelental. *Femtosecond optical absorption studies of nonequilibrium electronic processes in high T_c superconductors*. Applied Physics Letters **57**, 16, 1696 (1990). DOI: 10.1063/1.104140. 11

[Coh93] Coherent Laser Group. *Operator's Manual, The Coherent Mira 900-B Laser*. Coherent Inc., Santa Clara (1993). 34

[Coh94] Coherent Laser Group. *Operator's Manual, The Coherent Modell 9800 Optical Parametric Amplifier*. Coherent Inc., Santa Clara (1994). 34, 35

[Coh97] Coherent Laser Group. *RegA 9050 System Operator's Manual, Preliminary Version 2.1.* Coherent Inc., Santa Clara (1997). 34, 35

[Coh07] Coherent Laser Group. *Operator's Manual, Verdi V-18 Diode-Pumped Lasers.* Coherent Inc., Santa Clara (2007). 34

[Cor11] R. Cortés, L. Rettig, Y. Yoshida, H. Eisaki, M. Wolf, & U. Bovensiepen. *Momentum-Resolved Ultrafast Electron Dynamics in Superconducting $Bi_2Sr_2CaCu_2O_{8+\delta}$.* Physical Review Letters **107**, 097002 (2011). DOI: 10.1103/PhysRevLett.107.097002. 36, 73, 112

[Dag10] M. Daghofer, A. Nicholson, A. Moreo, & E. Dagotto. *Three orbital model for the iron-based superconductors.* Physical Review B **81**, 014511 (2010). DOI: 10.1103/PhysRevB.81.014511. 77

[Dah09] T. Dahm, V. Hinkov, S. V. Borisenko, A. A. Kordyuk, V. B. Zabolotnyy, J. Fink, B. Buechner, D. J. Scalapino, W. Hanke, & B. Keimer. *Strength of the spin-fluctuation-mediated pairing interaction in a high-temperature superconductor.* Nature Physics **5**, 3, 217 (2009). DOI: 10.1038/NPHYS1180. 120

[Dam03] A. Damascelli, Z. Hussain, & Z.-X. Shen. *Angle-Resolved Photoemission Studies of the Cuprate Superconductors.* Reviews of Modern Physics **75**, 473 (2003). DOI: 10.1103/RevModPhys.75.473. 2, 3, 9, 25, 75, 111, 113, 114, 116, 124, 134, 139, 146

[DC12] S. Dal Conte, C. Giannetti, G. Coslovich, F. Cilento, D. Bossini, T. Abebaw, F. Banfi, G. Ferrini, H. Eisaki, M. Greven, A. Damascelli, D. van der Marel, & F. Parmigiani. *Disentangling the Electronic and Phononic Glue in a High-T_c Superconductor.* Science **335**, 6076, 1600 (2012). DOI: 10.1126/science.1216765. 111

[DeC01] M. F. DeCamp, D. A. Reis, P. H. Bucksbaum, & R. Merlin. *Dynamics and coherent control of high-amplitude optical phonons in bismuth.* Physical Review B **64**, 092301 (2001). DOI: 10.1103/PhysRevB.64.092301. 11, 157

[Dek93] T. Dekorsy, W. Kütt, T. Pfeifer, & H. Kurz. *Coherent Control of LO-Phonon Dynamics in Opaque Semiconductors by Femtosecond Laser Pulses.* Europhysics Letters **23**, 3, 223 (1993). DOI: 10.1209/0295-5075/23/3/011. 11, 157

[Dek00] T. Dekorsy, G. Cho, & H. Kurz. *Coherent phonons in condensed media.* In Manuel Cardona & Gernot Güntherodt (Eds.), *Light Scattering in Solids VIII*, Vol. 76 of *Topics in Applied Physics.* Springer Berlin / Heidelberg (2000) 169–209. DOI: 10.1007/BFb0084242. 11, 69, 160

[Dem86] J. E. Demuth, W. J. Thompson, N. J. DiNardo, & R. Imbihl. *Photoemission-Based Photovoltage Probe of Semiconductor Surface and Interface Electronic Structure.* Physical Review Letters **56**, 1408 (1986). DOI: 10.1103/PhysRevLett.56.1408. 59

[Dem99] J. Demsar, K. Biljakovic, & D. Mihailovic. *Single Particle and Collective Excitations in the One-Dimensional Charge Density Wave Solid $K_{0.3}MoO_3$ Probed in Real Time by Femtosecond Spectroscopy.* Physical Review Letters **83**, 800 (1999). DOI: 10.1103/PhysRevLett.83.800. 17, 111, 119, 120, 122

[Dem03] W. Demtröder. *Laser Spectroscopy.* Springer, Berlin (2003). 34

[Den99] D. Denzler. *Untersuchungen zur Ultrakurzzeitdynamik photostimulierter Oberflächenreaktionen und der Energierelaxation in Metallen.* Diploma Thesis, Freie Universität Berlin (1999). 34

[DF00] N. Del Fatti, C. Voisin, M. Achermann, S. Tzortzakis, D. Christofilos, & F. Vallée. *Nonequilibrium electron dynamics in noble metals.* Physical Review B **61**, 16956 (2000). DOI: 10.1103/PhysRevB.61.16956. 2, 10, 63, 102

[Dil04] J.H. Dil, J.W. Kim, S. Gokhale, M. Tallarida, & K. Horn. *Self-organization of Pb thin films on Cu(111) induced by quantum size effects.* Physical Review B **70**, 4, 045405 (2004). DOI: 10.1103/PhysRevB.70.045405. 72, 167

[Dil06] J. H. Dil, J. W. Kim, T. Kampen, K. Horn, & A. R. H. F. Ettema. *Electron localization in metallic quantum wells: Pb versus In on Si(111).* Physical Review B **73**, 16, 161308 (2006). 54, 57, 58, 72, 167

[Dil07] J. H. Dil, T. U. Kampen, B. Huelsen, T. Seyller, & K. Horn. *Quantum Size Effects in Quasi-Free-Standing Pb Layers.* Physical Review B **75**, 16, 161401 (2007). DOI: 10.1103/PhysRevB.75.161401. 72, 167

[DiM95] E. DiMasi, M. C. Aronson, J. F. Mansfield, B. Foran, & S. Lee. *Chemical pressure and charge-density waves in rare-earth tritellurides.* Physical Review B **52**, 14516 (1995). DOI: 10.1103/PhysRevB.52.14516. 125, 127, 129

[Din96] H. Ding, M. R. Norman, J. C. Campuzano, M. Randeria, A. F. Bellman, T. Yokoya, T. Takahashi, T. Mochiku, & K. Kadowaki. *Angle-resolved photoemission spectroscopy study of the superconducting gap anisotropy in* $Bi_2Sr_2CaCu_2O_{8+x}$. Physical Review B **54**, R9678 (1996). DOI: 10.1103/PhysRevB.54.R9678. 114, 124

[Din01] H. Ding, J. R. Engelbrecht, Z. Wang, J. C. Campuzano, S.-C. Wang, H.-B. Yang, R. Rogan, T. Takahashi, K. Kadowaki, & D. G. Hinks. *Coherent Quasiparticle Weight and Its Connection to High-* T_c *Superconductivity from Angle-Resolved Photoemission.* Physical Review Letters **87**, 227001 (2001). DOI: 10.1103/PhysRevLett.87.227001. 116, 124

[Din08] H. Ding, P. Richard, K. Nakayama, K. Sugawara, T. Arakane, Y. Sekiba, A. Takayama, S. Souma, T. Sato, T. Takahashi, Z. Wang, X. Dai, Z. Fang, G. F. Chen, J. L. Luo, & N. L. Wang. *Observation of Fermi-surface-dependent nodeless superconducting gaps in* $Ba_{0.6}K_{0.4}Fe_2As_2$. Europhysics Letters **83**, 4, 47001 (6pp) (2008). DOI: 10.1209/0295-5075/83/47001. 77

[dJ10] S. de Jong, E. van Heumen, S. Thirupathaiah, R. Huisman, F. Massee, J. B. Goedkoop, R. Ovsyannikov, J. Fink, H. A. Dürr, A. Gloskovskii, H. S. Jeevan, P. Gegenwart, A. Erb, L. Patthey, M. Shi, R. Follath, A. Varykhalov, & M. S. Golden. *Droplet-like Fermi surfaces in the anti-ferromagnetic phase of* $EuFe_2As_2$ *, an Fe-pnictide superconductor parent compound.* Europhysics Letters **89**, 2, 27007 (2010). DOI: 10.1209/0295-5075/89/27007. 78, 80

[dlC08] C. de la Cruz, Q. Huang, J. W. Lynn, J. Li, W. Ratcliff, II, J. L. Zarestky, H. A. Mook, G. F. Chen, J. L. Luo, N. L. Wang, & P. Dai. *Magnetic order close*

to superconductivity in the iron-based layered $LaO_{1-x}F_xFeAs$ systems. Nature **453**, 7197, 899 (2008). DOI: 10.1038/nature07057. 77, 78, 87

[Don70] S. Doniach & M. Sunjic. *Many-electron singularity in X-ray photoemission and X-ray line spectra from metals.* Journal of Physics C **3**, 285 (1970). DOI: 10.1088/0022-3719/3/2/010. 63

[Don08] J. K. Dong, L. Ding, H. Wang, X. F. Wang, T. Wu, G. Wu, X. H. Chen, & S. Y. Li. *Thermodynamic properties of $Ba_{1-x}K_xF_2As_2$ and $Ca_{1-x}Na_xFe_2As_2$.* New Journal of Physics **10**, 12, 123031 (2008). DOI: 10.1088/1367-2630/10/12/123031. 104

[Dre09] A. J. Drew, Ch. Niedermayer, P. J. Baker, F. L. Pratt, S. J. Blundell, T. Lancaster, R. H. Liu, G. Wu, X. H. Chen, I. Watanabe, V. K. Malik, A. Dubroka, M. Rossle, K. W. Kim, C. Baines, & C. Bernhard. *Coexistence of static magnetism and superconductivity in $SmFeAsO_{1-x}F_x$ as revealed by muon spin rotation.* Nature Materials **8**, 4, 310 (2009). DOI: 10.1038/nmat2396. 76

[Dvo02] D. Dvorsek, V. V. Kabanov, J. Demsar, S. M. Kazakov, J. Karpinski, & D. Mihailovic. *Femtosecond quasiparticle relaxation dynamics and probe polarization anisotropy in $YSr_xBa_{2-x}Cu_4O_8$ ($x = 0, 0.4$).* Physical Review B **66**, 020510 (2002). DOI: 10.1103/PhysRevB.66.020510. 122

[EA87] H. E. Elsayed-Ali, T. B. Norris, M. A. Pessot, & G. A. Mourou. *Time-resolved observation of electron-phonon relaxation in copper.* Physical Review Letters **58**, 1212 (1987). DOI: 10.1103/PhysRevLett.58.1212. 10

[Ech00] P. M. Echenique, J. M. Pitarke, E. V. Chulkov, & A. Rubio. *Theory of Inelastic Lifetimes of Low-Energy Electrons in Metals.* Chemical Physics **251**, 1-3, 1 (2000). DOI: 10.1016/S0301-0104(99)00313-4. 106

[Ech04] P. M. Echenique, R. Berndt, E. V. Chulkov, Th. Fauster, A. Goldmann, & U. Höfer. *Decay of Electronic Excitations at Metal Surfaces.* Surface Science Reports **52**, 7-8, 219 (2004). DOI: 10.1016/j.surfrep.2004.02.002. 29, 57

[Ega10] T. Egami, B. V. Fine, D. Parshall, A. Subedi, & D. J. Singh. *Spin-Lattice Coupling and Superconductivity in Fe Pnictides.* Advances In Condensed Matter Physics **2010**, 164916 (2010). DOI: 10.1155/2010/164916. 109

[Ein05] A. Einstein. *Generation and Conversion of Light with Regard to a Heuristic Point of View.* Annalen der Physik **17**, 6, 132 (1905). DOI: 10.1002/andp.19053220607. 25

[Eis04] H. Eisaki, N. Kaneko, D. L. Feng, A. Damascelli, P. K. Mang, K. M. Shen, Z.-X. Shen, & M. Greven. *Effect of chemical inhomogeneity in bismuth-based copper oxide superconductors.* Physical Review B **69**, 064512 (2004). DOI: 10.1103/PhysRevB.69.064512. 55, 113

[Eng63] S. Engelsberg & J. R. Schrieffer. *Coupled Electron-Phonon System.* Physical Review **131**, 993 (1963). DOI: 10.1103/PhysRev.131.993. 106

[Ere10] I. Eremin & A. V. Chubukov. *Magnetic degeneracy and hidden metallicity of the spin-density-wave state in ferropnictides.* Physical Review B **81**, 2, 024511 (2010). DOI: 10.1103/PhysRevB.81.024511. 78

[Ern08] R. Ernstorfer, M. Harb, C. T. Hebeisen, G. Sciaini, T. Dartigalongue, I. Rajkovic, M. Ligges, D. von der Linde, Th. Payer, M. Horn von Hoegen, F.-J. Meyer zu Heringdorf, S. Kruglik, & R. J. D. Miller. *Atomic View of the Photoinduced Collapse of Gold And Bismuth.* In *Ultrafast Phenomena XVI.* 2008) . 148, 151

[Ern09] R. Ernstorfer, M. Harb, C. T. Hebeisen, G. Sciaini, Th. Dartigalongue, & R. J. D. Miller. *The Formation of Warm Dense Matter: Experimental Evidence for Electronic Bond Hardening in Gold.* Science **323**, 5917, 1033 (2009). DOI: 10.1126/science.1162697. 151

[Esc02] H. Eschrig, J. Fink, & L. Schultz. *15 Jahre Hochtemperatur-Supraleitung.* Physik Journal **1**, 45 (2002). 16

[Evt09] D. V. Evtushinsky, D. S. Inosov, V. B. Zabolotnyy, A. Koitzsch, M. Knupfer, B. Büchner, M. S. Viazovska, G. L. Sun, V. Hinkov, A. V. Boris, C. T. Lin, B. Keimer, A. Varykhalov, A. A. Kordyuk, & S. V. Borisenko. *Momentum dependence of the superconducting gap in* $Ba_{1-x}K_xFe_2As_2$. Physical Review B **79**, 054517 (2009). DOI: 10.1103/PhysRevB.79.054517. 124

[Fan92] W. S. Fann, R. Storz, H. W. K. Tom, & J. Bokor. *Direct Measurement of Nonequilibrium Electron-Energy Distributions in Subpicosecond Laser-Heated Gold Films.* Physical Review Letters **68**, 18, 2834 (1992). DOI: 10.1103/PhysRevLett.68.2834. 10, 29, 30, 63, 81

[Fan07] A. Fang, N. Ru, I. R. Fisher, & A. Kapitulnik. *STM Studies of* $TbTe_3$*: Evidence for a Fully Incommensurate Charge Density Wave.* Physical Review Letters **99**, 4, 046401 (2007). DOI: 10.1103/PhysRevLett.99.046401. 125, 129, 135, 139, 142

[Fau95] Th. Fauster & W. Steinmann. *Two-Photon Photoemission Spectroscopy of Image States.* Electromagnetic Waves: Recent Developments in Research, P. Halevi, Ed., Elsevier, Amsterdam **2**, 347 (1995). 3

[Fau11] D. Fausti, R. I. Tobey, N. Dean, S. Kaiser, A. Dienst, M. C. Hoffmann, S. Pyon, T. Takayama, H. Takagi, & A. Cavalleri. *Light-Induced Superconductivity in a Stripe-Ordered Cuprate.* Science **331**, 6014, 189 (2011). DOI: 10.1126/science.1197294. 3

[Fen00] D. L. Feng, D. H. Lu, K. M. Shen, C. Kim, H. Eisaki, A. Damascelli, R. Yoshizaki, J.-i. Shimoyama, K. Kishio, G. D. Gu, S. Oh, A. Andrus, J. O'Donnell, J. N. Eckstein, & Z.-X. Shen. *Signature of Superfluid Density in the Single-Particle Excitation Spectrum of* $Bi_2Sr_2CaCu_2O_{8+\delta}$. Science **289**, 5477, 277 (2000). DOI: 10.1126/science.289.5477.277. 116, 124

[Fer88] M. Ferray, A. L'Huillier, X. F. Li, L. A. Lompré, G. Mainfray, & C. Manus. *Multiple-harmonic conversion of 1064 nm radiation in rare gases.* Journal of Physics B **21**, 3, L31 (1988). DOI: 10.1088/0953-4075/21/3/001. 50

[Fer12] R. M. Fernandes, A. V. Chubukov, J. Knolle, I. Eremin, & J. Schmalian. *Preemptive nematic order, pseudogap, and orbital order in the iron pnictides.* Physical Review B **85**, 024534 (2012). DOI: 10.1103/PhysRevB.85.024534. 78, 87

[Fet03] A. L. Fetter & J. D. Walecka. *Quantum Theory of Many-Particle Systems*. Dover Books on Physics. Dover Publications (2003). 2

[Feu78] B. Feuerbacher, B. Fitton, & R. F. Willis. *Photoemission and the Electronic Properties of Surfaces*. John Wiley (1978). 27

[Fin07] J. Fink, S. Borisenko, A. Kordyuk, A. Koitzsch, J. Geck, V. Zabolotnyy, M. Knupfer, B. Büchner, & H. Berger. *Lecture Notes in Physics*, Vol. 715. Springer Berlin (2007) 295–325. 9

[Fin09] J. Fink, S. Thirupathaiah, R. Ovsyannikov, H. A. Dürr, R. Follath, Y. Huang, S. de Jong, M. S. Golden, Y.-Z. Zhang, H. O. Jeschke, R. Valentí, C. Felser, S. Dastjani Farahani, M. Rotter, & D. Johrendt. *Electronic structure studies of $BaFe_2As_2$ by angle-resolved photoemission spectroscopy*. Physical Review B **79**, 155118 (2009). DOI: 10.1103/PhysRevB.79.155118. 75, 77, 85

[Fis11] I. R. Fisher, L. Degiorgi, & Z.-X. Shen. *In-plane electronic anisotropy of underdoped '122' Fe-arsenide superconductors revealed by measurements of detwinned single crystals*. Reports on Progress in Physics **74**, 12, 124506 (2011). DOI: 10.1088/0034-4885/74/12/124506. 78

[FJ11] M. Fuglsang Jensen, V. Brouet, E. Papalazarou, A. Nicolaou, A. Taleb-Ibrahimi, P. Le Fèvre, F. Bertran, A. Forget, & D. Colson. *Angle-resolved photoemission study of the role of nesting and orbital orderings in the antiferromagnetic phase of $BaFe_2As_2$*. Physical Review B **84**, 014509 (2011). DOI: 10.1103/PhysRevB.84.014509. 78

[For94] R. L. Fork, O. E. Martinez, & J. P. Gordon. *Negative Dispersion Using Pairs of Prisms*. Optics Letters **9**, 5, 150 (1994). DOI: 10.1364/OL.9.000150. 35

[Frö54] H. Fröhlich. *On the Theory of Superconductivity: The One-Dimensional Case*. Proceedings of the Royal Society of London. Series A **223**, 296 (1954). DOI: 10.1098/rspa.1954.0116. 8, 19

[Fra11] K. J. Franke, G. Schulze, & J. I. Pascual. *Competition of Superconducting Phenomena and Kondo Screening at the Nanoscale*. Science **332**, 6032, 940 (2011). DOI: 10.1126/science.1202204. 139

[Fre09] J. K. Freericks, H. R. Krishnamurthy, & Th. Pruschke. *Theoretical Description of Time-Resolved Photoemission Spectroscopy: Application to Pump-Probe Experiments*. Physical Review Letters **102**, 136401 (2009). DOI: 10.1103/PhysRevLett.102.136401. 3

[Fri07] D. M. Fritz, D. A. Reis, B. Adams, R. A. Akre, J. Arthur, C. Blome, P. H. Bucksbaum, A. L. Cavalieri, S. Engemann, S. Fahy, R. W. Falcone, P. H. Fuoss, K. J. Gaffney, M. J. George, J. Hajdu, M. P. Hertlein, P. B. Hillyard, M. Horn von Hoegen, M. Kammler, J. Kaspar, R. Kienberger, P. Krejcik, S. H. Lee, A. M. Lindenberg, B. McFarland, D. Meyer, T. Montagne, E. D. Murray, A. J. Nelson, M. Nicoul, R. Pahl, J. Rudati, H. Schlarb, D. P. Siddons, K. Sokolowski-Tinten, Th. Tschentscher, D. von der Linde, & J. B. Hastings. *Ultrafast Bond Softening in Bismuth: Mapping A Solid's Interatomic Potential with X-Rays*. Science **315**, 633 (2007). DOI: 10.1126/science.1135009. 11

[Fuj84] J. G. Fujimoto, J. M. Liu, E. P. Ippen, & N. Bloembergen. *Femtosecond Laser Interaction with Metallic Tungsten and Nonequilibrium Electron and Lattice Temperatures.* Physical Review Letters **53**, 19, 1837 (1984). DOI: 10.1103/PhysRevLett.53.1837. 29

[Gad10] C. Gadermaier, A. S. Alexandrov, V. V. Kabanov, P. Kusar, T. Mertelj, X. Yao, C. Manzoni, D. Brida, G. Cerullo, & D. Mihailovic. *Electron-Phonon Coupling in High-Temperature Cuprate Superconductors Determined from Electron Relaxation Rates.* Physical Review Letters **105**, 257001 (2010). DOI: 10.1103/PhysRevLett.105.257001. 83, 105, 107, 123

[Gah04] C. Gahl. *Elektronentransfer- und Solvatisierungsdynamik in Eis adsorbiert auf Metalloberflächen.* PhD Thesis, Freie Universität Berlin (2004). 34

[Gar96] G. A. Garrett, T. F. Albrecht, J. F. Whitaker, & R. Merlin. *Coherent THz Phonons Driven by Light Pulses and the Sb Problem: What is the Mechanism?* Physical Review Letters **77**, 3661 (1996). DOI: 10.1103/PhysRevLett.77.3661. 12, 92

[Güd05] J. Güdde & U. Höfer. *Femtosecond Time-Resolved Studies of Image-Potential States at Surfaces and Interfaces of Rare-Gas Adlayers.* Progress in Surface Science **80**, 49 (2005). DOI: 10.1016/j.progsurf.2005.10.003. 3

[Güd07] J. Güdde, M. Rohleder, T. Meier, S. W. Koch, & U. Höfer. *Time-Resolved Investigation of Coherently Controlled Electric Currents at a Metal Surface.* Science **318**, 5854, 1287 (2007). DOI: 10.1126/science.1146764. 139

[Ged04] N. Gedik, P. Blake, R. C. Spitzer, J. Orenstein, R. Liang, D. A. Bonn, & W. N. Hardy. *Single-quasiparticle stability and quasiparticle-pair decay in* $YBa_2Cu_3O_{6.5}$. Physical Review B **70**, 014504 (2004). DOI: 10.1103/PhysRevB.70.014504. 111, 117, 119, 120

[Ged05] N. Gedik, M. Langner, J. Orenstein, S. Ono, Y. Abe, & Y. Ando. *Abrupt Transition in Quasiparticle Dynamics at Optimal Doping in a Cuprate Superconductor System.* Physical Review Letters **95**, 117005 (2005). DOI: 10.1103/PhysRevLett.95.117005. 17, 111, 121

[Gia09] C. Giannetti, G. Coslovich, F. Cilento, G. Ferrini, H. Eisaki, N. Kaneko, M. Greven, & F. Parmigiani. *Discontinuity of the ultrafast electronic response of underdoped superconducting* $Bi_2Sr_2CaCu_2O_{8+\delta}$ *strongly excited by ultrashort light pulses.* Physical Review B **79**, 224502 (2009). DOI: 10.1103/PhysRevB.79.224502. 111, 117, 119, 120, 122, 124

[Gof10] K. Gofryk, A. S. Sefat, M. A. McGuire, B. C. Sales, D. Mandrus, J. D. Thompson, E. D. Bauer, & F. Ronning. *Doping-dependent specific heat study of the superconducting gap in* $Ba(Fe_{1-x}Co_x)_2As_2$. Physical Review B **81**, 184518 (2010). DOI: 10.1103/PhysRevB.81.184518. 104

[Grü94] G. Grüner. *Density Waves in Solids*, Vol. 89 of *Frontiers in Physics.* Addison-Wesley (1994). 2, 3, 8, 15, 19, 20, 21, 22, 23, 24, 125, 138, 142, 147, 148, 152, 154, 157, 160

[Gra10a] J. Graf, S. Hellmann, C. Jozwiak, C. L. Smallwood, Z. Hussain, R. A. Kaindl, L. Kipp, K. Rossnagel, & A. Lanzara. *Vacuum space charge effect in laser-based solid-state photoemission spectroscopy.* Journal of Applied Physics **107**, 1, 014912 (2010). DOI: 10.1063/1.3273487. 49, 116

[Gra10b] S. Graser, A. F. Kemper, T. A. Maier, H.-P. Cheng, P. J. Hirschfeld, & D. J. Scalapino. *Spin fluctuations and superconductivity in a three-dimensional tight-binding model for $BaFe_2As_2$.* Physical Review B **81**, 214503 (2010). DOI: 10.1103/PhysRevB.81.214503. 77

[Gra11] J. Graf, C. Jozwiak, C. L. Smallwood, H. Eisaki, R. A. Kaindl, D-H. Lee, & A. Lanzara. *Nodal quasiparticle meltdown in ultrahigh-resolution pump-probe angle-resolved photoemission.* Nature Physics **7**, 10, 805 (2011). DOI: 10.1038/nphys2027. 36, 111, 116, 124, 168

[Gri81] G. Grimvall. *The Electron-Phonon Interaction in Metals.* North-Holland (1981). 8, 9

[Gro92] R. H. M. Groeneveld, R. Sprik, & A. Lagendijk. *Effect of a nonthermal electron distribution on the electron-phonon energy relaxation process in noble metals.* Physical Review B **45**, 5079 (1992). DOI: 10.1103/PhysRevB.45.5079. 10

[Gro95] R. H. M. Groeneveld, R. Sprik, & A. Lagendijk. *Femtosecond spectroscopy of electron-electron and electron-phonon energy relaxation in Ag and Au.* Physical Review B **51**, 11433 (1995). DOI: 10.1103/PhysRevB.51.11433. 10, 83

[Guo04] Y. Guo, Y. F. Zhang, X. Y. Bao, T. Z. Han, Z. Tang, L. X. Zhang, W. G. Zhu, E. G. Wang, Q. Niu, Z. Q. Qiu, J. F. Jia, Z. X. Zhao, & Q. K. Xue. *Superconductivity Modulated by Quantum Size Effects.* Science **306**, 5703, 1915 (2004). DOI: 10.1126/science.1105130. 4

[Gus98] V. E. Gusev & O. B. Wright. *Ultrafast nonequilibrium dynamics of electrons in metals.* Physical Review B **57**, 2878 (1998). DOI: 10.1103/PhysRevB.57.2878. 106

[Gwe98] G.-H. Gweon, J. D. Denlinger, J. A. Clack, J. W. Allen, C. G. Olson, E. DiMasi, M. C. Aronson, B. Foran, & S. Lee. *Direct Observation of Complete Fermi Surface, Imperfect Nesting, and Gap Anisotropy in the High-Temperature Incommensurate Charge-Density-Wave Compound $SmTe_3$.* Physical Review Letters **81**, 4, 886 (1998). DOI: 10.1103/PhysRevLett.81.886. 125, 127, 134

[Hah09] S. E. Hahn, Y. Lee, N. Ni, P. C. Canfield, A. I. Goldman, R. J. McQueeney, B. N. Harmon, A. Alatas, B. M. Leu, E. E. Alp, D. Y. Chung, I. S. Todorov, & M. G. Kanatzidis. *Influence of magnetism on phonons in $CaFe_2As_2$ as seen via inelastic x-ray scattering.* Physical Review B **79**, 220511 (2009). DOI: 10.1103/PhysRevB.79.220511. 104, 109

[Hai95] R. Haight. *Electron Dynamics at Surfaces.* Surface Science Reports **21**, 275 (1995). DOI: 10.1016/0167-5729(95)00002-X. 29

[Han90] S. G. Han, Z. V. Vardeny, K. S. Wong, O. G. Symko, & G. Koren. *Femtosecond optical detection of quasiparticle dynamics in high-T_c $YBa_2Cu_3O_{7-\delta}$ superconducting thin films.* Physical Review Letters **65**, 21, 2708 (1990). DOI: 10.1103/PhysRevLett.65.2708. 17, 111

[Har09] F. Hardy, P. Adelmann, T. Wolf, H. v. Löhneysen, & C. Meingast. *Large Anisotropic Uniaxial Pressure Dependencies of T_c in Single Crystalline $Ba(Fe_{0.92}Co_{0.08})_2As_2$.* Physical Review Letters **102**, 187004 (2009). DOI: 10.1103/PhysRevLett.102.187004. 55

[Har10] F. Hardy, T. Wolf, R. A. Fisher, R. Eder, P. Schweiss, P. Adelmann, H. v. Löhneysen, & C. Meingast. *Calorimetric evidence of multiband superconductivity in $Ba(Fe_{0.925}Co_{0.075})_2As_2$ single crystals.* Physical Review B **81**, 6, 060501 (2010). DOI: 10.1103/PhysRevB.81.060501. 104

[Has96] M. Hase, K. Mizoguchi, H. Harima, S. Nakashima, M. Tani, K. Sakai, & M. Hangyo. *Optical Control of Coherent Optical Phonons in Bismuth Films.* Applied Physics Letters **69**, 17, 2474 (1996). DOI: 10.1063/1.117502. 11, 157

[Has02] M. Hase, M. Kitajima, S.-i. Nakashima, & K. Mizoguchi. *Dynamics of Coherent Anharmonic Phonons in Bismuth Using High Density Photoexcitation.* Physical Review Letters **88**, 067401 (2002). DOI: 10.1103/PhysRevLett.88.067401. 11, 92, 97, 148

[Has03] M. Hase, M. Kitajima, A. M. Constantinescu, & H. Petek. *The Birth of a Quasiparticle in Silicon Observed in Time-Frequency Space.* Nature **426**, 51 (2003). DOI: 10.1038/nature02044. 11

[Has05] M. Hase, K. Ishioka, J. Demsar, K. Ushida, & M. Kitajima. *Ultrafast Dynamics of Coherent Optical Phonons and Nonequilibrium Electrons in Transition Metals.* Physical Review B **71**, 18, 184301 (2005). DOI: 10.1103/PhysRevB.71.184301. 11, 12, 69, 70, 92, 97

[Has10] M. Hase & M. Kitajima. *Interaction of coherent phonons with defects and elementary excitations.* Journal of Physics: Condensed Matter **22**, 7, 073201 (2010). DOI: 10.1088/0953-8984/22/7/073201. 11, 69, 97

[Has11] M. Hashimoto, R.-H. He, J. P. Testaud, W. Meevasana, R. G. Moore, D. H. Lu, Y. Yoshida, H. Eisaki, T. P. Devereaux, Z. Hussain, & Z.-X. Shen. *Reaffirming the $d_{x^2-y^2}$ Superconducting Gap Using the Autocorrelation Angle-Resolved Photoemission Spectroscopy of $Bi_{1.5}Pb_{0.55}Sr_{1.6}La_{0.4}CuO_{6+\delta}$.* Physical Review Letters **106**, 167003 (2011). DOI: 10.1103/PhysRevLett.106.167003. 114

[Hel10] S. Hellmann, M. Beye, C. Sohrt, T. Rohwer, F. Sorgenfrei, H. Redlin, M. Kalläne, M. Marczynski-Bühlow, F. Hennies, M. Bauer, A. Föhlisch, L. Kipp, W. Wurth, & K. Rossnagel. *Ultrafast Melting of a Charge-Density Wave in the Mott Insulator 1T-TaS_2.* Physical Review Letters **105**, 187401 (2010). DOI: 10.1103/PhysRevLett.105.187401. 148

[Hes90] D. R. Heslinga, H. H. Weitering, D. P. Vanderwerf, T. M. Klapwijk, & T. Hibma. *Atomic-Structure-Dependent Schottky-Barrier At Epitaxial Pb/Si(111) Interfaces.* Physical Review Letters **64**, 13, 1589 (1990). DOI: 10.1103/PhysRevLett.64.1589. 57

[Hüf03] S. Hüfner. *Photoelectron Spectroscopy.* Springer, Heidelberg (2003). 3, 9, 25, 27, 28, 139

[HM09] J. Herrero-Martín, V. Scagnoli, C. Mazzoli, Y. Su, R. Mittal, Y. Xiao, T. Brueckel, N. Kumar, S. K. Dhar, A. Thamizhavel, & L. Paolasini. *Magnetic structure of $EuFe_2As_2$ as determined by resonant x-ray scattering.* Physical Review B **80**, 134411 (2009). DOI: 10.1103/PhysRevB.80.134411. 83

[Hon09] I-P. Hong, C. Brun, F. Patthey, I. Yu. Sklyadneva, X. Zubizarreta, R. Heid, V. M. Silkin, P. M. Echenique, K. P. Bohnen, E. V. Chulkov, & W.-D. Schneider. *Decay mechanisms of excited electrons in quantum-well states of ultrathin Pb islands grown on Si(111): Scanning tunneling spectroscopy and theory.* Physical Review B **80**, 081409 (2009). DOI: 10.1103/PhysRevB.80.081409. 57, 139

[Hor84] K. Horn, B. Reihl, A. Zartner, D. E. Eastman, K. Hermann, & J. Noffke. *Electronic Energy Bands of Lead: Angle-Resolved Photoemission and Band-Structure Calculations.* Physical Review B **30**, 4, 1711 (1984). DOI: 10.1103/PhysRevB.30.1711. 4

[Hot99] A. Hotzel. *Elektronendynamik der Adsorbatbedeckten Cu(111)-Oberfläche.* PhD Thesis, Freie Universität Berlin (1999). 34, 44

[How04] P. C. Howell, A. Rosch, & P. J. Hirschfeld. *Relaxation of Hot Quasiparticles in a d-Wave Superconductor.* Physical Review Letters **92**, 037003 (2004). DOI: 10.1103/PhysRevLett.92.037003. 111, 119

[Hua08a] Q. Huang, Y. Qiu, W. Bao, M. A. Green, J. W. Lynn, Y. C. Gasparovic, T. Wu, G. Wu, & X. H. Chen. *Neutron-Diffraction Measurements of Magnetic Order and a Structural Transition in the Parent $BaFe_2As_2$ Compound of FeAs-Based High-Temperature Superconductors.* Physical Review Letters **101**, 257003 (2008). DOI: 10.1103/PhysRevLett.101.257003. 77, 78, 87

[Hua08b] Q. Huang, J. Zhao, J. W. Lynn, G. F. Chen, J. L. Luo, N. L. Wang, & P. Dai. *Doping evolution of antiferromagnetic order and structural distortion in $LaFeAsO_{1-x}F_x$.* Physical Review B **78**, 054529 (2008). DOI: 10.1103/PhysRevB.78.054529. 76

[Hub63] J. Hubbard. *Electron Correlations in Narrow Energy Bands.* Proceedings of the Royal Society of London **276**, 1365, 238 (1963). DOI: 10.1098/rspa.1963.0204. 2

[Hun95] S. Hunsche, K. Wienecke, T. Dekorsy, & H. Kurz. *Impulsive Softening of Coherent Phonons in Tellurium.* Physical Review Letters **75**, 9, 1815 (1995). DOI: 10.1103/PhysRevLett.75.1815. 11

[Hup03] M. Hupalo, J. Schmalian, & M. C. Tringides. *Devil's Staircase in Pb/Si(111) Ordered Phases.* Physical Review Letters **90**, 216106 (2003). DOI: 10.1103/PhysRevLett.90.216106. 57

[Ino10] D. S. Inosov, J. T. Park, P. Bourges, D. L. Sun, Y. Sidis, A. Schneidewind, K. Hradil, D. Haug, C. T. Lin, B. Keimer, & V. Hinkov. *Normal-state spin dynamics and temperature-dependent spin-resonance energy in optimally doped $BaFe_{1.85}Co_{0.15}As_2$.* Nature Physics **6**, 3, 178 (2010). DOI: 10.1038/nphys1483. 93

[Ish06] K. Ishioka, M. Kitajima, & O. V. Misochko. *Temperature dependence of coherent A_{1g} and E_g phonons of bismuth.* Journal of Applied Physics **100**, 9, 093501 (2006). DOI: 10.1063/1.2363746. 11

[Ish08] K. Ishioka, M. Kitajima, & O. V. Misochko. *Coherent A_{1g} and E_g phonons of antimony.* Journal of Applied Physics **103**, 12, 123505 (2008). DOI: 10.1063/1.2940130. 11

[Ish10] K. Ishioka & O. V. Misochko. *Coherent Lattice Oscillations in Solids and their Optical Control.* In K. Yamanouchi, A. Giulietti, K. Ledingham, F.P. Schäfer, J.P. Toennies, & W. Zinth (Eds.), *Progress in Ultrafast Intense Laser Science*, Vol. 98 of *Springer Series in Chemical Physics*. Springer Berlin Heidelberg (2010) 23–63. DOI: 10.1007/978-3-642-03825-9. 11, 69, 70, 92, 160

[Jac99] J. D. Jackson. *Classical Electrodynamics.* John Wiley & Sons, Inc. (1999). 39

[Jee08] H. S. Jeevan, Z. Hossain, D. Kasinathan, H. Rosner, C. Geibel, & P. Gegenwart. *Electrical resistivity and specific heat of single-crystalline $EuFe_2As_2$: A magnetic homologue of $SrFe_2As_2$.* Physical Review B **78**, 052502 (2008). DOI: 10.1103/PhysRevB.78.052502. 55, 85

[Jes08] A. Jesche, N. Caroca-Canales, H. Rosner, H. Borrmann, A. Ormeci, D. Kasinathan, H. H. Klauss, H. Luetkens, R. Khasanov, A. Amato, A. Hoser, K. Kaneko, C. Krellner, & C. Geibel. *Strong coupling between magnetic and structural order parameters in $SrFe_2As_2$.* Physical Review B **78**, 180504 (2008). DOI: 10.1103/PhysRevB.78.180504. 78

[Jia07] J. F. Jia, S. C. Li, Y. F. Zhang, & Q. K. Xue. *Quantum Size Effects Induced Novel Properties in Two-Dimensional Electronic Systems: Pb Thin Films on Si(111).* Journal of the Physical Society of Japan **76**, 8, 082001 (2007). DOI: 10.1143/JPSJ.76.082001. 139

[Jia09] S. Jiang, H. Xing, G. Xuan, C. Wang, Z. Ren, C. Feng, J. Dai, Z. Xu, & G. Cao. *Superconductivity up to 30 K in the vicinity of the quantum critical point in $BaFe_2(As_{1-x}P_x)_2$.* Journal of Physics: Condensed Matter **21**, 38, 382203 (2009). DOI: 10.1088/0953-8984/21/38/382203. 75, 76

[Joh09] S. L. Johnson, P. Beaud, E. Vorobeva, C. J. Milne, É. D. Murray, S. Fahy, & G. Ingold. *Directly Observing Squeezed Phonon States with Femtosecond X-Ray Diffraction.* Physical Review Letters **102**, 175503 (2009). DOI: 10.1103/PhysRevLett.102.175503. 11

[Joh10] D. C. Johnston. *The puzzle of high temperature superconductivity in layered iron pnictides and chalcogenides.* Advances in Physics **59**, 6, 803 (2010). DOI: 10.1080/00018732.2010.513480. 75, 109

[Kab99] V. V. Kabanov, J. Demsar, B. Podobnik, & D. Mihailovic. *Quasiparticle relaxation dynamics in superconductors with different gap structures: Theory and experiments on $YBa_2Cu_3O_{7-\delta}$.* Physical Review B **59**, 1497 (1999). DOI: 10.1103/PhysRevB.59.1497. 18, 122

[Kab05] V. V. Kabanov, J. Demsar, & D. Mihailovic. *Kinetics of a Superconductor Excited with a Femtosecond Optical Pulse.* Physical Review Letters **95**, 147002 (2005). DOI: 10.1103/PhysRevLett.95.147002. 17, 111, 117, 120, 121

[Kab08] V. V. Kabanov & A. S. Alexandrov. *Electron relaxation in metals: Theory and exact analytical solutions.* Physical Review B **78**, 17, 174514 (2008). DOI: 10.1103/PhysRevB.78.174514. 10, 83, 107

[Kag57] M. I. Kaganov, I. M. Lifshitz, & L. V. Tanatarov. *Relaxation Between Electrons and the Crystalline Lattice.* Soviet Physics JETP-USSR **4**, 2, 173 (1957). 10

[Kai05] R. A. Kaindl, M. A. Carnahan, D. S. Chemla, S. Oh, & J. N. Eckstein. *Dynamics of Cooper pair formation in $Bi_2Sr_2CaCu_2O_{8+\delta}$.* Physical Review B **72**, 060510 (2005). DOI: 10.1103/PhysRevB.72.060510. 17, 111, 117, 119, 120, 121

[Kam11] H. Kamerlingh Onnes. Commun. Phys. Lab. Univ. Leiden 120b, 122b, 124c (1911). 13

[Kam08] Y. Kamihara, T. Watanabe, M. Hirano, & H. Hosono. *Iron-Based Layered Superconductor $La[O_{1-x}F_x]FeAs$ ($x = 0.05$ - 0.12) with $T_c = 26$ K.* Journal of the American Chemical Society **130**, 11, 3296 (2008). DOI: 10.1021/ja800073m. 73

[Kan10] Ch. Kant, J. Deisenhofer, A. Günther, F. Schrettle, A. Loidl, M. Rotter, & D. Johrendt. *Magnetic and superconducting transitions in $Ba_{1-x}K_xFe_2As_2$ studied by specific heat.* Physical Review B **81**, 014529 (2010). DOI: 10.1103/PhysRevB.81.014529. 104

[Kim03] A. M.-T. Kim, C. A. D. Roeser, & E. Mazur. *Modulation of the bonding-antibonding splitting in Te by coherent phonons.* Physical Review B **68**, 012301 (2003). DOI: 10.1103/PhysRevB.68.012301. 11, 98

[Kim06] H. J. Kim, C. D. Malliakas, A. T. Tomić, S. H. Tessmer, M. G. Kanatzidis, & S. J. L. Billinge. *Local Atomic Structure and Discommensurations in the Charge Density Wave of $CeTe_3$.* Physical Review Letters **96**, 226401 (2006). DOI: 10.1103/PhysRevLett.96.226401. 125, 127

[Kim12] K. W. Kim, A. Pashkin, H. Schäfer, M. Beyer, M. Porer, T. Wolf, C. Bernhard, J. Demsar, R. Huber, & A. Leitenstorfer. *Ultrafast transient generation of spin-density-wave order in the normal state of $BaFe_2As_2$ driven by coherent lattice vibrations.* Nature Materials (2012). DOI: 10.1038/nmat3294. 3, 73, 98

[Kir05] C. Kirkegaard, T. K. Kim, & Ph. Hofmann. *Self-energy determination and electron-phonon coupling on Bi(110).* New Journal of Physics **7**, 1, 99 (2005). DOI: 10.1088/1367-2630/7/1/099. 9

[Kir07] P. S. Kirchmann, M. Wolf, J. H. Dil, K. Horn, & U. Bovensiepen. *Quantum Size Effects in Pb/Si(111) Investigated by Laser-Induced Photoemission.* Physical Review B **76**, 7, 075406 (2007). DOI: 10.1103/PhysRevB.76.075406. 54, 57, 58, 61, 71

[Kir08a] P. S. Kirchmann. *Ultrafast Electron Dynamics in Low-Dimensional Materials.* PhD Thesis, Freie Universität Berlin (2008). 34, 36, 45, 46, 54, 58, 61, 69, 70, 71, 125, 143

[Kir08b] P. S. Kirchmann & U. Bovensiepen. *Ultrafast Electron Dynamics in Pb/Si(111) Investigated by Two-Photon Photoemission.* Physical Review B **78**, 3, 035437 (2008). DOI: 10.1103/PhysRevB.78.035437. 57, 58, 61, 125

[Kir08c] P. S. Kirchmann, L. Rettig, D. Nandi, U. Lipowski, M. Wolf, & U. Bovensiepen. *A Time-of-Flight Spectrometer for Angle-Resolved Detection of Low Energy Electrons in Two Dimensions.* Applied Physics A **91**, 2, 211 (2008). DOI: 10.1007/s00339-008-4422-5. 45, 46, 48, 141

[Kir10] P. S. Kirchmann, L. Rettig, X. Zubizarreta, V. M. Silkin, E. V. Chulkov, & U. Bovensiepen. *Quasiparticle lifetimes in metallic quantum-well nanostructures.* Nature Physics **6**, 782 (2010). DOI: 10.1038/nphys1735. 3, 4, 54, 57, 58, 61, 66, 69

[Kis05] T. Kiss, F. Kanetaka, T. Yokoya, T. Shimojima, K. Kanai, S. Shin, Y. Onuki, T. Togashi, C. Zhang, C. T. Chen, & S. Watanabe. *Photoemission spectroscopic evidence of gap anisotropy in an f-electron superconductor.* Physical Review Letters **94**, 5, 057001 (2005). DOI: 10.1103/PhysRevLett.94.057001. 52

[Kis08] T. Kiss, T. Shimojima, K. Ishizaka, A. Chainani, T. Togashi, T. Kanai, X.-Y. Wang, C.-T. Chen, S. Watanabe, & S. Shin. *A versatile system for ultrahigh resolution, low temperature, and polarization dependent Laser-angle-resolved photoemission spectroscopy.* Review of Scientific Instruments **79**, 023106 (2008). DOI: DOI:10.1063/1.2839010. 58

[Kit04] C. Kittel. *Introduction to Solid State Physics.* Wiley, London (2004). 8, 13

[Kno96] E. Knoesel, A. Hotzel, T. Hertel, M. Wolf, & G. Ertl. *Dynamics of Photoexcited Electrons in Metals Studied with Time-Resolved Two-Photon Photoemission.* Surface Science **368**, 1-3, 76 (1996). DOI: 10.1016/S0039-6028(96)01032-1. 139

[Kno97] E. Knoesel. *Ultrakurzzeit-Dynamik elektronischer Anregungen auf Metalloberflächen.* PhD Thesis, Freie Universität Berlin (1997). 34, 44

[Kno98] E. Knoesel, A. Hotzel, & M. Wolf. *Temperature Dependence of Surface State Lifetimes, Dephasing Rates and Binding Energies on Cu(111) Studied with Time-Resolved Photoemission.* Journal of Electron Spectroscopy and Related Phenomena **88**, 577 (1998). DOI: 10.1016/S0368-2048(97)00178-3. 57

[Koi08] A. Koitzsch, D. Inosov, J. Fink, M. Knupfer, H. Eschrig, S. V. Borisenko, G. Behr, A. Köhler, J. Werner, B. Büchner, R. Follath, & H. A. Dürr. *Valence-band and core-level photoemission spectroscopy of* $LaFeAsO_{1-x}F_x$. Physical Review B **78**, 180506 (2008). DOI: 10.1103/PhysRevB.78.180506. 78

[Koi09] A. Koitzsch, D. S. Inosov, D. V. Evtushinsky, V. B. Zabolotnyy, A. A. Kordyuk, A. Kondrat, C. Hess, M. Knupfer, B. Büchner, G. L. Sun, V. Hinkov, C. T. Lin, A. Varykhalov, & S. V. Borisenko. *Temperature and Doping-Dependent Renormalization Effects of the Low Energy Electronic Structure of* $Ba_{1-x}K_xFe_2As_2$ *Single Crystals.* Physical Review Letters **102**, 167001 (2009). DOI: 10.1103/PhysRevLett.102.167001. 102

[Kom04] H. Komoda, T. Sato, S. Souma, T. Takahashi, Y. Ito, & K. Suzuki. *High-resolution angle-resolved photoemission study of incommensurate charge-density-wave compound* $CeTe_3$. Physical Review B **70**, 195101 (2004). DOI: 10.1103/PhysRevB.70.195101. 127

[Koo10] J. Koo, J. Park, S. K. Cho, K. D. Kim, S.-Y. Park, Y. H. Jeong, Y. J. Park, T. Y. Koo, K.-P. Hong, C.-H. Lee, J.-Y. Kim, B.-K. Cho, K. B. Lee, & H.-J. Kim. *Magnetic and Structural Phase Transitions of $EuFe_2As_2$ Studied via Neutron and Resonant X-ray Scattering.* Journal of the Physical Society of Japan **79**, 11, 114708 (2010). DOI: 10.1143/JPSJ.79.114708. 78

[Kor06a] J. D. Koralek, J. F. Douglas, N. C. Plumb, Z. Sun, A. V. Fedorov, M. M. Murnane, H. C. Kapteyn, S. T. Cundiff, Y. Aiura, K. Oka, H. Eisaki, & D. S. Dessau. *Laser Based Angle-Resolved Photoemission, the Sudden Approximation, and Quasiparticle-Like Spectral Peaks in $Bi_2Sr_2CaCu_2O_{8+\delta}$.* Physical Review Letters **96**, 017005 (2006). DOI: 10.1103/PhysRevLett.96.017005. 26, 36, 52, 58

[Kor06b] A. A. Kordyuk, S. V. Borisenko, V. B. Zabolotnyy, J. Geck, M. Knupfer, J. Fink, B. Büchner, C. T. Lin, B. Keimer, H. Berger, A. V. Pan, S. Komiya, & Y. Ando. *Constituents of the Quasiparticle Spectrum Along the Nodal Direction of High-T_c Cuprates.* Physical Review Letters **97**, 017002 (2006). DOI: 10.1103/PhysRevLett.97.017002. 111

[Kor07] J. D. Koralek, J. F. Douglas, N. C. Plumb, J. D. Griffith, S. T. Cundiff, H. C. Kapteyn, M. M. Murnane, & D. S. Dessau. *Experimental Setup for Low-Energy Laser-Based Angle Resolved Photoemission Spectroscopy.* Review of Scientific Instruments **78**, 5, 053905 (2007). DOI: 10.1063/1.2722413. 26

[Kum11] P. Kumar, A. Bera, D. V. S. Muthu, A. Kumar, U. V. Waghmare, L. Harnagea, C. Hess, S. Wurmehl, S. Singh, B. Büchner, & A. K. Sood. *Raman evidence for the superconducting gap and spin-phonon coupling in the superconductor $Ca(Fe_{0.95}Co_{0.05})_2As_2$.* Journal of Physics: Condensed Matter **23**, 25, 255403 (2011). DOI: 10.1088/0953-8984/23/25/255403. 92

[Kus05] P. Kusar, J. Demsar, D. Mihailovic, & S. Sugai. *A systematic study of femtosecond quasiparticle relaxation processes in $La_{2-x}Sr_xCuO_4$.* Physical Review B **72**, 014544 (2005). DOI: 10.1103/PhysRevB.72.014544. 111, 120, 122

[Kus08] P. Kusar, V. V. Kabanov, J. Demsar, T. Mertelj, S. Sugai, & D. Mihailovic. *Controlled Vaporization of the Superconducting Condensate in Cuprate Superconductors by Femtosecond Photoexcitation.* Physical Review Letters **101**, 22, 227001 (2008). DOI: 10.1103/PhysRevLett.101.227001. 111, 117, 120, 122

[Kus11] P. Kusar, T. Mertelj, V. V. Kabanov, J.-H. Chu, I. R. Fisher, H. Berger, L. Forró, & D. Mihailovic. *Anharmonic order-parameter oscillations and lattice coupling in strongly driven 1T-TaS_2 and $TbTe_3$ charge-density-wave compounds: A multiple-pulse femtosecond laser spectroscopy study.* Physical Review B **83**, 035104 (2011). DOI: 10.1103/PhysRevB.83.035104. 157

[Lan76] H. H. Landolt & R. Börnstein. *Numerical Data and Functional Ralationships in Science and Technology.* New Series. Springer, Berlin (1976). 69

[LaS00] S. LaShell, E. Jensen, & T. Balasubramanian. *Nonquasiparticle structure in the photoemission spectra from the Be(0001) surface and determination of the electron self energy.* Physical Review B **61**, 2371 (2000). DOI: 10.1103/PhysRevB.61.2371. 9

[Lav05] J. Laverock, S. B. Dugdale, Zs. Major, M. A. Alam, N. Ru, I. R. Fisher, G. Santi, & E. Bruno. *Fermi surface nesting and charge-density wave formation in rare-earth tritellurides.* Physical Review B **71**, 8, 085114 (2005). DOI: 10.1103/PhysRevB.71.085114. 127, 134

[Lee74] P. A. Lee, T. M. Rice, & P. W. Anderson. *Conductivity from Charge or Spin Density Waves.* Solid State Communications **14**, 703 (1974). DOI: 10.1016/0038-1098(74)90868-0. 23

[Lee81] P. A. Lee, P. H. Citrin, P. Eisenberger, & B. M. Kincaid. *Extended x-ray absorption fine structure - its strengths and limitations as a structural tool.* Reviews of Modern Physics **53**, 769 (1981). DOI: 10.1103/RevModPhys.53.769. 88

[Lee07] W. S. Lee, I. M. Vishik, K. Tanaka, D. H. Lu, T. Sasagawa, N. Nagaosa, T. P. Devereaux, Z. Hussain, & Z.-X. Shen. *Abrupt onset of a second energy gap at the superconducting transition of underdoped Bi2212.* Nature **450**, 7166, 81 (2007). DOI: 10.1038/nature06219. 136, 139

[Les09] C. Lester, J.-H. Chu, J. G. Analytis, S. C. Capelli, A. S. Erickson, C. L. Condron, M. F. Toney, I. R. Fisher, & S. M. Hayden. *Neutron scattering study of the interplay between structure and magnetism in* $Ba(Fe_{1-x}Co_x)_2As_2$. Physical Review B **79**, 144523 (2009). DOI: 10.1103/PhysRevB.79.144523. 76, 78

[Lin54] J. Lindhard. *On the Properties of a Gas of Charged Particles.* Matematisk-Fysiske Meddelelser Kongelige Danske Videnskabernes Selskab **28**, 8, 1 (1954). URL `http://www.sdu.dk/media/bibpdf/Bind20-29\Bind\mfm-28-8.pdf`. 20

[Lis04a] M. Lisowski, P. A. Loukakos, U. Bovensiepen, & M. Wolf. *Femtosecond Dynamics and Transport of Optically Excited Electrons in Epitaxial Cu Films on Si(111)-*7×7. Applied Physics A **79**, 4-6, 739 (2004). DOI: 10.1007/s00339-004-2591-4. 57

[Lis04b] M. Lisowski, P.A. Loukakos, U. Bovensiepen, J. Stähler, C. Gahl, & M. Wolf. *Ultra-fast dynamics of electron thermalization, cooling and transport effects in Ru(001).* Applied Physics A **78**, 165 (2004). DOI: 10.1007/s00339-003-2301-7. 10, 30, 63, 81, 83, 88, 102, 103

[Lis05a] M. Lisowski. *Elektronen- und Magnetisierungsdynamik in Metallen untersucht mit zeitaufgelöster Photoemission.* PhD Thesis, Freie Universität Berlin (2005). 10, 29, 30, 34, 102, 103

[Lis05b] M. Lisowski, P. A. Loukakos, A. Melnikov, I. Radu, L. Ungureanu, M. Wolf, & U. Bovensiepen. *Femtosecond Electron and Spin Dynamics In Gd(0001) Studied by Time-Resolved Photoemission and Magneto-Optics.* Physical Review Letters **95**, 137402 (2005). DOI: 10.1103/PhysRevLett.95.137402. 3, 11, 30

[Lit08] A. P. Litvinchuk, V. G. Hadjiev, M. N. Iliev, Bing Lv, A. M. Guloy, & C. W. Chu. *Raman scattering study of* $K_xSr_{1-x}Fe_2As_2$ *(x=0.0, 0.4).* Physical Review B **78**, 6, 060503 (2008). DOI: 10.1103/PhysRevB.78.060503. 92, 93, 152, 154

[Lit11] A. P. Litvinchuk, Bing Lv, & C. W. Chu. *Raman scattering study of electron-doped $Pr_xCa_{1-x}Fe_2As_2$ superconductors.* Physical Review B **84**, 092504 (2011). DOI: 10.1103/PhysRevB.84.092504. 93

[Liu08] C. Liu, T. Inaoka, S. Yaginuma, T. Nakayama, M. Aono, & T. Nagao. *Disappearance of the Quasi-One-Dimensional Plasmon at the Metal-Insulator Phase Transition of Indium Atomic Wires.* Physical Review B **77**, 20, 205415 (2008). DOI: 10.1103/PhysRevB.77.205415. 77, 111, 119, 120, 122

[Liu09] G. Liu, H. Liu, L. Zhao, W. Zhang, X. Jia, J. Meng, X. Dong, J. Zhang, G. F. Chen, G. Wang, Y. Zhou, Y. Zhu, X. Wang, Z. Xu, C. Chen, & X. J. Zhou. *Band-structure reorganization across the magnetic transition in $BaFe_2As_2$ seen via high-resolution angle-resolved photoemission.* Physical Review B **80**, 134519 (2009). DOI: 10.1103/PhysRevB.80.134519. 78

[Lob01] A. I. Lobad & A. J. Taylor. *Coherent Phonon Generation Mechanism in Solids.* Physical Review B **64**, 18, 180301 (2001). DOI: 10.1103/PhysRevB.64.180301. 160

[Lue09] H. Luetkens, H.-H. Klauss, M. Kraken, F. J. Litterst, T. Dellmann, R. Klingeler, C. Hess, R. Khasanov, A. Amato, C. Baines, M. Kosmala, O. J. Schumann, M. Braden, J. Hamann-Borrero, N. Leps, A. Kondrat, G. Behr, J. Werner, & B. Buchner. *The electronic phase diagram of the $LaO_{1-x}F_xFeAs$ superconductor.* Nature Materials **8**, 4, 305 (2009). DOI: 10.1038/nmat2397. 76

[Luh02] D.-A. Luh, T. Miller, J. J. Paggel, & T.-C. Chiang. *Large Electron-Phonon Coupling at an Interface.* Physical Review Letters **88**, 25, 256802 (2002). DOI: 10.1103/PhysRevLett.88.256802. 66

[MA06] L. Miaja-Avila, C. Lei, M. Aeschlimann, J. L. Gland, M. M. Murnane, H. C. Kapteyn, & G. Saathoff. *Laser-Assisted Photoelectric Effect from Surfaces.* Physical Review Letters **97**, 113604 (2006). DOI: 10.1103/PhysRevLett.97.113604. 50

[Ma10] F.-j. Ma, Z.-y. Lu, & T. Xiang. *Electronic structures of ternary iron arsenides AFe_2As_2; (A = Ba, Ca, or Sr).* Frontiers of Physics in China **5**, 150 (2010). DOI: 10.1007/s11467-009-0076-9. 77

[Mah70a] G. D. Mahan. *Angular Dependence of Photoemission in Metals.* Physical Review Letters **24**, 19, 1068 (1970). DOI: 10.1103/PhysRevLett.24.1068. 27

[Mah70b] G. D. Mahan. *Theory of Photoemission in Simple Metals.* Physical Review B **2**, 11, 4334 (1970). DOI: 10.1103/PhysRevB.2.4334. 27

[Mal05] C. Malliakas, S. J. L. Billinge, H. J. Kim, & M. G. Kanatzidis. *Square Nets of Tellurium: Rare-Earth Dependent Variation in the Charge-Density Wave of $RETe_3$ (RE = Rare-Earth Element).* Journal of the American Chemical Society **127**, 18, 6510 (2005). DOI: 10.1021/ja0505292. 125

[Mal09] W. Malaeb, T. Yoshida, A. Fujimori, M. Kubota, K. Ono, K. Kihou, P. M. Shirage, H. Kito, A. Iyo, H. Eisaki, Y. Nakajima, T. Tamegai, & R. Arita. *Three-Dimensional Electronic Structure of Superconducting Iron Pnictides Observed by Angle-Resolved Photoemission Spectroscopy.* Journal of the Physical Society of Japan **78**, 12, 123706 (2009). DOI: 10.1143/JPSJ.78.123706. 80

[Man09] B. Mansart, D. Boschetto, A. Savoia, F. Rullier-Albenque, A. Forget, D. Colson, A. Rousse, & M. Marsi. *Observation of a coherent optical phonon in the iron pnictide superconductor $Ba(Fe_{1-x}Co_x)_2As_2$ ($x = 0.06$ and 0.08).* Physical Review B **80**, 17, 172504 (2009). DOI: 10.1103/PhysRevB.80.172504. 12, 73, 83, 92, 97

[Man10] B. Mansart, D. Boschetto, A. Savoia, F. Rullier-Albenque, F. Bouquet, E. Papalazarou, A. Forget, D. Colson, A. Rousse, & M. Marsi. *Ultrafast transient response and electron-phonon coupling in the iron-pnictide superconductor $Ba(Fe_{1-x}Co_x)_2As_2$.* Physical Review B **82**, 2, 024513 (2010). DOI: 10.1103/PhysRevB.82.024513. 10, 73, 103, 105, 108

[Man11] B. Mansart, V. Brouet, E. Papalazarou, M. Fuglsang Jensen, L. Petaccia, S. Gorovikov, A. N. Grum-Grzhimailo, F. Rullier-Albenque, A. Forget, D. Colson, & M. Marsi. *Orbital nature of the hole-like Fermi surface in superconducting $Ba(Fe_{1-x}Co_x)_2As_2$.* Physical Review B **83**, 064516 (2011). DOI: 10.1103/PhysRevB.83.064516. 78, 80

[Mat06] Y. Matsumoto & K. Watanabe. *Coherent Vibrations of Adsorbates Induced by Femtosecond Laser Excitation.* Chemical Reviews **106**, 10, 4234 (2006). DOI: 10.1021/cr050165w. 11, 12, 148

[Mat07] S. Mathias, L. Miaja-Avila, M. M. Murnane, H. Kapteyn, M. Aeschlimann, & M. Bauer. *Angle-resolved photoemission spectroscopy with a femtosecond high harmonic light source using a two-dimensional imaging electron analyzer.* Review of Scientific Instruments **78**, 8, 083105 (2007). DOI: 10.1063/1.2773783. 50, 98

[Mat10] S. Mathias, A. Ruffing, F. Deicke, M. Wiesenmayer, M. Aeschlimann, & M. Bauer. *Band structure dependence of hot-electron lifetimes in a Pb/Cu(111) quantum-well system.* Physical Review B **81**, 155429 (2010). DOI: 10.1103/PhysRevB.81.155429. 3, 57, 72, 167

[Maz08] I. I. Mazin, D. J. Singh, M. D. Johannes, & M. H. Du. *Unconventional Superconductivity with a Sign Reversal in the Order Parameter of $LaFeAsO_{1-x}F_x$.* Physical Review Letters **101**, 057003 (2008). DOI: 10.1103/PhysRevLett.101.057003. 73

[Maz10] I. I. Mazin. *Superconductivity gets an iron boost.* Nature **464**, 7286, 183 (2010). DOI: 10.1038/nature08914. 73, 75, 77

[McD95] B. A. McDougall, T. Balasubramanian, & E. Jensen. *Phonon contribution to quasiparticle lifetimes in Cu measured by angle-resolved photoemission.* Physical Review B **51**, 13891 (1995). DOI: 10.1103/PhysRevB.51.13891. 106

[McM68] W. L. McMillan. *Transition Temperature of Strong-Coupled Superconductors.* Physical Review **167**, 331 (1968). DOI: 10.1103/PhysRev.167.331. 108

[McP87] A. McPherson, G. Gibson, H. Jara, U. Johann, T. S. Luk, I. A. McIntyre, K. Boyer, & C. K. Rhodes. *Studies of multiphoton production of vacuum-ultraviolet radiation in the rare gases.* Journal of the Optical Society of America B **4**, 4, 595 (1987). DOI: 10.1364/JOSAB.4.000595. 50

[Mei33] W. Meissner & R. Ochsenfeld. *Ein neuer Effekt bei Eintritt der Supraleitfähigkeit.* Naturwissenschaften **21**, 787 (1933). DOI: 10.1007/BF01504252. 13

[Mel03] A. Melnikov, I. Radu, U. Bovensiepen, O. Krupin, K. Starke, E. Matthias, & M. Wolf. *Coherent Optical Phonons and Parametrically Coupled Magnons Induced by Femtosecond Laser Excitation of the Gd(0001) Surface.* Physical Review Letters **91**, 227403 (2003). DOI: 10.1103/PhysRevLett.91.227403. 11, 12, 70

[Mel08] A. Melnikov, A. Povolotskiy, & U. Bovensiepen. *Magnon-Enhanced Phonon Damping at Gd(0001) and Tb(0001) Surfaces Using Femtosecond Time-Resolved Optical Second-Harmonic Generation.* Physical Review Letters **100**, 24, 247401 (2008). DOI: 10.1103/PhysRevLett.100.247401. 89, 92, 93

[Mer04] M. Merschdorf, C. Kennerknecht, & W. Pfeiffer. *Collective and single-particle dynamics in time-resolved two-photon photoemission.* Physical Review B **70**, 19, 193401 (2004). DOI: 10.1103/PhysRevB.70.193401. 57

[Mer09] T. Mertelj, V. V. Kabanov, C. Gadermaier, N. D. Zhigadlo, S. Katrych, Z. Bukowski, J. Karpinski, & D. Mihailovic. *Photoinduced Quasiparticle Relaxation Dynamics in Near-optimally Doped $SmFeAsO_{0.8}F_{0.2}$ Single Crystals.* Journal of Superconductivity and novel Magnetism **22**, 6, 575 (2009). DOI: 10.1007/s10948-009-0468-7. 73

[Mer10] T. Mertelj, P. Kusar, V. V. Kabanov, L. Stojchevska, N. D. Zhigadlo, S. Katrych, Z. Bukowski, J. Karpinski, S. Weyeneth, & D. Mihailovic. *Quasiparticle relaxation dynamics in spin-density-wave and superconducting $SmFeAsO_{1-x}F_x$ single crystals.* Physical Review B **81**, 224504 (2010). DOI: 10.1103/PhysRevB.81.224504. 73, 83, 92, 105

[Mey11] M. Meyer. *Ultrafast Electron Dynamics at Alkali/Ice Structures Adsorbed on a Metal Surface.* PhD Thesis, Freie Universität Berlin (2011). 34

[Mil02] M. Milun, P. Pervan, & D. P. Woodruff. *Quantum Well Structures in Thin Metal Films: Simple Model Physics in Reality?* Reports on Progress in Physics **65**, 2, 99 (2002). DOI: 10.1088/0034-4885/65/2/201. 57, 66

[Mis07a] O. V. Misochko, M. V. Lebedev, H. Schäfer, & T. Dekorsy. *Coherent A_1 phonons in Te studied with tailored femtosecond pulses.* Journal of Physics: Condensed Matter **19**, 40, 406220 (2007). DOI: 10.1088/0953-8984/19/40/406220. 11, 157

[Mis07b] O. V. Misochko, R. Lu, M. Hase, & M. Kitajima. *Coherent control of the lattice dynamics of bismuth near the lindemann stability limit.* Journal of Experimental and Theoretical Physics **104**, 245 (2007). DOI: 10.1134/S1063776107020094. 157

[Mit09a] R. Mittal, L. Pintschovius, D. Lamago, R. Heid, K.-P. Bohnen, D. Reznik, S. L. Chaplot, Y. Su, N. Kumar, S. K. Dhar, A. Thamizhavel, & Th. Brueckel. *Measurement of Anomalous Phonon Dispersion of $CaFe_2As_2$ Single Crystals Using Inelastic Neutron Scattering.* Physical Review Letters **102**, 21, 217001 (2009). DOI: 10.1103/PhysRevLett.102.217001. 104

[Mit09b] R. Mittal, S. Rols, M. Zbiri, Y. Su, H. Schober, S. L. Chaplot, M. Johnson, M. Tegel, T. Chatterji, S. Matsuishi, H. Hosono, D. Johrendt, & Th. Brueckel. *Phonon spectra in $CaFe_2As_2$ and $Ca_{0.6}Na_{0.4}Fe_2As_2$: Measurement of the pressure and temperature dependence and comparison with ab initio and shell model calculations.* Physical Review B **79**, 14, 144516 (2009). DOI: 10.1103/PhysRevB.79.144516. 104

[Moe93] W. Moench. *Semiconductor Surfaces and Interfaces.* Springer, Berlin-Heidelberg (1993). 57, 59

[Moo10] R. G. Moore, V. Brouet, R. He, D. H. Lu, N. Ru, J.-H. Chu, I. R. Fisher, & Z.-X. Shen. *Fermi surface evolution across multiple charge density wave transitions in $ErTe_3$.* Physical Review B **81**, 073102 (2010). DOI: 10.1103/PhysRevB.81.073102. 125, 127, 130, 132, 134, 136, 138, 139

[Moo12a] R. G. Moore. *private communication* (2012). Geballe Laboratory for Advanced Materials and Department of Applied Physics, Stanford University, Stanford, California, USA. 135, 136, 151

[Moo12b] R. G. Moore, W. S. Lee, P. S. Kirchman, Y. D. Chuang, M. Trigo, L. Patthey, D. H. Lu, O. Krupin, M. Yi, D. A. Reis, D. Doering, P. Denes, W. F. Schlotter, J. J. Turner, G. Hay, P. Hering, T. Benson, J.-H. Chu, I. R. Fisher, Z. Hussain, & Z.-X. Shen. *Ultrafast lattice dynamical response to the electronic excitation of the charge density wave in $TbTe_3$* (2012). To be published. 149, 151, 159

[Mor10] B. Moritz, T. P. Devereaux, & J. K. Freericks. *Time-resolved photoemission of correlated electrons driven out of equilibrium.* Physical Review B **81**, 165112 (2010). DOI: 10.1103/PhysRevB.81.165112. 3

[Mur05] É. D. Murray, D. M. Fritz, J. K. Wahlstrand, S. Fahy, & D. A. Reis. *Effect of lattice anharmonicity on high-amplitude phonon dynamics in photoexcited bismuth.* Physical Review B **72**, 060301 (2005). DOI: 10.1103/PhysRevB.72.060301. 157

[Mur08] R. A. Murdick, R. K. Raman, Y. Murooka, & C.-Y. Ruan. *Photovoltage dynamics of the hydroxylated Si(111) surface investigated by ultrafast electron diffraction.* Physical Review B **77**, 245329 (2008). DOI: 10.1103/PhysRevB.77.245329. 57

[Nek08] I. Nekrasov, Z. Pchelkina, & M. Sadovskii. *Electronic structure of prototype AFe_2As_2 and ReOFeAs high-temperature superconductors: A comparison.* JETP Letters **88**, 144 (2008). DOI: 10.1134/S0021364008140166. 77

[Nes98] W. Nessler, S. Ogawa, H. Nagano, H. Petek, J. Shimoyama, Y. Nakayama, & K. Kishio. *Femtosecond Time-Resolved Study of the Energy and Temperature Dependence of Hot-Electron Lifetimes in $Bi_2Sr_2CaCu_2O_{8+\delta}$.* Physical Review Letters **81**, 4480 (1998). DOI: 10.1103/PhysRevLett.81.4480. 119

[Ni08] N. Ni, S. L. Bud'ko, A. Kreyssig, S. Nandi, G. E. Rustan, A. I. Goldman, S. Gupta, J. D. Corbett, A. Kracher, & P. C. Canfield. *Anisotropic thermodynamic and transport properties of single-crystalline $Ba_{1-x}K_xFe_2As_2$ (x=0 and 0.45).* Physical Review B **78**, 1, 014507 (2008). DOI: 10.1103/PhysRevB.78.014507. 85

[Nic03] E. J. Nicol & J. P. Carbotte. *Comparison of s - and d -wave gap symmetry in nonequilibrium superconductivity.* Physical Review B **67**, 214506 (2003). DOI: 10.1103/PhysRevB.67.214506. 18, 124

[Nor88] T. J. Norton, R. W. Airey, B. L. Morgan, P. D. Read, & J. R. Powell. *A 40mm MCP Intensifier for Photon Counting.* Academic Press (1988) 41–53. 48

[Nor98] M. R. Norman, M. Randeria, H. Ding, & J. C. Campuzano. *Phenomenology of the low-energy spectral function in high-T_c superconductors.* Physical Review B **57**, R11093 (1998). DOI: 10.1103/PhysRevB.57.R11093. 116, 124

[Nor05] M. R. Norman, D. Pines, & C. Kallin. *The pseudogap: friend or foe of high T_c?* Advances in Physics **54**, 8, 715 (2005). DOI: 10.1080/00018730500459906. 116, 122

[Nor08] M. R. Norman. *High-Temperature Superconductivity in the Iron Pnictides.* Physics **1**, 21 (2008). DOI: 10.1103/Physics.1.21. 75, 77

[Nor11] M. R. Norman. *The Challenge of Unconventional Superconductivity.* Science **332**, 6026, 196 (2011). DOI: 10.1126/science.1200181. 2, 16, 17

[Nyq28] H. Nyquist. *Certain topics in telegraph transmission theory.* Transactions of the American Institute of Electrical Engineers **47**, 617 (1928). 89

[Oka11] Y. Okano, H. Katsuki, Y. Nakagawa, H. Takahashi, K. G. Nakamura, & K. Ohmori. *Optical manipulation of coherent phonons in superconducting $YBa_2Cu_3O_{7-\delta}$ thin films.* Faraday Discuss. **153**, 375 (2011). DOI: 10.1039/C1FD00070E. 157

[Ono07] T. Onozaki, Y. Toda, S. Tanda, & R. Morita. *Coherent Double-Pulse Excitation of Charge-Density-Wave Oscillation.* Japanese Journal of Applied Physics **46**, 2, 870 (2007). DOI: 10.1143/JJAP.46.870. 157, 159

[Owe72] C. S. Owen & D. J. Scalapino. *Superconducting State under the Influence of External Dynamic Pair Breaking.* Physical Review Letters **28**, 24, 1559 (1972). DOI: 10.1103/PhysRevLett.28.1559. 18, 124

[Pag99] J. J. Paggel, T. Miller, & T.-C. Chiang. *Quantum-Well States as Fabry-Pérot Modes in a Thin-Film Electron Interferometer.* Science **283**, 1709 (1999). DOI: 10.1126/science.283.5408.1709. 57

[Pag10] J. Paglione & R. L. Greene. *High-temperature superconductivity in iron-based materials.* Nature Physics **6**, 9, 645 (2010). DOI: 10.1038/nphys1759. 75

[Par75] W. H. Parker. *Modified heating theory of nonequilibrium superconductors.* Physical Review B **12**, 9, 3667 (1975). DOI: 10.1103/PhysRevB.12.3667. 18, 124

[Pei55] R. E. Peierls. *Quantum Theory of Solids.* Oxford University Press, New York (1955). 19

[Pen76] J. B. Pendry. *Theory of Photoemission.* Surface Science **57**, 2, 679 (1976). DOI: 10.1016/0039-6028(76)90355-1. 26

[Per06] L. Perfetti, P. A. Loukakos, M. Lisowski, U. Bovensiepen, H. Berger, S. Biermann, P. S. Cornaglia, A. Georges, & M. Wolf. *Time Evolution of the Electronic Structure of 1T-TaS_2 Through the Insulator-Metal Transition.* Physical Review Letters **97**, 067402 (2006). DOI: 10.1103/PhysRevLett.97.067402. 3, 11, 30, 36, 87

[Per07] L. Perfetti, P. A. Loukakos, M. Lisowski, U. Bovensiepen, H. Eisaki, & M. Wolf. *Ultrafast electron relaxation in superconducting $Bi_2Sr_2CaCu_2O_{8+\delta}$ by time-resolved photoelectron spectroscopy.* Physical Review Letters **99**, 19, 197001 (2007). DOI: 10.1103/PhysRevLett.99.197001. 10, 30, 36, 73, 102, 103, 105, 108, 111, 116, 122, 123

[Per08] L. Perfetti, P. A. Loukakos, M. Lisowski, U. Bovensiepen, M. Wolf, H. Berger, S. Biermann, & A. Georges. *Femtosecond Dynamics of Electronic States in the Mott Insulator 1T-TaS_2 by Time Resolved Photoelectron Spectroscopy.* New Journal of Physics **10**, 5, 053019 (2008). DOI: 10.1088/1367-2630/10/5/053019. 30, 36, 148

[Pet97] H. Petek & S. Ogawa. *Femtosecond Time-Resolved Two-Photon Photoemission Studies of Electron Dynamics in Metals.* Progress in Surface Science **56**, 4, 239 (1997). DOI: 10.1016/S0079-6816(98)00002-1. 3, 29, 57, 139

[Pet11] J. C. Petersen, S. Kaiser, N. Dean, A. Simoncig, H. Y. Liu, A. L. Cavalieri, C. Cacho, I. C. E. Turcu, E. Springate, F. Frassetto, L. Poletto, S. S. Dhesi, H. Berger, & A. Cavalleri. *Clocking the Melting Transition of Charge and Lattice Order in 1T-TaS_2 with Ultrafast Extreme-Ultraviolet Angle-Resolved Photoemission Spectroscopy.* Physical Review Letters **107**, 177402 (2011). DOI: 10.1103/PhysRevLett.107.177402. 87, 148

[Pic89] W. E. Pickett. *Electronic structure of the high-temperature oxide superconductors.* Reviews of Modern Physics **61**, 433 (1989). DOI: 10.1103/RevModPhys.61.433. 113, 114

[Pie07] A. Pietzsch, A. Föhlisch, F. Hennies, S. Vijayalakshmi, & W. Wurth. *Interface photovoltage dynamics at the buried BaF_2/Si interface: Time resolved laser-pump/synchrotron-probe photoemission.* Applied Physics A **88**, 587 (2007). DOI: 10.1007/s00339-007-4072-z. 57

[Pin66] D. Pines & P. Nozieres. *The Theory of Quatum Liquids*, Vol. I of *Advanced Book Classic Series.* W. A. Benjamin, Inc. (1966). 106

[Plu82] E. W. Plummer & W. Eberhardt. *Angle-resolved Photoemission As A Tool For the Study of Surfaces.* Advances In Chemical Physics **49**, 533 (1982). DOI: 10.1002/9780470142691.ch8. 28

[Ram08] R. K. Raman, Y. Murooka, C.-Y. Ruan, T. Yang, S. Berber, & D. Tománek. *Direct Observation of Optically Induced Transient Structures in Graphite using Ultrafast Electron Crystallography.* Physical Review Letters **101**, 077401 (2008). DOI: 10.1103/PhysRevLett.101.077401. 151

[Ran09] Y. Ran, F. Wang, H. Zhai, A. Vishwanath, & D.-H. Lee. *Nodal spin density wave and band topology of the FeAs-based materials.* Physical Review B **79**, 014505 (2009). DOI: 10.1103/PhysRevB.79.014505. 77

[Rec06] V. Recoules, J. Clerouin, G. Zerah, P. M. Anglade, & S. Mazevet. *Effect of intense laser irradiation on the lattice stability of semiconductors and metals.* Physical Review Letters **96**, 5, 055503 (2006). DOI: 10.1103/PhysRevLett.96.055503. 148, 151

[Rei10] J.-Ph. Reid, M. A. Tanatar, X. G. Luo, H. Shakeripour, N. Doiron-Leyraud, N. Ni, S. L. Bud'ko, P. C. Canfield, R. Prozorov, & L. Taillefer. *Nodes in the gap structure of the iron arsenide superconductor* $Ba(Fe_{1-x}Co_x)_2As_2$ *from c" axis heat transport measurements.* Physical Review B **82**, 064501 (2010). DOI: 10.1103/PhysRevB.82.064501. 104

[Ren08] Z.-A. Ren, W. Lu, J. Yang, W. Yi, X.-L. Shen, Zheng-Cai, G.-C. Che, X.-L. Dong, L.-L. Sun, F. Zhou, & Z.-X. Zhao. *Superconductivity at 55 K in Iron-Based F-Doped Layered Quaternary Compound* $Sm[O_{1-x}F_x]FeAs$. Chinese Physics Letters **25**, 6, 2215 (2008). DOI: 10.1088/0256-307X/25/6/080. 75

[Ret02] B. Rethfeld, A. Kaiser, M. Vicanek, & G. Simon. *Ultrafast Dynamics of Nonequilibrium Electrons in Metals Under Femtosecond Laser Irradiation.* Physical Review B **65**, 21, 214303 (2002). DOI: 10.1103/PhysRevB.65.214303. 10, 30, 63, 102

[Ret08] L. Rettig. *Ultraschnelle Elektronendynamik in Pb/Si(111) Quantentrögen.* Diploma Thesis, Freie Universität Berlin (2008). 34, 45, 46, 54, 58, 61, 69

[Ret12a] L. Rettig, R. Cortés, S. Thirupathaiah, P. Gegenwart, H. S. Jeevan, M. Wolf, J. Fink, & U. Bovensiepen. *Ultrafast Momentum-Dependent Response of Electrons in Antiferromagnetic* $EuFe_2As_2$ *Driven by Optical Excitation.* Physical Review Letters **108**, 097002 (2012). DOI: 10.1103/PhysRevLett.108.097002. 30, 36, 74, 148

[Ret12b] L. Rettig, P. S. Kirchmann, & U. Bovensiepen. *Ultrafast dynamics of occupied quantum well states in Pb/Si(111).* New Journal of Physics **14**, 2, 023047 (2012). DOI: 10.1088/1367-2630/14/2/023047. 58

[Rez09] D. Reznik, K. Lokshin, D. C. Mitchell, D. Parshall, W. Dmowski, D. Lamago, R. Heid, K.-P. Bohnen, A. S. Sefat, M. A. McGuire, B. C. Sales, D. G. Mandrus, A. Subedi, D. J. Singh, A. Alatas, M. H. Upton, A. H. Said, A. Cunsolo, Yu. Shvyd'ko, & T. Egami. *Phonons in doped and undoped* $BaFe_2As_2$ *investigated by inelastic x-ray scattering.* Physical Review B **80**, 214534 (2009). DOI: 10.1103/PhysRevB.80.214534. 93, 104

[Rhi03] H.-S. Rhie, H. A. Dürr, & W. Eberhardt. *Femtosecond Electron and Spin Dynamics in* Ni/W(110) *Films.* Physical Review Letters **90**, 247201 (2003). DOI: 10.1103/PhysRevLett.90.247201. 3

[Ric04] D. A. Ricci, T. Miller, & T.-C. Chiang. *Chemical Tuning of Metal-Semiconductor Interfaces.* Physical Review Letters **93**, 13, 136801 (2004). DOI: 10.1103/PhysRevLett.93.136801. 57, 58

[Ric09] P. Richard, T. Sato, K. Nakayama, S. Souma, T. Takahashi, Y.-M. Xu, G. F. Chen, J. L. Luo, N. L. Wang, & H. Ding. *Angle-Resolved Photoemission Spectroscopy of the Fe-Based* $Ba_{0.6}K_{0.4}Fe_2As_2$ *High Temperature Superconductor:*

Evidence for an Orbital Selective Electron-Mode Coupling. Physical Review Letters **102**, 047003 (2009). DOI: 10.1103/PhysRevLett.102.047003. 102

[Ric11] P. Richard, T. Sato, K. Nakayama, T. Takahashi, & H. Ding. *Fe-based superconductors: an angle-resolved photoemission spectroscopy perspective*. Reports on Progress in Physics **74**, 12, 124512 (2011). DOI: 10.1088/0034-4885/74/12/124512. 3, 25, 77

[Roe04] C. A. D. Roeser, M. Kandyla, A. Mendioroz, & E. Mazur. *Optical control of coherent lattice vibrations in tellurium*. Physical Review B **70**, 212302 (2004). DOI: 10.1103/PhysRevB.70.212302. 157

[Roe06] RoentDek Handels GmbH. *Software for RoentDek Hexanode*, 1. Edt. (2006). 45

[Roh05] M. Rohleder, K. Duncker, W. Berthold, J. Gudde, & U. Hofer. *Momentum-resolved dynamics of Ar/Cu(100) interface states probed by time-resolved two-photon photoemission*. New Journal of Physics **7**, 103 (2005). DOI: 10.1088/1367-2630/7/1/103. 139

[Roh11] T. Rohwer, S. Hellmann, M. Wiesenmayer, C. Sohrt, A. Stange, B. Slomski, A. Carr, Y. Liu, L. M. Avila, M. Kallane, S. Mathias, L. Kipp, K. Rossnagel, & M. Bauer. *Collapse of long-range charge order tracked by time-resolved photoemission at high momenta*. Nature **471**, 490 (2011). DOI: 10.1038/nature09829. 3, 30, 36, 50, 87, 98, 148

[Ron98] F. Ronning, C. Kim, D. L. Feng, D. S. Marshall, A. G. Loeser, L. L. Miller, J. N. Eckstein, I. Bozovic, & Z.-X. Shen. *Photoemission Evidence for a Remnant Fermi Surface and a d-Wave-Like Dispersion in Insulating $Ca_2CuO_2Cl_2$*. Science **282**, 5396, 2067 (1998). DOI: 10.1126/science.282.5396.2067. 114

[Rot67] A. Rothwarf & B. N. Taylor. *Measurement of Recombination Lifetimes in Superconductors*. Physical Review Letters **19**, 1, 27 (1967). DOI: 10.1103/PhysRevLett.19.27. 17, 120

[Rot08a] M. Rotter, M. Tegel, & D. Johrendt. *Superconductivity at 38 K in the Iron Arsenide $(Ba_{1-x}K_x)Fe_2As_2$*. Physical Review Letters **101**, 107006 (2008). DOI: 10.1103/PhysRevLett.101.107006. 76

[Rot08b] M. Rotter, M. Tegel, D. Johrendt, I. Schellenberg, W. Hermes, & R. Pöttgen. *Spin-density-wave anomaly at 140 K in the ternary iron arsenide $BaFe_2As_2$*. Physical Review B **78**, 020503 (2008). DOI: 10.1103/PhysRevB.78.020503. 85

[Rot10] C. R. Rotundu, B. Freelon, T. R. Forrest, S. D. Wilson, P. N. Valdivia, G. Pinuellas, A. Kim, J.-W. Kim, Z. Islam, E. Bourret-Courchesne, N. E. Phillips, & R. J. Birgeneau. *Heat capacity study of $BaFe_2As_2$: Effects of annealing*. Physical Review B **82**, 144525 (2010). DOI: 10.1103/PhysRevB.82.144525. 104

[Rot11] C. R. Rotundu & R. J. Birgeneau. *First- and second-order magnetic and structural transitions in $Ba(Fe_{1-x}Co_x)_2As_2$*. Physical Review B **84**, 092501 (2011). DOI: 10.1103/PhysRevB.84.092501. 78

[Row69] J. M. Rowell, W. L. McMillan, & W. L. Feldmann. *Phonon Spectra in Pb and $Pb_{40}Tl_{60}$ Determined by Tunneling and Neutron Scattering.* Physical Review **178**, 3, 897 (1969). DOI: 10.1103/PhysRev.178.897. 69

[Ru06] N. Ru & I. R. Fisher. *Thermodynamic and Transport Properties of YTe_3, $LaTe_3$, and $CeTe_3$.* Physical Review B **73**, 033101 (2006). DOI: 10.1103/PhysRevB.73.033101. 125

[Ru08] N. Ru, C. L. Condron, G. Y. Margulis, K. Y. Shin, J. Laverock, S. B. Dugdale, M. F. Toney, & I. R. Fisher. *Effect of Chemical Pressure on the Charge Density Wave Transition in Rare-Earth Tritellurides RTe_3.* Physical Review B **77**, 3, 035114 (2008). DOI: 10.1103/PhysRevB.77.035114. 56, 125, 127, 128, 129, 142, 160

[Rul98] C. Rullière. *Laser Spectroscopy.* Springer, Berlin (1998). 34

[Saa08] G. Saathoff, L. Miaja-Avila, M. Aeschlimann, M. M. Murnane, & H. C. Kapteyn. *Laser-assisted photoemission from surfaces.* Physical Review A **77**, 022903 (2008). DOI: 10.1103/PhysRevA.77.022903. 50

[Sac06] A. Sacchetti, L. Degiorgi, T. Giamarchi, N. Ru, & I. R. Fisher. *Chemical pressure and hidden one-dimensional behavior in rare-earth tri-telluride charge-density wave compounds.* Physical Review B **74**, 125115 (2006). DOI: 10.1103/PhysRevB.74.125115. 127, 139

[Sac07] A. Sacchetti, E. Arcangeletti, A. Perucchi, L. Baldassarre, P. Postorino, S. Lupi, N. Ru, I. R. Fisher, & L. Degiorgi. *Pressure Dependence of the Charge-Density-Wave Gap in Rare-Earth Tritellurides.* Physical Review Letters **98**, 026401 (2007). DOI: 10.1103/PhysRevLett.98.026401. 127, 139

[Sai01] R. Saito, A. Jorio, A. G. Souza Filho, G. Dresselhaus, M. S. Dresselhaus, & M. A. Pimenta. *Probing Phonon Dispersion Relations of Graphite by Double Resonance Raman Scattering.* Physical Review Letters **88**, 027401 (2001). DOI: 10.1103/PhysRevLett.88.027401. 93

[Sav96] S. Y. Savrasov & D. Y. Savrasov. *Electron-Phonon Interactions and Related Physical Properties of Metals from Linear-Response Theory.* Physical Review B **54**, 23, 16487 (1996). DOI: 10.1103/PhysRevB.54.16487. 4, 69

[Sch87] R. W. Schoenlein, W. Z. Lin, J. G. Fujimoto, & G. L. Eesley. *Femtosecond studies of nonequilibrium electronic processes in metals.* Physical Review Letters **58**, 1680 (1987). DOI: 10.1103/PhysRevLett.58.1680. 117

[Sch93] A. Schilling, M. Cantoni, J. D. Guo, & H. R. Ott. *Superconductivity above 130 K in the Hg-Ba-Ca-Cu-O system.* Nature **363**, 6424, 56 (1993). DOI: 10.1038/363056a0. 111

[Sch94] C. A. Schmuttenmaer, M. Aeschlimann, H. E. Elsayed-Ali, R. J. D. Miller, D. A. Mantell, J. Cao, & Y. Gao. *Time-Resolved Two-Photon Photoemission from Cu(100): Energy Dependence of Electron Relaxation.* Physical Review B **50**, 8957 (1994). DOI: 10.1103/PhysRevB.50.8957. 57

[Sch08a] F. Schmitt, P. S. Kirchmann, U. Bovensiepen, R. G. Moore, L. Rettig, M. Krenz, J.-H. Chu, N. Ru, L. Perfetti, D. H. Lu, M. Wolf, I. R. Fisher,

& Z.-X. Shen. *Effect of the Amplitude Mode and the Transient Melting of A Charge Density Wave on the Electronic Structure of $TbTe_3$*. Science **321**, 5896, 1649 (2008). DOI: 10.1126/science.1160778. 3, 11, 30, 36, 87, 125, 132, 141, 143, 147, 148, 152, 169

[Sch08b] F. Schmitt, W. S. Lee, D.-H. Lu, W. Meevasana, E. Motoyama, M. Greven, & Z.-X. Shen. *Analysis of the spectral function of $Nd_{1.85}Ce_{0.15}CuO_4$ obtained by angle-resolved photoemission spectroscopy.* Physical Review B **78**, 100505 (2008). DOI: 10.1103/PhysRevB.78.100505. 9

[Sch09] W. Schnelle, A. Leithe-Jasper, R. Gumeniuk, U. Burkhardt, D. Kasinathan, & H. Rosner. *Substitution-induced superconductivity in $SrFe_{2-x}Ru_xAs_2$ ($0 < x < 2$)*. Physical Review B **79**, 214516 (2009). DOI: 10.1103/PhysRevB.79.214516. 75

[Sch10] H. Schäfer, V. V. Kabanov, M. Beyer, K. Biljakovic, & J. Demsar. *Disentanglement of the Electronic and Lattice Parts of the Order Parameter in a 1D Charge Density Wave System Probed by Femtosecond Spectroscopy.* Physical Review Letters **105**, 066402 (2010). DOI: 10.1103/PhysRevLett.105.066402. 3

[Sch11a] F. Schmitt, P. S. Kirchmann, U. Bovensiepen, R. G. Moore, J.-H. Chu, D. H. Lu, L. Rettig, M. Wolf, I. R. Fisher, & Z.-X. Shen. *Ultrafast electron dynamics in the charge density wave material $TbTe_3$*. New Journal of Physics **13**, 6, 063022 (2011). DOI: 10.1088/1367-2630/13/6/063022. 30, 36, 87, 88, 125, 143, 148, 152, 154, 155

[Sch11b] F. T. Schmitt. *Electronic Structure and Collective Excitations in Correlated Materials - Frequency and Time domain perspectives.* PhD Thesis, Stanford University, Stanford, USA (2011). 52, 125, 136

[Sea79] M. P. Seah & W. A. Dench. *Quantitative Electron Spectroscopy of Surfaces: A Standard Data Base for Electron Inelastic Mean Free Paths in Solids.* Surface and Interface Analysis **1**, 2 (1979). DOI: 10.1002/sia.740010103. 25, 26, 135

[Sef08] A. S. Sefat, R. Jin, M. A. McGuire, B. C. Sales, D. J. Singh, & D. Mandrus. *Superconductivity at 22 K in Co-Doped $BaFe_2As_2$ Crystals.* Physical Review Letters **101**, 117004 (2008). DOI: 10.1103/PhysRevLett.101.117004. 76

[Sef09] A. S. Sefat, M. A. McGuire, R. Jin, B. C. Sales, D. Mandrus, F. Ronning, E. D. Bauer, & Y. Mozharivskyj. *Structure and anisotropic properties of $BaFe_{2-x}Ni_xAs_2$ (x=0, 1, and 2) single crystals.* Physical Review B **79**, 094508 (2009). DOI: 10.1103/PhysRevB.79.094508. 104

[Sek09] Y. Sekiba, T. Sato, K. Nakayama, K. Terashima, P. Richard, J. H. Bowen, H. Ding, Y.-M. Xu, L. J. Li, G. H. Cao, Z.-A. Xu, & T. Takahashi. *Electronic structure of heavily electron-doped $BaFe_{1.7}Co_{0.3}As_2$ studied by angle-resolved photoemission.* New Journal of Physics **11**, 2, 025020 (2009). DOI: 10.1088/1367-2630/11/2/025020. 80

[She95] Z.-X. Shen & D. S. Dessau. *Electronic Structure and Photoemission Studies of LaTe Transition-Metal Oxides - Mott Insulators and High-Temperature Superconductors.* Physics Reports **253**, 1 (1995). DOI: 10.1016/0370-1573(95)80001-A. 25

[She12] W. Shen, Y. Ge, A. Y. Liu, H. R. Krishnamurthy, T. P. Devereaux, & J. K. Freericks. *Transient creation of a gapless charge density wave via an ultrafast laser pulse* (2012). To be published. 149

[Shi04] J. Shi, S.-J. Tang, B. Wu, P. T. Sprunger, W. L. Yang, V. Brouet, X. J. Zhou, Z. Hussain, Z.-X. Shen, Z. Zhang, & E. W. Plummer. *Direct Extraction of the Eliashberg Function for Electron-Phonon Coupling: A Case Study of* Be($10\bar{1}0$). Physical Review Letters **92**, 186401 (2004). DOI: 10.1103/PhysRevLett.92.186401. 9

[Shi10] T. Shimojima, K. Ishizaka, Y. Ishida, N. Katayama, K. Ohgushi, T. Kiss, M. Okawa, T. Togashi, X.-Y. Wang, C.-T. Chen, S. Watanabe, R. Kadota, T. Oguchi, A. Chainani, & S. Shin. *Orbital-Dependent Modifications of Electronic Structure across the Magnetostructural Transition in $BaFe_2As_2$.* Physical Review Letters **104**, 057002 (2010). DOI: 10.1103/PhysRevLett.104.057002. 28, 80

[Shi11a] T. Shimojima, F. Sakaguchi, K. Ishizaka, Y. Ishida, T. Kiss, M. Okawa, T. Togashi, C.-T. Chen, S. Watanabe, M. Arita, K. Shimada, H. Namatame, M. Taniguchi, K. Ohgushi, S. Kasahara, T. Terashima, T. Shibauchi, Y. Matsuda, A. Chainani, & S. Shin. *Orbital-Independent Superconducting Gaps in Iron Pnictides.* Science **332**, 6029, 564 (2011). DOI: 10.1126/science.1202150. 80, 101

[Shi11b] T. Shimojima, F. Sakaguchi, K. Ishizaka, Y. Ishida, W. Malaeb, T. Yoshida, S. Ideta, A. Fujimori, T. Kiss, M. Okawa, T. Togashi, C.-T. Chen, S. Watanabe, Y. Nakashima, A. Ino, H. Anzai, M. Arita, K. Shimada, H. Namatame, M. Taniguchi, S. Kasahara, T. Terashima, T. Shibauchi, Y. Matsuda, M. Nakajima, S. Uchida, K. Kihou, C.H. Lee, A. Iyo, H. Eisaki, A. Chainani, & S. Shin. *Angle-resolved photoemission study on the superconducting iron-pnictides of $BaFe_2(As,P)_2$ with low energy photons.* Solid State Communications (2011). DOI: 10.1016/j.ssc.2011.12.032. 80

[Sif02] P. Siffalovic, M. Drescher, & U. Heinzmann. *Femtosecond time-resolved core-level photoelectron spectroscopy tracking surface photovoltage transients on p-GaAs.* Europhysics Letters **60**, 6, 924 (2002). DOI: 10.1209/epl/i2002-00306-3. 57

[Sin08] D. J. Singh. *Electronic structure and doping in $BaFe_2As_2$ and LiFeAs: Density functional calculations.* Physical Review B **78**, 094511 (2008). DOI: 10.1103/PhysRevB.78.094511. 77, 104

[Slo11] B. Slomski, F. Meier, J. Osterwalder, & J. H. Dil. *Controlling the effective mass of quantum well states in Pb/Si(111) by interface engineering.* Physical Review B **83**, 035409 (2011). DOI: 10.1103/PhysRevB.83.035409. 57, 58, 72, 167

[Smi85] N. V. Smith. *Phase Analysis of Image States and Surface States Associated with Nearly-Free-Electron Band Gaps.* Physical Review B **32**, 6, 3549 (1985). DOI: 10.1103/PhysRevB.32.3549. 66

[Sob12] J. A. Sobota, S. Yang, J. G. Analytis, Y. L. Chen, I. R. Fisher, P. S. Kirchmann, & Z.-X. Shen. *Ultrafast Optical Excitation of a Persistent Surface-State*

Population in the Topological Insulator Bi_2Se_3. Physical Review Letters **108**, 117403 (2012). DOI: 10.1103/PhysRevLett.108.117403. 124, 168, 169

[Stä07] J. Stähler. *Freezing Hot Electrons - Electron Transfer and Solvation Dynamics at D_2O and NH_3 - Metal Interfaces*. PhD Thesis, Freie Universität Berlin (2007). 34

[Sto08] J. G. Storey, J. L. Tallon, & G. V. M. Williams. *Pseudogap ground state in high-temperature superconductors*. Physical Review B **78**, 14(2008). DOI: 10.1103/PhysRevB.78.140506. 116

[Sto10a] L. Stojchevska, P. Kusar, T. Mertelj, V. V. Kabanov, X. Lin, G. H. Cao, Z. A. Xu, & D. Mihailovic. *Electron-phonon coupling and the charge gap of spin-density wave iron-pnictide materials from quasiparticle relaxation dynamics*. Physical Review B **82**, 012505 (2010). DOI: 10.1103/PhysRevB.82.012505. 83, 105, 107, 108

[Sto10b] J. G. Storey, J. W. Loram, J. R. Cooper, Z. Bukowski, & J. Karpinski. *The electronic specific heat of $Ba_{1-x}K_xFe_2As_2$ from 2K to 380K*. ArXiv e-prints (2010). 104

[Su09] Y. Su, P. Link, A. Schneidewind, Th. Wolf, P. Adelmann, Y. Xiao, M. Meven, R. Mittal, M. Rotter, D. Johrendt, Th. Brueckel, & M. Loewenhaupt. *Antiferromagnetic ordering and structural phase transition in $BaFe_2As_2$ with Sn incorporated from the growth flux*. Physical Review B **79**, 064504 (2009). DOI: 10.1103/PhysRevB.79.064504. 85

[Sug10] S. Sugai, Y. Mizuno, K. Kiho, M. Nakajima, C. H. Lee, A. Iyo, H. Eisaki, & S. Uchida. *Pairing symmetry of the multiorbital pnictide superconductor $BaFe_{1.84}Co_{0.16}As_2$ from Raman scattering*. Physical Review B **82**, 140504 (2010). DOI: 10.1103/PhysRevB.82.140504. 92

[Tak09] H. Takahashi, K. Kato, H. Nakano, M. Kitajima, K. Ohmori, & K. G. Nakamura. *Optical control and mode selective excitation of coherent phonons in $YBa_2Cu_3O_{7+\delta}$*. Solid State Communications **149**, 43-44, 1955 (2009). DOI: 10.1016/j.ssc.2009.07.037. 157

[Tan09] M. A. Tanatar, N. Ni, C. Martin, R. T. Gordon, H. Kim, V. G. Kogan, G. D. Samolyuk, S. L. Bud'ko, P. C. Canfield, & R. Prozorov. *Anisotropy of the iron pnictide superconductor $Ba(Fe_{1-x}Co_x)_2As_2$ ($x = 0.074$, $T_c = 23$ K)*. Physical Review B **79**, 094507 (2009). DOI: 10.1103/PhysRevB.79.094507. 104

[Tar88] J. M. Tarascon, Y. Le Page, P. Barboux, B. G. Bagley, L. H. Greene, W. R. McKinnon, G. W. Hull, M. Giroud, & D. M. Hwang. *Crystal substructure and physical properties of the superconducting phase* $Bi_4(Sr,Ca)_6Cu_4O_{16+x}$. Physical Review B **37**, 9382 (1988). DOI: 10.1103/PhysRevB.37.9382. 113

[Teg08] M. Tegel, M. Rotter, V. Weiss, F. Schappacher, R. Pottgen, & D. Johrendt. *Structural and magnetic phase transitions in the ternary iron arsenides $SrFe_2As_2$ and $EuFe_2As_2$*. Journal of Physics: Condensed Matter **20**, 45, 452201 (2008). DOI: 10.1088/0953-8984/20/45/452201. 83

[Thi10] S. Thirupathaiah, S. de Jong, R. Ovsyannikov, H. A. Dürr, A. Varykhalov, R. Follath, Y. Huang, R. Huisman, M. S. Golden, Y.-Z. Zhang, H. O. Jeschke, R. Valentí, A. Erb, A. Gloskovskii, & J. Fink. *Orbital character variation of the Fermi surface and doping dependent changes of the dimensionality in $BaFe_{2-x}Co_xAs_2$ from angle-resolved photoemission spectroscopy.* Physical Review B **81**, 104512 (2010). DOI: 10.1103/PhysRevB.81.104512. 80

[Thi11] S. Thirupathaiah, E. D. L. Rienks, H. S. Jeevan, R. Ovsyannikov, E. Slooten, J. Kaas, E. van Heumen, S. de Jong, H. A. Dürr, K. Siemensmeyer, R. Follath, P. Gegenwart, M. S. Golden, & J. Fink. *Dissimilarities between the electronic structure of chemically doped and chemically pressurized iron pnictides from an angle-resolved photoemission spectroscopy study.* Physical Review B **84**, 014531 (2011). DOI: 10.1103/PhysRevB.84.014531. 94, 168

[Tim99] T. Timusk & B. Statt. *The pseudogap in high-temperature superconductors: an experimental survey.* Reports on Progress in Physics **62**, 1, 61 (1999). DOI: 10.1088/0034-4885/62/1/002. 116

[Tog03] T. Togashi, T. Kanai, T. Sekikawa, S. Watanabe, C. Chen, C. Zhang, Z. Xu, & J. Wang. *Generation of vacuum-ultraviolet light by an optically contacted, prism-coupled $KBe_2BO_3F_2$ crystal.* Optics Letters **28**, 4, 254 (2003). DOI: 10.1364/OL.28.000254. 52

[Tor10] D. H. Torchinsky, G. F. Chen, J. L. Luo, N. L. Wang, & N. Gedik. *Band-dependent Quasiparticle Dynamics in Single Crystals of the $Ba_{0.6}K_{0.4}Fe_2As_2$ Superconductor Revealed by Pump-Probe Spectroscopy.* Physical Review Letters **105**, 027005 (2010). DOI: 10.1103/PhysRevLett.105.027005. 73

[Tor11] D. H. Torchinsky, J. W. McIver, D. Hsieh, G. F. Chen, J. L. Luo, N. L. Wang, & N. Gedik. *Nonequilibrium quasiparticle relaxation dynamics in single crystals of hole- and electron-doped $BaFe_2As_2$.* Physical Review B **84**, 104518 (2011). DOI: 10.1103/PhysRevB.84.104518. 73, 104

[Tre02] R. Trebino. *Frequency-Resolved Optical Gating: The Measurement of Ultrashort Laser Pulses.* Springer, Berlin (2002). 34, 37

[Tre07] R. Trebino. *GRENOUILLE Model 8-20 User's Guide, Swamp Optics, LLC.* Trebino, R., Atlanta (2007). 37

[Upt04] M. H. Upton, T. Miller, & T.-C. Chiang. *Absolute Determination of Film Thickness from Photoemission: Application to Atomically Uniform Films of Pb on Si.* Applied Physics Letters **85**, 7, 1235 (2004). DOI: 10.1063/1.1783019. 54, 57, 58, 61, 66

[Val99] T. Valla, A. V. Fedorov, P. D. Johnson, & S. L. Hulbert. *Many-Body Effects in Angle-Resolved Photoemission: Quasiparticle Energy and Lifetime of a Mo(110) Surface State.* Physical Review Letters **83**, 2085 (1999). DOI: 10.1103/PhysRevLett.83.2085. 9, 106

[Vil02] I. Vilfan, M. Henzler, O. Pfennigstorf, & H. Pfnür. *Anomalous Thickness Dependence of the Hall Effect in Ultrathin Pb Layers on Si(111).* Physical Review B **66**, 241306 (2002). DOI: 10.1103/PhysRevB.66.241306. 4

[Vil09] P. Vilmercati, A. Fedorov, I. Vobornik, U. Manju, G. Panaccione, A. Goldoni, A. S. Sefat, M. A. McGuire, B. C. Sales, R. Jin, D. Mandrus, D. J. Singh, & N. Mannella. *Evidence for three-dimensional Fermi-surface topology of the layered electron-doped iron superconductor* $Ba(Fe_{1-x}Co_x)_2As_2$. Physical Review B **79**, 220503 (2009). DOI: 10.1103/PhysRevB.79.220503. 28, 80, 105

[Voi00] J. Voit, L. Perfetti, F. Zwick, H. Berger, G. Margaritondo, G. Grüner, H. Höchst, & M. Grioni. *Electronic Structure of Solids with Competing Periodic Potentials*. Science **290**, 5491, 501 (2000). DOI: 10.1126/science.290.5491.501. 130, 131

[Wal11] S. Wall, D. Brida, S. R. Clark, H. P. Ehrke, D. Jaksch, A. Ardavan, S. Bonora, H. Uemura, Y. Takahashi, T. Hasegawa, H. Okamoto, G. Cerullo, & A. Cavalleri. *Quantum interference between charge excitation paths in a solid-state Mott insulator*. Nature Physics **7**, 2, 114 (2011). DOI: 10.1038/nphys1831. 87, 148

[Wan10] G.T. Wang, Y. Qian, G. Xu, X. Dai, & Z. Fang. *Gutzwiller Density Functional Studies of FeAs-Based Superconductors: Structure Optimization and Evidence for a Three-Dimensional Fermi Surface*. Physical Review Letters **104**, 047002 (2010). DOI: 10.1103/PhysRevLett.104.047002. 77

[Web87] C. Webb, S.-L. Weng, J. N. Eckstein, N. Missert, K. Char, D. G. Schlom, E. S. Hellman, M. R. Beasley, A. Kapitulnik, & Jr. J. S. Harris. *Growth of high* T_c *superconducting thin films using molecular beam epitaxy techniques*. Applied Physics Letters **51**, 15, 1191 (1987). DOI: 10.1063/1.98729. 136

[Wei02a] C. M. Wei & M. Y. Chou. *Theory of Quantum Size Effects in Thin Pb(111) Films*. Physical Review B **66**, 23, 233408 (2002). DOI: 10.1103/PhysRevB.66.233408. 4, 57, 61, 66

[Wei02b] M. Weinelt. *Time-Resolved Two-Photon Photoemission from Metal Surfaces*. Journal of Physics: Condensed Matter **14**, 43, R1099 (2002). DOI: 10.1088/0953-8984/14/43/202. 3, 29, 57, 139

[Wel09] U. Welp, G. Mu, R. Xie, A. E. Koshelev, W. K. Kwok, H. Q. Luo, Z. S. Wang, P. Cheng, L. Fang, C. Ren, & H. H. Wen. *Specific heat and phase diagrams of single crystal iron pnictide superconductors*. Physica C: Superconductivity **469**, 9-12, 575 (2009). DOI: 10.1016/j.physc.2009.03.011. 104

[Wid03] W. Widdra, D. Bröcker, T. Gießel, I. V. Hertel, W. Krüger, A. Liero, F. Noack, V. Petrov, D. Pop, P. M. Schmidt, R. Weber, I. Will, & B. Winter. *Time-Resolved Core Level Photoemission: Surface Photovoltage Dynamics of the* $SiO_2/Si(100)$ *Interface*. Surface Science **543**, 1-3, 87 (2003). DOI: DOI: 10.1016/j.susc.2003.07.005. 57, 60

[Wil09] S. D. Wilson, Z. Yamani, C. R. Rotundu, B. Freelon, E. Bourret-Courchesne, & R. J. Birgeneau. *Neutron diffraction study of the magnetic and structural phase transitions in* $BaFe_2As_2$. Physical Review B **79**, 184519 (2009). DOI: 10.1103/PhysRevB.79.184519. 78, 85

[Wol97] M. Wolf. *Femtosecond dynamics of electronic excitations at metal surfaces*. Surface Science **377-379**, 343 (1997). DOI: 10.1007/s00339-004-3127-7. 139

[Wra08] L. Wray, D. Qian, D. Hsieh, Y. Xia, L. Li, J. G. Checkelsky, A. Pasupathy, K. K. Gomes, C. V. Parker, A. V. Fedorov, G. F. Chen, J. L. Luo, A. Yazdani, N. P. Ong, N. L. Wang, & M. Z. Hasan. *Momentum dependence of superconducting gap, strong-coupling dispersion kink, and tightly bound Cooper pairs in the high-T_c $SrBa_{1-x}(K,Na)_xFe_2As_2$ superconductors.* Physical Review B **78**, 184508 (2008). DOI: 10.1103/PhysRevB.78.184508. 102

[Wu87] M. K. Wu, J. R. Ashburn, C. J. Torng, P. H. Hor, R. L. Meng, L. Gao, Z. J. Huang, Y. Q. Wang, & C. W. Chu. *Superconductivity at 93 K in a new mixed-phase Y-Ba-Cu-O compound system at ambient pressure.* Physical Review Letters **58**, 908 (1987). DOI: 10.1103/PhysRevLett.58.908. 111

[Wu09] D. Wu, N. Barišić, N. Drichko, S. Kaiser, A. Faridian, M. Dressel, S. Jiang, Z. Ren, L. J. Li, G. H. Cao, Z. A. Xu, H. S. Jeevan, & P. Gegenwart. *Effects of magnetic ordering on dynamical conductivity: Optical investigations of $EuFe_2As_2$ single crystals.* Physical Review B **79**, 15, 155103 (2009). DOI: 10.1103/PhysRevB.79.155103. 87

[Xia09] Y. Xiao, Y. Su, M. Meven, R. Mittal, C. M. N. Kumar, T. Chatterji, S. Price, J. Persson, N. Kumar, S. K. Dhar, A. Thamizhavel, & Th. Brueckel. *Magnetic structure of $EuFe_2As_2$ determined by single-crystal neutron diffraction.* Physical Review B **80**, 174424 (2009). DOI: 10.1103/PhysRevB.80.174424. 78, 83

[Yan85] Y.-X. Yan, Jr. E. B. Gamble, & K. A. Nelson. *Impulsive stimulated scattering: General importance in femtosecond laser pulse interactions with matter, and spectroscopic applications.* Journal of Chemical Physics **83**, 11, 5391 (1985). DOI: 10.1063/1.449708. 11, 92

[Yan09] L. X. Yang, Y. Zhang, H. W. Ou, J. F. Zhao, D. W. Shen, B. Zhou, J. Wei, F. Chen, M. Xu, C. He, Y. Chen, Z. D. Wang, X. F. Wang, T. Wu, G. Wu, X. H. Chen, M. Arita, K. Shimada, M. Taniguchi, Z. Y. Lu, T. Xiang, & D. L. Feng. *Electronic Structure and Unusual Exchange Splitting in the Spin-Density-Wave State of the $BaFe_2As_2$ Parent Compound of Iron-Based Superconductors.* Physical Review Letters **102**, 10, 107002 (2009). DOI: 10.1103/PhysRevLett.102.107002. 78

[Yeh00] V. Yeh, L. Berbil-Bautista, C. Z. Wang, K. M. Ho, & M. C. Tringides. *Role of the Metal/Semiconductor Interface in Quantum Size Effects: Pb/Si(111).* Physical Review Letters **85**, 5158 (2000). DOI: 10.1103/PhysRevLett.85.5158. 57, 58

[Yi09a] M. Yi, D. H. Lu, J. G. Analytis, J.-H. Chu, S.-K. Mo, R.-H. He, M. Hashimoto, R. G. Moore, I. I. Mazin, D. J. Singh, Z. Hussain, I. R. Fisher, & Z.-X. Shen. *Unconventional electronic reconstruction in undoped $(Ba,Sr)Fe_2As_2$ across the spin density wave transition.* Physical Review B **80**, 17, 174510 (2009). DOI: 10.1103/PhysRevB.80.174510. 78

[Yi09b] M. Yi, D. H. Lu, J. G. Analytis, J.-H. Chu, S.-K. Mo, R.-H. He, R. G. Moore, X. J. Zhou, G. F. Chen, J. L. Luo, N. L. Wang, Z. Hussain, D. J. Singh, I. R. Fisher, & Z.-X. Shen. *Electronic structure of the $BaFe_2As_2$ family of iron-pnictide superconductors.* Physical Review B **80**, 024515 (2009). DOI: 10.1103/PhysRevB.80.024515. 77

[Yi11a] M. Yi, D. Lu, J.-H. Chu, J. G. Analytis, A. P. Sorini, A. F. Kemper, B. Moritz, S.-K. Mo, R. G. Moore, M. Hashimoto, W.-S. Lee, Z. Hussain, T. P. Devereaux, I. R. Fisher, & Z.-X. Shen. *Symmetry-breaking orbital anisotropy observed for detwinned $Ba(Fe_{1-x}Co_x)_2As_2$ above the spin density wave transition.* Proceedings of the National Academy of Sciences **108**, 17, 6878 (2011). DOI: 10.1073/pnas.1015572108. 78

[Yi11b] M. Yi, D. H. Lu, R. G. Moore, K. Kihou, C.-H. Lee, A. Iyo, H. Eisaki, T. Yoshida, A. Fujimori, & Z.-X. Shen. *Electronic reconstruction through the structural and magnetic transitions in detwinned NaFeAs.* ArXiv e-prints (2011). URL `http://adsabs.harvard.edu/abs/2011arXiv1111.6134Y`. 78

[Yin08] Z. P. Yin, S. Lebègue, M. J. Han, B. P. Neal, S. Y. Savrasov, & W. E. Pickett. *Electron-Hole Symmetry and Magnetic Coupling in Antiferromagnetic LaFeAsO.* Physical Review Letters **101**, 047001 (2008). DOI: 10.1103/PhysRevLett.101.047001. 98, 109

[Ynd08] F. Yndurain & M. P. Jigato. *First Principles Calculation of Localized Surface Phonons and Electron-Phonon Interaction at Pb(111) Thin Films.* Physical Review Letters **100**, 205501 (2008). DOI: 10.1103/PhysRevLett.100.205501. 58, 70, 72, 167

[Ynd11] F. Yndurain. *Coupling of magnetic moments with phonons and electron-phonon interaction in $LaFeAsO_{1-x}F_x$.* Europhysics Letters **94**, 3, 37001 (2011). DOI: 10.1209/0295-5075/94/37001. 98

[Yus08] R. V. Yusupov, T. Mertelj, J.-H. Chu, I. R. Fisher, & D. Mihailovic. *Single-Particle and Collective Mode Couplings Associated with 1- and 2-Directional Electronic Ordering in Metallic RTe_3 ($R = Ho, Dy, Tb$).* Physical Review Letters **101**, 246402 (2008). DOI: 10.1103/PhysRevLett.101.246402. 152, 154, 156, 157

[Yus10] R. Yusupov, T. Mertelj, V. V. Kabanov, S. Brazovskii, P. Kusar, J.-H. Chu, I. R. Fisher, & D. Mihailovic. *Coherent dynamics of macroscopic electronic order through a symmetry breaking transition.* Nature Physics **6**, 9, 681 (2010). DOI: 10.1038/nphys1738. 147, 148, 157

[Zan88] A. Zangwill. *Physics at Surfaces.* Cambridge University Press, Cambridge (1988). 25, 39, 135

[Zbi09] M. Zbiri, H. Schober, M. R. Johnson, S. Rols, R. Mittal, Y. Su, M. Rotter, & D. Johrendt. *Ab initio lattice dynamics simulations and inelastic neutron scattering spectra for studying phonons in $BaFe_2As_2$: Effect of structural phase transition, structural relaxation, and magnetic ordering.* Physical Review B **79**, 6, 064511 (2009). DOI: 10.1103/PhysRevB.79.064511. 98, 104

[Zei92] H. J. Zeiger, J. Vidal, T. K. Cheng, E. P. Ippen, G. Dresselhaus, & M. S. Dresselhaus. *Theory for displacive excitation of coherent phonons.* Physical Review B **45**, 768 (1992). DOI: 10.1103/PhysRevB.45.768. 11, 92, 95

[Zha98] Z. Zhang, Q. Niu, & C.-K. Shi. *Electronic Growth of Metallic Overlayers on Semiconductor Substrates.* Physical Review Letters **80**, 5381 (1998). DOI: 10.1103/PhysRevLett.80.5381. 57

[Zha05] Y.-F. Zhang, J.-F. Jia, T.-Z. Han, Z. Tang, Q.-T. Shen, Y. Guo, Z. Q. Qiu, & Q.-K. Xue. *Band Structure and Oscillatory Electron-Phonon Coupling of Pb Thin Films Determined by Atomic-Layer-Resolved Quantum-Well States.* Physical Review Letters **95**, 096802 (2005). DOI: 10.1103/PhysRevLett.95.096802. 57

[Zha10] T. Zhang, P. Cheng, W.-J. Li, Y.-J. Sun, G. Wang, X.-G. Zhu, K. He, L. Wang, X. Ma, X. Chen, Y. Wang, Y. Liu, H.-Q. Lin, J.-F. Jia, & Q.-K. Xue. *Superconductivity in one-atomic-layer metal films grown on Si(111).* Nature Physics **6**, 104 (2010). DOI: 10.1038/nphys1499. 57

[Zha12] Y. Zhang, C. He, Z. R. Ye, J. Jiang, F. Chen, M. Xu, Q. Q. Ge, B. P. Xie, J. Wei, M. Aeschlimann, X. Y. Cui, M. Shi, J. P. Hu, & D. L. Feng. *Symmetry breaking via orbital-dependent reconstruction of electronic structure in detwinned NaFeAs.* Physical Review B **85**, 085121 (2012). DOI: 10.1103/PhysRevB.85.085121. 78

[Zhu04] X.-Y. Zhu. *Electronic Structure and Electron Dynamics at Molecule-Metall Interfaces: Implications for Molecule-based Electronics.* Surface Science Reports **56**, 1 (2004). DOI: 10.1016/j.surfrep.2004.09.002. 3

Publications

Publications in the framework of this thesis

R. Cortés, L. Rettig, Y. Yoshida, H. Eisaki, M. Wolf, & U. Bovensiepen.
Momentum-Resolved Ultrafast Electron Dynamics in Superconducting $Bi_2Sr_2CaCu_2O_{8+\delta}$.
Physical Review Letters **107**, 097002 (2011). DOI: 10.1103/PhysRevLett.107.097002.

L. Rettig, R. Cortés, S. Thirupathaiah, P. Gegenwart, H. S. Jeevan, T.Wolf, U. Bovensiepen, H. A. Dürr, J. Fink, and M. Wolf
Time- and angle-resolved photoemission spectroscopy of 122 Fe-pnictides
in: Ultrafast Phenomena XVII, ed. by M. Chergui, D. Jonas, E. Riedle, R. Schoenlein, A. Taylor, Oxford University Press (2011)

L. Rettig, R. Cortés, S. Thirupathaiah, P. Gegenwart, H. S. Jeevan, M. Wolf, J. Fink, & U. Bovensiepen.
Ultrafast Momentum-Dependent Response of Electrons in Antiferromagnetic $EuFe_2As_2$ *Driven by Optical Excitation.*
Physical Review Letters **108**, 097002 (2012). DOI: 10.1103/PhysRevLett.108.097002.

L. Rettig, P. S. Kirchmann, & U. Bovensiepen.
Ultrafast dynamics of occupied quantum well states in Pb/Si(111).
New Journal of Physics 14, 2, 023047 (2012). DOI: 10.1088/1367-2630/14/2/023047.

I. Avigo, R. Cortés, L. Rettig, S. Thirupathaiah, H. S. Jeevans, P. Gegenvart, T. Wolf, M. Ligges, M. Wolf, J. Fink, & Uwe Bovensiepen.
Coherent excitations and electron phonon coupling in $Ba/EuFe_2As_2$ *compounds investigated by femtosecond time- and angle-resolved photoemission spectroscopy.*
submitted to the Journal of Physics - Condensed Matter.
available online at: http://arxiv.org/abs/1204.4069.

In Preparation

K. Kummer, D. V. Vyalikh, L. Rettig, R. Cortés, Yu. Kucherenko, C. Krellner, C. Geibel, U. Bovensiepen, M. Wolf, & S. L. Molodtsov
Ultrafast quasiparticle dynamics in the heavy-fermion compound $YbRh_2Si_2$.

Publications concerning other topics

P. S. Kirchmann, L. Rettig, D. Nandi, U. Lipowski, M. Wolf, & U. Bovensiepen.
A Time-of-Flight Spectrometer for Angle-Resolved Detection of Low Energy Electrons in Two Dimensions.
Applied Physics A **91**, 2, 211, (2008). DOI: 10.1007/s00339-008-4422-5

F. Schmitt, P. S. Kirchmann, U. Bovensiepen, R. G. Moore, L. Rettig, M. Krenz, J.-H. Chu, N. Ru, L. Perfetti, D. H. Lu, M. Wolf, I. R. Fisher, & Z.-X. Shen.
Effect of the Amplitude Mode and the Transient Melting of A Charge Density Wave on the Electronic Structure of $TbTe_3$.
Science **321**, 1649, (2008) DOI: 10.1126/science.1160778

P. S. Kirchmann, L. Rettig, X. Zubizarreta, V. M. Silkin, E. V. Chulkov, & U. Bovensiepen.
Quasiparticle lifetimes in metallic quantum-well nanostructures.
Nature Physics **6**, 782 (2010). DOI: 10.1038/nphys1735.

F. Schmitt, P. S. Kirchmann, U. Bovensiepen, R. G. Moore, J.-H. Chu, D. H. Lu, L. Rettig, M. Wolf, I. R. Fisher, & Z.-X. Shen.
Ultrafast electron dynamics in the charge density wave material $TbTe_3$.
New Journal of Physics **13**, 6, 063022 (2011). DOI:10.1088/1367-2630/13/6/063022.

Academic Curriculum Vitae

The curriculum vitae is omitted in this online version due to data privacy.

Acknowledgments

Eine solche Arbeit ist sicherlich nicht ohne die Hilfe zahlreicher Menschen zu bewältigen. Es ist mir daher eine Freude, all jenen meinen Dank auszusprechen, die mich bei dieser Arbeit unterstützt und zu ihrem Gelingen beigetragen haben.

An erster Stelle möchte ich Martin Wolf für die Möglichkeit danken, diese Arbeit in seiner Arbeitsgruppe in einer freundlichen und aufgeschlossenen Atmosphäre zu beginnen. Für viele angeregte Diskussionen und inhaltliche Ideen bin ich ihm sehr zu Dank verpflichtet.

Ganz besonders möchte ich Uwe Bovensiepen für die hervorragende Betreuung meiner Arbeit danken. Vor allem die Freiheit, die ich bei der Ausgestaltung meiner Arbeit genießen durfte und die Möglichkeit, meine Ideen bestmöglich umzusetzen, weiß ich sehr zu schätzen, ebenso wie sein Entgegenkommen nach seinem Umzug an die Universität Duisburg-Essen, welches es mir erlaubte, meine Arbeit hier in Berlin zu beenden. Er hat mich oft auf die wichtigen Fragen und Ergebnisse aufmerksam gemacht, wenn ich mich im Dickicht der Daten zu verirren drohte. Insbesondere für die Möglichkeit von zwei Forschungsaufenthalten an der Stanford Universität bin ich sehr dankbar, während derer ich viele der Fertigkeiten lernen durfte, die zum Gelingen dieser Arbeit beigetragen haben. Ebenso haben die vielen internationalen Konferenzen, die ich besuchen durfte, mich sehr bereichert und meinen Blick in die Wissenschaftswelt erweitert.

Martin Weinelt danke ich für die Bereitschaft, mein Zweitgutachter zu werden, für viele erhellende Diskussionen und für sein Interesse an meiner Arbeit.

Bei Petra Tegeder möchte ich mich für die lange Zeit bedanken, in der ich das Labor noch benutzen durfte, um meine Messungen zu beenden. Der gesamten Arbeitsgruppe Tegeder danke ich für das Asyl das mir gewährt wurde, sowie für die stets freundliche und familiäre Atmosphäre.

I'd like to thank Rocio Cortés, who was an excellent lab partner in many of the experiments presented here. I learned a lot from her accurate and conscientious way of working and will keep the long evenings in the lab in good memory!

Patrick Kirchmann danke ich an dieser Stelle auch noch einmal für alles, was ich von ihm lernen durfte und für seine Hilfe bei der pTOF-Reparatur und der Probenpräparation.

I am very grateful to Prof. Z.-X. Shen for his warm welcome at the Stanford University and for the great times I had during my visits. Ganz besonders danke ich Felix Schmitt für alles, was ich von ihm lernen durfte und für die Messzeiten, die er extra für mich organisiert hat. In addition, I would like to thank Rob Moore, who taught me a lot about the Tritelluride physics and helped me greatly in explaining the Tight-Binding model to me. Ellie Lwin also was a great help in organizing my visit across the ocean.

I thank Prof. Ian Fisher and especially Jiun-Haw Chu from the Stanford University, who repeatedly provided excellent new Tritelluride samples even on very short notice and were always open to discuss new ideas for experiments.

Besonderer Dank gebührt auch Prof. Jörg Fink von der IFW Dresden, ohne dessen stete Unterstützung und Organisation von Proben die Messungen an den Fe-Pniktiden nicht möglich gewesen wären. Die vielen erhellenden Diskussionen haben sehr zu meinem

Verständnis der Physik der Pniktide beigetragen und die schnellen Antworten auf meine vielen Fragen waren eine große Hilfe. Ebenso danke ich Prof. P. Gegenwart und H. S. Jeevan von der Universität Göttingen und T. Wolf vom Karlsruhe Institute of Technology für die Bereitstellung exzellenter Fe-Pniktid-Proben. Furthermore, Setti Thirupathaiah is acknowledged for his support in the measurements on Fe pnictides.

Prof. Michael Bauer von der Universität Kiel und seiner Arbeitsgruppe danke ich für die Ermöglichung der HHG-Experimente an den Fe Pniktiden. Insbesondere Timm Rohwer, Ankatrin Stange, Stefan Hellmann und Kerstin Hanff sei hier für ihren Einsatz im Labor auch bis tief in die Nacht und die freundliche Atmosphäre gedankt.

I am grateful to Prof. H. Eisaki and Y. Yoshida from the Nanoelectronic Research Institute (AIST) in Tsukuba, Japan for providing the excellent BSCCO samples.

Vielen Dank auch an Dietgard Mallwitz und Peter West für ihre große Hilfe bei der Bewältigung der organisatorischen Aufgaben an der Uni und bei vielen kleinen und größeren Computerproblemen. Ebenso möchte ich Tina Boese für ihre hervorragende Organisation der vielfältigen bürokratischen Aufgaben und meiner Unterbringung in Duisburg danken. Der ZEDV danke ich für die großzügige Bereitstellung der nötigen Rechenpower zur Bewältigung der immensen pTOF-Datenberge.

Ich möchte auch allen anderen ehemaligen und aktuellen Mitgliedern der Ag Wolf und Ag Tegeder für die tolle Zusammenarbeit und Unterstützung danken. Von Sebastian Hagen und Marcel Krenz habe ich viel in Sachen Laser lernen dürfen, und ihre Hilfsbereitschaft weiß ich sehr zu schätzen. Ebenso sei hier Michael Meyer, Felix Leyssner, Lea Bogner, Chris Bronner, Stephan Meyer, Michael Schulze, und Erwan Varene für die gute und freundliche Atmosphäre innerhalb und außerhalb des Labors und für die Abwechslung währen der kleinen und größeren Pausen gedankt.

Allen fleißigen Korrekturlesern dieser Arbeit, insbesondere Uwe Bovensiepen und meinem Vater danke ich für ihre kritischen Blicke und konstruktiven Vorschläge, die sehr geholfen haben, dieser Arbeit den letzten Schliff zu verpassen.

Zu guter Letzt gilt mein ganz besonderer und persönlicher Dank meiner lieben Familie. Ohne die stete Unterstützung meiner Eltern hätte ich diesen Weg sicher nicht gehen können. Dir liebe Corinna danke ich für deine Unterstützung und dein Verständnis insbesondere in den letzten Wochen und Monaten!